ROTORCRAFT ENGINE AIR PARTICLE SEPARATION

A thesis submitted to the University of Manchester
for the degree of Doctor of Philosophy
in the Faculty of Engineering and Physical Sciences

2012

By
Nicholas Michael Bojdo
School of Mechanical, Aerospace & Civil Engineering

Contents

List of Tables

List of Figures

Abstract

The University of Manchester
Nicholas Michael Bojdo
Doctor of Philosophy
Rotorcraft Engine Air Particle Separation
1st October 2012

The present work draws together all current literature on particle separating devices and presents a review of the current research on rotor downwash-induced dust clouds. There are three types of particle separating device: vortex tube separators; inlet barrier filters; and inlet particle separators. Of the three, the latter has the longest development history; the former two are relatively new retrofit technologies. Consequently, the latter is well-represented in the literature, especially by computational fluid dynamics simulations, whereas the other two technologies, with specific application to rotorcraft, are found to be lacking in theoretical or numerical analyses. Due to their growing attendance on many rotorcraft currently in operation, they are selected for deeper investigation in the present work.

The inlet barrier filter comprises a pleated filter element through which engine bound air flows, permitting the capture of particles. The filter is pleated to increase its surface area, which reduces the pressure loss and increases the mass retention capability. As particles are captured, the filter's particle removal rate increases at the expense of pressure loss. The act of pleating introduces a secondary source of pressure loss, which gives rise to an optimum pleat shape for minimum pressure drop. Another optimum shape exists for maximum mass retention. The two optimum points however are not aligned. In the design of inlet barrier filters both factors are important. The present work proposes a new method for designing and analysing barrier filters. It is found that increasing the filter area by 20% increases cycle life by 46%. The inherent inertial separation ability of side-facing intakes decreases as particles become finer; for the same fine sand, forward-facing intakes ingest 30% less particulate than side-facing intakes. Knowledge of ingestion rates affords the prediction of filter endurance. A filter for one helicopter is predicted to last 8.5 minutes in a cloud of 0.5 grams of dust per cubic metre, before the pressure loss reaches 3000 Pascals. This equates to 22 dust landings.

An analytical model is adapted to determine the performance of vortex tube separators for rotorcraft engine protection. Vortex tubes spin particles to the periphery by a helical vane, whose pitch is found to be the main agent of efficacy. In order to remove particles a scavenge flow must be enacted, which draws a percentage of the inlet flow. This is also common to the inlet particle separator. Results generated from vortex tube theory, and data taken from literature on inlet particle separators permit a comparison of the three devices. The vortex tube separators are found to achieve the lowest pressure drop, while the barrier filters exhibit the highest particle removal rate. The inlet particle separator creates the lowest drag. The barrier filter and vortex tube separators are much superior to the inlet particle separator in improving the engine lifetime, based on erosion by uncaptured particles. The erosion rate predicted when vortex tube separators are used is two times that of a barrier filter, however the latter experiences a temporal (but recoverable post-cleaning) loss of approximately 1% power.

Lay Abstract

The University of Manchester
Nicholas Michael Bojdo
Doctor of Philosophy
Rotorcraft Engine Air Particle Separation
1st October 2012

The similarity between a Bedouin tribesman and Blackhawk helicopter may not be apparent at first. But consider the extreme environment that they endure, and you may see the connection. The desert hinterland provides numerous problems for their 'vital organs', which must continue to function amidst swirling dust and sand clouds. To protect his lungs, the Bedouin tribesman wraps his head with a cloth Keffiyeh; to protect its engines, the Blackhawk helicopter employs an engine inlet sand filter.

However, just as a cloth Keffiyeh is difficult to breathe through, so too is a helicopter sand filter. As air is drawn through a filter cloth, its flow is resisted by friction from the individual pores of the fabric. To maintain the required intake of air, more work is required to overcome this resistance. In the case of the Bedouin tribesman, he must inhale more strongly; in the case of the Blackhawk helicopter, more engine power is required. In the latter, this leaves less power available to lift the payload, thus reducing the helicopter's capability. To complicate matters, as a filter traps more dust particles on its surface, the resistance increases.

The work presented investigates this resistance, which can be influenced by the filter structure, local environment, and the helicopter's operation. By using computers to simulate the air flowing into the engine intake and through the filter, we can calculate the energy lost to friction. This allows us to predict the loss of engine power that a helicopter experiences when using these devices.

Declaration

No portion of the work referred to in this thesis has been submitted in support of an application for another degree or qualification of this or any other university or other institute of learning.

Copyright

Acknowledgments

I would firstly like to express my gratitude to my supervisor, Dr Antonio Filippone. Over the course of the doctoral study Antonio has been a constant source of support and advice both as a mentor and a friend. I am very grateful for his encouragement to get my research out into the open, which has benefited me hugely since I started and will continue to do so — “this is the way forward”. I have enjoyed our fruitful discussions in the office, often going back to basics with a scrap of paper, a pencil and some head-scratching to sort an engineering problem out — a welcome respite from staring at a computer screen all day.

I would like to thank my colleagues and friends in the student village, in particular Alastair and Neil, whose company over lunch or a game of squash has often been a much-needed distraction from the studying. I must also express thanks to Ben, whose proximity to my desk has lent itself well to hearing my constant moaning that, thanks to him, usually turns into laughter.

I must acknowledge the Engineering and Physical Sciences Research council for funding my studies through the Doctoral Training Award scheme. I would also like to thank the Royal Aeronautical Society for funding a conference to the United States, which was of great benefit to my progress.

Finally I wish to thank my family and good friends for their patience, especially during the last six months, when I lacked the time to meet up in Manchester or elsewhere, to make phone calls, or to pay a visit back home. Their love and support carried me through, and I am forever grateful.

Nomenclature

Acronyms & Abbreviations

AC	Air Cleaner
AFOSR	Air Force Office of Scientific Research
AGARD	Advisory Group for Aerospace Research and Development
BERP	British Experimental Rotor Programme
CDF	Cumulative Density Function
CFD	Computational Fluid Dynamics
DL	Disk Loading
DSTL	Defence Science & Technology Laboratory
DVE	Degraded Visual Environment
EAPS	Engine Air Particle Separator
Erfc	Complementary Error Function
FOD	Foreign Object Damage
FQF	Filter Quality Factor
IBF	Inlet Barrier Filter
IPS	Inlet Particle Separator
LIF	Life Improvement Factor
MEDEVAC	Medical Evacuation
MGT	Mean Gas Temperature
MTBO	Mean Time Between Overhaul
MURI	Multi-disciplinary University Research Initiative
PDF	Probability Density Function
PQF	Pleat Quality Factor
PSD	Particle Size Distribution
SAE	Society of Automotive Engineers
SFC	Specific Fuel Consumption
TOP	Takeoff Power
TX	Yarn Tex
VTS	Vortex Tube Separator

Roman Symbols

$\vec{a}$	acceleration
A	area
A_{inj}	particle injection area
b_{1-4}	drag model coefficients
c	particulate mass concentration
c_b	blade chord length
C_d	drag coefficient
C	viscous resistance coefficient
C_f	overall friction factor
C_T	thrust coefficient
d	diameter
d_{50}	cut diameter
$\overline{d}$	algebraic mean diameter
D	drag
D	inertial resistance coefficient
D_H	hydraulic diameter
$\hat{e}$	unit vector
E	overall efficiency
f	friction factor
f	number of particles in size range
F	force
g	gravitational constant
g	local duct perimeter
H	pitch
H_{ku}	Kuwubara hydrodynamic factor
I_t	turbulence intensity
k	coefficient of permeability
k	empirical constant
k_p	projected area shape factor
k_r	engine erosion factor
k_v	volume shape coefficient
K	Kozeny constant
K_{1-4}	empirical parameters for packing fraction
l_t	turbulence lengthscale
L	length
$\dot{m}$	mass flow rate

n	number
n_c	total number of particles per unit volume of dust cake
N_B	number of blades
N_p	number of particle size groups
N_R	number of rotors
N_{GG}	gas generator speed
p	static pressure
P	total pressure
P	penetration
Pe	Peclet number
q	dynamic pressure
Q	volume flow rate
r	radial position
R	radius
R_R	main rotor radius
Re	Reynolds number
s	spacing
S	scavenge proportion
S_v	surface area per unit volume
St	Stokes number
t	time
T	main rotor thrust
u	air velocity
U_t	terminal velocity
v	particle velocity
V	volume
w	main rotor downwash
W	power
Z	length

Greek Symbols

α	filter packing fraction
β	engine erosion correlation component
ϵ	porosity
ϕ	ingested particle diameter
φ	particle elongation ratio
Φ	particle shape factor
Γ_v	vortex strength
Γ_w	total wake strength
η	grade efficiency
κ	dynamic shape factor
μ_g	gas viscosity
θ	filter angle
θ_{pl}	pleat angle
ρ	density
σ	rotor disk solidity
ς	particle flatness ratio
τ_w	overall wall shear stress
υ	void function
Ω_s	wake convection frequency
Ω_R	rotor rotation frequency
ξ	layer efficiency
Ψ	Wadell sphericity
∞	freestream value

Mathematical Symbols

∇	difference operator
$\delta_{i,j}$	Kronecker delta
μ	algebraic mean diameter
μ_γ	geometric mean diameter
Π	product operator
σ	algebraic standard deviation
σ_γ	geometric standard deviation
Σ	summation operator

Subscripts

$[\cdot]_0$	number mean
$[\cdot]_3$	mass mean
$[\cdot]_{32}$	specific surface mean
$[\cdot]_{ae}$	aerodynamic
$[\cdot]_{avg}$	average quantity
$[\cdot]_A$	of intake approach
$[\cdot]_{bu}$	buoyancy
$[\cdot]_{ch}$	of pleat channel
$[\cdot]_{cn}$	centrifugal
$[\cdot]_{co}$	of collector
$[\cdot]_{core}$	of core flow
$[\cdot]_C$	of cake
$[\cdot]_d$	diffusional
$[\cdot]_D$	of intake duct
$[\cdot]_{eff}$	effective
$[\cdot]_E$	of single fibre (efficiency)
$[\cdot]_f$	of fibre
$[\cdot]_{fed}$	quantity fed
$[\cdot]_F$	of filter
$[\cdot]_{FC}$	filter capacity
$[\cdot]_g$	of gas
$[\cdot]_h$	of helix
$[\cdot]_i$	inertial
$[\cdot]_i$	interstitial
$[\cdot]_{inj}$	of particle injections
$[\cdot]_{inter}$	between yarn or fibre
$[\cdot]_{intra}$	within yarn or fibre
$[\cdot]_l$	long
$[\cdot]_m$	intermediate
$[\cdot]_m$	by mass
$[\cdot]_n$	short
$[\cdot]_N$	non-woven
$[\cdot]_p$	of particle
$[\cdot]_{pc}$	of collected particulate
$[\cdot]_{pe}$	escaped/unfiltered particulate
$[\cdot]_{pg}$	of gas-particle mix

$[.]_r$	radial component
$[.]_r$	interception
$[.]_re$	recovered
$[.]_s$	of scavenge conduit
$[.]_s$	sieving
$[.]_s$	superficial
$[.]_{scav}$	scavenge
$[.]_t$	of tube
$[.]_v$	of separating region
$[.]_v$	pertaining to volume
$[.]_v$	by volume
$[.]_v$	of vortex
$[.]_w$	of wake
$[.]_W$	woven
$[.]_z$	axial component
$[.]_\theta$	tangential component

Superscripts

$[.]^+$	dimensionless
$[.]^*$	optimum value
$[.]'$	corrected
$[.]'$	fluctuating

Chapter 1

Introduction

This chapter introduces the thesis, which outlines the context, details the motivation, and provides a description of the problem. At the end of the chapter can be found a summary of the work to be presented in this thesis.

Helicopters are required to operate in all manner of environments, but none poses a greater risk to the engine than one rich in dust and sand. As a helicopter operates to and from unprepared landing sites its downwash interacts with the ground, causing great plumes of sediment to be disturbed and lofted into the atmosphere. At the same time the engine is working close to full power to hover the rotorcraft, and draws a large amount of mass flow. In this situation an unprotected engine may ingest vast quantities of hard, high-inertia particles that can be particularly destructive to key components. The erosion of compressor blades, the glazing of combustion chamber walls and turbine blades, and the plugging of turbine blade cooling passages can all occur, contributing to a rapid reduction in the engine lifetime. In addition to the fiscal and temporal costs of increasing the number of engine overhauls, this event can be extremely hazardous to the pilot, who may experience a deterioration of engine performance and a shortfall of power - never a desirable contingency to deal with. As the number of desert operations have grown, it is hardly a surprise that the last 30 years have seen a massive advancement in engine protection technology.

Engine protection generally takes one of two forms: blade coatings; or intake filters. The former technology is relatively nascent in its application to helicopter engines and does not completely solve the problem [1]. The latter are commonly referred to as *Engine Air Particle Separators* or EAPS (*eeps*) systems. The technology is well developed and successful at preventing particles getting into the engine but comes with the price of a performance penalty. It is this performance penalty upon which the current work is based. The performance penalty arises from a disturbance to the air-particle streamline that must be enacted by the filter in order to capture or separate the particle from the air. Be it a filter fibre or deflector vane, the mechanism for disturbance exerts an aerodynamic drag force on the air, which is reflected in a loss of pressure across the device. If particles are arrested within the device, they too add to the drag force and cause pressure loss. The pressure deficit at the engine face means more fuel flow is required to achieve the same mass flow hence output power, leaving the engine with less capability for tasks such as heavy lift or takeoff in hot & high conditions. Supplementary to the added penalty of the system weight, some intake EAPS systems also require auxiliary power from the engine in the form of compressor bleed air, which also contributes to the power shortfall.

The conclusion to this is that despite preventing or at least mitigating the destructive effects of sand ingestion, the use of protection for helicopter engines is not without its costs. It is an essential piece of technology that performs its main duty well, but anecdotal evidence suggests that due to the performance loss, the protection is sometimes not worth having [1]. In some cases the performance loss is a function of time, which means the device needs constant monitoring and maintenance to avoid unanticipated failure. This contributes to through-life costs, which cover all aspects of procurement, maintenance, and replacement units, and must be considered in any business case. Therefore it can be appreciated that for operators working in dust-laden climes there is a ongoing debate about the worth of particle separators. To enrich this debate, it would be useful to predict the performance of a device for a given set of boundary conditions, in order to anticipate behaviour and ultimately operational merit. The work presented herein aims to achieve such a purpose, through investigation by qualitative and quantitative engineering analysis.

1.1 Motivation

Every form of automation requires some form of propulsion in order to move, usually provided by an engine that converts stored energy into kinetic energy. As with all energy conversion, the process is rarely 100% efficient: some energy is lost, usually to heat through friction, or through incomplete combustion. With this taken into account, engines are designed to deliver a certain power output for a given fuel input, and demonstrate this on the test bed. However, when installed in the airframe it is often found that the power delivered by the engine is lower than predicted. The sources of this shortfall are known as *installation losses*. The shortfall is common to all installed engines, but varies according to the engine type, the engine housing, the local environment, and the operation of the vehicle. Helicopter engines are no exception to this, and it is this power deficit that forms the wider context of the current work.

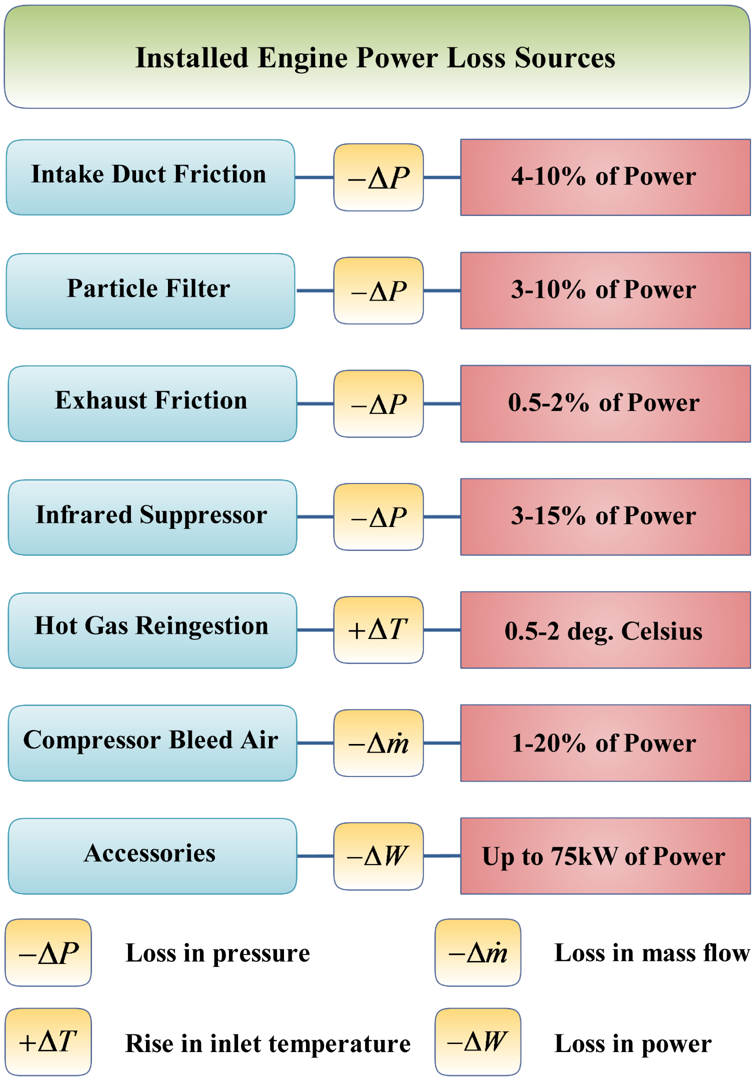

Figure 1.1: *Diagrammatic summary of typical sources of installed engine power loss, according to Prouty [2].*

The field of aerospace engineering under which installation losses fall is called *engine-airframe integration*. Within the discipline of rotorcraft it encompasses all aspects of incorporating the powerplant into the helicopter, from the mechanical links between the power shaft and the rotor gearbox to the blending of the air intake with the airframe. The loss sources are numerous, as neatly summarised by Prouty [2], an adaptation of which is given in Figure 1.1. Each source causes either a loss of pressure, a loss of mass flow, an increase in inlet temperature, or a combination of all three. The suggestion from the ranges given in Figure 1.1 is that evaluating the magnitude of these losses is rather difficult; no practical methods currently exist to properly quantify each installation loss, which means the shortfall in useful power may not often be realised until prototype testing. If these installation losses were quantified, it would be possible to predict the true helicopter performance at an earlier stage in the development process, or update established performance charts accordingly with new power envelopes. This condition represents the essence of the motivation behind the current work.

1.2 Problem Description

Of the sources listed in Figure 1.1, the particle separator is the most conducive and presently appropriate technology to extend to engineering analysis. It would be ineffectual to build up a model to predict duct and exhaust friction loss and exhaust gas reingestion without the specific geometry of the helicopter in question. The amount of compressor bleed and power for engine-mounted accessories is also somewhat difficult to ascertain without knowledge of the helicopter role, while infrared suppressors are applicable only to relatively small group of military aircraft. However, particle separators play a vital role in prolonging engine life and are employed widely in both the civil and military sectors. They are a relatively new technology whose development is ongoing but continually burdened by the unavoidable loss of engine performance.

The effect on the engine is manifold. Firstly, use of an EAPS system can incur a loss of mass flow, which means the compressor must work harder to achieve the required output pressure with a reduced amount of air. The additional work is performed by the turbine, whose mean gas temperature (MGT) rises in response to the extra fuel burn required to service the increased demand of the compressor. A higher MGT is not favoured since it reduces the lifetime of the turbine blades, while the additional fuel required to achieve the same power output increases the specific fuel consumption (SFC), a metric of engine efficiency (rate of fuel burn). The loss in pressure has a similar effect: if the compressor applies the same pressure ratio to air of a reduced pressure, then more fuel is burned to raise the temperature to supply the turbine with enough energy to achieve the same power output. A higher MGT creates an additional threat for military vehicles: a raised exhaust temperature produces a more visible infra-red signature. These negative effects are associated with engine performance.

Another problem caused by pressure loss is engine operability, which refers to the transient condition of the engine and its ability to reach steady state. Combining the use of an EAPS device and bleed flow to service onboard systems can result in an unsteady drain on engine power. The drop in pressure has adverse effects too: an operating limit known as the engine *surge line* indicates, for a range of mass flow, the points at which the inlet pressure is so low that the compressor blades are at risk of aerodynamic stall. The design point steady state operating line indicates a “safe” range of mass flows; any source of inlet pressure loss nudges the operating line closer to the surge line reducing the so-called *surge margin* hence creating operability problems. In a similar vein, an uneven distribution of pressure across the engine face can result in low pressure "sinks" at certain azimuthal positions. A compressor blade passing through such areas may underperform and possibly even stall, causing a reduction in stage efficiency and a vibration-inducing imbalance of aerodynamic loads. The non-uniform distribution is caused by interruptions to the intake flow as it passes through an EAPS device. These problems are summarised in Figure 1.2.

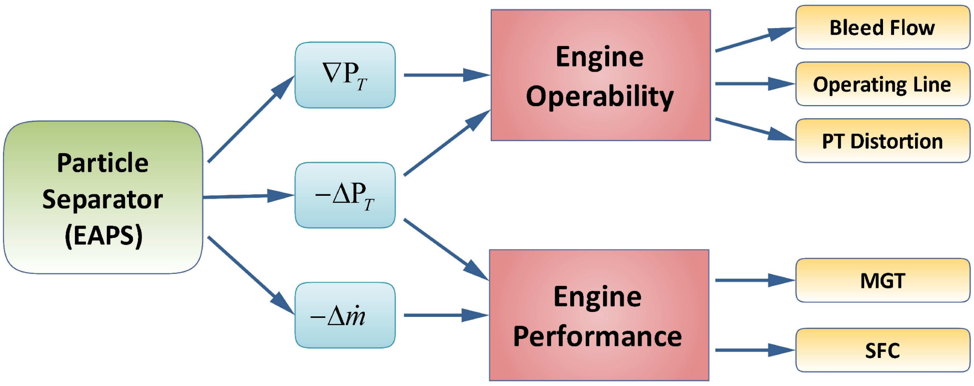

Figure 1.2: *Diagrammatic summary of the performance pitfalls of employing EAPS systems.*

Applying engineering analysis to gain a greater understanding of how these devices work may help to expedite improvements in design while providing predictions of their performance in order that an unknown quantity from Figure 1.1 may be eliminated. The aims of this thesis are therefore:

1. To identify and investigate the different types of EAPS systems.
2. To apply engineering analysis, where appropriate, to ascertain device performance.
3. To compare and contrast the different EAPS systems.
4. To make recommendations for device improvement through optimised design.

1.3 Summary of Work Presented

To introduce the subject, a background study on all physical processes and mechanisms involved in engine air particle separation are presented in Chapter 2. This encompasses the generation of a dust cloud by the helicopter downwash, the subsequent transport of material to the engine, the scientific classification of such material, and the devices employed to ensure it does not reach the engine. The damage caused by the ingestion of such particles in the event that they are not removed is also discussed.

To quantify the performance of engine air particle separating systems requires a good deal of theory, which is corralled from the literature and presented with systematic order in Chapter 3. The theory section begins with the governing equations of particulate dispersion and particle equations of motion, before elaborating on methods adopted to determine the severity of a dust cloud. Two of the three EAPS systems are amenable to analytical methods, which are subsequently detailed. The chapter ends with a selection of methods adopted to facilitate a comparison of the particle separators available to helicopter engines.

A large part of the present work has been performed using computational fluid dynamics (CFD). Chapter 4 describes the methodology followed to generate the data required to enact a parametric study into one of the EAPS devices. The results of this study are then described in full in Chapter 5, with analysis of the flow field and explanation of the phenomenological effects that are exploited to expedite superior device performance.

The latter half of the work presents the main findings of the study, putting to practical use the results obtained from the parametric study. This part is split into two main themes: design and performance. Chapter 6 proposes a design protocol for the device studied using CFD, and verifies this with a performance case study. Chapter 7 pits each EAPS device against each other to assess and compare device efficacy.

The work is completed with a summary of conclusions in Chapter 8 and suggestions for further work in Chapter 9.

Chapter 2

Background & Literature Survey

This chapter contextualises the study with a review of the brownout problem — the key concern for helicopters operating in dust-rich environments. It then introduces the technology of particle separation and presents a literature survey of the three main technologies employed to protect engines from sand ingestion.

2.1 Introduction

Dusty environments are found all across the globe, as a result of millions of years of wind erosion and other geomorphologic processes. Thanks to their operational versatility and ability to land on unprepared sites, helicopters frequently encounter such environments. In certain areas of operation such as south-east Asia and the Middle East, the dry and dusty conditions are found at high altitudes, where the air is less dense and sometimes hotter. This medley of harsh conditions can be particularly troublesome to a helicopter engine, which must continue to deliver required power for the task in hand. If no protection is provided to the engine, the performance deteriorates rapidly due to damage by sand and dust. If there is any loose sediment around the landing site, it will be disturbed from rest by the rotor downwash as the helicopter lands or takes off. If the sediment is small enough, a dust cloud forms and the chances of particle ingestion are increased. The degree of ingestion is dependent on a number of factors that relate to the properties of the sand, the design parameters of the rotor, and the location of the intake with respect to the rotor disk. Once it is established that a helicopter needs protection from sand ingestion, there are three main technologies available to implement at the engine intake, all of which vary in their method of separating particles. The first part of this literature review is intended to contextualise the whole study by describing the problem of brownout, and why this is hazardous to the helicopter engine's health. This provides impetus for the employment of an EAPS system. The chapter introduces these particle separating technologies with a survey of the current literature that pertains to their function.

2.2 The Brownout Problem

Brownout is a very serious problem for helicopter pilots. It occurs when the helicopter is landing or taking off above a loose sediment bed such as the desert floor. In normal forward flight, a helicopter generates lift by inducing a mass of air to flow through the rotor disk. The downward momentum of air is balanced by an upward lift force on the rotor disk which keeps the helicopter airborne. The flow of air leaving the rotor disk is known as the *downwash* and is delineated by a series of *trailing blade tip vortices* that convect towards the ground. Tip vortices are an aerodynamic consequence of the difference in pressure between the two surfaces of a lift-generating blade. The vortex is characterised by a low pressure core which is sometimes visible if the moisture in the air condenses. This phenomenon is depicted in Figure 2.1.

Figure 2.1: *The formation of trailing blade tip vortices, visualised by the condensation of water in the low pressure core. (Photograph © the Author).*

The blade tip vortices and downwash combine to form the main rotor wake. In dusty environments, the impingement of the wake flow and the tip vortices on the ground causes particles to be disturbed from the sediment bed, leading to the formation of a dust cloud. The dust cloud is a dangerous event for the pilot. As the intensity increases, a situation known as *degraded visual environment* (DVE) occurs, whereby the pilot loses the spatial orientation cues required to safely fly the aircraft. It has been reported that the occurrence of brownout is the primary cause of human factor related mishaps during military operations [3], causing losses of aircraft and personnel [4]. The problem is not limited to airworthiness issues; blade erosion and wear on various mechanical parts, and a deterioration of engine performance due to the ingestion of particulate are also caused by brownout clouds. The latter of these is of the greatest interest in the present work.

The brownout phenomenon is studied to gain a greater understanding of the particulate that an engine might ingest. A dust sample from a desert environment will contain a dispersion of particle diameter, shape, hardness and mineral composition, all of which are important properties for the prediction of EAPS performance and engine deterioration. The range of diameters is represented by a particle size distribution (PSD) which describes the proportion by mass, number or other dimension of a given particle size. The PSD at the engine intake is dependent on the mechanisms causing the formation of the brownout cloud during operations close to the dusty ground. However, before the dynamics of the brownout cloud can be understood, it is first necessary to understand the broad characteristics of the flow during operations near the ground. This is helpfully described by Philipps & Brown [5], who describe the transition from hover to moderate forward flight out of the influence of the ground.

In the so called *hover mode*, the downwash impinges on the ground and is forced radially outward in a *groundwash jet*, as depicted in Figure 2.2a. As a result of wake instabilities and dissipation, the groundwash jet stagnates, inducing the flow to recirculate back towards the rotor. As the rotorcraft begins to move forward, the flow enters the *recirculatory mode*, where the "donut-ring" shape found in hover becomes distorted resulting in the formation of a large vortex at the rotor disk leading edge, as shown in Figure 2.2b. This causes an appreciable portion of the flow near to the ground to be reingested through the forward portion of the rotor; a particularly dangerous mode if that air contains a high concentration of dust. At higher forward speeds, the distorted donut widens to form a characteristic bow-shape, and passes under the rotor, as seen in Figure 2.2c. This is known as the *ground-vortex mode*. Disturbed dust may reach appreciable heights but cannot be reingested through the rotor. At a certain forward speed the ground-impingement point passes the rearward extent of the rotor, and the flow structure is said to be very similar to that created by the rotor when operating in *free air*. This is illustrated in Figure 2.2d. The formation of the subsequent brownout cloud during modes of operation near the ground is discussed in the proceeding sections, followed by a discussion of what this means for the engine.

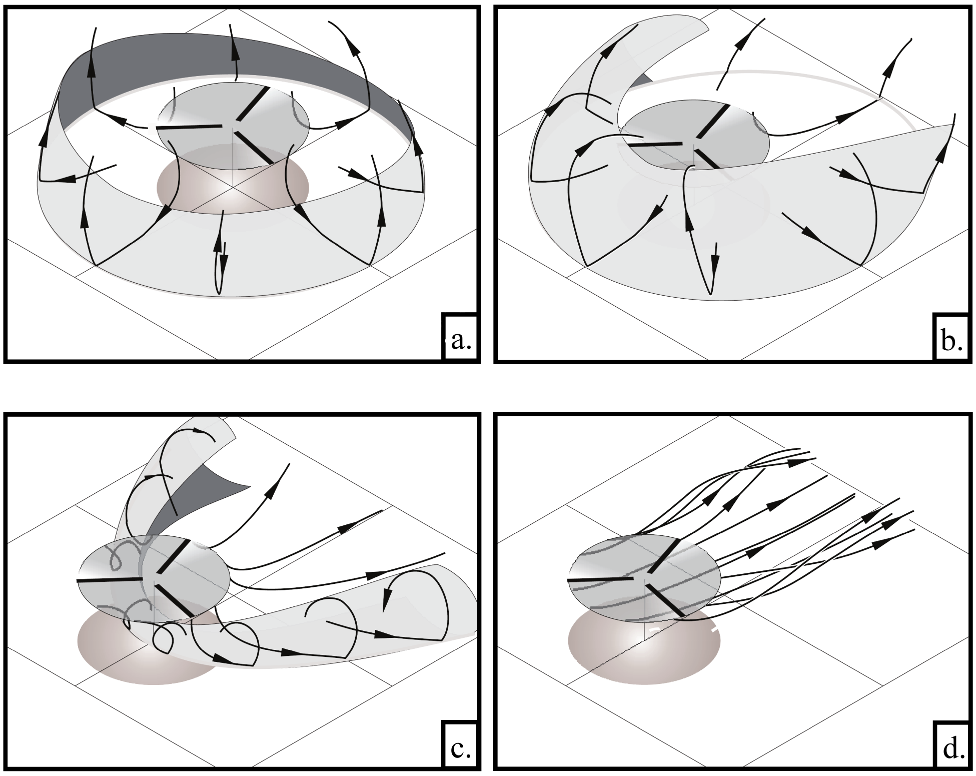

Figure 2.2: *Flow modes and associated geometry of the brownout cloud (as represented by the shaded surface) that is produced by a rotor when operating close to the ground during: a. hover mode; b. recirculatory mode; c. ground vortex mode; d. free air mode. Source: Ref. [5].*

2.2.1 Dust Cloud Generation

Recent investigations into the study of the brownout phenomenon have been motivated by anecdotal evidence, which suggests that a developing dust cloud can vary in severity and extent for different rotorcraft due to certain rotor design features. The difficulties encountered in modelling brownout caused by rotor wake interaction with the ground are related to the unsteady resultant flowfield, non-uniform particulate concentrations, and the transfer of momentum and energy between the carrier and sediment phases. A short review of the current literature on the study of brownout is included in the work of Johnson *et al.* [6], in which a series of experiments were performed with a two-bladed rotor system in hover over a sediment bed. Using laser-sheet imagery, the effects of rotor wake interaction with the ground and the role of vortices in sediment uplift were studied.

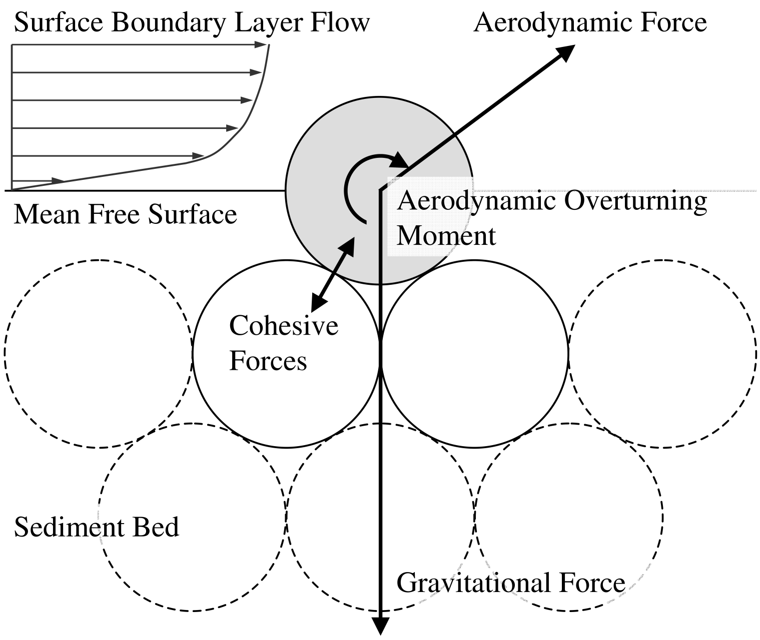

Figure 2.3: *Forces acting on sediment particles at rest beneath a boundary layer flow. Adapted from Ref. [6].*

The work describes the mechanism of mobilisation and transport of loose particles from a sediment bed. Much of the theory of sediment mobilisation is described in a book by Bagnold [7]. Bagnold observed that to be released from rest, the mean surface boundary flow over a particle in the sediment bed must exceed a *threshold friction velocity*, at which the aerodynamic forces acting on the particle exceed the gravitational and cohesive forces holding it down, causing an aerodynamic overturning moment. These forces are illustrated in Figure 2.3. Further release of particles was observed to occur due to bombardment by saltating particles and particles re-ingested through the rotor disk. Subsequently, three main transport modes occur: surface creep, saltation, and suspension. It is the latter of these that must occur if the generation of a brownout cloud is to occur. Suspension in the flow outside of the sediment bed boundary layer occurs if the vertical drag on the particle is greater than its immersed weight. In atmospheric winds, whenever the vertical component of the carrier fluid velocity is greater than or equal to the settling velocity of the particle, suspension will happen. Once suspended, the particles follow trajectories based on the relative magnitude of the forces acting upon them.

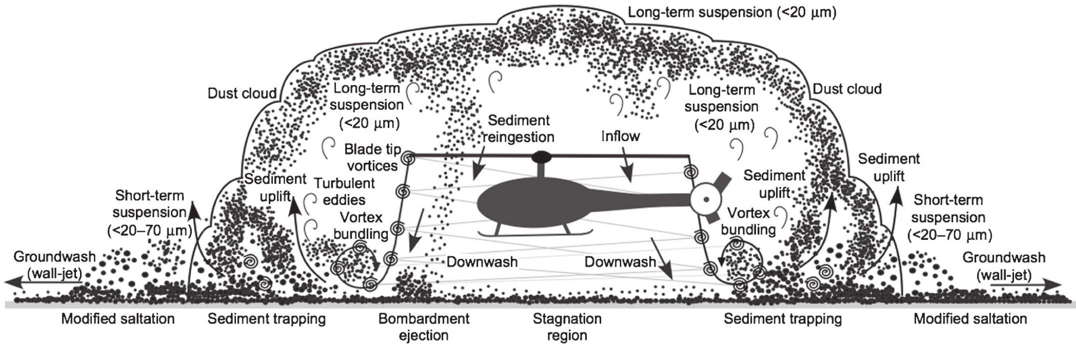

Figure 2.4: *A schematic of near-ground aerodynamics and the subsequent brownout dust cloud problem. Source: Ref. [3].*

The same process is observed with tip vortices impinging on the ground during a helicopter landing. The horizontal component of the vortex first augments the downwash to beyond the threshold velocity, while the vertical component lofts the particle upwards. As they emanate radially outwards, younger vortices are observed to roll up and merge into older vortices [6], which augments the upwash velocity and lofts particles higher into the air. The consequence of this is significant uplifting of particles into the flow domain surrounding the rotor disk, in the form of a brownout cloud. This whole process is depicted beautifully in Figure 2.4.

Since some of the downwash flow is ultimately re-ingested through the rotor disk, it follows that some particles may arrive at the engine intake. The size distribution of these particles is dependent on the upwash velocity; the upwash velocity is dependent on the strength and frequency of the tip vortices. The downwash too plays a part by adding to the surface shear, which increases as the rotorcraft approaches the ground. The successful prediction of a brownout cloud therefore entails the accurate prediction of the three-dimensional, unsteady flowfield combined with calculations of particle trajectories and non-uniform particulate concentrations.

2.2.2 Brownout Modelling

In recent years, several groups worldwide have been conducting research into the brownout problem. Most notably, a team led by Gordon Leishman at the University of Maryland has been conducting a Multi-disciplinary University Research Initiative (MURI) since 2008, awarded by the Air Force Office of Scientific Research (AFOSR), to comprehensively investigate rotorcraft brownout, investigating through small-scale experiments and numerical methods fundamentals of rotor and airframe aerodynamics in near-ground operation, fundamentals of particle suspension, and mitigation techniques [6], [8], [9], [3]. Elsewhere, Wachspress *et al.* at Continuum Dynamics have been developing high fidelity brownout models for real-time flight simulations [10], [11], [12], [13]; while Phillips & Brown *et al.* spent a period of time investigating the effects of rotor parameters such as blade twist and tip shape on the resultant dust cloud [14], [5], [15]. The field suffers from a lack of real full-scale experimental data, although the recent series of "Sandblaster II" tests conducted by the U.S. Army in 2007 at the Yuma Proving grounds in Arizona is a useful and well-cited reference [16].

Two routes for mitigation that utilise the results of these studies are explored in the literature. The first route is to alter the geometry or operating conditions of the rotorcraft in such a way that the resulting brownout cloud is modified to a shape that is more conducive to the piloting task (see Refs. [14], [9]). This follows the unexpected success of the infamous "BERP" profiled blade tip found on EH-101 Merlin rotorcraft, whose unique twist is thought to be responsible for the "donut-effect" that creates the brownout-reducing curtain of clean-air around the vehicle. The second route is to employ an onboard system to augment the pilot's conventional cues by using, for example, sensors or electronically-generated imagery (see Refs. [17], [18], [19]).

A requirement for both routes is a deeper understanding of the evolution of the dust cloud, which is increasingly being met by high-fidelity computational models. A substantial introduction to the subject and a review of the recent progress in brownout modelling is given by Phillips & Brown [5], in particular comparing the merits of an Euler approach preferred by the same authors, versus a Lagrangian approach favoured by Leishman *et al.* and Wachspress *et al.*. In the Euler approach, the particulate load in the flowfield is represented by a density distribution, whose evolution is governed by a particle transport equation for the fluid convection and diffusion due to the particles' random motion. In the Lagrangian approach, particles are individually tracked as they respond to changes in the drag force exerted on them by the fluid. Their trajectories are determined numerically by integrating the equations of motion. The Lagrangian model is favoured for its straightforward use and versatile application, whereas the Euler approach is considered more mathematically rigorous and does not suffer the inaccuracies of the former that are caused when particles become diffuse within the flow [5]. The comparison of methods is made difficult by the lack of real-world, full-scale data, and in any case this field is relatively young. Therefore it could be considered premature to judge a particular method on its current facility.

2.2.3 Brownout Severity

While investigations into brownout mitigation through design are ongoing, the fact that certain rotor features influence the developing dust cloud additionally implies that there may be a difference in brownout severity, shape and size from one rotorcraft to the next. The Sandblaster II program, among achieving other outcomes, showed this to be true. Six rotorcraft of varying rotor characteristics and disk loadings were tested. Test airframes performed a hover-taxi manoeuvre in such a way that the nose of the rotorcraft was always clear of the developing dust cloud (Figure 2.2c) to minimise risk. Samples of the dust cloud concentration were taken at several locations that varied in distance from the rotor tip and height above the ground. The three main objectives of the effort were to develop quantitative field information relating to:

1. Dust cloud densities and particle size distributions
2. Spatial distributions (heights, distances from rotors)
3. Relationship of dust cloud densities to downward rotor force referred to as disk loading

This is relevant to the present work, since the performance of an EAPS device, and indeed engine deterioration, may be dependent on the concentration of the dust ingested by the engine. While there are no data pertaining to particulate density at the engine intake, the results of the Sandblaster II provide a useful starting point and can be used in conjunction with current theories to estimate the severity of the brownout cloud for a given helicopter. These are given in Table 2.1. The sampling station locations are shown in Figure 2.5.

Table 2.1: *Mean Dust Cloud Concentrations for at Each Sampler Height for 6 Different Rotorcraft at the Yuma Proving Grounds, Arizona [16].*

	Disk	Mean Dust Concentration (gm^{-3})						
	Loading	F	A1	A2	B1	B2	B3	B4
Airframe	(Nm^{-2})	(0.5m)	(0.5m)	(1.4m)	(0.5m)	(2m)	(4.5m)	(7m)
UH-1	240	—	—	0.31	—	0.22	0.25	0.15
CH-46	287	—	—	0.43	—	0.64	0.45	0.43
HH-60	383	1.20	2.09	1.16	2.50	2.19	1.90	1.59
CH-53	479	1.64	3.33	1.96	2.11	1.98	1.49	1.44
V-22	958	1.10	3.47	1.62	1.17	1.28	0.11	1.05
MH-53	479	1.75	3.19	2.11	0.44	0.49	0.49	0.42

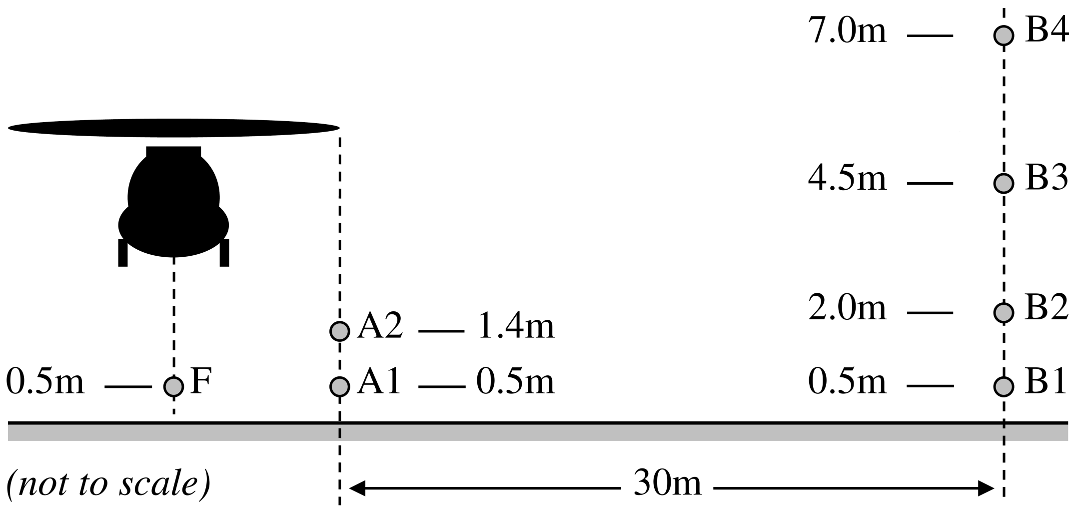

Figure 2.5: *Brownout dust sampling locations used in Sandblaster II experiments [16].*

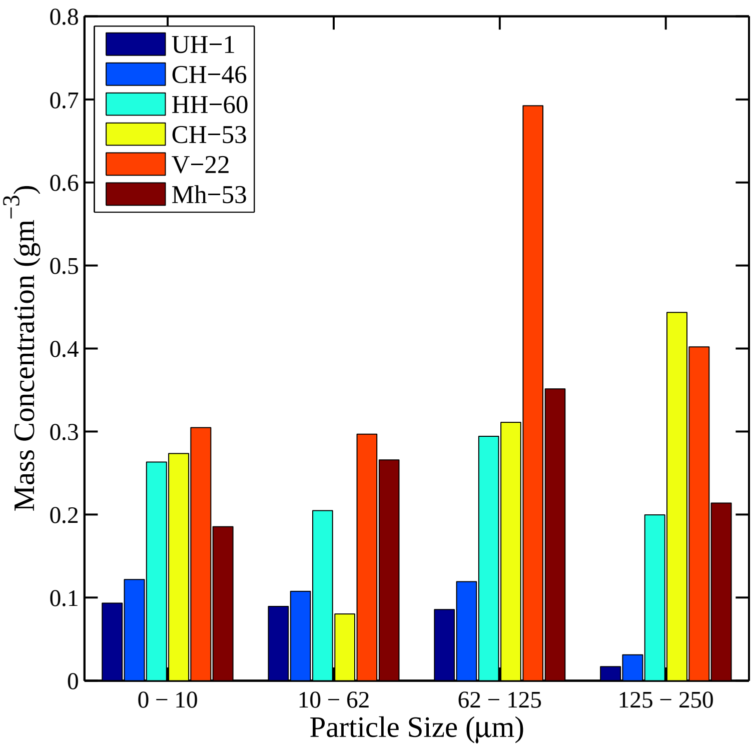

Figure 2.6: *Mass concentrations by particle size band at the rotor tip location for six rotorcraft, as taken from Sandblaster II tests [16].*

The results generally imply that a higher disk loading creates a denser dust cloud, due to a stronger groundwash jet. The samples taken were also graded into size bands, shown in Figure 2.6. These data show that a bigger proportion of larger particles are lofted into the air at the rotor tip as disk loading is increased. This is expected due to the larger downwash pressure and higher velocity groundwash jet. However these date do not link the dust concentration at the rotor disk to the strength of the vortical upwash mechanism.

The link between rotor design parameters and dust cloud density is explored numerically in the work of Phillips & Brown [5], who observe that for the same thrust coefficient, a lesser twisted blade produces a more diffuse dust distribution, however the reverse of this is observed when the configuration is a tandem rotor [14]. The same authors also investigated the effect of blade tip shape, concluding that there was no observable effect among the shapes studied other than for the BERP rotor which exhibited a greater preponderance of dust in the ground vortex and less immediately below the rotor than the other shapes. Interestingly, the predicted density distribution does not completely corroborate with the observations made on the EH-101 Merlin, hence there may be other rotorcraft parameters that affect the brownout cloud, such as fuselage size and blade root cutout. A study by Wadcock *et al.* [20] compared a CFD analysis of the EH-101 Merlin airframe with an experimentally-backed CFD analysis of a UH-60 Blackhawk. It postulates that the superior brownout behaviour of the EH-101 could be due to bluff nature of the cabin body, which extends unusually far forward to 70% of the rotor radius and may consequently reduce the outwash in the 3rd azimuthal quadrant, hence reduce shear stress at the sediment bed and uplift fewer particles. The paper also provides substantial images, both experimentally and computationally derived, of the UH-60 and EH-101 rotor induced flowfields that could be useful for engine intake analysis. Elsewhere operators have suggested the cause may be the substantially higher downwash strength (typically around 12% larger) arising from the lift distribution created by the unique twist of the BERP blade.

While the recent studies into the brownout phenomenon have given the community a greater understanding of the physics involved, it appears that CFD models have yet to demonstrate conclusive correlation between particular rotorcraft design parameters and cannot predict cloud intensity for the generic helicopter. Efforts to mitigate brownout are, to a degree, confused by the number of rotorcraft parameters, some of which are aerodynamically interdependent, that can influence the vortical wake. They include: rotor disk loading, blade loading coefficient, tip speed, rotational frequency, number of blades, tip shape, number of rotors, rotor configuration, fuselage shape, type and location of the tail rotor. To help focus new research, a study by Milluzzo & Leishman [3] took a more qualitative approach by looking at the growing body of photographic and videographic evidence of brownout generation and linking dust cloud severity to particular design parameters and operational characteristics of a given rotorcraft. Severity is based on several factors: the density of the brownout cloud; the horizontal and vertical coverage of the cloud; the tendency for recirculation of dust through the rotor wake; and the relative distance of the rotor wake off the ground when the dust cloud starts to develop. A low order correlation is proposed, based the assumption that the resultant shear at the ground (the fundamental cause of particle mobilisation) is proportional to some combined average of the downwash flow velocities and the flow induced by the convecting blade tip vortices. By estimating the average downwash velocity, the total wake strength, and the trailing vortices' impingement frequency with classical or low order methods, the rapidity at which the brownout dust cloud develops can be linked to the key rotor design parameters.

2.2.4 Dust Concentration at the Intake

The purpose of the brownout study is to provide context to the current work. It is also conducted to gain a greater understanding of the conditions at the engine intake that will become integral to EAPS design. It has been shown that the severity of the brownout cloud and therefore the dust concentration is unique to the rotorcraft in question; the same holds true of the intake position and inflow conditions. The intake mass flow rate is dependent on the current operational mode (hover or forward flight) and the size of the engine, which is chosen to meet the requirements of the given rotorcraft. Generally speaking, the larger the aircraft the larger the mass flow requirement. The mass flow requirement is met by increasing the size of the engine or the number of powerplants, and must be set very early in the rotorcraft design. The decision is key, because the placement of the engine determines many other rotorcraft systems such as the power transmission, exhaust duct, and intake/airframe integration; and is paramount to setting weights & balance.

While the downstream design effects require that the engine position is decided early, its position is rather arbitrary. However from the standpoint of EAPS design, the engine position thence intake location may have a significant effect on the mass of particulate ingested. In his book on intake aerodynamics, Seddon notes that an intake face orientated parallel to the flow (i.e. a sideways- or upwards-facing intake) can offer a degree of protection by inertial separation [21]. In most light, single-engine helicopters the powerplant is located behind the main rotor mast, with its turboshaft axis aligned with the horizontal axis of the vehicle and its exhaust to the rear, above the tail boom as modelled on the AgustaWestland AW109 in Figure 2.7a. Occasionally its axis is at an angle such that the exhaust is beneath the tail boom, for example on the Robinson R-66 pictured in Figure 2.7b. This arrangement is more typical for civilian aircraft (see also MD500) due to the low stealth capabilities of an unshielded hot exhaust. Despite their similar placement, these engines are served by intakes in different locations. The two AW109 intakes are located on each side of the aircraft, under the rotor mast facing sideways, whereas the R-66 intakes face forward and are lodged in the sides of the main rotor cowl. In a third embodiment of rearward-located powerplants, the inlets of the twin-engine Eurocopter EC135 are shrouded within a crowded plenum chamber, as shown in Figure 2.7c. In this example there is no visible profiled intake on the airframe to serve the engine — the installed engine performance is not known but it is assumed that the required mass flow is met by drawing in air through the gap between the engine compartment cowl and the rotor mast. In the three examples mentioned, the engine air intake is shown in three different locations.

Figure 2.7: *Different engine installations and intake types: a. AgustaWestland AW109, sideways-facing intake; b. Robinson R-66, submerged engine; c. Eurocopter EC135, plenum chamber installation; d. Sikorsky S-76, forward-facing side intake; e. Eurocopter Super Puma, pitot intake*. (*Image reproduced under Creative Commons licence (CC BY-NC 2.0), © U.S. Pacific Fleet).*

In the same book [21], Seddon looks at helicopter intakes from an aerodynamic perspective. He breaks the intakes into four distinct types:

1. Pitot intake
2. Forward-facing side intake
3. Sideways-facing intake
4. Plenum chamber installation

As the engine size and number increases, the first two types become more common. Moving from light to medium helicopters, the engines (usually two or three in number) migrate outboard and forwards out of the rotor mast shadow to utilise ram pressure during cruise. This is exemplified by the Sikorsky S-76 in Figure 2.7d. On medium-lift rotorcraft such as the Eurocopter Super Puma shown in Figure 2.7e, the engines sit side-by-side above the cabin, with their intakes facing into the flow. This is the classic *pitot intake* mentioned by Seddon, which differs from the second type by virtue of its isolation from airframe boundary layer. Forward-facing side intakes do benefit from ram pressure recovery, but receive air at a lower total pressure due to friction losses with the section of airframe ahead of the intake.

The intake location is significant to particulate ingestion by the engine during a brownout landing. While simulations show that during hover much of the sediment is uplifted in an area greater than one rotor radius (see Figure 2.8a), anecdotal evidence suggests that in some cases the uplifted dust can be reingested through the rotor disk forming a large dome-shaped cloud that engulfs the helicopter. Some of this dust is likely to reach the engine intakes. Furthermore, during low-speed taxiing in a brownout cloud, a helicopter can enter a "recirculatory mode" (see Figure 2.2b) whereby sediment disturbed by the convecting vortices ahead of the moving helicopter is entrained through the forward half of the rotor disk. This is depicted in Figure 2.8b, which illustrates the dust density distribution of a five-bladed rotor in slow forward flight, in the absence of an airframe (note: no colour bar is provided with the image). In this situation a more forward-located intake may ingest a more highly concentrated particulate than if it were located behind the rotor mast. While exact dust concentrations may never be known without proper real-world sampling, this qualitative analysis at least provides some information for predicting how an EAPS device may perform during brownout, and what damage, if any, will occur to the engine if particles are ingested.

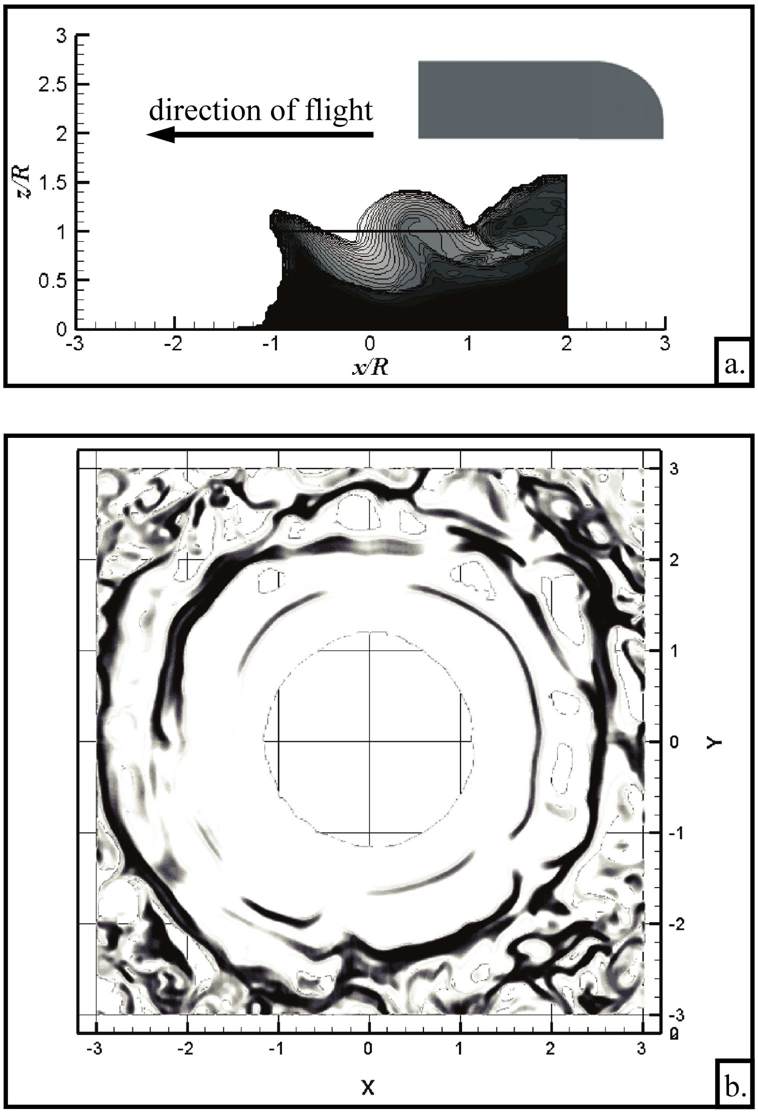

Figure 2.8: *Results of Euler-approach simulation of rotor-induced dust cloud showing: a. dust density distribution in the flow surrounding a five-bladed rotor in slow forward flight (as visualised on the vertical plane through the longitudinal centreline of the rotor; darker areas show denser dust regions); b. regions of maximal particulate uplift from the ground (darker areas show denser dust regions). Source: Ref. [5].*

2.2.5 Damage to Turboshaft Engines

The type of damage caused by the ingested particulate is wide-ranging and affects the whole engine, although it is the compressor at which performance degrades most [22]. In particular, damage to compressor blades includes blunted leading edges, sharpened trailing edges, reduced blade chords and increased pressure surface roughness (see Figure 2.9a). In addition to erosion, performance loss can arise from the deposition of molten impurities on combustor walls and turbine vanes, leading to flow path modification (see Figure 2.9b). Such observations are made from numerous experimental and numerical investigations into the various aspects of particle ingestion, erosion, and deposition; a review is given by Hamed *et al.* [23]. Notably, it was found that even small particles of 1 to 30 μm in size can cause severe damage to exposed components.

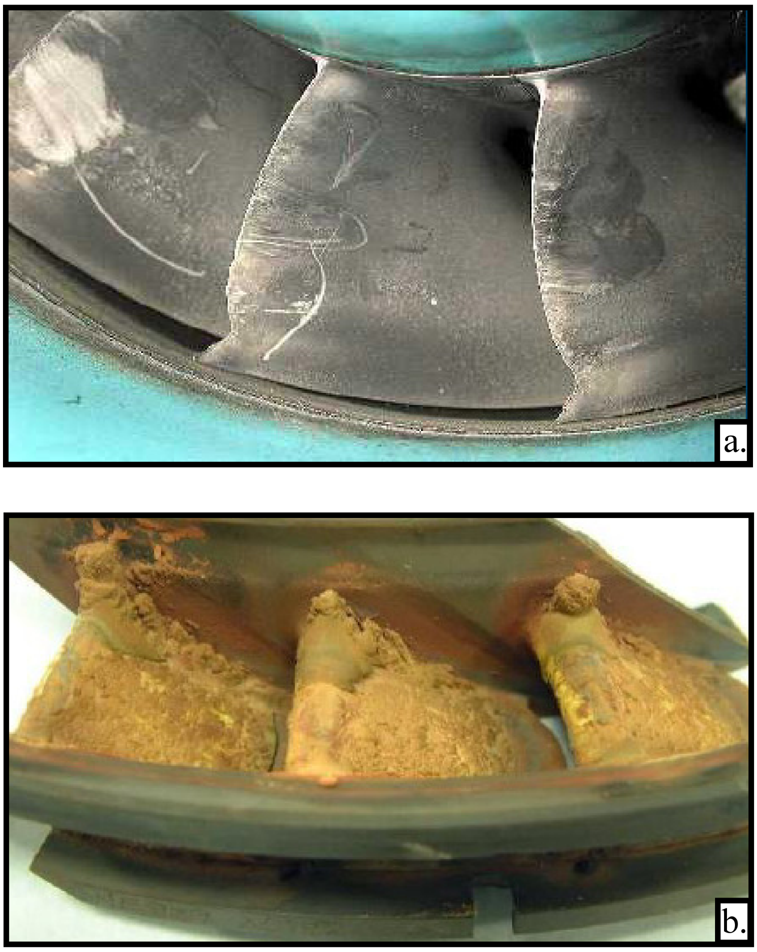

Figure 2.9: *Effects of particle ingestion on key turboshaft engine components, illustrating: a. leading and trailing edge erosion of compressor blades; b. agglomeration of molten impurities on turbine blades. Images © Crown Copyright.*

There are numerous examples of just how damaging particle ingestion can be for an engine. Severe erosion during the Vietnam War led to engines being withdrawn after just 100 hours of service, while more recently, during the first Gulf War, unprotected Lycoming T-53 engines lasted as little as 20 hours [23]. Similarly, during operations Desert Storm and Desert Shield in the early nineties saw GE T-64 engines lasting around 120 hours between removals, nearly depleting the U.S. Navy / Marine Corps inventory of CH-53 engines [1]. After several decades of such experience, it would nowadays be opined as negligent to omit the employment of some variant of engine protection. However, even with protection some particles manage to get through and cause damage to the engine.

A two-part study by van der Walt & Nurick [22], [24] proposes and validates a first-order approach for predicting the engine life of helicopters operating in dusty environments. Since most of the erosion occurs on the compressor and especially on the first stage, the analysis is concentrated on (and indeed limited to) this part of the turboshaft engine. It links the erosion rate of metal plates to key variables, such as blade material properties, quartz content, particle hardness, and particle shape. In particular, it reports that erosion rate is almost directly proportional to the percentage of quartz in the dust. It also finds that erosion rate is increased at higher impact velocities, and climbs linearly with particle size up to a critical diameter. The study is introduced by justifying the employment of EAPS, but continues to develop a theory of erosion per unit mass of particulate ingested to account for particles that evade capture in the separation process. Notably, the trends observed highlight the importance of knowing the dust properties of the environment of operation when predicting engine deterioration.

2.2.6 Summary

In an ideal world, the full three-dimensional dust density distribution of each rotorcraft studied, verified with real data, could be obtained. Additionally, the sand particle size and shape distribution at the helicopter intakes would also be known. Of course in reality this is not the case, and what *is* available in the literature is exploited to provide as much information as possible about the particulate properties in the flow around the engine intake. From the results of the Sandblaster II program, typical dust concentrations for rotorcraft of varying disk loading could be extracted, along with a breakdown of mass fractions of particle size groups at the rotor tip. From the work of Phillips & Brown [5], the relative dust concentrations could be estimated for a given radial position. From the work of Milluzzo & Leishman [3], the general severity of the brownout cloud could be estimated for a given set of rotor parameters. These can be combined to yield a particle size distribution and a particulate mass concentration for a given rotorcraft operating in a brownout cloud. This information can be used to ascertain the performance of an EAPS system and ultimately predict the deterioration of the engine.

2.3 Engine Air Particle Separating Technologies

Helicopter operation within a brownout situation has demonstrated the vulnerability of turboshaft engines to the ingestion of foreign objects, in particular dust and sand (see Section 2.2.5). For this reason, helicopter engines are equipped with advanced separator systems to protect their rotating components from erosion and damage. To understand the importance of particle separators on modern helicopters, it is helpful to quote some performance figures. A light utility helicopter with an engine mass flow of 5.9 kgs^{-1} drawing particulate-laden air with a dust mass concentration of 2.5 gm^{-3} ingests around 0.7 kg of sand per minute. According to experiments by van der Walt & Nurick [22], for an engine of this size there can be a loss of one per cent power after ingesting just 7 kg of particulate, or operating for just ten minutes in a typical brownout cloud.

The threats to an engine's performance are not limited to sand ingestion: in marine environments, an engine may be vulnerable to corrosion and flame-out as a consequence of saltwater consumption; in areas of vegetation such as grassy fields, foliage may clog the air intake passage, causing flow distortion and high pressure losses; and in most operations foreign objects such as rocks, birds and chunks of ice may devastate a compressor blade, causing a profusion of problems for the engine. Under these demanding conditions, the use of inlet filters or other means of air-borne particle separation is therefore essential, if at least to provide a physical barrier to such threats. However, the use of particle separators does not quite solve the problem; in fact, it creates considerable side effects; these include the added weight and drag, the power requirements to operate the new systems, the need for constant inspection, reliability issues and the inevitable costs that arise from installing such devices, including ground logistics.

The use of filters is by no means limited to helicopters. Nearly every piece of machinery operating in dirty environments has some sort of air filter, or EAPS system, as was defined in Chapter 1. As a consequence, much of the technology developed for helicopter applications has relied on technical applications elsewhere. EAPS belong to one of three categories:

1. Vortex Tube Separators (VTS), that rely on centrifugal forces created by cyclone-like systems (Figure 2.10a.)

2. Inlet Particle Separators (IPS), that rely on rapid change in curvature of the inlet geometry (Figure 2.10b.)

3. Inlet Barrier Filters (IBF), that rely on a mesh in front of the inlets to arrest the particles (Figure 2.10c.)

Figure 2.10: *The three types of EAPS technology: a. Vortex Tube Separator (VTS); b. Inlet Particle Separator (IPS); c. Inlet Barrier Filter (IBF)*. (*Image reproduced under Creative Commons licence (CC BY-NC 2.0), © U.S. Army).*

Separators in the second category are available by default on some modern turboshaft engines, and some manufacturers indicate that they can be coupled with the other two categories of filters. For this reason, they can be considered a category apart, whilst vortex tubes and inlet barrier filters are more like retrofit technologies. The decision to implement an IPS system is made much earlier in the aircraft design process, dictated by the requirements of the airframe manufacturer, whereas VTS and IBF technologies tend to be implemented on request from the operator. IPS devices are therefore designed by the engine manufacturer, whilst VTS and IBF technologies are outsourced by the airframe manufacturer to private companies. A summary of known applications of the three technologies is shown in Table 2.2.

Table 2.2: *EAPS application list database.*

Manufacturer	Model	VTS	IPS	IBF
AgustaWestland	AW-119 Koala	•		•
	AW 109	•		
	AW 139	•		
	NH-90	•	•	
	AW 101 / EH-101 Merlin		•	
Bell	Bell 205	•		•
	Bell 206B	•		•
	Bell 407			•
	Bell 429			•
	OH-58-D			•
	Bell 214 ST		•	
	Bell 525		•	
	AH-1W/Z/Y		•	
Eurocopter	EC 130/550			•
	AS 350	•		•
	EC 120	•		•
	AS 330/332	•		
	EC 135	•		
	EC 225/725	•		
	Gazelle	•		
	Puma/SuperPuma/Oryx	•	•	
	SA315B Lama	•		
	SA316 Alouette	•		
	EC 665 Tiger	•		
McDonnell-Douglas	MD-500			•
	MD-900/902			•
	MD-600N			•
	MDHI OH-6			•
Sikorsky	UH-60 A/L/S Blackhawk		•	•
	SH-3	•		
	S-76 A+/A++/C+	•		•
	S-60 Seaking	•		
Boeing	CH-47 D/F/S/E/G Chinook	•		
	AH-64 A/D Apache		•	•

The first IPS system was installed in the General Electric T700 turboshaft engine for the UH-60 Blackhawk, and was an integral part of the engine design. Later, the same engine was used on the AH-64 Apache as a default option. However, more recently it has been recognised that the use of IPS systems can lead to unwanted pressure drops at the inlet even in cases when a separator is not needed. Thus, a drawback of IPS systems, designed as part of the engine, is their lack of flexibility. VTS systems have enjoyed relative success when retrofitted to existing aircraft. The Centrisep "EAPS" system devised by Pall Aerospace was first supplied to the RAF for operation on the CH-47 Chinook in 1990, during the Gulf War. Operating in desert environments at average flying times of 145 hours, there were no engine rejections as a result of erosion. In contrast at the time, the U.S. Army's fleet of CH-47 helicopters which were not fitted with engine protection, suffered an engine rejection rate of 20 to 40 engines per 1000 flight hours due to erosion [25]. The success of the VTS system has led to expansion of the technology into the civilian sector for rotorcraft of all size, with many manufacturers implementing the VTS system at the design stage. In contrast to the previous two technologies, IBF systems are relatively young. The advancements in filtration material technology have allowed barrier filters to provide particle separation solutions with a competitive pressure loss. Furthermore, many operators are now replacing the current EAPS system with IBF, sacrificing increased maintenance time for higher, dependable separation efficiency.

EAPS systems are assessed by a number of criteria, the most important being their efficiency of particle removal. To assess efficiency, devices are tested fairly requires internationally recognised standard dusts. Several exist, representing specific size distributions that represent or replicate the typical environments in which the device may be required to operate. Arizona sand has been used for testing turboshaft particle separators and other heavy equipment components for decades. A number of sub-categories of Arizona sand exist, including: Arizona Road Dust, Arizona Silica, AC Fine and AC Coarse Test Dusts, J726 Test Dusts, and more recently ISO Ultrafine, ISO Fine, ISO Medium and ISO Coarse Test Dusts. Many military and industrial specifications require the use of Arizona Test Dust and refer to one or more of the above names. In the current work, the AC Fine and AC Coarse test dust specifications are used throughout to quantify EAPS separation efficiency, both as quoted from the literature and in models derived as part of the study due to their resemblance to typical desert environments of helicopter operation. Their specific properties are given later in Chapter 4.

In spite of the increased interest in inlet particle separation, the technical literature on this subject is rather limited, with much of the information derived from international patents, manufacturer's specifications (often unsubstantiated by technical data), operating flight manuals (where data are required for certification) and unofficial documents. To clarify the matter, there are no less than 100 international patents on engine particle separators, some of which demonstrate a small advancement of the art without showing any technical performance. The only publication with a wide technical scope is an AGARD Lecture Series [26], a document now out of print and difficult to retrieve. Seddon [21] in his book on intake aerodynamics devotes about one page to helicopter engine inlets. However, filtration & separation is an engineering branch on its own, with applications on all types of machinery, with a considerable publication record. The proceeding chapter provides a patent survey of the key technologies, and a review of literature on their methods of separation.

2.4 Vortex Tube Separators

As particulate-laden air enters a vortex tube separator, it is first met by a set of helical vanes, which impart a radial and tangential component of velocity to the flow, inducing rotation. Particles in the air are of greater specific gravity, and so experience a greater centrifugal force in this rotation. Owing to the effects of inertia, this causes the particles to be thrown outwards towards the periphery of the tube. The vanes bestow a similar fate to heavier particles too, by virtue of a design which deflects or trains particles on impact radially outwards. A second, narrower tube in the base of the device physically separates the flow into two streams; the core air flow continues to the engine inlet whilst the particulate-laden “dirty air” is scavenged to the atmosphere.

A survey of patents pertaining to different embodiments of the vortex tube separator concept was performed. The diagram shown in Figure 2.11 is an example of such a vortex particle separator, illustrating one embodiment of Ref. [27]. The outer tube, labelled 12 in Figure 2.11, has an inner diameter of 18mm, a total length of 60 mm, and a vortex generating region of length 20 mm; however these dimensions vary between applications. The area labelled 20 in Figure 2.11 is known as the separation region, in which the vortex forms a clean air core. Adjacent to this and common to all VTS is a second tube of smaller diameter but co-axial with the main tube, through which the clean core air (26) flows. In this example it is tapered, increasing in diameter downstream, but in other inventions the diameter may remain constant. The design often depends on the means for removing the dirty air. The centrifuged particulate matter (22) proceeds through the annular orifice between the inner and outer tube and arrives at a scavenge passage, such as that labelled 46. The dirty air is then often scavenged away through holes either in the base of the passage, or the tube walls (48) and proceeds into a chamber common to all scavenge tube outlets and discharged to the environment. A fan or blower is usually provided to energise the scavenge air flow, which constitutes from 5% to 20% of the primary airflow. The primary airflow entering the device in this example is based on a mass flow 4.4 gs^{-1}, but this will clearly vary among devices of differing dimension, and local pre-inlet flow conditions.

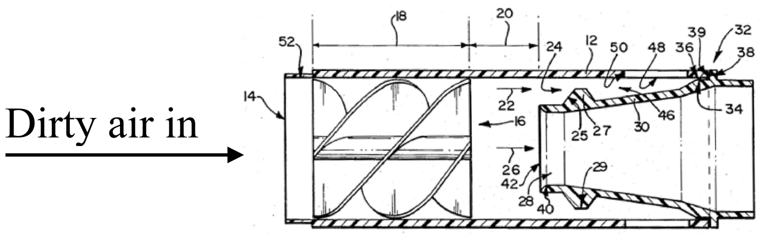

Figure 2.11: *Vortex tube separator according to US Patent 4,985,058 [27].*

As with all devices of intake protection, there is a constant battle between achieving good separation efficiency for a minimum pressure loss. Aside from altering the arrangement of the tubes, patents often pertain to inventions which improve separation efficiency for no extra loss of pressure, and vice versa. Some aim to improve the system efficiency by modifying the helical vanes, or the arrangement of the tube. The importance of such adjustments is embodied in a sentence found in Ref [27]: "If the separation efficiency of the inlet system increases from 94% to 95%, the life expectancy [of the engine] is doubled, and if the efficiency then increases to 97%, the life expectancy is doubled again."

2.4.1 Theoretical & Experimental Literature

As a starting point for low order models and qualitative descriptions of particle separation by vortices, the book Fundamentals of Particle Technology by Holdich [28] is a valuable resource. The technology behind vortex tube separators (VTS) is developed from cyclone separators used, for example, in bagless household vacuum cleaners. In this embodiment, particulate-laden air enters a cylindrical chamber tangentially causing fluid rotation within the chamber and a subsequent radial imbalance in particulate concentration, which can then be bifurcated. However, such devices rely on large mass flow rates and thus power consumption, which is at a premium for helicopters. On a smaller scale, an embodiment known as an inline vortex separator can be utilised, wherein the flow enters a tube axially and maintains this axial direction whilst a swirl component is applied via static helical vanes. This is depicted in Figure 2.11, which is taken from a patent of a vortex tube separator for helicopter applications. This depiction is typical of the tubes used widely today. A plurality of such tubes is arranged on one or more panels which comprise a box that sits in front of the engine air intakes. There must be a sufficient number of tubes to supply the engine with mass flow. Not shown in Figure 2.11 is the scavenge chamber into which the particles are drawn, and the extension of the collector tube through the depth of this scavenge chamber to a sealed cavity that becomes the engine intake duct. There is much scope for how these are arranged, often dependent on the helicopter to which an array is being fitted, as discussed further in Ref. [29].

The flow inside a vortex tube separator is complex and not fully understood. Empirical and semi-empirical models have been developed, but their usefulness is often limited to the geometry. Additionally, there are many factors that affect the device performance. The key geometrical design parameters are the helix pitch, number of blades, outer tube diameter, inner tube (known as the collector) diameter, and axial distance between the helix and the collector. Furthermore, the behaviour changes according to the axial velocity, which is a function of mass flow rate. Owing to this large array, much of the literature contains case-specific computational fluid dynamics (CFD) studies verified with experimental results. Klujszo *et al.* [30] conducted a parametric study on an inline cyclone separator, concluding: that increasing the blade pitch angle improved separation at the expense of pressure drop; that there is a limiting axial velocity for a given tube beyond which separation efficiency does not improve; that gradual turning of the flow reduces pressure loss; and that the implementation of a back cone aft of the helix can enhance performance by displacing a separated flow region in which inadvertent mixing would otherwise draw unwanted particles into the core. However unlike the VTS in Figure 2.11, the scavenge chamber in Klujszo's work was not fluidised. A similar study by Hobbs [31] on a much larger scale demonstrated the case-specific nature of CFD of vortex tubes.

In the present work, the vortex tubes are required to supply a sufficient mass flow of clean air to a helicopter engine. Due to the wide range of intake geometries and engine sizes, it is probable that no single design is optimum for all rotorcraft. Therefore a more general analytical model is required that can be used for an initial, low order prediction of VTS performance and can be applied to numerous embodiments of the vortex tube separator. Such a mathematical model was derived by Ramachandran *et al.* [32] to predict the separation efficiency and pressure drop of an inline cyclone separator. The authors verified the model with experimental data and illustrated a good prediction, despite using simplifying assumptions. The validation was conducted with aerosol particles that migrated radially under centrifugal force, and adhered to the tube walls where they could be counted. This differs from the embodiment shown in Figure 2.11, in which particles are captured once they breach a radial position equal to the radius of the inner tube (collector).

2.4.2 Scavenge Flow

The design of the scavenge flow means has been found to be very important in dictating the overall efficiency of the system. In Ref. [33] it is reported that "The efficiency of a vortex separator is a function of the centrifugal forces developed, the length of the spinning zone, and the proportion of the scavenge flow to clean air flow. Of course, an optimum clean air flow is always the primary desideratum. Therefore the scavenge air should be controlled at the minimum to give effective particle separation."

The problems connected with controlling the scavenge flow appear to depend on the design of the vortex tube base. For example, a device may employ a conduit in the side wall of the scavenge passage for extracting the dirty air to a desired location. If the orifice becomes clogged, there is risk that flow will re-circulate and enter the clean air flow tube, exacerbating an already underperforming device. Furthermore, owing to the high rotational velocities, any particles that fail to be extracted will continue to circulate inside the scavenge passage, abrading the walls. This could lead to catastrophic failure. Inventions such as adding a split washer-style flange at the scavenge entrance alleviates problems such as this, but leads to further losses. Similarly, an increase in complexity not only affects manufacturability, but increases the possibility of turbulence within the scavenge passage, leading to the risk of re-ingestion into the clean air flow.

2.4.3 Helical Vane Design

Whilst the main task of the helical vane is to turn the air and cause a vortex, there have been many modifications to the vane leading edge, airfoil shape, hub length, chord length, vane trailing edge and vane surface, all driven by the need for greater separation efficiency and a lower pressure loss. In almost all cases, there are four vanes in a set, each with a chord length of at least 90 degrees measured along the tube circumference such that each vane overlaps its neighbour. According to Monson & Rosendahl [34], such an overlap ensures the application of swirl-force to each dust-air particle, either aerodynamically or by direct deflection.

The leading edge angle of attack determines the swirl angle of the influent air; a larger angle of attack produces greater swirl per unit travel at the expense of greater pressure drop. Monson & Rosendahl [34] continue by pointing out that the desired angle of attack for a good balance generally lies in the range of 55 to 70 degrees. If space constraints dictate a shorter hub, then a high angle of attack might be preferred to achieve the suggested vane overlap of at least 90 degrees.

A patent study has revealed some of the parameters that can be improved to achieve a greater efficiency. For example, in U.S. Patent 3,517,821 [35] it has been shown that employing an ellipsoidal leading edge and modifying the high pressure surface to gradually alter the flow path of the air into a spiral lowers pressure losses. A similar modification of the low pressure surface improves the pressure coefficient further, by reducing the intensity of a vortex that adjacent to the leading edge of prior art vanes due to flow separation. The same inventors also determined experimentally that feathering the trailing edge narrows the width of the wake trailing off the vanes, which lowers the pressure losses proportionally.

It is clear that such improvements are in most cases specific to an existing VTS, and since no mathematical links have so far been found, modifications are invariably established through experiments. Other inventors have developed other ideas to improve efficiency for no loss of pressure, such as a second set of vanes located where the clean air tube usually lies, to separate finer particles [36]; or grooves spanning the vane length which serve to divert water droplets and other particles that adhere to the vane surface, to the tube periphery [37]. While no general mathematical theory has been established for helical vane design in Vortex Tube Separators, no one can doubt the underlying scientific principles behind these improvements.

2.4.4 Vortex Tube Arrangement

As previously discussed, VTS are invariably arranged in a vortex cleaner array, defined by Roach [38] as an assembly composed of a plurality of vortex cleaners mounted together as a unit with their axes arranged in parallel, or a group of such assemblies. It continues to state that six rows of vortex air cleaners is the maximum number of rows generally used in air cleaners for good cleaning efficiency, but earlier inventions pertain to panels containing much larger numbers of VTS arranged side by side to comprise a panel, such as in U.S. Patent 3,449,891 [39] depicted in Figure 2.12. This particular patent refers to several embodiments of an idea in which panels of tubes are arranged to form a box or cylinder, labelled 40. Such an arrangement creates a chamber which, when a bypass door (60) is opened, can provide axial airflow to the engine inlets (20). This permits almost full performance of the engine when operating in clean environments, and an emergency system should the separator become clogged. However, care must be taken to ensure that the ram recovery offered by forward-facing tubes does not create a large pressure imbalance between the array panels.

Improvements in the arrangement of VTS have been seen most recently to be driven by abating noise from the engine, as stricter regulations at airports are introduced. One source of rotorcraft noise is that which emanates from the compressor, especially at high mass flow rates during take-off. However, if rotorcraft are expected to land in dusty environments too, a particle separator is essential in addition to existing noise attenuation devices. One such device, by Roach [38], in which sound absorption panels inside the clean air chamber are positioned just aft of the VTS, are arranged in curved, dog-legged, or in angled formation. This arrangement abates sound waves by deflecting the airflow, but unfortunately leads to additional pressure losses in this embodiment of around 0.65 kPa, which is an increase of almost 50% on the pressure losses from the particle separating device. Nevertheless, it is an increasingly essential piece of hardware for rotorcraft, and the pressure losses are somewhat alleviated by deceleration of the air in the chamber. Such an invention highlights the increasingly complex and novel approaches being invented in the industry to further enhance the capabilities of VTS devices.

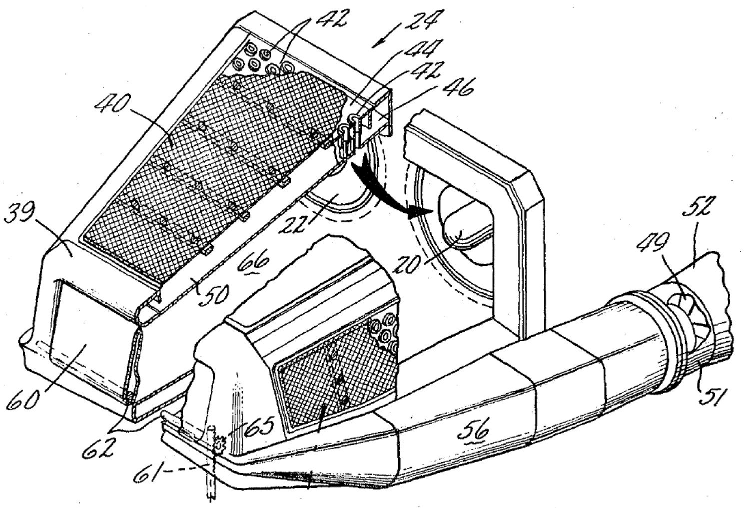

Figure 2.12: *Vortex Cleaner Array with Bypass Door from U.S. Patent 3,449,891 [39]*

2.5 Inlet Barrier Filters

The term "Inlet Barrier Filter" is applicable to a product that consists of both a filter medium and a means of attachment to the aircraft. In addition to the filter, an IBF consists of a cowling to replace an existing section of the airframe (or be incorporated into a new design), a frame with attachment points, and often a hydraulic-powered bypass door to allow unrestricted air into the engine in case of filter failure. It is installed at the engine intake of a helicopter to filter all engine-bound air. On larger helicopters such as the UH-60 Black Hawk they may be added as an appendage; on smaller models, such as the Eurocopter AS 350, they are designed into the airframe as a fully integrated device. To reach the engine inlet, air must pass through what is known as a barrier filter. A barrier filter is a panel typically comprised of a blended woven fabric or fibrous filter, folded into a series of *pleats* and restrained in shape by two epoxy-coated wire meshes. The pleat provides a large surface area, whilst the wire mesh provides reinforcement against foreign object damage and protects the filter material. Several combs provide structural support to the filter, to retain its shape. A diagrammatic breakdown of an IBF is provided in Figure 2.13, taken from U.S. Patent 6,595,742 [40]. The filter is mechanically bonded to the frame through adhesion or physical connection, and is sealed with a potting material, which prevents unfiltered air from seeping through gaps in the join. Once the air has passed through the filter panels, it reaches a chamber from where it is further drawn into the engine via aerodynamically-profiled ducting, as depicted in Figure 2.14.

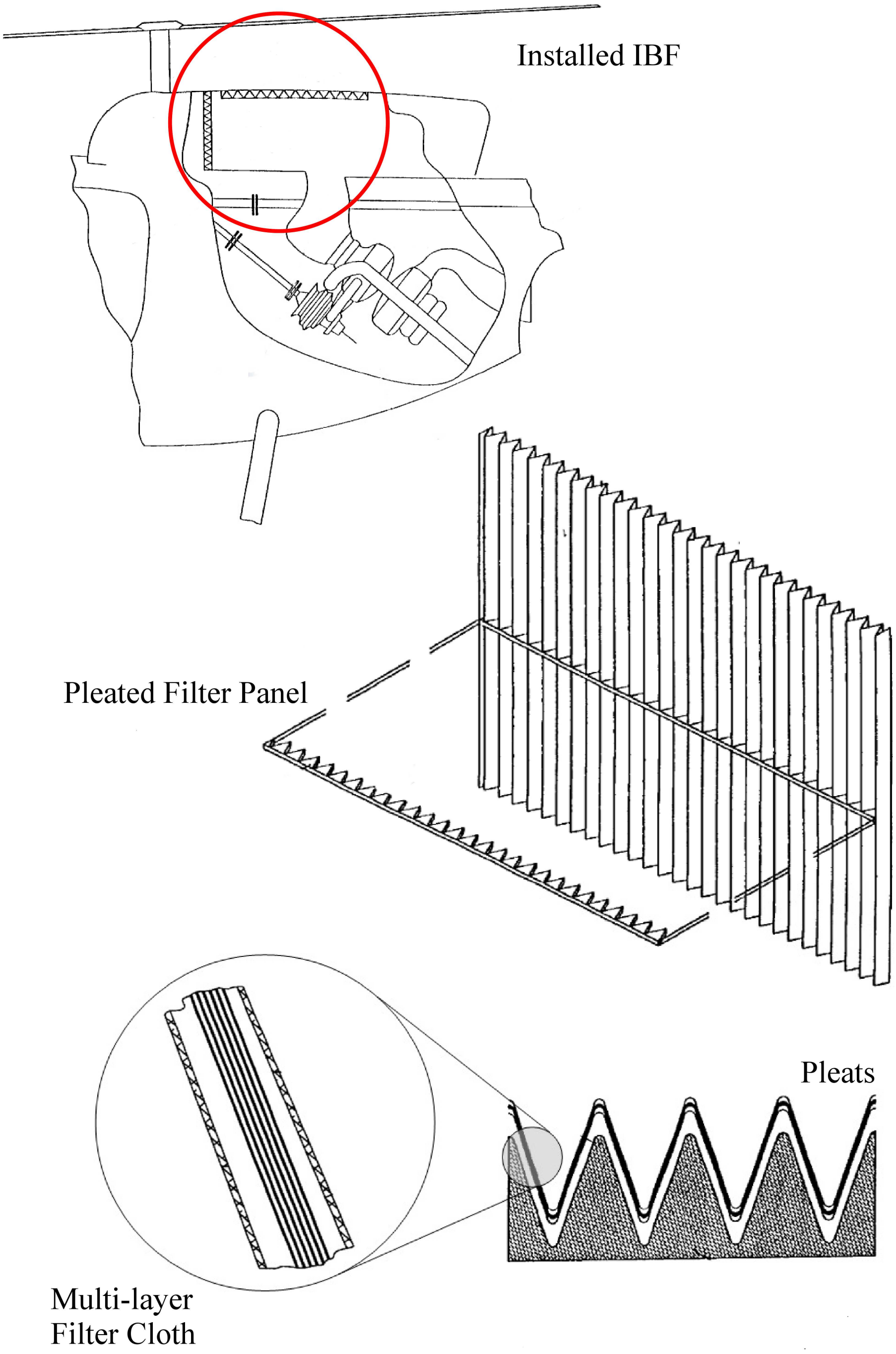

Figure 2.13: *Diagrammatic breakdown of key components of an Inlet Barrier Filter, according to U.S. Patent 6,595,742 [40].*

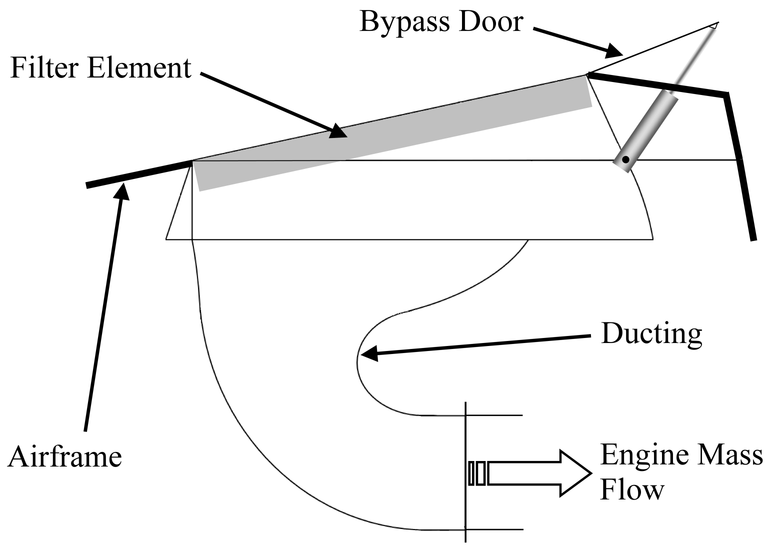

Figure 2.14: *Diagrammatic representation of one embodiment of an Inlet Barrier Filter.*

Inlet Barrier Filters (IBF) are employed throughout the rotorcraft industry to provide protection to engines from potential blade erosion and Foreign Object Damage (FOD) caused by particulate ingestion. They were first developed in the 1960s for the U.S. Army helicopters operating in South East Asia, although this technology was later abandoned for the IPS design (detailed in Section 2.6). Later in 1991 the technology was revisited, with the development of a large filter assembly for the CH-47D. A 50% reduction in clean pressure drop was demonstrated. However, continued use was met with opposition due to design constraints, technical requirements, servicing and producibility and the program was terminated. In a similar exercise, at the request of US Army Aviation Systems Command, McDonnell Douglas Helicopters developed a filter in 1991 for the AH-64, but discontinued the program after initial flight tests due to lack of funding and interest [41]. While direct procurement by the US Army has fluctuated, since the early 1990s development of IBF has continued, most notably through the private sector by Donaldson Filtration Solutions (formerly Air Filtration Systems, formerly a subsidiary of Westar Corporation), and there now exists a wide range of air intake IBF solutions available for small and medium-sized rotocraft.

The method of particle extraction differs from other devices such as the IPS, by physically stopping particulate matter with a porous screen. This yields exceptionally high separation efficiencies of up to 99.3% (tested with Arizona AC Coarse Test Dust) for a relatively low initial loss in pressure. However this loss increases with time, owing to the gradual formation of cake upon the surface of the filter, which further impedes flow. To reduce this problem, the filter is inspected and maintained regularly with wash cycles, and eventually replaced. The filter element is comprised of layers of woven cotton or fibrous mats, sandwiched in a pleated wire mesh. Inlet Barrier Filters are easily adapted, a fact which along with their exceptionally high separation efficiency contributes to their growing attendance on many modern rotorcraft.

2.5.1 Theoretical & Experimental Literature

There are currently no studies in the literature that predict the performance of an installed IBF using CFD or analytical theory of pleats of this size other than those published by this author (see Refs. [42], [43], [44], [45]). Of work pertaining to IBF, there are two notable contributions. The first is a joint presentation by Scimone & Frey *et al.* [41] presented at the 56th Annual Forum of the American Helicopter Society. In this paper the authors detail the background, filter media technology, design considerations, and predict the effect on engine performance and lifetime increase using simulation programs. While providing useful insight into the state of the art, no allusion is made to the design particulars of the IBF and no real test results are given. Instead the focus is on comparing the IBF technology to the other particle separators and describing the main design considerations of an IBF. These are discussed in Chapter 6. Furthermore, the transient state (due to clogging) is only discussed in relation to activation of the bypass door - a necessary safety feature which allows unfiltered air to the engine in the event of IBF failure.

Elsewhere in the literature is a contribution by Ockier *et al.* [46] in which the flight testing and certification of an IBF for the Eurocopter EC145 is given. Details of the instrumentation used during flight testing are provided, along with the manifold tests for contingencies such as "icing". Clogging of the IBF is simulated on the test bed by use of perforated metal plates of varying open area. Trends obtained during flight tests are given in the form of engine power charts, but results are sanitised of real data. The most significant detail that can be inferred from this work is the temporal loss of pressure across the IBF, which was obtained during extensive operational evaluation in the Mojave Desert, California. Again no actual data are provided but the pressure loss is shown to rise to a "caution level" after 10 minutes in a heavy dust cloud, and to a "warning level" after 12 minutes spent in the dust during takeoff and landing (equivalent to 30 landings in full brownout conditions, according to the authors). While exact data for the pressure drop at different stages of a filter cycle are unknown, this author has learnt from conversations with manufacturers and surveying patents, that ball park figures for the clean filter pressure loss and the acceptable limit of pressure loss when the filter is clogged, are 600 Pa and 3000 Pa respectively. Combining this information with that given by Ockier *et al.* provides reference point for results obtained in the present work through theoretical analysis.

Despite the lack of literature directly pertaining to IBF theory, the physical processes involved in air filtration by porous media are well represented within the field of *filtration and separation*, and can be extrapolated to IBF analysis. This is covered in the next chapter. There is also a handful of patents that provide an insight into IBF construction.

2.5.2 Filter Element Design

Any restriction to the airflow at the inlet of an engine will result in a performance loss, regardless of what measures are put in place to reduce this effect. Engines are designed to receive a consistent and stable flow of clean laminar air; deviations from this prevent the engine operating at full performance. Therefore a first design consideration is to ensure that the filter element is properly sized to permit an adequate quantity of air to the engine without a large loss of pressure. This is a general design driver for all types of intake protection. It has been found that the pressure drop across a filter is reduced by increasing the effective surface area of the filter. Furthermore, it has been shown that in order to achieve optimal life in erosive environments, the filter should be sized such that the mean velocity of the air approaching the filter element at the engine's commercial Take Off Power (TOP) is less than 30 fts^{-1} (9.1 ms^{-1}), and preferably in the range of about 15 fts^{-1} (4.6 ms^{-1}) to 25 fts^{-1} (7.6 ms^{-1}), as reported by Scimone [40]. The velocity of influent air is determined by calculating the volumetric flow rate per unit of effective filter surface area. Therefore if the volumetric flow rate of the engine is known, the aforementioned mean velocities can be used as a ratio value to appropriately size the filter's projected area.

The total *surface* area of a filter is governed by the *pleat density.* The pleat density is also known as the *pleat count*, and is expressed as pleats per unit length, usually inches. By inverting the pleat count the *pleat pitch*, or *pleat width* can be found, expressed in the reference unit. The filtration area is the total area of a single pleat multiplied by the number of pleats. Sizing may be accomplished by altering the pleat height, pleat pitch, or altering the shape of the filter within the confines of the opening (for example by curving the surface). A typical pleat height lies in the range of 1 to 3 inches (2.54 to 7.62 cm), and pleat spacing may be 3 to 6 pleats per inch (1.2 to 2.4 pleats per cm). Filter elements are typically sized with a sixfold total surface area over profile area. As well as increasing the filter surface area for no increase in projected area, pleating has the added benefit of creating structural rigidity within the filter element.

The filter medium itself is a key piece of equipment in the system, since increasing the separation efficiency by just a few tenths of a percent can drastically improve the overall performance of the engine. In addition to providing high separation efficiency, the material must also be resistant to damage by water and other liquids it may encounter during operation. The filter medium is often manufactured from polyester, felt, or most commonly, woven cotton. In the case of cotton, the filter is constructed from three to six overlapping layers, woven into a grid pattern. To further improve efficiency the filter may also be impregnated with oil, which not only helps to capture finer particles by providing a "tack barrier", but also functions as a good indicator of usage by changing from red or green to brown or black, with increased contamination. The use of oil also bestows upon the filter an ability to repel water, which helps to prevent absorption and prolongs life.

2.5.3 Pleat Design

The arrangement of the pleats is the key design parameter. Pleat design is a challenge of compromises. The act of pleating allows the volume of air to be distributed over a larger area than the filter's projected area which has the effect of reducing the velocity perpendicular to the filter surface. The volume flow rate divided by the total filtration area is sometimes called the *superficial velocity*; reducing the superficial velocity generally reduces the pressure drop, but can also have an adverse effect on the ability of the filter to capture particles. This is the first compromise. The second, main compromise arises from a phenomenological effect that emerges as a result of pleating. The gap produced by the act of folding, known as the *pleat channel* provides a constriction to the air. While air at the channel walls (or filter medium surface) decelerates and subsequently permeates the medium, the core air flow in the channel accelerates. This creates shear layers within the fluid akin to a boundary layer, which cause a loss of pressure to viscous drag. The narrower the pleat channel i.e. the greater the pleat density, the greater the loss in pressure. Hence the benefit of pleating to alleviating pressure loss through filter medium is increasingly diminished as the number of pleats across the span increases. This also means that there is an *optimum pleat density* at which the pressure drop is least.

This phenomenon is the crux of most studies in the literature. Some have tried to theorise the loss of pressure due to pleating, while others aim to identify key design features that affect the optimum point such as the filter medium's *permeability*. The permeability of a porous medium is its ability to transmit fluid — a lower permeability means a greater resistance. Several studies have investigated the optimum pleat design point (pleat count and pleat depth) at which the pressure drop is minimum. Pui & Chen [47] solved a modified version of the Navier-Stokes equations for steady laminar flow through porous media (known as the Darcy-Lapwood-Brinkman equations), using a finite element method for six media of varying permeability. They found that the optimum pleat count (for fixed pleat depth) increases with decreasing permeability.

Lücke & Fissan [48] used these results to verify their own work, which used approximate solutions to the Navier-Stokes equations to make similar conclusions, but on more realistic pleat shapes than the rectangular sections used in Pui & Chen's work.

Other studies look at whether the pressure drop is affected by the method of pleating. Subrenat *et al.* [49] contest that a side effect of increasing pleat count is an overlapping of the filter media at each fold, which reduces the effective cross section available to the flow. If pleat count continued to increase, the filter would eventually resemble a solid homogeneous structure of thickness equal to the pleat depth, and the fluid would flow only through the head of the pleat. This would raise the pressure drop considerably. This is supported in a study by Wakeman *et al.* [50], in which a simulation is performed on a pleated cartridge filter typically used in the filtration of hydraulic fluids for aeronautical applications. While the filtrate and operating pressure differ greatly from the application discussed in the present study, the conclusions drawn can be applied. Wakeman *et al.* found that the effects of pleat crowding and pleat deformation contributed to a loss in filtration area, which increased with number of pleats. Furthermore, the effect of material folding was seen to compress the material (depthwise) through spanwise tension, and thus lower the local permeability at a location through which a larger proportion of fluid flows. The consequence of these pleating effects is a further increase in pressure loss.

However, these contributions differ from the current study in volume flow rate which is an order of magnitude lower than those typically experienced by IBF; and in application, which is typically in the removal of aerosols from ventilation air. One consequence of this is described in the work of Rebaï *et al.* [51], in which a semi-analytical model of gas flow in fibrous filters is developed for large filtration velocities in automotive applications. It is mentioned that in the work of Lücke & Fissan it is assumed that the velocity profiles in the pleat gap are parabolic, but at high flow rates the profile is much more flat. Rebaï *et al.* recognize this and base their model on existing approximations to the local Navier-Stokes equations derived from similarity solutions for uniform channels with porous walls. Their resulting one-dimensional model allows prediction of filter performance for a number of pleat shapes subjected to high flow volume rate. The results closely match simulations with CFD solutions, and show that this model is a useful and computationally less expensive tool for modeling laminar flow at high velocity through a pleated filter. However, it must be remembered that such filters are used in the automotive industry, hence operate at a smaller lengthscale and volume flow rate to what is expected of IBF.

In addition to minimising pressure drop, the pleat design can be tuned to optimise another performance parameter relating to the endurance of the filter. It is called the holding capacity, and refers to the total mass of particulate a filter can retain before the pressure drop reaches a certain level. In a follow-up study, Rebaï *et al.* [52] introduce particles into their model to investigate the effect of pleat density on filter capacity. They find that an optimum pleat count exists at which the filter retains a maximum mass of particles for a given pressure drop. Crucially, the optimum number of pleats for enduring performance was found to be greater than that for initial performance. They found that the optimum design point was sensitive to the flow conditions and the depth of the pleat: a lower volume flow rate tended to nudge the design point to a smaller pleat count, while the optimum for a shallower pleat favoured a higher pleat count. The application in this study is automotive, and the authors assumed a narrow bandwidth of particles and neglected any inertial effects. Nevertheless it provides useful conclusions for the current work.

2.5.4 Applications

The application of IBF is evident on all helicopters up to medium-size. In the past, rotorcraft such as the UH-60 Black Hawk may have been constructed without intake protection in mind. Consequently the airframe has had to be modified to incorporate a barrier filter system. U.S Patent 7,192,562 [53] for example pertains to an engine air filter and sealing system for the UH-60 Black Hawk, which is simply added to the airframe ahead of the engine inlets, as illustrated in Figure 2.15. The addition is a box comprising three filter panels and a front-facing bypass door.

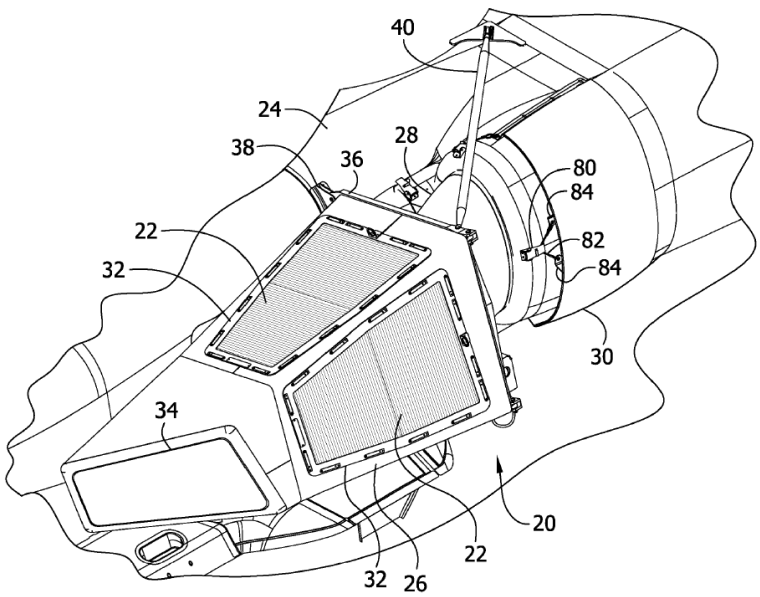

Figure 2.15: *Engine Air Filter for the Sikorsky UH-60 Black Hawk, according to U.S. Patent 7,192,562 [53].*

The blending of intake protection with the airframe is particularly difficult for larger rotorcraft, as the greater power requirements are typically met by employing two large engines which invariably "jut out". Intakes in the sides of the airframe provide the engine with sufficient air and in many cases can easily be fitted with intake protection. Engine manufacturers may leave a plenum chamber ahead of the engine intake such as in the Bell 206B, which allows space for intake protection to be installed to the customers needs, be it an IBF or EAPS system. In this helicopter, the intake protection is found submerged within the airframe. In other embodiments, such as the MD 500, the filter is blended into the sides of the airframe. Such a choice allows for a greater filter planform area, which may be required for larger engines.

2.6 Inlet Particle Separators

The term "Inlet Particle Separator" refers to a device which is integral to a gas turbine engine, fitted at the air inlet for the purpose of cleaning influent, particulate-laden air. A radial or tangential component of velocity is imparted to influent air, followed by a length of ducting, causing a change in direction of the flow stream. The linear momentum of particles entrained in the air hinders such a rapid change of direction, which allows for their easy separation from the core air stream. The now highly concentrated stream of particles is encouraged into a scavenge conduit and extracted away, as the clean air continues to the engine. IPS change in shape, size and type, depending on the engine mass flow rate or whether they are applied to a radial or front facing inlet. Devices may contain swirl vanes too, which augment separation by the deflection or centrifuging of particles. Furthermore, improvements to existing IPS can be made possible by new technologies such as active flow control and adaptive surfaces, which can modify the device during operation to optimise performance to a current flight condition.

The most clear-cut distinction between IPS devices is in their application, to either a front facing inlet or a radial inlet. A front facing, axial IPS device imparts a radial component of velocity to the incoming flow, whilst accelerating the flow through an annular duct, and uses an annular splitter to separate the flow into dirty and clean air. A radial inlet scavenges off particulate from the outer walls of a spiral or U-shaped duct, via "scoops" located in the periphery of the duct, relying on the principle that particles will be centrifuged outward as the flow turns through a duct. Swirl vanes are often employed in addition to front facing inlet to impart a tangential component of velocity to the flow and further enhance separation. Design of the scavenging system is also something which is heavily deliberated over, requiring much thought to minimise weight and maximise compactness. For example, the scavenged particulate may be exhausted through a radial spiral, or an axial duct. Further application of vanes is also sometimes seen, as an additional separator, for de-swirling purposes or to prevent particulate being regurgitated back into the engine.

2.6.1 General Features

Front-facing IPS are comprised of a central body, co-axial with the engine surrounded by a cowl, and a splitter positioned to divide the airflow into a dirty flow stream and a clean flow stream. The central body, labelled 16 in Figure 2.16, directs influent air through an annular duct of decreasing area between itself and a cowl 18. The shape of the central body is such that the radius of the annular duct increases with axial distance from the inlet to a point, and then decreases to the engine inlet at the point labelled (14). This shape creates a peak (15) at which the flow makes a rapid turn, remaining attached to the inner surface of the annular duct by viscous forces. The geometry of the annular duct causes acceleration of the particulate-laden air up to the peak, which adds linear momentum to the particles. At the peak, most of the particles are unable to turn with the flow due to their inertia, which projects the particles radially outward. An annular splitter 17 bifurcates the airflow, segregating the particles into a scavenge conduit (19), along with 10% to 30% of the air flow. The particles are then discharged to the atmosphere, as the clean air follows the inner wall of the central body to the engine.

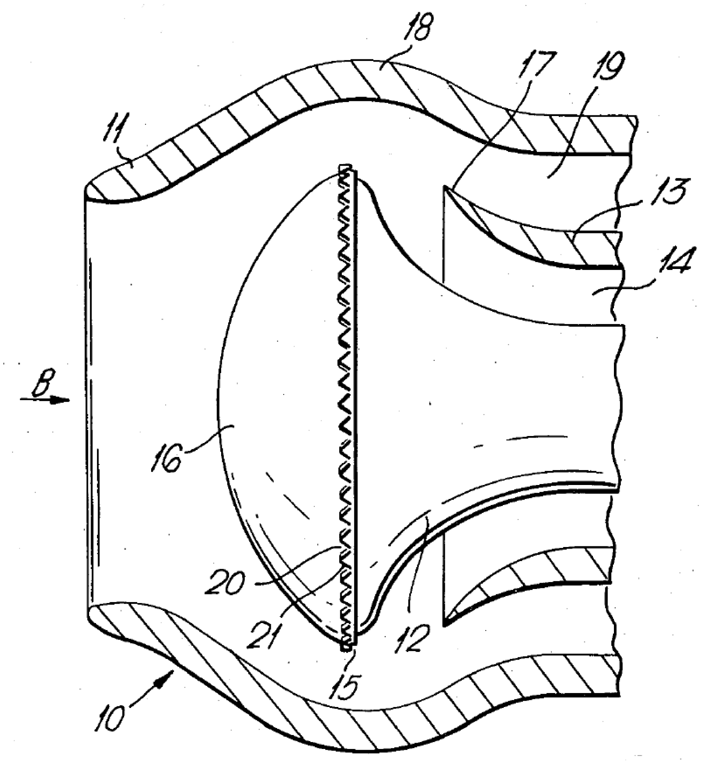

Figure 2.16: *Front-facing IPS according to U.S. Patent 4,389,227 [54].*

Another objective of the IPS is to deflect heavy particulate or other foreign objects in to the scavenge conduit. This type of pollution may be too heavy to be entrained in the flow, and so designers must ensure that if particles are to bounce off surfaces, their rebound will be directed into the scavenge chamber.

Radial inlet or scroll type IPS devices may be integrated into an engine, such as in U.S. Patent 6,134,874 [55] shown in Figure 2.17, or may have been designed as an addition to a forward facing inlet as in U.S. Patent 3,993,463 [56] illustrated in Figure 2.18. In the former case, it can be seen that the particle separator has been designed integral to the engine by the engine manufacturer. It is unlikely therefore, that similar embodiments exist, although the concept of designing an air cleaner into the engine is often performed by the manufacturer. The latter type of radial separator is designed more as a retrofit to an existing engine, and is added to a front facing inlet, where space constraints or otherwise prevent the use of an axial IPS.

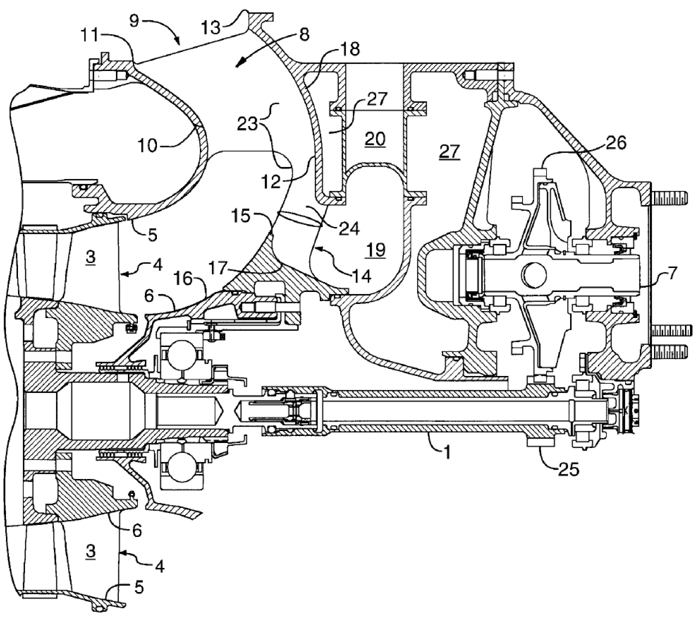

Figure 2.17: *Front-facing scroll-type IPS according to U.S. Patent 6,134,874 [55].*

In the embodiment featured in Figure 2.17, air is drawn into the axial compressor through one of two axially symmetric radial inlets (11) with a concave duct (10). The forward surface (12) forces the air into an arcuate path, which centrifuges heavier particles through the bypass duct (14). A cusp lip (15) acts as a flow splitter, for diverting bypass airflow into the bypass duct. Dirty air is collected from both radial inlets by an annular conduit 19 and extracted to the atmosphere by exhaust driven jet pumps.

The radial separator shown in Figure 2.18 is affixed to a forward facing engine inlet. Air is drawn in radially, through a helicoidal duct (100) which spirals inwardly to the engine inlet (110). The heaviest particles are initially guided into a scavenge conduit (115) which is separated from the main flow path (106) by a wall (114). The resulting scavenge channel (104) follows the duct outer wall and is further supplied with dirty air by "louvers" (116) which scavenge centrifuged particles from the duct periphery. The dirty air is then exhausted to the atmosphere, providing approximately 80% to 85% of the influent air as relatively clean inlet air to the engine.

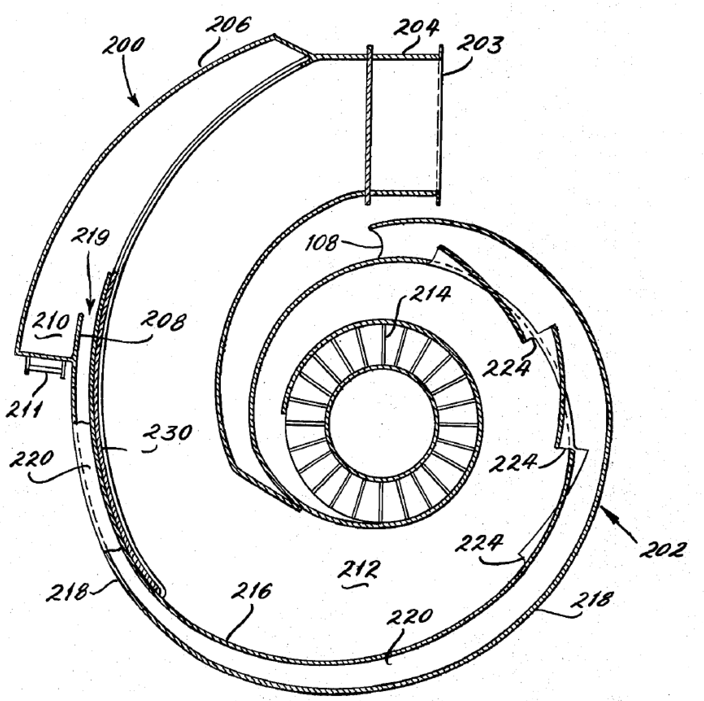

Figure 2.18: *Radial IPS according to U.S. Patent 3,993,463 [56].*

There are advantages and disadvantages to both axial and radial separators. Axial separators are often selected for engines with dynamic or ram intakes, which are aligned perpendicular to the airflow to augment pressure recovery. They or their ducted inlets are located ahead of the main rotor mast, which minimises the risk of exhaust gas re-ingestion. This is in contrast to radial separators, which are found on engines with "static" intakes, and are often located aft of the rotor mass. Static intakes receive airflow through air inlets aligned parallel to the airflow, which when coupled with a radial inlet of the type shown in Figure 2.17 can lead to increased flow distortion at the compressor inlet. However, radial inlets are more compact and if integrated into the engine as in U.S. Patent 6,134,874 [55], carry a significantly lower weight penalty over front-facing axial IPS devices.

In addition to the three different types of IPS, there are many other manifestations of the principle, or additions to existing designs. The main design drivers are increased separation efficiency or a lower pressure loss. This may include a novel centre body design, the addition of swirl vanes, an improved scavenging system, but in most cases patented developments pertain to the actual separation technique. For a full review of the variations on design see Filippone & Bojdo [42].

2.6.2 Theoretical & Experimental Literature

This type of separator is more amenable to a computational fluid dynamics modelling; in fact, most of the technical literature on particle separators focuses on IPS systems. This is perhaps due to the relatively simple design (see Figure 2.19). Since ultimately the IPS work on the principle of separating the particulate and the "clean" air through bifurcating tubes, the prediction of phenomena such as collision and rebound are essential. One such example of theory is available in Hamed *et al.* [57]. These authors used a combination of deterministic and stochastic particle bounce models with Lagrangian tracking on a fully turbulent solution of the Reynolds-averaged Navier-Stokes equations. The particle's path was integrated within the RANS solution up to the collision or bouncing point. The rebound was stochastic and produced new initial conditions for particle tracking. To calculate the separation efficiency, several thousand particles have to be tracked from the inlet. The work of Vittal *et al.* [58] follows a similar approach, and focuses on the concept of a "vaneless" separator. Particle paths were predicted through a Lagrangian tracking, although the method only accounted for boundary layer corrections. The comparisons with tests indicate that the separation efficiency was up to 90% with a fine sand and a scavenge flow rate in excess of 14%. For a coarse sand the efficiency was 5% higher. Musgrove *et al.* [59] addressed the computational design of an IPS for a jet engine with louver-type channels placed downstream of the *combustor*, and a collection chamber for the separated particles. However, this technology does not appear to be useful for turboshaft engines, for which the particle separation must be *upstream* of the compressor.

Saeed & Al-Garni [60] developed a numerical method based on an inverse design approach. The method uses various levels of approximations, including the reduction of the IPS to a set of airfoil-like bodies. The particles are tracked with a Lagrangian method. Crucially, this theory lacks an appropriate model for particle rebound from a solid surface, and is based on an inviscid flow model, an unlikely event in the best of cases.

The most recent theoretical work on IPS is that of Taslim & Spring *et al.* [61]. These authors used CFD methods coupled with particle dynamics to predict the scavenge efficiency of a conventional inlet design. The main contribution of this work was the model of the particle impact, in particular the restitution coefficient and the inelastic effects. They also investigated the effect of sand properties such as shape and density, and inlet geometry. They concluded that extremely fine particles (smaller than 10μm) cannot be practically separated.

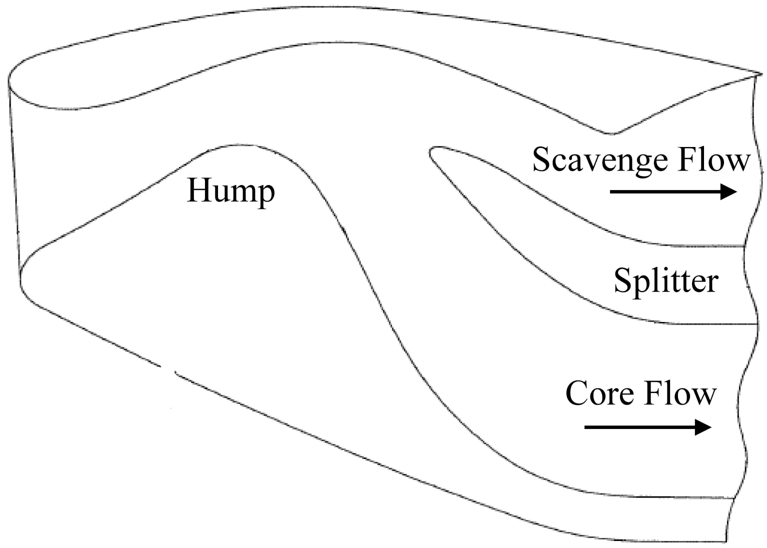

Figure 2.19: *Diagrammatic representation of a generic Inlet Particle Separator.*

It is evident that the field of IPS analysis by computational fluid dynamics modelling is ripe with academic study. This is due to the ease with which IPS devices are suited to this type of analysis. However, despite the scope for geometrical changes and the various solvers that be used, the field appears rather limited in diversity. In all cases reviewed including those not cited in this paper, the particle separator is axial type, and the separator means as per conventional hub and splitter arrangement.

Furthermore, it can be invoked from such papers as those cited above, that the performance of a hub and splitter are very much dependent on the local flow conditions, which in turn are determined by the engine mass flow requirements. Therefore each study case is limited to the engine for which the IPS system is designed. The sensitivity of IPS design to local conditions renders universal analysis even more difficult when considering the real life situation, in which the particulate will undoubtedly differ from those test sands used to verify CFD data. While this may be a common problem in all areas of particle separator analysis, it highlights the case-specific techniques that are needed for IPS theoretical analysis. Therefore it is concluded that IPS theory is not conducive to the more holistic approach adopted in the analysis of VTS and IBF technologies.

2.7 Summary

The subject area of Engine Air Particle Separation concerns, but is not limited to, operation of helicopters in dusty environments. When landing or taking off in such conditions, the main downwash of the rotor interacts with the loose sediment creating a brownout cloud. An unprotected engine can suffer extensive damage to its compressor and turbine if operating in such a cloud. Fortunately there are technological solutions that remove sand and allow cleaner air to continue to the engine. These solutions are introduced in this chapter. Vortex tube separators and inlet particle separators both exploit a particle's inertia to remove it from the core air stream, while inlet barrier filters arrest a particle's motion by capturing it among its fibres. The key features of each device have been discussed, accompanied with qualitative assessment of their effectiveness. The two main performance indicators are pressure loss and separation efficiency; determination of these is essential for any quantitative comparison of the devices.

In order to enact a quantitative assessment, knowledge of the particulate to be separated is required. For this reason a comprehensive study on particle classification was provided. In particular, it is recognised that no two particles are identical, and representing a sand numerically involves the use of a particle size distribution. Particle size distributions vary from one location to the next, and can be analysed using a number of techniques for comparison. The size distribution will also contain a range of particle shapes, which can be descriptively categorised using the Wadell (degree of) sphericity. The size and shape distribution is important because it may affect the resulting brownout cloud. The creation and resulting shape of a brownout cloud is difficult to predict, as it is caused by the interaction of unsteady rotor wake features with loose sediment. The rotor wake is different for each rotorcraft and each stage of the approach to and departure from a landing site, however some consistency has been noted among rotorcraft with certain common design parameters. The sand is disturbed by fluid shear layers rubbing tangentially across the sediment bed, or by bombarding particles that have been reingested through the rotor disk. The rapidity of cloud generation can be linked to the convecting tip vortices, the strength of which can be linked back to the geometry of the rotor blade. Combining knowledge of the particulate properties, the sediment uplift mechanisms, the brownout signature of a given rotorcraft, and the function of particle separating devices, it is possible to create a model for engine air particle separation.

Chapter 3

Engine Air Particle Separation Theory

This chapter presents the key equations that are used to model the performance of engine air particle separation devices. The physical processes involved in dust cloud generation, sediment uplift, particle transport, particle capture and engine erosion are described in theoretical form, to facilitate device comparison. This is followed by the theory of pressure loss and particle separation by vortex tube separators and to deeper level, inlet barrier filters.

3.1 Introduction

To achieve the aims set out in the introduction requires a multi-disciplinary understanding of how the brownout cloud affects engine performance. In between the engine and the dusty atmosphere sits a piece of technology that extracts sand from the air. The physical processes involved in uplifting sand particle from the sediment bed, transporting it to the intake, and extracting it from the air are multifarious; further mechanisms are at work if the particle evades capture to interact with the engine components. There exists a great deal of theory surrounding this topic. In particular, the theory of sediment uplift and dust cloud generation borrows from classical particle transport equations Newton's Laws of motion, and dips into recent theories concerning helicopter operation close to the ground; the theory of particle extraction from air is deep-rooted in the field of filtration and separation; and engine damage by particulate ingestion fits under the remit of transient engine performance.

The differences in particle extraction between each EAPS device are described qualitatively in Section 2.3. The literature review revealed the current state of the art in terms of EAPS theory: plenty of CFD work exists on inlet particle separators, while in comparison vortex tubes and inlet barrier filters have received little attention in the open rotorcraft research. Since ultimately there are limited time and resources, the present work omits the IPS systems from theoretical analysis, instead relying on the current literature to provide performance data for comparison with the other EAPS systems. Of the remaining two systems, vortex tubes have received more attention for other applications, and the 1st order theory has been shown to produce some good results [32]; in the proceeding section the theory is adopted for rotorcraft applications. In contrast with the other separators, the theory of inlet barrier filters for rotorcraft is under-represented in aerospace. For this reason it is investigated in much more depth; there is plenty of theory within the filtration and separation field that can be applied here. Applying existing models and performing deeper analysis of IBF performance will facilitate a cross-comparison of all EAPS systems' behaviour in the mitigation of engine damage.

3.2 Particulate Classification and Representation

In a sample of dust, no two particles are identical. As an example, Figure 3.1 is a magnification of a sample from a desert area in the Middle East, which shows a range of particles from rounded to platelet shaped. This simple fact makes particle classification a rather troublesome affair. While accurate measuring equipment exists, it would be impossible to measure every single particle in a given sample. Instead, it is common to represent a sample of particles with a mean or characteristic diameter. However, if the particles are highly irregular in shape, the difficulty is of which dimension to use to obtain the diameter. A simple basis for engineering calculations is the concept of the *equivalent spherical diameter*, in which some physical property of the particle is related to a sphere that would have equality in the same property. The equivalent spherical diameter depends on the property chosen. For example, the face width of perfectly cubic particle would be $\sqrt{\pi/6}$ times the diameter of a sphere of equal surface area, but $\sqrt[3]{\pi/6}$ times the diameter of a sphere of equal volume.

If the equivalent diameter of each particle in a dust sample *could* be determined, then a range of diameters of varying quantity would be found. This is called a *particle size distribution*. The common approach is to split the sample into size bands and measure the number or mass of particles within a size band. The result is a curve that illustrates the proportion of each size band relative to the whole sample. This curve can be expressed algebraically, or manipulated to show other properties of the distribution. This data is important to EAPS design because it can inform the designer of which are the most abundant particles in a given area, allowing the device to be tailored accordingly. It may also permit more accurate predictions of engine wear. The following presents the essential theory behind particulate classification, representation, and is introduced with how the important particle properties are related to the dust that may reach the engine in a brownout cloud.

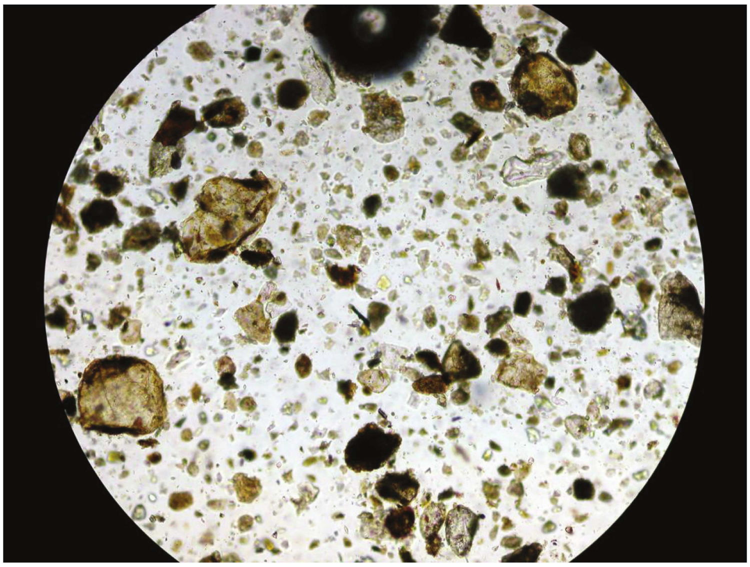

Figure 3.1: *Photograph of a dust sample from south-west Asia under magnification showing range of particle shapes, sizes and composition. Photograph © John Chandler.*

3.2.1 Particulate Mass Ingested

The disturbance of dust from the sediment bed creates a dispersion of particles in the surrounding air. In Section 2.2.3 typical dust concentrations of $\simeq 3.5$ gm^{-3} were quoted from the Sandblaster II tests [16]. This information is used to estimate the mass of dust reaching the engine. If incompressible flow is assumed, the mass flow of air-particle mix entering the engine intake system is given by:

$$\dot{m}_p = c_m \dot{m}_a \tag{3.1}$$

where c_m is the particulate mass concentration and $\dot{m}_a$ is the engine mass flow rate. The particulate mass concentration is related to the brownout dust concentration as:

$$c_m = \frac{\rho_p V_p}{\rho_{pg} V_{pg}} = \frac{c_v}{\rho_{pg}} \tag{3.2}$$

where V corresponds to volume, and c_v is the particulate volume concentration expressed as mass of particles per unit volume of air-particle mix. The dual-phase density, ρ_{pg} can be expressed in terms of the individual phase densities by considering the mass proportions:

$$V_{pg}\rho_{pg} = \rho_p V_p + \rho_g V_g \tag{3.3}$$

which reduces to:

$$\rho_{pg} = c_v + \rho_g(1 - \frac{c_v}{\rho_p}) \tag{3.4}$$

Substituting Equation 3.4 into Equation 3.2 and simplifying yields an expression for the dust mass concentration as a function of the brownout concentration and the two phases' respective densities:

$$c_m = \frac{1}{\rho_g/c_v + (1 - \rho_g/\rho_p)} \tag{3.5}$$

Thence Equation 3.5 can be used with Equation 3.1 to determine the mass of particles reaching the engine based on the local dust concentration, constituent densities (assumed constant) and engine inlet conditions.

3.2.2 Particle Classification

The mass of particles reaching the engine will contain a range of sizes and shapes. An indication of this is given in the Sandblaster II test results [16] and Figure 2.6. The distribution of particle sizes is likely to vary from one location to the next. As an example, Figures 3.2 and 3.3 illustrate the percentage by mass of 6 different sand samples from different locations across the globe; the variation is notable. The main minerals present in these samples are Quartz, Calcite, Albite and Dolomite, which have a specific gravity of $\simeq 2.7$; the particle shapes are not known. The dust may also contain compounds of iron, as shown in Figure 3.1 which are separated when the sample is magnetised. To ascertain the performance of an EAPS system would be nigh on impossible if each individual particle were to be considered; instead the range of particles and shapes can be represented by a characteristic length or an algebraic function. A dust sample such as in Figure 3.2 can be discretised into size bands by sieving or other method, to achieve the data presented in Figure 3.3. The number of particles in a given size band is counted and expressed as a fraction of the total number, and usually presented in one of two ways: as a histogram showing the percentage by mass of each range; or as cumulative undersize curve, whereby the particles are summed from on size band to the next such that the abscissa gives the fraction of the total number of particles *below* a given size.

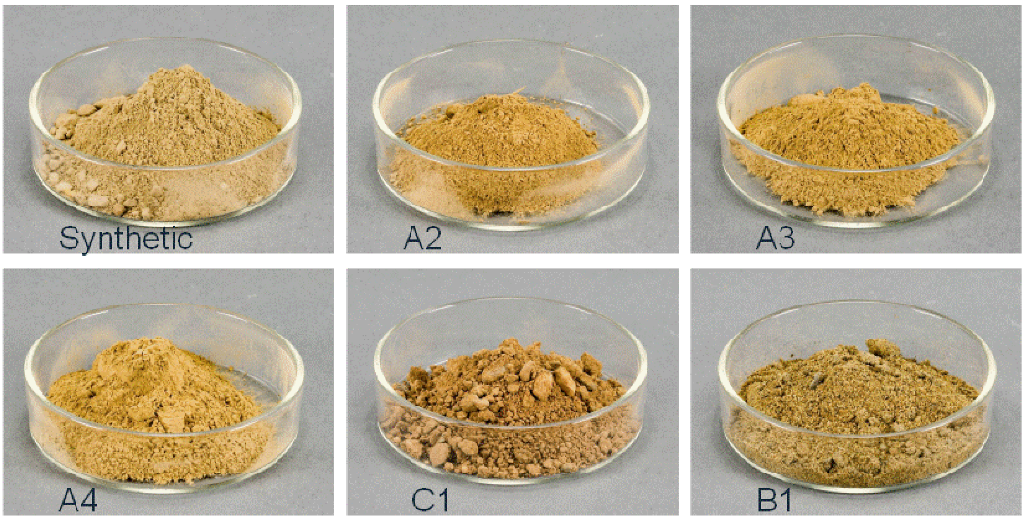

Figure 3.2: *Photographs showing 6 sand samples from locations across the globe. Reproduced with permission by DSTL.*

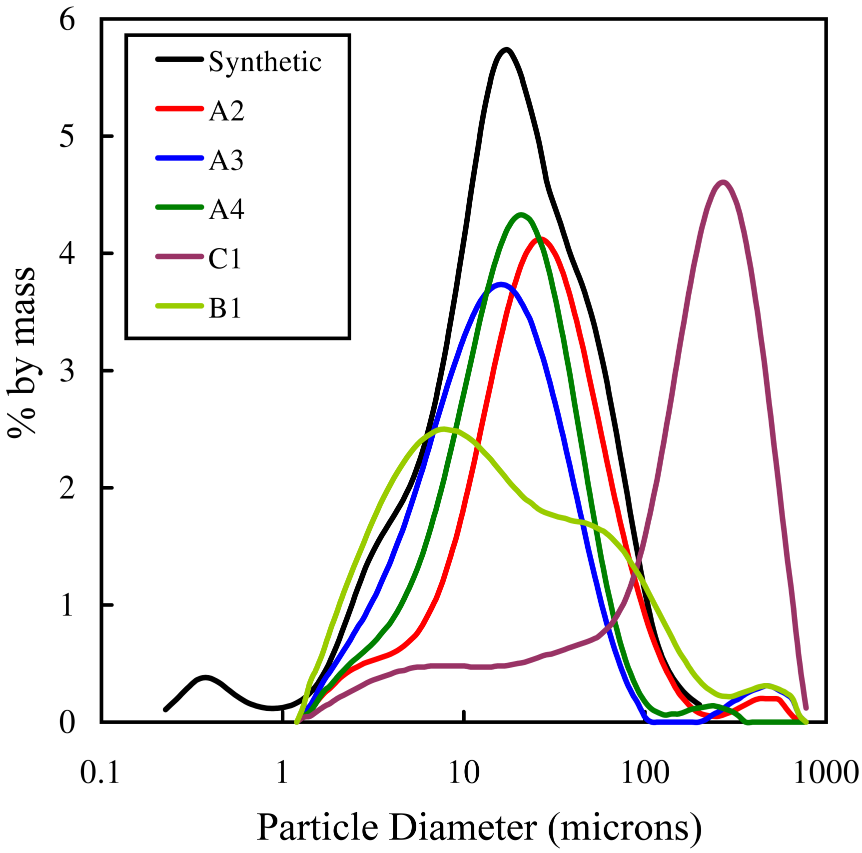

Figure 3.3: *Particle diameter proportions as percentage by mass of six sand samples from locations across the globe. Reproduced with permission by DSTL.*

For particle transport modelling, it may be more useful to express the distribution by mass fraction rather than number. This can be achieved by conversion from the number distribution as follows, as given by Holdich [28]. The mass of a single particle is:

$$m_p = k_v d_p^3 \rho_p \tag{3.6}$$

where d_p is the particle diameter and k_v is the *volume shape coefficient*. For spheres, the volume shape coefficient is $\pi/6$ ($\simeq 0.524$); i.e. it is the factor that the diameter cubed must be multiplied by in order to give the volume of the shape. For sand it is said to be in the region of 0.26 to 0.28. The mass of all particles in a given size range is therefore:

$$m_p = k_v d_p^3 \rho_p f \tag{3.7}$$

where f is the number of particles in that size range. The mass fraction $m_{p,i}^+$, within a size range and compared to the total mass of the distribution, is the mass in the size range divided by the mass of the entire distribution:

$$m_{p,i}^+ = \frac{k_v d_{p,i}^3 \rho_p f_i}{\sum k_v d_{p_i}^3 \rho_p f_i} = \frac{d_{p,i}^3 f_i}{\sum d_{p,i}^3 f_i} \tag{3.8}$$

in which the density and volume shape coefficient are assumed to be constant throughout the all the size grades and can therefore be cancelled. The index i corresponds to the size range. This is the same expression for volume distribution, since mass scales proportionally with volume. To use Equation 3.8, a representative particle diameter is required for the size band; this is usually the mid-point of the grade. Since mass increases as diameter cubed, it follows that the size distribution curve by mass will be nudged towards the coarser end of the diameter spectrum, in comparison with a number distribution. In comparing different dust types for consideration in EAPS modelling, the mass is the most important, as all systems utilise particle inertia.

Another important parameter to represent a size distribution by is the *specific surface area per unit volume*. For a sphere, the surface area is πd_p^2 and the volume is $\pi d_p^3/6$, so the specific area per unit volume is:

$$S_v = \frac{6}{d_p} \tag{3.9}$$

Comparing particle diameters in this way can be more useful to transport and fluid flow problems, especially in porous media because a surface cake composed of particles with a large surface area will exert a greater amount of viscous drag on the fluid per unit volume. The specific surface can be found for the whole distribution by considering the total surface area divided by the total volume of the distribution:

$$S_v = \frac{k_p \sum \bar{d}_{p,i}^2 f_i}{k_v \sum \bar{d}_{p,i}^3 f_i} \tag{3.10}$$

where k_p is the projected area shape factor, which is $\pi/4$ for a sphere. If Equation 3.8 is rewritten as:

$$\bar{d}_{p,i}^2 f_i = \frac{m_{p,i}^+}{\bar{d}_{p,i}} \sum \bar{d}_{p,i}^3 f_i \tag{3.11}$$

it can be substituted into Equation 3.10. The subsequent equation reduces to:

$$S_v = \frac{k_p}{k_v} \sum \frac{m_{p,i}^+}{\bar{d}_{p,i}} \tag{3.12}$$

In non-dimensional form for each particle size group, this is written as:

$$S_{v,i}^+ = \frac{k_p}{k_v} \frac{m_{p,i}^+ / \bar{d}_{p,i}}{S_v} \tag{3.13}$$

The size distributions by number, mass and specific surface are useful for comparing dusts from different parts of the world, for certain motivations. However from a modelling standpoint it would be more useful to represent the distribution with a single particle size. This is achieved by using a mean diameter. The mean diameter can be calculated for each type of distribution by a method that suits the modelling application (e.g. mass-based for inertial transport, specific surface-based for low Reynolds number drag). The mean diameter is calculated as an arithmetic mean or a geometric mean, for the three distribution types. The simplest way to calculate the mean is to use the fractional amount, hence the arithmetic mean diameters by number, mass (volume) and specific surface are:

$$\bar{d}_{p,0} = \sum_{i=1}^{N_p} \bar{d}_{p,i} n_i^+ \tag{3.14}$$

$$\bar{d}_{p,3} = \sum_{i=1}^{N_p} \bar{d}_{p,i} m_i^+ \tag{3.15}$$

$$\bar{d}_{p,32} = \sum_{i=1}^{N_p} \bar{d}_{p,i} S_{v,i}^+ \tag{3.16}$$

respectively, while the geometric mean diameters are:

$$\mu_{\gamma,0} = \prod_{i=1}^{N_p} \bar{d}_{p,i}^{n_i} \tag{3.17}$$

$$\mu_{\gamma,3} = \prod_{i=1}^{N_p} \bar{d}_{p,i}^{m_i} \tag{3.18}$$

$$\mu_{\gamma,32} = \prod_{i=1}^{N_p} \bar{d}_{p,i}^{S_{v,i}} \tag{3.19}$$

The extent of the variation of the size range from these means can be expressed by their associated standard deviations. The arithmetic standard deviation is given as:

$$\sigma = \sqrt{\frac{1}{N_p}\sum_{i=1}^{N_p}(d_{p,i} - \bar{d}_p)^2} \tag{3.20}$$

while the geometric standard deviation is given as:

$$\sigma_\gamma = \sqrt{\frac{1}{N_p}\sum_{i=1}^{N_p}(\ln d_{p,i} - \ln \mu_\gamma)^2} \tag{3.21}$$

where N is the number of particle size ranges.

3.2.3 Particle Shape

Particle shape can considerably influence the nature of the brownout dust cloud. A flat, flaky particle will descend like a feather oscillating from side to side and take much longer to reach the ground than a more rounded, heavily eroded particle. This increases its chances of reaching the engine, where its potential for damage may also depend upon its shape, or sharpness. Much like the particle size, particle shape distributions can be obtained with certain imaging techniques (see for example Ref. [62]), but for low order analysis the particle shape can be approximated using the Wadell sphericity (Ψ), given as:

$$\Psi = \frac{\text{surface area of sphere of equal volume to the particle}}{\text{surface area of the particle}} \tag{3.22}$$

This uses the property that the sphere has the smallest surface area per unit volume of any shape. Hence, the value of sphericity will be fractional, or unity for the case of a sphere. A selection of shape descriptors, corresponding sphericity and typical examples are given in Table 3.1.

Table 3.1: *Common particle shape descriptors and associated sphericities as described by Wadell. Adapted from Ref. [28].*

Descriptor	Wadell's Sphericity	Example
Spherical	1.000	glass beads, calibration latex
Rounded	0.820	water worn solids
Cubic	0.806	sugar, calcite
Angular	0.660	crushed minerals
Flaky	0.540	gypsum, talc
Platelet	0.220	clays, kaolin

The descriptors in Table 3.1 can be approximated from visual inspection, however numerical classification is made by direct measurement which can be difficult to achieve. In many low order models of particle transport and sedimentology a spherical particle is assumed. When the shape is irregular, certain dimensional parameters are used to express the non-sphericity of the particle, such as flatness and elongation ratio, angularity, degree of sphericity, flakiness index, and shape index. Determining these parameters by direct measurement is made complicated by the choice of reference axes. To build up a reliable picture of the shape variability within a sample ultimately requires a combination of measuring techniques. Fractal analysis, i.e. sorting a sample into diameter bands, is achieved by sieving; the projected area can be assessed by microscope; the surface area is estimated from the particle's light scattering ability measured by Fraunhofer diffraction; while particle chord length can be determined by focused beam (laser) reflectance measurement.

A description of the key irregular particle shape parameters is given by Uthus *et al.* [63]. There are three orthogonal dimensions to be determined: the *longest* length L_l; the *intermediate* length L_m; and the *short* length L_n. The flatness ratio ς and elongation ratio φ are computed using these lengths as follows:

$$\varsigma = \frac{L_n}{L_m} \tag{3.23}$$

$$\varphi = \frac{L_m}{L_l} \tag{3.24}$$

The shape of the aggregates can be described by a shape factor Φ and the sphericity Ψ. The shape factor is the ratio of the elongation ratio and the flatness ratio:

$$\Phi = \frac{\varsigma}{\varphi} \tag{3.25}$$

A round or cubic particle will have a shape factor equal to 1. If the shape factor is less than 1, the particle is more elongated and thin. A blade shaped particle will have a shape factor greater than 1. The sphericity is defined by Equation 3.22, but can also be expressed by the flatness and elongation ratios:

$$\Psi = \frac{12.8\sqrt[3]{\varsigma^2\varphi}}{1+\varsigma(1+\varphi)+6\sqrt{1+\varsigma^2(1+\varphi^2)}} \tag{3.26}$$

Another parameter connected with the particle shape and utilised in particle classification is the volume shape coefficient k_v, whose relevance to the subject is introduced and described in Equation 3.6 in Section 3.2.2. For a singular particle its application is rather benign, since there is no precise reference diameter to use, and the volume can be measured directly. It is more useful at expressing the shape of a generic particle within a distribution, in which the reference diameter has more relevance for the application as discussed in Section 3.2.2. However, some models may require specific particle data rather than distribution properties in order to model particle transport using the equations of motion. By definition, the sphericity equation gives important information about the particle shape that is relevant to particle drag, but is too specific to apply to the whole distribution. Since both scales are required here, an expression linking the sphericity and the shape coefficient would be useful.

The volume shape coefficients can be expressed in terms of one another by considering each of their definitions. Consider the an irregular-shaped particle under inspection. Equating its volume ($k_v d_p^3$) to a sphere and rearranging for the sphere's diameter d_s gives:

$$d_s = \left(\frac{6k_v}{\pi}\right)^{1/3} d_p \tag{3.27}$$

where k_v is recalled as the factor by which the particle diameter cubed is multiplied to calculate the volume. The surface area of a sphere is πd_s^2; assuming the surface area of an irregular-shaped particle is calculated in the same way but for a characteristic diameter, the sphericity can be written:

$$\Psi = \frac{\pi(6\pi^{-1}k_v)^{2/3}d_p^2}{\pi d_p^2} = \left(\frac{6k_v}{\pi}\right)^{1/3} \tag{3.28}$$

rearranging for k_v:

$$k_v = \frac{\pi\Psi^{3/2}}{6} \tag{3.29}$$

Hence an angular particle with $\Psi = 0.540$ according to Table 3.1 will have a volume shape coefficient of $k_v \simeq 0.28$. The limitation of this generalisation is that the shape coefficient cannot exceed $\pi/6$, the value of k_v for a sphere, which by the true definition of sphericity may occur in nature. However, the shape coefficient for sand is approximately what is calculated for an particle of sphericity between "angular" and "flaky", therefore this approximation is deemed valid for the present application.

3.2.4 Algebraic Representation of Dust

The mass fraction distribution curves presented in Figure 3.3 are more useful to analysis if represented algebraically. With caution to reliability, the mean and standard deviations calculated above can be utilised to achieve this. Without lack of generality as shown in Figure 3.3, the dust samples found in nature can be assumed to have a log-normal distribution, represented by a probability density function (PDF):

$$\mathrm{PDF}(x,\mu,\sigma) = \frac{1}{x\sigma\sqrt{2\pi}} \exp\left[-\frac{(\ln x-\mu)^2}{2\pi^2}\right] \tag{3.30}$$

where μ is the mean particle size and σ is the standard deviation of their own respective natural logarithm. This is a well-known distribution, whose characteristics are given in several mathematics textbooks. If the geometric mean μ_γ and standard deviation σ_γ are known from a particle sample such as described above, then the values of μ and σ in Equation 3.30 are:

$$\mu = \ln \mu_\gamma - \frac{1}{2}\left(1+\frac{\sigma_\gamma}{\mu_\gamma^2}\right) \tag{3.31}$$

$$\sigma^2 = \ln\left(1+\frac{\sigma_\gamma}{\mu_\gamma^2}\right) \tag{3.32}$$

The cumulative density function is written:

$$\mathrm{CDF}(x,\mu,\sigma) = \frac{1}{2}\mathrm{Erfc}\left[-\frac{\log x-\mu}{\sigma\sqrt{2}}\right] \tag{3.33}$$

The functions of x expressed by Equations 3.30 and 3.33 will be useful in theorising particle separation. Every EAPS system's ability to capture a given particle is dependent on the particle diameter, hence a prediction of the separation efficiency is likely to be expressed as a function of particle size. Coupled with the dimensional analysis techniques described above, these final equations provide the necessary data for the performance prediction of an EAPS system in a given dusty environment.

3.2.5 Particle Equations of Motion

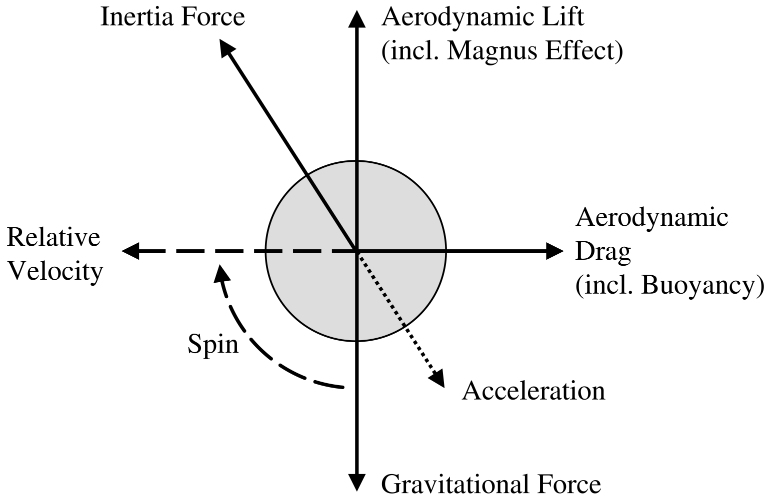

Figure 3.4: *Body forces contributing to particle motion in the air. Adapted from Ref. [6].*

To begin modelling the efficacy of an EAPS system, it is necessary to understand the motion of a particle in the air. The numerous forces are depicted in Figure 3.4. The trajectory of a particle through the air can be modelled by a Lagrangian approach, applying Newton's Second Law of Motion. During particle movement, the forces acting on a particle include interparticle forces, the gravitational and fluid drag forces, and a buoyancy force. According to tests by van der Walt *et al.* [64], the dust concentration at which particle-on-particle interactions become non-negligible is around 49 gm^{-3}. This is beyond even the peak dust concentrations of 5 gm^{-3} anticipated during a brownout cloud (see Section 2.2.3). Therefore the interparticle forces are discounted here. The Newtonian momentum equation for a sand particle of mass m_p, diameter d_p, acceleration $\vec{a}$ and frontal area A_p in the Lagrangian framework is given by:

$$m_p\vec{a} - k_v\rho_g d_p^3\vec{a} = \frac{1}{2}C_d\rho_p\vec{v}^2A_p + m_p\vec{g} \tag{3.34}$$

where C_d is the drag coefficient, ρ_g is the air density, and $\hat{e}$ is the unit vector in the direction of interest. The particle relative velocity $\vec{v}$ expressed in cylindrical coordinates is given by:

$$\vec{v} = \sqrt{(u_r - v_r)^2 + (u_\theta - v_\theta)^2 + (u_z - v_z)^2} \tag{3.35}$$

where the subscripted u and v are the air and particle velocities in the radial (r), tangential (θ) and axial (z) directions, respectively. Similarly the acceleration vector is given by:

$$\vec{a} = \frac{dv}{dt} = \left[\frac{dv_r}{dt} - \frac{v_\theta^2}{r}\right]\hat{e_r} + \left[\frac{dv_\theta}{dt} + \frac{v_r v_\theta}{r}\right]\hat{e_\theta} + \frac{dv_z}{dt}\hat{e_z} \tag{3.36}$$

where $\hat{e}$ is the unit vector in the direction of interest. Equation 3.34 can be written as:

$$\begin{aligned}\vec{a} &= \left(\frac{C_d \rho_p \vec{v} A_p}{2m_p - 2k_v \rho_g d_p^3}\right)(\vec{u} - \vec{v}) + \frac{m_p \vec{g}}{m_p - k_v \rho_g d_p^3} \\ &= \left[C(u_r - v_r) + G\right]\hat{e_r} + \left[C(u_\theta - v_\theta) + G\right]\hat{e_\theta} + \left[C(u_z - v_z) + G\right]\hat{e_z} \end{aligned} \tag{3.37}$$

with $C = C_d \rho_p \vec{v} A_p / 2m_p - 2k_v \rho_g d_p^3$ and $G = m_p \vec{g}/m_p - k_v \rho_g d_p^3$ for simplicity. Comparing Equations 3.36 and 3.37, the components of the particle acceleration in different directions can be written as:

$$\begin{aligned}\frac{dv_r}{dt} &= C(u_r - v_r) + \frac{v_\theta^2}{r} + G \\ \frac{dv_\theta}{dt} &= C(u_\theta - v_\theta) - \frac{v_r v_\theta}{r} + G \\ \frac{dv_z}{dt} &= C(u_z - v_z) + G \end{aligned} \tag{3.38}$$

Calculation of the particle drag coefficient is dependent on the particle Reynolds number, which is given as:

$$\mathrm{Re}_p = \frac{\rho_g(\vec{u} - \vec{v})d_p}{\mu_g} \tag{3.39}$$

A particle can be expected to pass through a range of Reynolds numbers as it reaches the engine. Accurate drag models exist, including those for non-spherical particles which employ a shape factor, such as the model by Haider & Levenspiel [65]:

$$C_d = \frac{24}{\mathrm{Re}_p}\left(1 + b_1 \mathrm{Re}_p^{b_2}\right) + \frac{b_3 + \mathrm{Re}_p}{b_4 + \mathrm{Re}_p} \tag{3.40}$$

where the coefficients b_i are a function of a shape parameter. Equation 3.40 is valid for Reynolds numbers below 10^5.

3.2.6 Particle Settling Velocity

One of the fundamental problems is to decide which particles to filter. Sufficiently small particles, once lifted from the ground, stay aloft for a considerable time; larger particles tend to fall under the effect of their own weight. Thus, although the ingestion of larger particles can be more damaging, their occurrence is less likely. A particle descending under its own weight experiences an upwards force of buoyancy and fluid drag; when the forces become balanced the particle has reached *terminal settling velocity.* The magnitude of the drag force depends on the Reynolds number of the particle. At $\mathrm{Re}_p < 2$ the drag can be estimated by Stokes Law. Under these conditions there is no turbulence, hence the terminal descent speed is given as:

$$U_t = \frac{(\rho_p - \rho_g)d_p^2 g}{18\mu_g} \tag{3.41}$$

The Arizona AC Fine test dust consists of particles between 2 and 80 μm, but all the particles below 10 μm make up about 50% of the total mass. A 10 μm particle has a terminal velocity of $U \simeq 0.00833$ ms^{-1}, whilst a 80 μm descends at about 0.5 ms^{-1}. To justify the use of Stokes' law in the derivation presented here, the Reynolds numbers of the particles are relatively small. For a descent speed of 0.5 ms^{-1}, an 80 μm particle has a $\mathrm{Re}_p \simeq 2.9$, which is around the point at which turbulent effects become non-negligible. Using Stokes drag for larger diameters will result in an over-prediction of the terminal settling velocity due to the emergence of the form drag component.

A settling velocity of 0.5 ms^{-1} may just be low enough to be picked up by the engine, or at least entrained well into the dust cloud. Unfortunately, such statements are true only for particles that are forced only once. The helicopter environment causes an intermittent forcing of the particles, some of which are on the ground, and others are aloft in a cloud of dust. The combination of rotor downwash, helicopter movement and helicopter configuration greatly complicates the matter. See Section 2.2.

3.2.7 Brownout Severity

The link between rotorcraft design parameters and the severity of the characteristic brownout cloud is reported by the Sandblaster II test results [16] and later studies based on video evidence by Milluzzo & Leishman [3]. A review of these findings is given in Section 2.2.3. The study by Milluzzo & Leishman attempted to illustrate a trend between brownout severity and two macroscale parameters:

1. Total Wake Strength
2. Wake Vortex Impingement Rapidity

The former is related to the strength of the downwash which can be directly related to the rotorcraft weight or rotor size; the latter is related to the rotational frequency of the main rotor and the number of blades. These parameters can be derived from rotor design parameters.

The derivation begins with consideration of the main mechanism that causes disturbance of particles from the ground: fluid shear. The fluid shear develops in the boundary layer at the sediment surface that forms as the downwash impinges on the ground and emanates away radially as a groundwash jet. The strength of the groundwash slipstream can be approximated by application of classic momentum theory for a hovering rotor. In the far wake, the slipstream velocity w is linearly proportional to the average induced velocity in the plane of the rotor disk. By assuming ideal wake contraction with a rotor in free air, then w is exactly two times the induced velocity at the rotor disk:

$$w = 2\sqrt{\frac{T}{2\rho_g A_R}} = \sqrt{\frac{2DL}{\rho_g}} \tag{3.42}$$

where T is the rotor thrust (approximately equal to rotorcraft weight for a single rotor system), A_R is the rotor area and DL is the rotor disk loading. Milluzzo states that in practice, non-ideal effects increase the average wake velocities by about 10-20%, but operations in ground effect (when the downwash cannot freely escape from the rotor) will affect wake velocities as a function of rotor plane distance off the ground. Typical maximum wake velocities are around $0.7w$ to $1.2w$, hence Equation 3.42 is a reasonable first order approximation to the maximum average groundwash velocity.

The second main mechanism for sediment uplift is entrainment by the interaction of convecting tip vortices with the ground (see Figure 2.4). The strength of the tip vortices, Γ_v, that are trailed by each of the rotor blades can be approximated by:

$$\Gamma_v \approx k\left(\frac{C_T}{\sigma}\right)(\Omega_R R_R)c_b \tag{3.43}$$

where from vortex theory $k = 2$ in hover (although other values may be used based on empirical evidence), C_T is the thrust coefficient, σ is the rotor solidity, Ω_R is the rotational frequency of the rotor, R_R is the rotor radius, and c_b is the average blade chord length. The blade loading coefficient, C_T/σ, can be written as:

$$\frac{C_T}{\sigma} = \frac{T}{\rho_g A_b \Omega_R^2 R_R^2} \tag{3.44}$$

where A_b is the are of the blades. For a given viscous core size (and hence vorticity distribution), the peak velocities in the wake flow will be proportional to Γ_v.

It has been observed in experiments that the convecting tip vortices roll up into one another to create a supervortex. The net circulation of this supervortex is proportional to the number of merging vortices and their strengths. According to Milluzzo & Leishman the tendency for tip vortices to merge is related to their number (i.e. the number of blades) and their axial spacing (i.e. a combined disk loading and ground proximity effect. In this regard, a *normalised total wake strength*, Γ_w, can be defined which is the product of the tip vortex strength and the total number of rotor blades, normalised with $\Omega_R R^2$:

$$\Gamma_w^* = \frac{N_R N_b}{\Omega_R R_R^2}\Gamma_v \approx k N_R N_b (C_T/\sigma)\frac{\Omega_R R_R c_b}{\Omega_R R_R^2} \tag{3.45}$$

where N_R is the number of rotors and N_b is the number of blades.

Another hypothesis about brownout cloud formation suggests that the average *rate* at which sediment is entrained into the flow can be correlated with the frequency at which the individual blade tip vortices impinge on the ground, which is governed by the number of blades and the rotor rotational velocity. Referred to as the *wake convection frequency*, it is defined by:

$$\Omega_s = N_R N_b \Omega_R \tag{3.46}$$

From this relationship it can be inferred that a rotorcraft with a greater number of blades and/or higher rotor rotational speeds may tend to uplift more sediment from the ground per unit time, all other factors being equal. The wake convection frequency can be used to establish a quantitative *brownout metric* by establishing a *reduced frequency*, defined as:

$$k_s = \frac{\Omega_s c_b}{2\Omega_R R_R} \tag{3.47}$$

and comparing it with the normalised total wake strength given by Equation 3.45 and the normalised downwash, defined as:

$$w^* = \frac{w}{\Omega_R R_R} \tag{3.48}$$

where the average downwash w is given by Equation 3.42. Since the total wake strength can be viewed as a measure of the intensity of the brownout cloud; reduced frequency can be viewed as a measure of the speed at which the cloud forms; and the average downwash can be considered as the rate at which the cloud convects radially from the rotorcraft; it follows that a rotorcraft with high values of the former two parameters does not necessarily create a severe brownout cloud if its disk loading is large. Similarly a rotorcraft of moderate disk loading may suffer a terribly dangerous cloud formation if either of the two other parameters is large.

In these derivations, the authors wish to make clear that in this low-order analysis no distinction is made between the effects of rotor configuration (i.e. a two-rotor system may refer to tandem or coaxial arrangement of rotor disks). Additionally, no accounting has been made for rotor-airframe interaction effects; indeed it was alluded to in Section 2.2.3 that the blocking effect of the extended Merlin cabin body may help to reduce the brownout phenomenon.

Nevertheless these analytical solutions provide a useful starting point. Milluzzo & Leishman apply these metrics to many rotorcraft of known design parameters to generate quantitative data to corroborate anecdotal evidence and video footage of rotorcraft brownout generation. For all rotorcraft for which the authors have data, they plot the reduced frequency against the normalised total wake strength, and against the normalised average downwash. Based on the qualitative evidence, they establish three levels of brownout severity which demarcate the plots into areas bounded by key values of the abscissae and ordinates mentioned above.

Rotorcraft with Level 1 brownout characteristics generally stir up limited amounts of dust, which in any case is blown radially away posing little risk of reingestion into the rotor disk. Level 2 rotorcraft are characterised by their creating of a cloud of much greater vertical extent, which increases the risk of reingestion and a denser brownout cloud overall. Level 3 rotorcraft generate the most severe brownout clouds in which dense plumes or columns of dust are stirred up and recirculated through the rotor disk propagating the process. Zero visibility is reported in such clouds; a very dangerous situation for the pilot and probably for the unprotected engine too. For the data set used in their study, Milluzzo & Leishman suggest the boundaries given in Table 3.2.

Table 3.2: *Numerical boundaries for brownout severity levels based on rotor design parameter assessment criteria, as described by Milluzzo & Leishman [3].*

Level 1	Level 2	Level 3
$0 < \Gamma_w^* \leq 0.12$	$0.12 < \Gamma_w^* \leq 0.18$	$0.18 < \Gamma_w^* \leq 0.3$
$0 < w^* \leq 0.112$	$0.112 < w^* \leq 0.17$	$0.17 < w^* \leq 0.2$
$0 < k_s \leq 0.035$	$0.035 < k_s \leq 0.06$	$0.06 < k_s \leq 0.14$

The objective of this section is to try to predict the severity of a brownout cloud of a given rotorcraft in order to anticipate the concentration of particles at its engine intake. While not providing exact details of the local particulate concentrations, the anticipated severity level can be married with test data such as the Sandblaster II results to give an indication of what each level means in terms of dust cloud density. The method is still young and doubtlessly needs corroborative data, but it at least allows some educated estimates to be made about the particulate mass concentrations that a given helicopter engine can be expected to ingest. This will be visited in later chapters.

3.3 Inlet Barrier Filter Theory

IBF performance is assessed by a number of indicators. The first is the *capture efficiency* of the filter, which is the proportion of matter removed by a given filter from a given particulate-laden feed. It is also referred to as the *separation efficiency* or the *collection efficiency*, and owing to the different capture mechanisms described above it depends upon the particle and filter properties. Filters are often rated with a single efficiency, which refers to its efficacy in a specific particulate feed such as a test dust.

In reality, a given filter may perform better or worse depending on its construction and the environment in which it is operating and will improve in capture efficiency as it collects more particles. In the case of IBF, a huge range of particle shapes and sizes can be encountered, which means the separation efficiency will vary from location to location. To establish how an IBF filter medium performs across such conditions, a method to calculate filter efficiency based on particle size and degree of contamination is required.

The other important IBF performance indicator is *pressure drop*. While protecting the engine from foreign object damage, a side effect of the filter's presence is an inherent loss in pressure. This occurs due to friction exerted on the air by the constituent fibres of the filter. Furthermore as the filter collects particles, the total surface area on which friction acts increases and the pressure drop rises. The evolution of this rise can be split into two stages. The first corresponds to particles collecting within the filter, in a process known as depth filtration. It is during this stage that the separation efficiency is augmented. When the filter reaches its *holding capacity*, the particles begin to settle on the surface, forming what is known as the *filter cake*. This represents the second stage of pressure drop evolution, in which the filter cloth acts merely as a support for the cake, which now takes over as the principle filtration medium. This duality is considered in a second method, developed in the present work to predict the loss in pressure across an IBF system.

Broadly speaking, there are two methods of filtration. The first method is *depth filtration*, which refers to particle capture within the filter medium, whereby individual fibres in the fabric intercept particles by one or more capture mechanisms. Owing to the influence of fluid viscous forces at small particle Reynolds number, the dominance of any one capture mechanism changes with the slurry properties and filter structure. To accurately model depth filtration is difficult and has attracted much attention in the literature, including whole books dedicated to the subject (Refs. [66], [67]). The second method of filtration is known as *surface filtration*, in which particles collect on the surface of a filter or mesh and begin to form a cake. As the cake builds up, it acts as a filter itself and replaces the filter medium as the main barrier to particles. Once a layer has formed over the original filter, only particles smaller than the interstitial pores can permeate through. Both processes are relevant to IBF.

There are also two different categories of fabric filters: *nonwoven* and *woven*. The former are fibrous beds, made up of a random assortment of fibres that operate mainly by depth filtration. The latter are fibrous yarns ordered in a lattice formation that mainly employ surface filtration. IBF currently employ a multilayer woven fabric on the surface of which larger particles collect, but the collection of smaller particles may also occur within the layers and within the yarns, thus augmenting the filtration process.

Most of the existing IBF contain an oil-impregnated woven cotton filter, but a new non-woven fabric is being introduced, which purportedly offers a higher separation ability with the requirement of a tacking agent.

A particle's motion within the fluid is dependent on its size, shape, mass, temperature and velocity (linear and angular); while its adhesion to the fibres of the filter or another particle will depend upon its coefficient of restitution, surface roughness and charge, along with all the varying fluid properties that may influence attractive and repulsive forces including the tacking agent. However, it is possible to deconstruct the problem to gain a greater understanding of the mechanisms at work in order to realise the relevance of particle capture in the context of IBF modelling. First, it is useful to provide a brief description of the filter structure and the basic properties that are used to calculate the two main performance parameters of a porous medium: pressure drop and separation efficiency.

3.3.1 Porous Media Pressure Drop

There are two types of porous media contributing to the pressure drop across IBF device: the filter medium and the surface cake. The surface cake does not appear immediately, but accumulates once the filter has reached *capacity*, which will change according to the particulate properties but is invariably given as a mass per unit area, for a filter of a given thickness. The capture of particles adds a source of drag to the filter, and causes the pressure drop to increase over time. This temporal rise is significant as the effect of the IBF on engine performance will therefore be transient. Furthermore, there is a discontinuity in the pressure rise (as observed by Rebaï *et al.* [52]) when the surface cake begins to form, characterised by an increase in gradient. The investigation of this transient pressure drop begins with a look at the fundamentals of fluid flow through porous media.

There is a great deal of literature in this important area of filtration & separation which can become overwhelming, however a neat summary of the fundamentals of porous media flow was found in a book by Holdich [28]. The history of determining pressure loss through porous media dates back to the 1850s, when Darcy observed a linear relationship between flow rate and head loss through beds of sand. The well known *Darcy's Law* is based upon his findings:

$$\frac{\Delta P}{L} = \frac{\mu}{k}\frac{dV}{dt}\frac{1}{A} \tag{3.49}$$

where ΔP is the pressure drop, L is the length of the sand bed, μ is the fluid viscosity, dV is the fluid volume passed through in a time of dt, and A is the sand bed cross-sectional area. The important coefficient of proportionality, k, also referred to as the *coefficient of permeability*, is a scalar property that coupled with the viscosity expresses the ease at which a fluid is transported through a porous matrix. It therefore depends on the internal geometrical properties of the porous matrix. A permeability of zero would give rise to infinite resistance. A number of researchers have attempted to fit theoretical or semi-empirical models to experimental data to obtain a general expression for k based on properties of the porous matrix. The most famous of these is the Kozeny-Carman equation, which was derived from the Hagen-Poiseuille equation for laminar flow of fluid in a circular channel:

$$\frac{\Delta P}{L} = \frac{32\mu}{d_{ch}^2} u_i \tag{3.50}$$

where d_{ch} is the characteristic channel diameter, and u_i is the mean channel velocity. In extension to porous media, the interstitial velocity — velocity within the pores — is analogous to the channel velocity, while the characteristic length was deduced by Kozeny as the volume open to the fluid flow divided by the total surface area over which it must flow. If the medium porosity is ϵ, then the interstitial velocity and characteristic channel diameter are:

$$d_{ch} = \frac{AL\epsilon}{AL(1-\epsilon)S_v} = \frac{\epsilon}{(1-\epsilon)S_v} \tag{3.51}$$

$$u_i = \frac{U_s}{\epsilon} \tag{3.52}$$

where S_v is the specific surface area per unit volume and U_s is the superficial velocity. If the superficial velocity is written instead as the volume flow rate per unit cross-sectional area and Equations 3.51 and 3.52 are substituted into Equation 3.50, the widely-known Kozeny-Carman equation is formed:

$$\frac{\Delta P}{L} = \mu_g \left[\frac{K(1-\epsilon)^2 S_v^2}{\epsilon^3}\right] \frac{dV}{dt}\frac{1}{A} \tag{3.53}$$

where K is the *Kozeny constant* containing the constants, which includes a factor to account for the tortuosity of the flow channel. Comparing with the Darcy Equation 3.49, the permeability coefficient is therefore:

$$k = \frac{\epsilon^3}{K(1-\epsilon)^2 S_v^2} \tag{3.54}$$

The Kozeny constant K can be verified with experiment, but an initial approximation is given by Ergun as 150 (see Chapter 5.11 Bear [68]).

The Kozeny-Carman equation is reliably applicable for laminar flow only; i.e. for viscous drag by the fluid on the surface of the particles or fibres in the porous matrix.

The limit of its applicability is defined by a modified form of the Reynolds number which uses the Kozeny characteristic dimension from Equation 3.51 as the reference length and the interstitial velocity as the reference velocity:

$$\mathrm{Re}'_p = \frac{\epsilon}{(1-\epsilon)S_v}\frac{U_s}{\epsilon}\frac{\rho}{\mu_g} \tag{3.55}$$

The deviation from the proportional relationship is said to occur at Re'_p in the range of 1 to 10 [68], although Holdich [28] claims laminar flow predominates at $\mathrm{Re}'_p <$ 2. Figure 3.5 gives a schematic representation of results of a typical one-dimensional experiment in which the rate of flow is gradually increased. Forcheimer is said to be the first to suggest a non-linear relationship between flow rate and pressure drop at large Reynolds number, attributing the divergence to the appearance of turbulence. However, while the Kozeny-Carman equation is fundamentally based on pipe flow, the onset of turbulence is observed at a Reynolds number several orders of magnitude lower than in pipes. Furthermore, the laminar to turbulent transition is gradual. Several researchers have attempted to explain this phenomenon, refuting Forcheimer's explanation that it is due to the inhomogeneity of the medium (large pores "tripping" turbulence earlier than smaller pores) and instead proposing that inertial forces are always present in porous media due to pore tortuosity but only become prevalent at $\mathrm{Re}'_p > 1$. In fact, experiments show that full turbulence is only observed at Re'_p of between 60 and 150. The discussion continues; a review of suggestions up to 1972, as just discussed, is given in Chapter 5.11 of Bear [68].

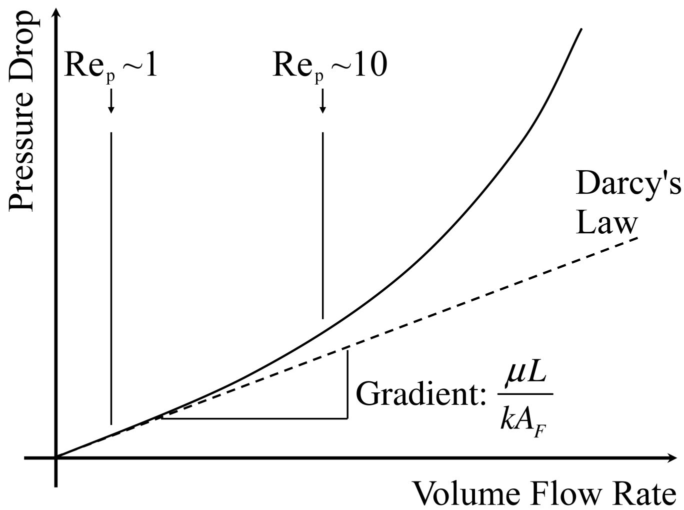

Figure 3.5: *The deviation from the proportionality relationship between pressure drop and flow rate at increasing Reynolds number. Adapted from Bear [68].*

If the physics remains unresolved, there is definite consensus on the non-linearity and the Reynolds number at which it appears. The non-linearity is accounted for by adding a quadratic term to the Darcy equation. Expressed in terms of the volume flow rate, the pressure gradient across a porous medium at all Reynolds number is given as:

$$-\nabla p = \mu_g \frac{Q}{A} C + \frac{1}{2}\rho_g \left(\frac{Q}{A}\right)^2 D \tag{3.56}$$

where Q is the volume flow rate, and the constants C and D represent the *viscous* and *inertial* resistance coefficients, respectively. The viscous resistance term is simply the inverse of the permeability coefficient, given by Equation 3.54 (although this could be adapted to fit experimental data). The inertial resistance term however is often derived empirically; again a comprehensive review of derivations is given in Bear. For a fibrous filter medium used in IBF applications, it is assumed that the fibre diameter is constant. The viscous and inertial resistance terms as given by Ergun for the filter medium are:

$$C = \frac{150(1-\epsilon_F)^2}{\epsilon_F^3 d_f^2} \tag{3.57}$$

$$D = \frac{3.5(1-\epsilon_F)}{\epsilon_F^3} \tag{3.58}$$

where d_f is the fibre diameter.

The equations presented so far are applicable to a clean filter. During operation, it is known that the IBF filter captures particles of many different shapes and sizes within its pores, between its constituent fibres or yarns. It is not known, however, exactly how the pressure drop evolves during this period of clogging, as much will depend on the particle size distribution and the local flow conditions which are liable to change. However, it may be possible to ascertain the particulate mass held by the medium at capacity. The mass of particles collected, m_{pc}, is related to the efficiency of the filter by:

$$\dot{m}_{pc} = E_{IBF}\dot{m}_p \tag{3.59}$$

where E_{IBF} is the overall capture efficiency of the IBF and $\dot{m}_p$ is the mass flow rate of particles reaching the filter, given by Equation 3.1. The overall capture efficiency is derived later in Section 3.3.3. To model the effect of the particle accumulation on pressure drop, it is assumed that the additional volume acquired by the filter serves to decrease the medium porosity. The porosity in Equations 3.57 and 3.58 can be written as a function of mass:

$$\epsilon_F(m_{pc}) = \epsilon_F(0) - \frac{\bar{\rho_p} m_{pc}}{Z_F A_F} \tag{3.60}$$

where $\epsilon_F(0)$ is the initial filter porosity (clean state), $\bar{\rho_p}$ is the mean particle density, A_F is the total filtration area and m_{pc} is the mass collected over the period of time spent ingesting particulates. From this relationship it can be seen that the rate of decrease of filter porosity can be alleviated by a larger filtration surface area, or a thicker filter.

It is recalled that there are two types of porous media contributing to the pressure drop. When the mass collected within the filter medium surpasses the holding capacity, the particles collect on the surface as a cake. The cake thickness is also a function of the mass collected:

$$Z_c = \frac{\bar{\rho_p} m_{pc}}{\epsilon_c A_F} \tag{3.61}$$

where ϵ_c is the cake porosity. The cake porosity is not easy to ascertain, since it depends upon the constituent particles. Generally speaking a size distribution with a large spread of particle diameters will result in a denser cake, since the smaller particles fill up the spaces in between the larger particles. It also depends on the particle shape, since particles of a greater specific surface exhibit more drag. The porosity may also change due to compression, however analyses suggest that the compressive forces in this application would not be large enough to make a significant difference [45]. Owing to the denser cake, the rate of increase of pressure drop during cake formation is expected to be greater than during filter clogging. The equations used to predict pressure drop across the filter could be used here, but would be limited to a monodisperse distribution. To model the cake performance a different model is proposed.

Cake filtration is a field in its own right. It is commonly referred to as the process in which separation of particles from slurries is effected by the continued accumulation of solids on the original medium surface. In solid-liquid filtration, it is exploited in environmental applications in the removal of toxic impurities from biological waste; in solid-gas filtration it is used to improve the efficiency of pollutant removal for example in bag filters for incinerators. For IBF it too aids the separation effort, but more attention is paid to the side effect of cake formation, which is the elevated pressure drop.

Much of the current literature on cake filtration aims to establish a more accurate model for pressure drop prediction, in particular looking at the role of porosity and the characteristic particle diameter (see work of Tiller *et al.* [69], [70], [71], [72]; Aguiar *et al.* [73], [74], [75]). The models invariably take the form of Equation 3.56 but for changes to the coefficients to account for polydispersity of the particle sizes. One study by Wakeman *et al.* [76] finds that using the mean diameter of a PSD as the characteristic length can underestimate the pressure drop; instead they suggest that a better estimate would be obtained if the 5% or 10% size on the cumulative density curve were used in the Kozeny-Carman equation.

Many of the studies in the literature use low Reynolds number Stokesian flow through the cake, which maybe typical of the application on which they are based. In extension of any theory to IBF, the Reynolds number is expected to be higher, hence the inertial term cannot be neglected. A study by Endo *et al.* [77] develops a general theory for a polydisperse distribution for high Reynolds number flow. Three assumptions are made in the derivation:

1. Particle size distribution obeys the log-normal distribution as follows:

$$f(\ln d_p) = \frac{1}{\sqrt{2\pi}\ln\sigma_g}\exp\left[-\frac{(\ln d_p - \ln d_{pg})^2}{2\ln^2\sigma_g}\right] \tag{3.62}$$

   where d_{pg} is the geometric mean diameter and σ_g is the geometric standard deviation.

2. Particles are packed randomly and the cake structure is uniform, even if cake compression occurs.

3. The void function $\upsilon(\epsilon_c)$ depends only on porosity ϵ_c.

The void function is implemented to account for the effect of local neighbouring particles on the apparent change of viscosity of the fluid depending on the porosity or the particle concentration. The apparent fluid viscosity increases with the increase of the particle concentration.

The derivation begins by considering the pressure drop as resulting from the drag force acting on all the particles in the layer. The balance of forces is:

$$\Delta P_c A_c = F_c \frac{u_i}{U_s} A_c Z_c \tag{3.63}$$

where ΔP_c is the pressure drop in the dust cake layer, F_c is the sum of the drag force acting on each particle per unit volume of dust cake, U_s is the superficial velocity, u_i is the interstitial velocity, A_c is the cake filtration area, and Z_c is the cake thickness. The velocities are related to the cake porosity ϵ_c by Equation 3.52. Due to the uniform porosity the pressure drop is assumed to rise linearly with cake height.

To estimate the drag force on a single particle within the Stokesian and non-Stokesian regimes, the following expression is used, which can be applied to very large Reynolds number ($\mathrm{Re}_p \leq 10^4$) based on particle diameter [78]:

$$F_p = \frac{\pi}{8} d_v^2 \rho_g u_i^2 \left(0.55 + \frac{4.8}{\sqrt{\mathrm{Re}_{p,c}}}\right)^2 \kappa \tag{3.64}$$

and

$$\mathrm{Re}_{p,c} = \frac{\rho_g u_i d_v}{\mu_g} \tag{3.65}$$

where $\mathrm{Re}_{p,c}$ is the particle Reynolds number in the cake, d_v is the volume equivalent diameter and κ is the dynamic shape factor, which is defined as the ratio of the drag force on the particle in question to that on a sphere of the volume equivalent diameter. Considering all particles in the cake, the drag force can be written as:

$$
\begin{aligned}
F_c =& \int_{-\infty}^{\infty} F_p \upsilon(\epsilon_c) n_c f(\ln d_v)\, \mathrm{d}(\ln d_v) \\
=& \frac{\pi}{8}(0.3025)\rho_g u_i^2 \kappa \upsilon(\epsilon_c) n_c d_{vg}^2 \exp(2\ln\sigma_g) \\
&+ \frac{\pi}{8}(5.28)\sqrt{\rho_g\mu_g}\, u_i^{1.5} \kappa \upsilon(\epsilon_c) n_c d_{vg}^{1.5} \exp\left(\frac{9}{8}\ln^2\sigma_g\right) \\
&+ \frac{\pi}{8}(23.04)\mu_g u_i \kappa \upsilon(\epsilon_c) n_c d_{vg} \exp\left(\frac{1}{2}\ln^2\sigma_g\right)
\end{aligned} \tag{3.66}
$$

where n_c is the total particle number per unit volume of dust cake, d_{vg} is the geometric mean diameter of d_v, and σ_g is the geometric standard deviation.

The relationship between n_c and porosity and ϵ_c is:

$$
\begin{aligned}
\epsilon_c &= 1 - \int_{-\infty}^{\infty} \frac{\pi}{6} d_v^3 n_c f(\ln d_v)\, \mathrm{d}(\ln d_v) \\
&= 1 - \frac{\pi}{6} n_c \exp\left(3\ln d_{vg} + \frac{9}{2}\ln^2\sigma_g\right)
\end{aligned} \tag{3.67}
$$

Substituting Equation 3.66 and Equation 3.67 to eliminate n_c, F_c is given by:

$$
\begin{aligned}
F_c =& \frac{3}{4}(0.3025)\rho_g u_i^2 \kappa \upsilon(\epsilon) \frac{1-\epsilon}{d_{vg}\exp\left(\frac{5}{2}\ln^2\sigma_g\right)} \\
&+ \frac{3}{4}(5.28)\sqrt{\rho_g\mu_g}\, u_i^{1.5} \kappa \upsilon(\epsilon) \frac{1-\epsilon}{d_{vg}^{1.5}\exp\left(\frac{27}{8}\ln^2\sigma_g\right)} \\
&+ \frac{3}{4}(23.04)\mu_g u_i \kappa \upsilon(\epsilon) \frac{1-\epsilon}{d_{vg}^2\exp(4\ln\sigma_g)}
\end{aligned} \tag{3.68}
$$

Substituting Equation 3.68 into Equation 3.63:

$$
\begin{aligned}
\Delta P_c &= F_c \frac{u_i}{U_a} Z_c \\
&= 0.2269\rho_g U_a^2 Z_c \frac{(1-\epsilon)\upsilon(\epsilon)}{\epsilon^3} \frac{\kappa}{d_{vg}\exp\left(\frac{5}{2}\ln^2\sigma_g\right)} \\
&+ 3.96\sqrt{\rho_g\mu_g}\, U_a^{1.5} Z_c \frac{(1-\epsilon)\upsilon(\epsilon)}{\epsilon^{2.5}} \frac{\kappa}{d_{vg}^{1.5}\exp\left(\frac{27}{8}\ln^2\sigma_g\right)} \\
&+ 17.28\mu_g U_a Z_c \frac{(1-\epsilon)\upsilon(\epsilon)}{\epsilon^2} \frac{\kappa}{d_{vg}^2\exp\left(4\ln^2\sigma_g\right)}
\end{aligned} \tag{3.69}
$$

which is of the form:

$$
\Delta P_c = AU_a^2 + BU_a^{1.5} + CU_a \tag{3.70}
$$

Table 3.3: *Particle size and shape distribution parameters of the four powders tested by Endo et al. [77] to verify Equation 3.69.*

Dust Name/Type	d_{vg} (μm)	σ (-)	κ (-)	ρ_p (gcm^{-3})
AC Fine Test Dust	2.0	1.8	1.5	2.65
Alumina Particles	2.0	1.2	1.05	2.42
Alumina Particles	0.7	1.4	1.05	2.42
Talc Particles	2.3	2.0	2.04	2.7

Equation 3.69 was compared with experimental tests on four dusts with the properties given in Table 3.3. In the experiments, dust cake height, pressure drop and final cake mass were measured for each of the four powders. Results for all dusts were shown to correlate well using the theoretical equation. Any spread in the data was attributed to the void function $\upsilon(\epsilon)$, which in theory is a function of only the porosity but seems to depend on the particle size distribution and shape. Hence the void function is an important parameter of the cake which should be determined experimentally for a given dust if Equation 3.69 is to be applied with confidence. In the absence of data from the field, an estimate for the void function is used:

$$\upsilon(\epsilon) = 165\frac{(1-\epsilon_c)}{\epsilon_c^2} \tag{3.71}$$

This is derived from an experimental study by Choi *et al.* [79] in which the dust cake compressibility of fine fly ashes (from a coal power plant of fluidized bed combustor) was investigated. The particle size distributions were represented by geometric mean diameters of 1.2, 2.2, and 3.6 μm, geometric standard deviations of 1.4 1.6 and 1.6, and adjusted dynamic shape factors of 1.15, 1.28 and 1.64 respectively. The cakes were tested at face velocities of 0.02 to 0.08 ms^{-1}. The size distribution is narrower than what is expected in desert conditions (see Section 3.2), while a typical filtration velocity in an IBF system is around 1.5 ms^{-1}.

As alluded to in Section 2.5.3, the total pressure drop is a combination of the loss of pressure through the filter cloth, the loss through the cake, and the loss within the pleat channels. The final source of pressure loss is more difficult to predict, since it depends on the shape of the boundary layer at the filter surface, which can change in the depthwise direction, and can alter depending on the permeability of the medium and the flow conditions. Like the medium loss due to decreasing porosity and cake loss due to increasing thickness, the pleat channel loss is also dependent on the quantity of mass collected. Cake layers build up within the pleat channels and reduce the constriction for the air. The resulting changes to the flow field are difficult to predict with analytical models. For this reason, the present work uses computational fluid dynamics to solve the Navier-Stokes equations within the pleat channels (and across the filter medium) to calculate the total pressure loss as a function of collected mass. This is addressed in later sections. The equation for the total pressure loss across the IBF considering all solutions is therefore:

$$\Delta P_{IBF}(m_{pc}) = \Delta P_F(m_{pc}) + \Delta P_c(m_{pc}) + \Delta P_{ch}(m_{pc}) \tag{3.72}$$

where ΔP_F is the filter medium pressure drop, ΔP_c is the cake pressure drop, and ΔP_{ch} is the pressure loss in the pleat channels, all of which are functions of mass collected.

3.3.2 Filter Parameters

Before embarking on particle separation theory, some filter parameters pertaining to the construction are defined. Due to their more ordered construction, there are more parameters to be defined that relate to woven fabric filters; non-wovens are dealt with first.

Non-woven Fibrous Filters

The two most important parameters are the fibre diameter d_f and the packing fraction α. The packing fraction is the proportion of filter volume occupied by the fibres; it is the opposite of the porosity (proportion of void spaces in *any* porous medium) and is called the medium *solidosity* when referring to a surface cake. It is defined as follows:

$$\alpha = \frac{V_f}{V_F} = \frac{\pi d_f^2 L_f}{A_F Z_F} \tag{3.73}$$

where V_f is the volume of fibres, V_F is the filter volume, L_f is the total length of all fibres, A_F is the filter area and Z_F is the filter depth. Generally speaking, a larger packing fraction means a better separation ability at the expense of greater pressure drop.

The mean pore size, important for the capture of the larger particles, is equivalent to the *interfibre* distance. The distance between the fibres is related to the packing fraction and dependent on the arrangement of the fibre centres. The densest is a staggered arrangement, with centres triangulated. In this formation the interfibre distance, s_f is:

$$s_f = \frac{d_f}{\alpha^{1/2} 12^{1/4}} \tag{3.74}$$

Woven Fabric Filters

A woven fabric filter is made up of yarns. A yarn is spun from a long bundle of fibres and laid in a pattern called a *weave*. The weave is made up of strong *warp* yarns which provide support, and bulkier *weft* yarns which act as filler. The lay sequencing can affect filter performance; for more details see Purchas & Sutherland [80]. In addition to the weave, the filter structure is affected by parameters such as yarn thickness and yarn density, which are themselves influenced by *packing fraction* — the ratio of material volume to porous matrix volume — and yarn *twist* — the spun yarn tightness. One key parameter that defines a filter fabric is the yarn Tex, which is the weight in grams of 1,000 m of yarn. For a given yarn diameter it is possible to determine the yarn bulk density:

$$\rho_y = \frac{4TX}{\pi d_y^2 \cdot 10^3} \tag{3.75}$$

Where d_y is the yarn diameter, and TX refers to the yarn Tex.

Due to its two-part structure, the packing fraction of a woven filter is ambiguous. The *intrayarn packing fraction* is the volume of cotton fibers that occupies a length of yarn, or:

$$\alpha_{intra} = \frac{V_f}{V_y} = \frac{m_f \rho_y}{m_y \rho_f} \tag{3.76}$$

where m refers to the mass of each volume component. Since the mass is the same for both the fibers and the yarn, it follows that:

$$\alpha_{intra} = \frac{\rho_y}{\rho_f} \tag{3.77}$$

Therefore knowing the fiber density, the intra-yarn packing fraction can be found. The density of cotton lies between 1.54 gcm^{-3} and 1.56 gcm^{-3}. The *interyarn packing fraction* is the ratio of fabric density to yarn density:

$$\alpha_{inter} = \frac{\rho_F}{\rho_y} \tag{3.78}$$

where ρ_F is the fabric bulk density, which is given as part of the filter data. For clarity, it is pointed out that the yarn density is also a bulk density: it is the density of the yarn as if it were a solid mono-filament, of volume corresponding to the yarn diameter d_y and mass corresponding to the mass of all the fibers in one yarn, m_f. The remaining parameter required is the filter thickness, which is usually provided for a given cotton fabric.

The interyarn pore size is determined from the warp and weft density, which are given as a number of threads per unit length. If the thread or yarn diameter is known, it is possible to ascertain the spacing between each yarn. The maximum pore diameter is taken from the minimum thread density, be it the warp or weft. The intra-yarn pore size is a more arbitrary figure, calculated by considering the intra-yarn packing fraction and fiber diameter. The contribution of fibers to the width of a yarn is divided by the fiber diameter to determine the number of fibers along a line cross-section of yarn. Assuming there is an equal quantity of interstices to fibers, the inter-fiber pore size is calculated by dividing the remaining width across the yarn by the number of fibers.

Transient Packing Fraction

In both cases the accumulation of particles within the filter medium causes a change in the internal structure that can affect both the pressure drop and the separation efficiency. In a simplification used for the present work, the transient packing fraction is simply the opposite of the transient porosity expressed by Equation 3.60:

$$\alpha(m_{pc}) = \alpha_{(0)} + \frac{\bar{\rho}_p m_{pc}}{Z_F A_F} \tag{3.79}$$

where $\alpha_{(0)}$ is the initial filter packing fraction, given by Equation 3.73. The mass of captured particles, m_{pc}, is given by Equation 3.59.

3.3.3 Separation Efficiency

The separation efficiency of fibrous filters is usually determined experimentally and quoted as part of the finished product. Efficiency is determined by tests with standard dusts, for example, a cotton filter may be quoted as having an efficiency of 99.3% for Arizona AC Coarse test dust. Particle capture by filter fibres is not easy to predict. Aside from the highly unorganised arrangement of fibres within the mat, the main difficulty arises from the variation of the different capture mechanisms with Stokes number. Such theories of fibre-particle interaction are outlined in depth in the books of Davies [67] and Brown [66]. The four main capture mechanisms are:

1. *Diffusion*, by which particles are intercepted by fibres as they wander in random Brownian motion, crossing fluid streamlines.

2. *Direct Interception*, by which particles follow fluid streamlines around a fibre, but are intercepted by virtue of their bulk.

3. *Inertial Impaction*, by which particles possessing too much inertia cannot negotiate the flow path around the fibre and leave the streamline to deposit on the fibre surface.

4. *Sieving*, by which a particle is arrested due to its diameter exceeding the diameter of the interfibre pores.

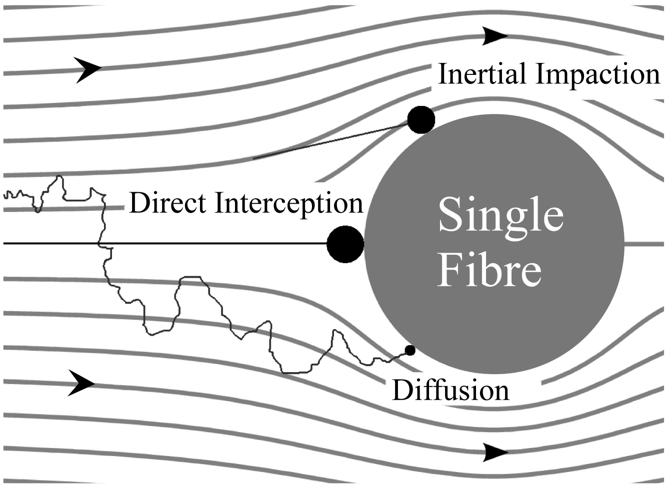

Figure 3.6: *The four single fibre capture mechanisms.*

These are depicted in Figure 3.6. Collectively these mechanisms yield a single fibre efficiency which can be combined with the depth and porosity of the whole filter to determine the overall separation efficiency. Other capture mechanisms may also be present, such as van der Waals' force (arising from a charge imbalance) or electrostatic attraction. The presence of each mechanism largely depends on the particle size, the particle incident velocity, the fluid viscosity, and the diameter and charge carrying capabilities of the fiber. Given that the material used for IBF filters is cotton, and that the smallest particle size of interest is one micron, the electrostatic and Van der Waals forces is discounted at this stage, leaving the four capture mechanisms described above for consideration in the present work.

Single Fiber Theory considers the capture efficiency of an individual fiber when all capture mechanisms are being utilised by it. If the fibers are randomly assorted, this theory can be used to calculate the overall capture efficiency of a fabric filter. A well known method given by Brown [66] assumes that the four capture mechanisms act independently, and thus have individual respective capture efficiencies. For example, a fraction $(1-\eta_1)$ of particulate would escape if the first mechanism acted alone. If this were then subject to a second process, a fraction $(1-\eta_1)(1-\eta_2)$ would escape. For a system of multiple capture mechanisms, the total single fibre efficiency is thus:

$$1-\eta_N = \prod_{j=1}^{N}(1-\eta_j) \tag{3.80}$$

where η is the capture efficiency. Hence for the four capture mechanisms considered above, the overall single fibre efficiency is:

$$\eta_E = 1-(1-\eta_d)(1-\eta_r)(1-\eta_i)(1-\eta_s) \tag{3.81}$$

where the subscripts E, d, r, i, and s refer to the total, diffusional, interception, inertial and sieving mechanisms respectively. The individual mechanisms' efficiencies are the subject of much theoretical debate, and invariably become derived through case-specific experiments. Furthermore, as previously alluded to, there is a heavy non-linear dependency on Stokes number and Reynolds number (given in Equation 3.39). The Stokes number is given as:

$$St = \frac{d_p^2 \rho_p U_p}{18 \mu_g d_f} \tag{3.82}$$

where U_p is the particle velocity. While the Stokes number is valid, the particle is assumed to be in suspension in the moving air and thus has the same velocity as the local gas. At low Stokes number, below 0.025, the particles motion is interfered with by bombardment of gas molecules, as in Brownian diffusion. As the diameter hence Stokes drag increases, the particle begins to follow fluid streamlines. If the particle passes close enough to touch the fibre it may be directly intercepted. Beyond a Stokes number of 0.2 the particle's inertia causes it to cross streamlines. It increasingly fails to negotiate the disturbance to flow caused by the presence of a fibre, and is captured. As particle Reynolds number increase further, the phenomenon of particle bounce may begin to occur, whereby the adhesive forces present at the particle-fibre interface are no longer strong enough and the particle evades capture. At this point along the Stokes number scale there is a temporary dip in collection efficiency. As the diameter increases further, however, there is a rapid rise in capture efficiency as the fibrous mat begins to act like a sieve. This journey through Stokes number is depicted in Figure 3.7. These numerous processes make the prediction of particle fate through a filter rather difficult.

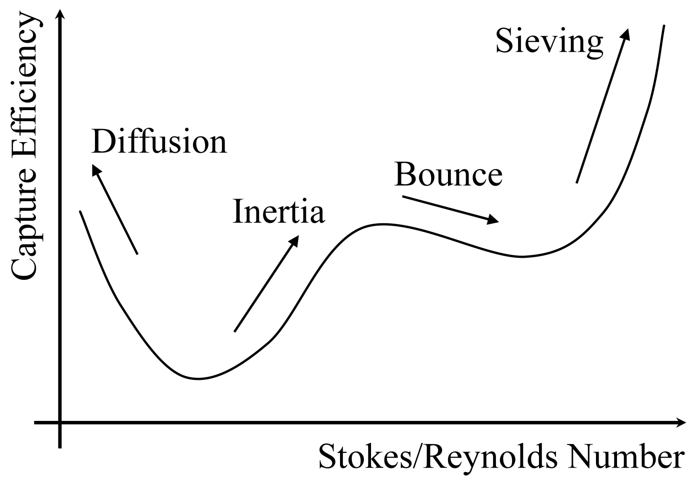

Figure 3.7: *The variation in dominance of the main capture mechanisms.*

Nevertheless, models do exist to allow an estimation of single fibre efficiency under given conditions. Dealing with each in turn, the diffusional efficiency is expressed by

Davies [67] as:

$$\eta_d = 1.5\mathrm{Pe}^{-2/3} \tag{3.83}$$

where Pe is the Peclet number, which is a measure of the particle diffusivity within the fluid. The direct interception efficiency acts over a small range of Stokes number, and is given by Davies as:

$$\eta_r = \frac{(1-\alpha)R_1^2}{H_{Ku}(1+R)^{\frac{2}{3(1-\alpha)}}} \tag{3.84}$$

where R is the particle to diameter ratio, expressed as:

$$R = \frac{d_p}{d_f} \tag{3.85}$$

and H_{ku} is the Kuwubara hydrodynamic factor which relates to the flowfield around the fibre. It is expressed as:

$$H_{ku} = -0.5\ln\alpha - 0.75 + \alpha - 0.25\alpha^2 \tag{3.86}$$

where α is the transient filter packing fraction, given by Equation 3.79. The direct interception mechanism can be augmented by a tacking agent on the fibres (such as oil in the case of IBF).

The inertial impaction efficiency is expressed in its most general form according to Brown [66] as:

$$\eta_i = \frac{St^2e^3}{St^3e^3 + 0.77\left(1 + \frac{K_3}{\mathrm{Re}^{1/2}} + \frac{K_4}{\mathrm{Re}}\right)St^2e^2 + 0.58} \tag{3.87}$$

where e is a function of the packing fraction, given by:

$$e = 1 + K_1\alpha + K_2\alpha^2 \tag{3.88}$$

In Equations 3.87 and 3.88, the parameters K_{1-4} are fitted to experimental data on the filter used. In the absence of this information, typical values can be taken from Brown for real and model filters whose packing fraction is of a similar order to that of the filters used for IBF applications.

The sieving efficiency is calculated by considering the arrangement of fibres in the filter medium as a set of parallel cylinders. If the mean distance between fibres, or pore size is smaller than the particle diameter, the particle is captured. Of course this is complicated by the range of particle shapes — a platelet shaped particle may be permitted in one orientation but not in another — but as has been discussed there are a number of ways to surmount this problem and find a mean reference diameter such as the Sauter (d_{32}) diameter given by Equation 3.19. Supposing the particle diameter d_p is one such diameter, the sieving efficiency is given by:

$$\eta_s = \frac{d_p + d_f}{s_f - d_f} \tag{3.89}$$

where s_f is the interfibre distance, given by Equation 3.74.

Combining the efficiencies of the four capture mechanisms by Equation 3.81 achieves the capture efficiency of a single fibre, but to find the efficiency of the whole filter a separate model is required. IBF use either a non-woven fibrous filter or a woven fabric filter. The overall efficiency of a homogeneous fibrous filter is derived from the layer efficiency, described by Brown [66]. The penetration of identical particles through a homogeneous filter that captures particles throughout its depth is related to the thickness. The number of particles captured by a layer of thickness δz will be proportional to the number incident, N, to the thickness δz and to a constant ξ describing the efficiency of the filter:

$$\delta N = -\xi N \delta z \tag{3.90}$$

In limiting conditions Equation 3.90 becomes a simple differential equation with the solution:

$$N(z) = N(0)\exp(-\xi z) \tag{3.91}$$

where ξ is the *layer efficiency* or filtration index, expressed in units of number removed per unit length, and 0 refers the initial condition. Manipulation of this equation gives the penetration P of a particle, defined as the proportion of particles of identical diameter remaining at a distance z from the layer face:

$$\ln(P) = \ln\frac{N(z)}{N(0)} = -\xi z \tag{3.92}$$

which means that the penetration of the aerosol through the filter, plotted on a logarithmic scale against depth on a linear scale gives a straight line, the gradient of which is directly proportional to the layer efficiency of the filter material. Using Equation 3.73, the filter depth can be expressed as:

$$Z_F = \frac{\pi d_f^2 L_f}{4\alpha A_F} \tag{3.93}$$

The relationship between layer efficiency and single fibre efficiency is derived by considering that if a fibre in a filter is orientated at right angles to the flow, the area that it presents to the flow is equal to the product of the length and the diameter of the fibre. A fiber that has an efficiency of unity removes from the air all of the particles that would lie within the volume swept out by its area and the velocity vector of the air, assumed to be flowing uniformly. The single fibre efficiency is defined as the quotient of the number of particles actually removed and the number removed by a 100% efficient fibre. Assuming that all fibres lie perpendicular to the to the airflow, the single fibre efficiency can be expressed as:

$$\eta_E = \frac{\xi Z_f}{L_f d_f / A_F} \tag{3.94}$$

Hence it is related to the layer efficiency by substituting Z_F from Equation 3.93:

$$\eta_E = \frac{\xi \pi d_f (1-\alpha)}{4\alpha} \tag{3.95}$$

The extra factor $(1-\alpha)$ is added by some authors (in the majority of the literature) to account for the fact that the fraction, α, of the filter volume occupied by the fibres is unavailable to the airflow, hence the mean velocity of the air within the filter is higher by a factor of $(1-\alpha)^{-1}$ than the velocity of the air approaching the filter. Comparing this form with the true fibre efficiency, which is determined by the capture mechanisms as in Equation 3.81, it can be seen that under certain conditions the single fibre efficiency may exceed unity. Rearranging Equation 3.95 for ξ and substituting into Equation 3.92, the penetration of a monodisperse particulate in a homogeneous fibrous filter is written:

$$P = \exp\left(-\frac{4\alpha Z_F \eta_E}{\pi(1-\alpha) d_f}\right) \tag{3.96}$$

Of course, the likelihood of each particle having identical dimensions is very low; in reality the distribution is polydisperse which means a different layer efficiency for each particle size. In a polydisperse distribution, a particle size band is represented by a characteristic diameter and constitutes a mass fraction of the total concentration (see Section 3.2). The mass fraction can be represented by a probability density function, and it was discussed above that the single fibre efficiency too is a function of particle diameter. Over the whole depth of the filter, the penetration ultimately expresses the proportion of particles that are not captured; its opposite is the proportion that are retained, hence it expresses the overall efficiency of the filter. Recalling the transiency of the packing fraction, the general relationship for the separation efficiency of a homogeneous fibrous filter expressed in terms of the key filter parameters, as a function of particle size and collected mass is:

$$E_{F,N}(x,m) = 1 - \int_{x_1}^{x_2} \mathrm{PDF}(x,\mu,\sigma) \exp\left(-\frac{4\alpha(m_{pc}) Z_F \eta_E(x)}{\pi(1-\alpha(m_{pc})) d_f}\right) \,\mathrm{d}x \tag{3.97}$$

where x refers to the particle diameter, m_{pc} refers to the total mass of particles collected within the filter, and $\mathrm{PDF}(x,\mu,\sigma)$ is the probability density function of the particle size distribution, as given in Equation 3.30. This can be used when the filtration medium employed in the IBF is a fibrous filter.

For woven fabric filters, the same formula can be used but the calculation of the single fibre efficiency is slightly different owing to the ordered arrangement of yarn-spun fibres that renders it inhomogeneous. An experiment by Bénesse *et al.* [81] however, revealed that the effects of non-homogeneity on filtration decrease with increasing layers of woven fabric filter, due to the inter-yarn pores becoming increasingly blocked by adjacent layers. Knowing that woven fabric filters for IBF contain 3 to 6 plies of cloth [40], it is reasonable to apply a modified single fiber theory to determine its overall efficiency. In a later study, Bénesse *et al.* [82] develop this approach. It is proposed that single fibre theory for homogeneous media can be extended to woven fabrics if the filter is defined as an assembly of two homogeneous porous structures: the *inter-yarn pore level* (between the yarns); and the *intra-yarn pore level* (within the yarns). This is due to the differing filtration behaviour of the two levels. The yarn is considered as a mono-filament fibre within a fibrous filter bed, whilst the individual fibers are considered constituents of a separate fibrous bed with the dimensions of the yarn. Parameters of these separate fibrous media such as filament diameter or filament density can be obtained from the cloth manufacturer or by direct measurement, and are defined in Section 3.3.2.

Considering first the intra-yarn level, the separation efficiency is given by Equation 3.97 with the filter depth exchanged for the yarn diameter and the packing fraction given by Equation 3.77:

$$\eta_{intra} = 1 - \exp\left(-\frac{4}{\pi}\frac{\alpha_{intra}}{(1-\alpha_{intra})}\frac{d_y \eta_f}{d_f}\right) \tag{3.98}$$

where η_f is the efficiency of a single fibre within the yarn. Next the yarn is considered as a single fibre in a fibrous bed with a depth equal to the total woven filter depth, and a packing fraction given by Equation 3.78. The single *yarn* capture efficiency is found with Equation 3.81, using the same capture mechanism formulae but for a different reference length:

$$\eta_{inter} = 1 - (1-\eta_{d,inter})(1-\eta_{r,inter})(1-\eta_{i,inter})(1-\eta_{s,inter}) \tag{3.99}$$

Now consider that the efficiency of the whole filter is dependent on the performance of the yarns and the fibres. The same principle for multiple capture mechanisms can be adopted to express the equivalent single fibre efficiency of a woven filter as a function of the individual capture efficiencies given by Equations 3.98 and 3.99:

$$\eta_W = 1 - (1-\eta_{inter})(1-\eta_{intra}) \tag{3.100}$$

Continuing with the analogy, the overall separation efficiency of a multi-layer woven fabric filter used in IBF applications, expressed in the form of Equation 3.97 is given by:

$$E_{F,W}(x,m) = 1 - \int_{x_1}^{x_2} \mathrm{PDF}(x,\mu,\sigma)\exp\left(-\frac{4\alpha(m_{pc})Z_F\eta_W(x)}{\pi(1-\alpha(m_{pc}))d_f}\right)\mathrm{d}x \tag{3.101}$$

The choice of Equation 3.101 or Equation 3.97 is dependent on the filter medium employed in a given IBF, and relies upon knowledge of the filter parameters such as fibre and yarn thicknesses, and packing fractions. A general expression for IBF separation efficiency is therefore:

$$E_{IBF} = \begin{cases} E_{F,W}(x,m) & \text{if a } \textbf{woven} \text{ filter is used} \\ E_{F,N}(x,m) & \text{if a } \textbf{non-woven} \text{ filter is used} \end{cases} \tag{3.102}$$

3.3.4 Summary

In the preceding sections, the theory concerning the two most important performance parameters of IBF was presented. Their importance will be recognised in the following chapters. Separation theory is taken mainly from the book on Air Filtration by Brown [66]. Four different mechanisms combine to yield an overall separation efficiency for the filter; the dominance of these mechanisms is a function of the Stokes number and later the Reynolds number and particle diameter. At a certain diameter the particle may bounce of the filter; this is difficult to predict and is neglected at the current level. A slightly modified version of the method presented by Brown is suggested by Bénesse *et al.* [81] to calculate the separation efficiency when the filter medium is a woven fabric filter; however there is no similar distinction in the calculation of pressure drop. The pressure drop equation is an adaptation of the well-known Darcy equation that includes an inertial term to account for the diversion from linear proportionality between flow rate and pressure drop found at Reynolds numbers greater than ten. A different equation taken from the work of Endo *et al.* [77] is used to predict the pressure drop across a filter cake.

The calculation of the separation efficiency and the pressure drop depends on the type of filter medium used (woven or non-woven), the properties of the filter, the properties of the accumulating dust, and the inflow conditions. If these values are known, it is possible to predict the performance of an IBF device. The lengthy derivation of the pressure drop equation implies that much emphasis is placed on knowledge of the environment of operation, much like when trying to predict the Brownout cloud generation, or damage to the engine. The sensitivity of the IBF performance to such factors will be investigated in the proceeding sections. The modelling is also made complicated by the presence of the pleats, which will also be investigated in the following chapters.

3.4 Vortex Tube Separators Theory

Vortex tubes theory has been derived in the literature (see Section 2.4) but nowadays much of the work on VTS design is performed using CFD. The exact flow physics within the vortex tube is not fully understood, but some authors have formulated theory to predict particle motion and resultant viscous pressure drop with some good agreement with experiment. Conclusions of note indicate that the performance of a vortex tube is sensitive to geometrical parameters such as helix pitch, turning length, and scavenge proportion. The following section provides mathematical derivations from classical mechanics and turbulent boundary layer theory to obtain expressions for the pressure drop and separation efficiency of a vortex tube. Such a mathematical model was derived by Ramachandran *et al.* [32] for an inline cyclone separator of a similar embodiment to the tubes used in VTS arrays.. The authors verified the model with experimental data and illustrated a good prediction, despite using simplifying assumptions. The validation was conducted with aerosol particles that migrated radially under centrifugal force, and adhered to the tube walls where they could be counted. This differs from the embodiment shown in Figure 2.11, in which particles are captured once they breach a radial position equal to the diameter of the inner tube (collector).

3.4.1 Pressure Drop

Assume the vortex tube resembles the embodiment shown in Figure 3.8, which is a simplified diagram of a typical vortex tube used in VTS devices. The axial velocity of the particles and the air is assumed to be equal on entering the tube. The mass of the particles entering is dependent on the mass concentration of the particulate, c_m, but is considered to be sufficiently small to allow the axial velocity of the air-particle mix u_t, to be calculated by applying conservation of mass for the gas alone [42]:

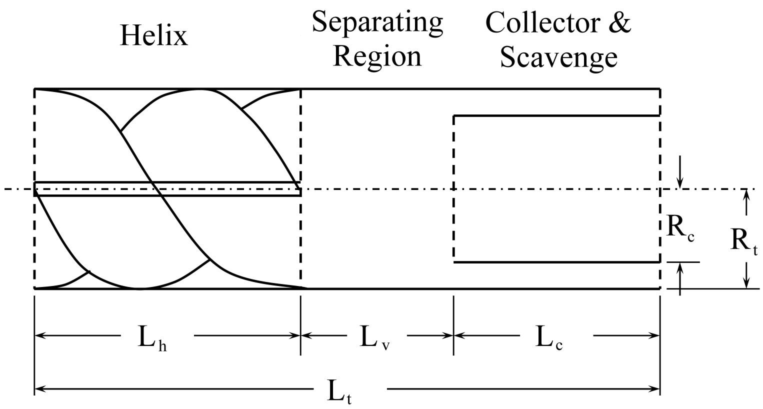

Figure 3.8: *Diagrammatic representation of a single vortex tube separator, illustrating key geometrical parameters.*

$$u_t = \frac{\dot{m}_t(1 + c_m)}{\rho_g A_t - \rho_g A_p + \rho_p A_p} \simeq \frac{\dot{m}_t}{\rho_g A_t} \tag{3.103}$$

where $\dot{m}_t$ is the tube mass flow, A_t is the tube area and A_p is the total projected area of all the particles. The particles enter the tube and are thrown to the periphery by a 4-bladed (cross-shaped profile) helical vane, which has a pitch H_t defined as the axial distance travelled by the gas in one revolution of the helix. The tangential velocity of the gas at a distance r from the axis of the cylinder is:

$$u_\theta = 2\pi r \frac{u_t}{H_t} \tag{3.104}$$

It is assumed that the gas has no radial component of velocity, that the axial component of velocity is invariant along the tube, and that the tangential component varies with radial position. The net velocity of the gas is the vector sum of these two components:

$$u_{VTS} = \sqrt{u_t^2 + u_\theta^2} = u_t \sqrt{1 + \frac{2\pi r}{H_t}^2} \tag{3.105}$$

The value of u_{VTS} varies from a minimum at $r = 0$ to a maximum at $r = R_t$, the tube radius. The average velocity u_{avg} through the helical section of the tube can be calculated as an area-weighted average of u_{VTS}, which simplifies to:

$$u_{avg} = u_t \frac{4\pi}{3R_t^2 H_t^2} \left[\left(\frac{H_t^2}{4\pi^2} + R_t^2 \right)^{3/2} - \left(\frac{H_t}{4\pi^2} \right)^{3/2} \right] \tag{3.106}$$

The pressure drop through the tube is the sum of the loss due to friction and the dynamic pressure required to fluidise the tangential velocity component in the helix. Inertial losses are expected, but neglected in this low order analysis due to a lack of information about the blade shape. The loss due to friction is calculated for each section of the separator: the helix (h), the separating region (v) (between the helix and the collector), the collector (co), and the scavenge conduit (s) (the annulus between the collector and tube walls). See Figure 3.8. The loss is calculated from the Darcy-Weisbach relationship for flow through a cylinder:

$$\Delta P = \rho_g \frac{f L U^2}{2 D_H} \tag{3.107}$$

where f is the friction factor, L is the section length, U is the average gas velocity through the section, and D_H is the section hydraulic diameter. The friction factor [83] is given by:

$$\frac{1}{f} = -1.8 \log \left(\frac{6.9}{\mathrm{Re}_g} \right) \tag{3.108}$$

where Re_g is the Reynolds number of the cylinder flow, given as:

$$\mathrm{Re}_g = \frac{\rho_g U D_H}{\mu_g} \tag{3.109}$$

The hydraulic diameter for each section of the tube is different. For the helix it is calculated from:

$$D_{H,h} = \frac{4\pi R_t}{(2\pi + 2N_h)} \tag{3.110}$$

where N_h is the number of helical vanes. For the separating region and collector it is equivalent to their respective diameters ($D_{H,v} = 2R_t$ and $D_{H,co} = 2R_{co}$); and for the scavenge conduit it is given by:

$$D_{H,s} = D_{H,t} - D_{H,co} \tag{3.111}$$

The pressure drop due to the required dynamic pressure through the helix is given by:

$$\Delta q_h = \rho_g \frac{u_{avg}^2 - u_t^2}{2} \tag{3.112}$$

If the vortex tube is facing forwards and the rotorcraft is moving forwards at a speed faster than the tube axial velocity, there is an additional term to include to account for ram pressure recovery, given by:

$$\Delta P_{ram} = \begin{cases} \frac{1}{2}\rho_g \left(U_\infty - U_a\right)^2 & \text{if } U_\infty > u_t \\ 0 & \text{if } U_\infty \leq U_a \end{cases} \tag{3.113}$$

In the interests of VTS performance prediction, the total tube pressure drop can be segregated into two parts: the core pressure drop of the air flow continuing to the engine, and the scavenge pressure drop of the proportion of flow to be ejected with the separated particles. It assumed that the pressure distribution at the collector face is uniform, hence the pressure loss at the entry to both the collector and the scavenge is a summation of the helix pressure loss and the separating region pressure loss; the remaining pressure loss for the collector and scavenge are calculated from Equation 3.107 using the respective hydraulic diameters. The pressure drop of the tube core is thus:

$$\Delta P_{core} = \Delta P_h + \Delta q_h + \Delta P_v + \Delta P_{co} - \Delta P_{ram} \tag{3.114}$$

while the pressure drop of the scavenged proportion of the flow is:

$$\Delta P_{scav} = \Delta P_h + \Delta q_h + \Delta P_v + \Delta P_s - \Delta P_{ram} \tag{3.115}$$

For brevity, the portions of the tubes represented by Equations 3.114 and 3.115 are shown in Figure 3.9.

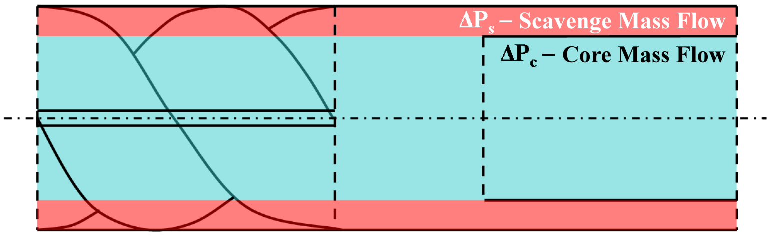

Figure 3.9: *Breakdown of the tube mass flow into the two key areas, core and scavenge, required for VTS pressure drop prediction.*

3.4.2 Separation Efficiency

Entering the helix, a particle will experience three forces: a centrifugal force F_{cn} caused by its helicoidal motion; a buoyancy force F_{bu} caused by the displacement of gas; and an aerodynamic force F_{ae}, which is equal to the Stokes resistance. For a spherical particle of radial position r, they are given by the following:

$$F_{cn} = \frac{1}{6}\pi\rho_p d_p^3 \frac{u_\theta^2}{r} \tag{3.116}$$

$$F_{bu} = -\frac{1}{6}\pi\rho_g d_p^3 \frac{u_\theta^2}{r} \tag{3.117}$$

$$F_{ae} = -3\pi d_p \mu_g u_r \tag{3.118}$$

Assuming the process has reached steady state, the balance of forces is:

$$F_{cn} + F_{bu} + F_{ae} = 0 \tag{3.119}$$

which can be solved for the particle's radial velocity:

$$v_{pr} = \frac{(\rho_p - \rho_g)}{18\mu_g} d_p^2 \frac{v_{p\theta}^2}{r} \tag{3.120}$$

It is assumed that the particle tangential velocity is equal to the gas tangential velocity, hence $v_{p\theta} = u_\theta$. Substituting Equation 3.104 in Equation 3.120 at a radial distance corresponding to the collector distance gives:

$$v_{pr,r=R_{co}} = \frac{(\rho_p - \rho_g)}{18\mu_g} d_p^2 \frac{u_t^2 R_{co}}{H_t^2} \tag{3.121}$$

The collector radius is related to the scavenge proportion S by simple geometry, if it is assumed that the axial velocity at the collector entry is equal to that at the scavenge entry:

$$R_{co}^2 = (1 - S)R_t^2 \tag{3.122}$$

A simplification here is that the density of the fluid before and after the collector, and within the scavenge is equal to the gas density. In practice, the scavenge will have a large proportion of particles and therefore a larger density than the clean, core flow. It is assumed that at the design stage this is not considered. Consider the cylinder depicted in Figure 3.8. A mass balance on an infinitesimal slice of length dL of the collector gives:

$$Q_g c_v = Q_g(c_v - dc_v) - v_{p,r=R_{co}}(2\pi R_{co})c_v dL \tag{3.123}$$

where c_v is the dust volume concentration (expressed as mass per unit volume; see Equation 3.2) entering the slice, $(c_v - dc_v)$ is the concentration of particles leaving the slice, and $v_{p,R_{co}} c_v dL$ is the rate of particle removal into the scavenge conduit. Substituting Equation 3.121 into Equation 3.123, rearranging, and integrating over the length of the separating region L_v yields:

$$\frac{c_{v,L=L_h+L_v}}{c_{v,L=L_h}} = \exp\left(-Q_g \frac{8\pi}{18\mu_g} d_p^2 \frac{L_v}{R_{co}^2 H_t^2}\right) \tag{3.124}$$

Since the term on the left hand side represents the concentration of particles remaining at the collector entrance, the separation or *grade* efficiency can be expressed by:

$$\eta_{grade} = 1 - \exp\left(-Q_g \frac{8\pi}{18\mu_g} d_p^2 \frac{L_v}{R_{co}^2 H_t^2}\right) \tag{3.125}$$

The above equation, adapted for the present work from Ramachandran *et al.* [32], assumes plug flow of gas through the tube, uniform concentration and complete lateral mixing due to turbulence in each transverse cross-section. It also neglects the situation of particles bouncing off the helical vane or becoming re-entrained in the core flow after deflection from the tube walls, an event that is likely and may hinder or aid separation. These are reasonable assumptions as a first-order approximation. The cut diameter, d_{50}, is a length commonly used in the design of cyclone separators. For a particular tube and design mass flow, it corresponds to the diameter of particles collected with 50% efficiency. Based on Equation 3.125, the cut diameter is:

$$d_{50} = \sqrt{\frac{18\mu_g(\ln 2)R_{co}^2 H_t^2}{8\pi\rho_p Q_g L_v}} \tag{3.126}$$

If the anticipated range of particle sizes is expressed by a probability density function as described in Section 3.2.4, the general relationship for separation efficiency can be expressed in terms of the cut diameter and particle diameter by substituting Equation 3.126 into Equation 3.125:

$$\eta_{VTS}(x) = 1 - \exp\left[-\ln 2\left(\frac{\mathrm{PDF}(x,\mu,\sigma)}{d_{50}}\right)^2\right] \tag{3.127}$$

where x refers to the particle diameter, and $\mathrm{PDF}(x,\mu,\sigma)$ is the probability density function of the particle size distribution, as given in Equation 3.30. Hence for a given vortex tube, the separation efficiency can be found for a range of particle sizes.

3.5 EAPS Comparison Theory

The emergence of the three different particle separating systems over the last thirty years or so raises the question of which device is the most efficacious in enhancing engine performance. System efficacy can be measured by a number of criteria; two have been visited in the preceding chapters, namely pressure drop and efficiency. The best EAPS system will remove 100% of the particles from the dusty air passing through it for no loss of pressure. It will not require any additional power from the engine in order to operate, and will not contribute to airframe drag. The ideal EAPS system would also be lightweight, low-cost and low maintenance. Clearly a device that matches these criteria does not exist, but in the comparison of particle separators these drivers act as barometers to assessing EAPS efficacy. The following section outlines low-order theoretical models used later in the present work to compare the EAPS devices.

3.5.1 Overall Separation Efficiency

The IBF and VTS separation efficiencies given by Equations 3.102 and 3.127 are expressed as a function of particle size. For a simpler comparison, it would be useful to express the efficiency as a single figure, as is favoured by EAPS manufacturers. To achieve this, a mean separation efficiency can be calculated for the whole distribution, for a given device. Suppose the size mass fraction of a dust is represented by a function $f(x)$. The mean efficiency can be expressed algebraically as:

$$\overline{E}_{EAPS} = \int_{x_{min}}^{x_{max}} E_{EAPS}(x) f(x)\,\mathrm{d}x \tag{3.128}$$

or in terms of fractional size groups as:

$$\overline{E}_{EAPS} = \sum_{i=1}^{N_p} m_i(1 - E_{EAPS}(d_i)) \tag{3.129}$$

where N_p is the number of size bands, d_i is the diameter of the size band, and m_i is the mass expressed as a fraction of the total distribution mass. The mass distribution can also be expressed by a single figure, or mass mean diameter or effective diameter, as given by Equation 3.15.

For devices that scavenge, rather than collect particles, a correction must be applied to determine the true separation efficiency, since a portion of the air is removed from the influent mass flow. The overall efficiency given by the equations above calculates the mass of particles removed from the total mass fed, which is greater than what would have ordinarily been sucked into the engine. The correction is quite straightforward: the particle mass flow in the scavenge line post separation is a summation of the mass of particles originally within the scavenge proportion, and the mass of particles extracted from the core mass flow proportion by way of the *corrected* separation efficiency, E':

$$\dot{m}_{p,scav} = S\dot{m}_{p,fed} + E'_{EAPS}(1 - S)\dot{m}_{p,fed} \tag{3.130}$$

where $\dot{m}_{p,fed}$ is the particle mass flow rate fed into the vortex tube and $\dot{m}_{p,scav}$ is the mass of particles scavenged. The equations used to derived the efficiencies stated above involved the whole system architecture, and therefore refer to the fraction of mass extracted from the total mass fed, or:

$$\overline{E}_{EAPS} = \frac{\dot{m}_{p,scav}}{\dot{m}_{p,fed}} \tag{3.131}$$

Dividing Equation 3.130 through by $\dot{m}_{p,fed}$, substituting in Equation 3.131, and rearranging thus gives an expression for the corrected separation efficiency as a function of the overall efficiency and the scavenge proportion:

$$E'_{EAPS} = \frac{1}{1 - S}(\overline{E}_{EAPS} - S) \tag{3.132}$$

This means that the corrected separation efficiency is lower than the overall efficiency calculated in Equations 3.128 and 3.129. For example an EAPS device that scavenges 10% of the flow, and achieves an overall separation efficiency of 90% will achieve a corrected efficiency of 88.8%. Note, however, that the "unfiltered" 11.2% will be split between the scavenge line and the core mass flow; the corrected efficiency should only be used to compare devices, as it does not calculate how much dust will be ingested by the engine. For this, the prior equations relating to grade efficiency must be used.

3.5.2 Power Required

Another basis for comparison is the total additional power required by the engine to cater for all requirements of the EAPS system. There are three sources of power loss, not all of which are present for every EAPS device:

1. *EAPS Scavenge Pumps* which require power to suck particles away from the core air flow as part of the separation mechanism.
2. *Device Pressure Loss* which is a form of drag arising from the air passing through the EAPS system and being resisted by friction from integral parts of the device.
3. *Drag* which arises from an enlargement of the airframe to accommodate and support the EAPS system.

VTS Power Required

The vortex tube arrays carry the biggest potential for power consumption, as all three sources are present. Drag arises from the box-like structure that is required to support the tubes (see Figure 2.10); a scavenge pump is required to energise the separated particulate stream; and pressure loss arises from friction with the walls of the multiple tubes that comprise the array. The work done per unit time can be expressed in a number of ways. Firstly, the scavenge power required is given as:

$$W_{scav,VTS} = \dot{m}_s \Delta P_{scav} \tag{3.133}$$

where ΔP_{scav} is given by Equation 3.115, and $\dot{m}_s$ is the scavenge mass flow rate, of which the scavenged particles make up a large proportion and contribute to the density of the fluid in that region. It is given as:

$$\dot{m}_s = \dot{m}_{g,s} + \dot{m}_{p,s} = \dot{m}_g (S + \eta_{VTS} c_m) \tag{3.134}$$

where S is the scavenge proportion, related to the VTS geometry by Equation 3.122. It is likely that Equation 3.133 does not account for all the power required. In the arrangement shown in Figure 2.10 and in other such embodiments there is a “scavenge chamber” into which the scavenge conduits exhaust the particles. It is in essence a tube bundle in cross flow, as the scavenge pump draws air from the chamber tangentially across all the tubes that carry the clean air to the engine. The additional drag and pressure loss through detached flow is assumed to be non-negligible, but cannot be reasonable theorised without prior knowledge of the chamber’s geometry. In this low-order analysis it is catered for by simply doubling the power required expressed by Equation 3.133.

The power required to maintain core mass flow when overcoming the pressure loss through the VTS adopts a similar method:

$$W_{core,VTS} = \dot{m}_g (1 - S) \Delta P_{core} \tag{3.135}$$

where ΔP_{core} is given by Equation 3.114.

The device drag is calculated by considering the total surface area occupied by the tubes and the supporting planform area. Assuming that all vortex tubes collectively are designed to supply a design point mass flow $\dot{m}_E$ of air to the engine via each one of their collectors, the number of tubes required is:

$$N_t = \frac{\dot{m}_E}{\dot{m}_c} = \frac{\dot{m}_E}{\rho_g u_g \pi R_c^2} \tag{3.136}$$

It can be inferred visually from Figure 2.10a that a panel of vortex tubes has a larger area than the total tube area, due to the requirements for support. If the total frontal area is A_P, the total drag acting on the panel is:

$$D_{VTS} = \begin{cases} \frac{1}{2}\rho_g (A_P - N_t A_t) U_\infty^2 + (N_t A_t)(U_\infty - u_g)^2 & \text{if } U_\infty > u_g \\ \\ \frac{1}{2}\rho_g (A_P - N_t A_t) U_\infty^2 & \text{if } U_\infty \leq u_g \end{cases} \tag{3.137}$$

where A_P is the VTS panel projected area. The power required to overcome drag is:

$$W_{D,VTS} = D_{VTS} U_\infty \tag{3.138}$$

Summing Equations 3.133, 3.135, and 3.138 yields the total power required for the VTS system:

$$W_{VTS} = 2W_{scav,VTS} + W_{core,VTS} + W_{D,VTS} \tag{3.139}$$

IBF Power Required

The power requirements of the IBF differ to the VTS by the lack of a scavenge pump. There is a considerable and transient pressure loss across the filter that must be opposed by the engine:

$$W_{F,IBF}(m_{pc}) = \dot{m}_g (\Delta P_{IBF}(m_{pc}) + \Delta P_{re}) \tag{3.140}$$

where ΔP_{IBF} is the total loss across the IBF filter, as given by Equation 3.72, and ΔP_{IBF} is any pressure recovered due to the forward motion of the aircraft. It is assumed that unlike the VTS, the supporting structure for the IBF does not contribute a significant amount to the device drag. The pressure recovery exists at forward speeds greater than the engine face velocity, or:

$$\Delta P_{re} = \begin{cases} \frac{1}{2}\rho_g \left(U_\infty - U_a\right)^2 & \text{if } U_\infty > U_a \\ 0 & \text{if } U_\infty \leq U_a \end{cases} \tag{3.141}$$

The IBF drag is assumed to be a form drag created by the deceleration of air into the intake, hence can be calculated similarly:

$$D_{IBF} = \begin{cases} \frac{1}{2}\rho_g A_F \left(U_\infty - U_a\right)^2 & \text{if } U_\infty > U_a \\ 0 & \text{if } U_\infty \leq U_a \end{cases} \tag{3.142}$$

The power required to overcome this drag is:

$$W_{D,IBF} = D_{IBF} U_\infty \tag{3.143}$$

Summing Equations 3.140 and 3.143 gives an expression for the total power required to service the IBF:

$$W_{IBF}(m_{pc}) = W_{F,IBF}(m_{pc}) + W_{D,IBF} \tag{3.144}$$

It should be remembered that owing to the build up of particles on the filter's surface, the power required to overcome the pressure drop given by Equation 3.140 is a function of the total mass collected, given by Equation 3.59. Importantly, this means Equation 3.144 is transient: the power required to employ an IBF device increases over time.

IPS Power Required

The IPS is mounted to the front of the engine and is therefore assumed to pose no additional drag to the airframe; there are no significant adjustments to the intake to accommodate the IPS that would increase the drag. Therefore the power requirement to counter drag is neglected here. However, like the VTS, a scavenge pump is required to extract the separated particles from the core air flow which requires power. The pressure loss across an IPS is mainly attributable to skin friction at the walls of the separator, but as the flow turn angle increases, the contribution to pressure drop of form drag increases [61]. The total pressure loss can be segregated into core and scavenge flows and combined with respective mass flow rates to calculate the total power required:

$$W_{IPS} = W_{core,IPS} + W_{scav,IPS} = \dot{m}_g(1 - S)\Delta P_{core} + \dot{m}_g S \Delta P_{scav} \tag{3.145}$$

EAPS Power Required

From the above it is clear that the power required to employ a particle separating device depends on the system chosen. At least one technology requires an increasing dedication of engine power, while two others draw power for scavenge pumps. In summary, the power lost to the EAPS system is given by:

$$W_{EAPS}(m_{pc}) = \begin{cases} W_{VTS} & \text{if } \textbf{Vortex Tube Separator} \text{ used} \\ W_{IBF}(m_{pc}) & \text{if } \textbf{Inlet Barrier Filter} \text{ used} \\ W_{IPS} & \text{if } \textbf{Inlet Particle Separator} \text{ used} \end{cases} \tag{3.146}$$

where W_{VTS}, $W_{IBF}(m_{pc})$ and W_{IPS} are given by Equations 3.139, 3.144 and 3.145 respectively. This permits an assessment of the devices based on their power demand from the engine.

3.5.3 Engine Erosion

The ultimate goal of an EAPS device is to increase the lifetime of a helicopter engine. Each EAPS system is different; some have lower separation efficiencies, while others exert an increasing load on the engine. If the EAPS system employed does not achieve 100% efficiency, particles that evade separation will cause damage to the engine. The engine performance will continue to deteriorate, albeit more slowly. The performance cost of employing an EAPS system has been visited already in the theory; a complete assessment tool would consider both the power lost to servicing the EAPS and any erosion due to unavoidable particulate ingestion.

To facilitate such a tool, a model is needed that predicts engine erosion. Fortunately there are some in the literature, as described in Section 2.2.5. The work of van der Walt & Nurick [22] provides a theory for predicting the power deterioration rate as a function of particle impact velocity and diameter. The power deterioration rate for a filtered helicopter engine is given as:

$$W_r = k_r \phi U^{\beta} \tag{3.147}$$

where U is the impact velocity, and β is a correlation exponent. The constant k_r is dependent on the engine and erodent properties that are all assumed to be constant for a specific engine and dust type, hence Equation 3.147 describes a linear relationship between the mass ingested and the power lost to erosional effects. This linear relationship is proven in van der Walt & Nurick's study for up to 10% power deterioration after an initial unsteady stage in which power is actually observed to increase. (This is due to dust polishing of the blade surface at the very beginning of erosion). For the case of a sparse dust distribution in which particle-on-particle interactions are negligible, the engine power loss is given by:

$$\Delta W = k_r m_{pe} U^{\beta} \phi \tag{3.148}$$

where m_{pe} is the mass of ingested particles. If the mass distribution can be expressed by fraction and analytically as a function of the particle diameter, Equation 3.148 can be written more generally as:

$$\Delta W = k_r U^\beta m_{pe} \int_{\phi_{min}}^{\phi_{max}} f(\phi)\phi \, \mathrm{d}\phi \tag{3.149}$$

where $f(\phi)$ is a function describing the fractional particle size distribution of the ingested particulate. Introducing the mean separation efficiency for the dust PSD from Equation 3.128 allows the ingested particulate to be written in terms of the total mass of particles reaching the intake:

$$\Delta W = k_r U^\beta (1 - \overline{E}_{EAPS}) m_p \int_{\phi_{min}}^{\phi_{max}} f(\phi)\phi \, \mathrm{d}\phi \tag{3.150}$$

This can now be divided through by m_p to express the erosion rate, or the power loss per unit mass of particles ingested by the EAPS device.

$$W_r(m_p) = k_r U^\beta (1 - \overline{E}_{EAPS}) \int_{\phi_{min}}^{\phi_{max}} f(\phi)\phi \, \mathrm{d}\phi \tag{3.151}$$

If the factor $k_r U^\beta$ is known for a particular engine and dust, the only remaining unknown is the function that describes the size distribution of the ingested particulate, $f(\phi)$. The PSD of the ingested particulate is related to the grade efficiency of the EAPS device, $E_{EAPS}(x)$, which calculates the separation ability of the device for a given particle size x. In algebraic form, it relates the ingested PSD to the brownout PSD:

$$f(\phi) = (1 - E_{EAPS}(x)) PDF(x, \mu, \sigma) \tag{3.152}$$

Hence if the dust cloud size distribution is expressed by a function, such as a log-normal distribution, the ingested PSD can be found. Alternatively, if the dust cloud distribution is expressed by size bands and mass proportions, the integral over $f(\phi)$ can be expressed as a sum of the filtered size mass fractions:

$$\int_{\phi_{min}}^{\phi_{max}} f(\phi)\phi \, \mathrm{d}\phi \equiv \sum_{i=\phi_{min}}^{\phi_{max}} (1 - E_{EAPS}(d_i)) m_i^+ d_i \tag{3.153}$$

where d_i is the representative diameter of the ith size group in the dust cloud PSD and $E_{EAPS}(d_i)$ is the corresponding separation efficiency. Incidentally, the sum on the right hand side is effectively the mean particle diameter by mass as given by Equation 3.15, which simplifies the expression further. Substitution of whichever of these is most appropriate into Equation 3.151 yields enough information to predict the erosion rate of a given engine in a given dust cloud.

3.5.4 Engine Longevity

There are now two identified sources of engine power loss for a helicopter operating in dusty environment with particle separating technology:

1. Power required to overcome EAPS.
2. Power lost due to erosion by ingested particulate.

Since each EAPS system will carry different power penalties but will achieve varying levels of separation efficiency, the power loss provides a useful metric in comparing the key technologies. Summing the sources of loss, the rate of reduction in available engine power for an EAPS-fitted rotorcraft, as a function of dust mass fed is:

$$W_E(m_p) = W_r(m_{pe}) + W_{EAPS}(m_{pc}) \tag{3.154}$$

where m_p is the mass of particles entering the intake as given by Equation 3.1, m_{pc} is the mass collected by an EAPS device (only applicable to IBF) as given by Equation 3.59, and m_{pe} is the mass of particle that evade capture and is ingested by the engine. The latter quantity is related to m_p by the efficiency of the EAPS system in a similar way to the mass captured by an IBF:

$$m_{pe} = (1 - E_{EAPS})m_p \tag{3.155}$$

When the system features dual flow paths, it must be remembered that m_p refers to the mass of particles entering the device. Since a portion of the mass flow is scavenged, this is greater than the mass that would enter an unprotected engine of the same mass flow. However, Equation 3.127 accounts for this by including the scavenge flow portion S in the efficiency expression given for VTS and IPS devices. For completeness, the three EAPS devices' efficiencies are summarily given as:

$$E_{EAPS} = \begin{cases} E_{VTS} & \text{if } \textbf{Vortex Tube Separator} \text{ used} \\ E_{IBF} & \text{if } \textbf{Inlet Barrier Filter} \text{ used} \\ E_{IPS} & \text{if } \textbf{Inlet Particle Separator} \text{ used} \end{cases} \tag{3.156}$$

where E_{VTS} and E_{IBF} are given by Equations 3.127 and 3.102 respectively. The IPS efficiency E_{IPS} is not given analytically in the present work, but takes the same form as Equation 3.127 and its value can be taken from test cases in the literature. All are functions of the particle size. The IBF separation efficiency here is a function of mass collected; in Section 3.3 it was explained that the filter packing fraction, which affects both the pressure drop and the separation efficiency, increases with collected mass, hence is also a function of time.

3.5.5 Engine Improvement Index

A perhaps simpler method for comparing EAPS devices is to calculate the resulting extension to engine life over unprotected engines. Scimone & Frey [41] discuss a study by Textron Lycoming which investigated the potential gains offered by EAPS employment. It used a Life Cycle Cost Model to predict the increased Mean Time Between Removal (MTBR) offered by installing a particle separator. It found a hundredfold increase in MTBR can be achieved when using an IBF. In a similar study, mentioned in the contribution by van der Walt & Nurick [24], the VTS is quoted as been able to achieve an MTBR of between 10 and 25 times the unprotected engine. An important point is made: that such predicted values are sensitive to local conditions, dust type, and dust concentration, so such figures need to be treated as benchmark figures.

From an analytical standpoint, however, verified models can be useful to cross-compare EAPS devices. A simple method is to express life extension as the ratio of the erosion rate of an unprotected engine to the erosion rate of a protected engine. If the integral for the ingested particulate in Equation 3.151 is represented by a effective mean diameter by mass proportion, ϕ_{eff}, the erosion rate for a protected engine simplifies to:

$$W_r(m_p) = (1 - \overline{E}_{EAPS})\phi_{eff} \tag{3.157}$$

The erosion rate of an unprotected engine takes the same form as this, but omits the separation efficiency term (or simply $\overline{E}_{EAPS} = 0$) and uses the effective (arithmetic) mean diameter by mass of the dust cloud, d_{eff}. Hence the lifetime improvement factor, LIF, is given by:

$$LIF = \frac{d_{eff}}{(1 - \overline{E}_{EAPS})\phi_{eff}} \tag{3.158}$$

This can be used as a quick and effective tool to compare EAPS devices in many environments, provided the analytical expressions for separation efficiency and PSD data are known.

3.6 Summary

This chapter provides all the equations necessary to facilitate the ultimate aim of quantifying EAPS performance. The important equations correspond to the properties of the sand reaching the engine, and the physics of particle separation. The theory of pressure loss as a result of drag by the device walls or fibres is also presented, to afford calculation of the performance penalty of employing EAPS technology. Of the three technologies, only the VTS and IBF are elaborated on, the latter in the most detail due to its underrepresentation in the literature. Finally the chapter is concluded with equations to assess the improvement to engine life that can be achieved when engine protection is fitted.

The equations of particle classification borrow from classical theory and statistical analysis. A probability density function can be used to express the size distribution of a dust algebraically. Alternatively, if the dust has been obtained from the field, it can be analysed and discretised into size bands with corresponding mass proportions. Knowledge of the particle size distribution is important for the calculation of separation efficiency. The ability of an IBF or VTS to remove a particle depends on the particle's diameter. Therefore separation efficiency is more accurately expressed as a grade efficiency, i.e. an efficiency as a function of particle size. Combining the grade efficiency with the particulate size distribution by mass allows the overall efficiency to be determined for a given sand. Without a specific sand in question, expressing the overall efficiency of an EAPS device is meaningless. Similarly, the efficiency is closely linked to the velocity of the particle; if the device is operating off-design, it may not achieve the desired separation efficiency.

The theory of pressure loss borrows from modified versions of Darcy's Law and turbulent boundary layer theory. It allows the power required to service an EAPS system to be predicted. Combining the power required to cater for pressure loss with power to cater for drag and scavenge pumps allows the overall demand on the engine to be quantified. An additional model is also provided to calculate the loss in engine power due to erosion by ingested particulate, which will occur since no system can remove 100% of the particles. This model also allows the effect of EAPS to be compared to the huge curtailment of engine life when no protection is provided.

Chapter 4

Methodology

This chapter outlines the procedure adopted in using computational fluid dynamics to perform a parametric study of inlet barrier filter design. To facilitate the study, the problem is broken into two lengthscales. An overview of the computational methods and practices employed is also given.

4.1 Introduction

In the introduction to the theory section, it was intimated that there would be a deeper investigation into the performance of the IBF. This is due to there being a substantial lack of research in this area in the literature. Vortex tubes are well covered by analytical theory, while inlet particle separators have been investigated by CFD studies in the literature. The present work aims to bring the understanding of inlet barrier filters to the same level, in order to more rigorously investigate the effects of EAPS systems on engine performance. To undertake this, a method is proposed that initially breaks the problem down into more manageable parts. Following this a procedure is laid out for a series of computational simulations that aim to investigate the effects of IBF design features on pressure loss, separation efficiency and holding capacity (see Section 3.3) through parametric study.

Modelling of IBF is made complicated by the wide bandwidth of lengthscales involved. The performance can be affected as much by micrometre-sized changes in particle size just as by centimetre-sized changes to the intake geometry. To ease modelling, the problem is broken down into three scales:

1. Intake Scale
2. Pleat Scale
3. Fibre Scale

These are depicted in Figure 4.1. Of the three scales, two are taken forward for computational fluid dynamics modelling: the Intake Scale and the Pleat Scale; the Fibre Scale is covered by the theory detailed in Section 3.3. Since the separation efficiency is mainly an internal process of the filter medium, it acts at the fibre scale and therefore is not directly modelled by CFD in the present work. However, the theoretical prediction can be enhanced by knowledge of the local flow conditions, which can be inherited from numerical simulation of the fluid passing through a filter pleat.

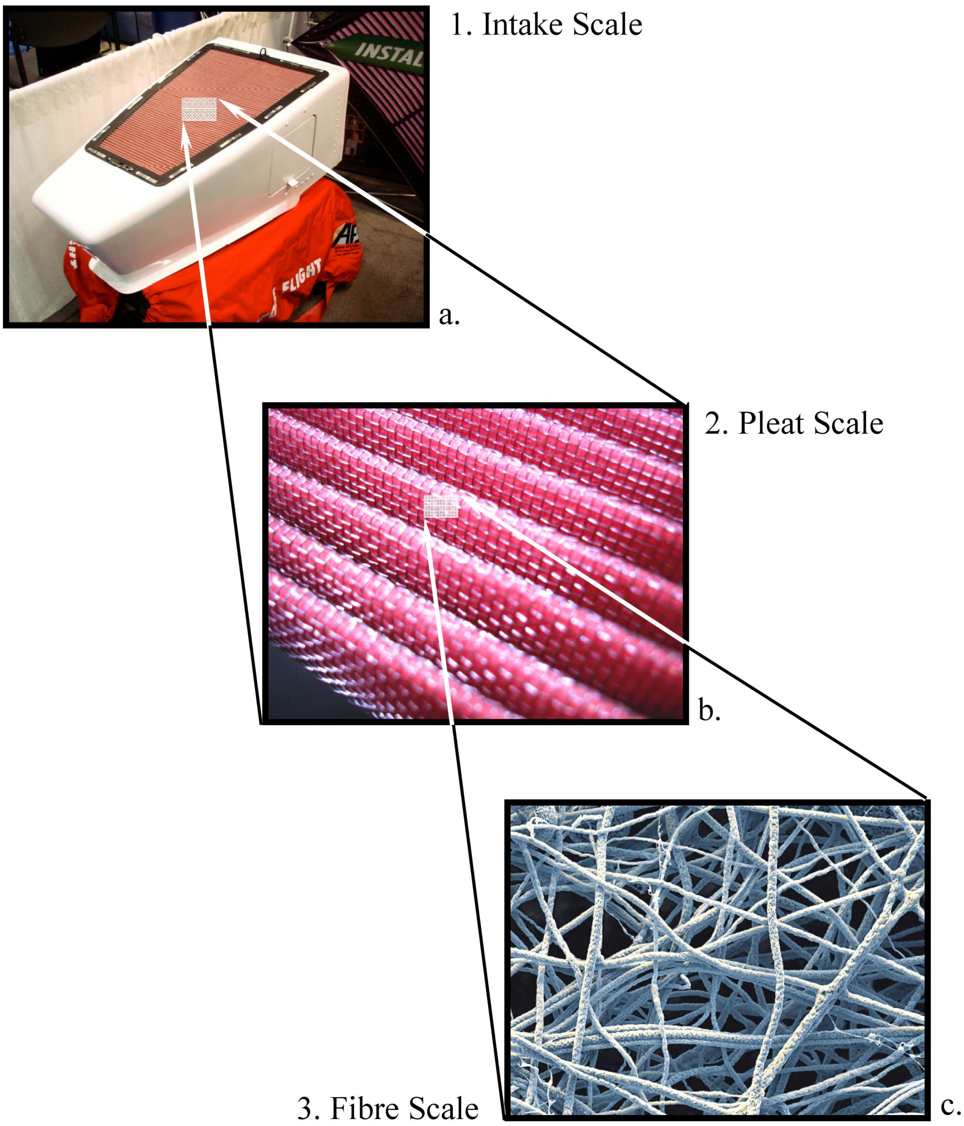

Figure 4.1: *Breakdown of IBF into more manageable parts for analysis: a. Intake Scale; b. Pleat Scale; c. Fibre Scale*. *Fibre Scale Image reproduced under Creative Commons licence (CC BY-NC 2.0), © BASF - The Chemical Company.*

The main motivation for the numerical study is to investigate the phenomena associated with filtration by pleated porous media, with particular attention to performance transiency. In pleat design, it is known that an optimum configuration exists for minimum pressure drop and maximum holding capacity; as part of the study this will be sought for IBF applications (see Section 2.5.3). Another important feature is the "elbow" in the pressure loss curve that indicates the point at which a surface cake forms. Knowledge of this may be critical to predicting IBF performance: the already-transient state is not ideal for the engine, but it could be compounded by a sudden increase in inlet pressure loss. It would be useful to ascertain the ferocity of the discontinuity, and the point at which it occurs. To investigate these phenomena, a parametric study is performed on a single pleat section using CFD.

Since the IBF panel is made up of several scores of pleats, it may be that the transition from internal clogging to surface filtration is more gradual, as some parts of the filter reach capacity before others. It was mentioned in Section 2.2.4 that intake orientation can aid inertial separation; it is probable that the way in which the IBF is integrated into the airframe may also impact on its performance. To investigate these hypotheses, a second parametric study is performed using CFD, but at a larger scale.

Combining the two levels of modelling with the Fibre Scale will allow a complete picture of IBF performance in a number of operational conditions to be formed. The parametric study will reveal the effect on performance of altering key geometric variables, to permit design optimisation. The important performance variables to investigate are the dust properties and the inlet mass flow, as these are likely to change most from one environment to the next and from one rotorcraft to the next. By determining correlations between these variables and the IBF performance will facilitate the wider aim of assessing and comparing the efficacy of all three particle separating technologies.

4.2 Pleated Filter Simulation

A computational fluid dynamics experiment is conducted to improve understanding of pleated filter behaviour for helicopter inlet barrier filters. An IBF module and a close-up of a filter pleat are shown in Figures 4.1a and 4.1b. There are two main objectives for the CFD parametric study of a filter pleat:

1. Investigate the effect of filter clogging and cake formation on the pressure loss evolution.

2. Determine the optimum pleat design for a given set of flow boundary conditions.

The use of CFD to determine pleated filter diagnostics is not new, however there have been no studies at these lengthscales or Reynolds numbers (characteristic length being the channel width). The nearest study in the literature is the semi-analytical model for the clogging of pleated filters proposed by Rebaï *et al.* [52] discussed in Section 2.5.3, which uses assumptions or simplifications that cannot be applied here. The total pressure drop across an IBF is attributable to three sources, as given by Equation 3.72. While the filter medium and surface cake losses can be predicted with well-established theory, the loss in the channel proves more difficult to model. Rebaï's model assumes knowledge of the shape of the velocity profiles within the pleat channels to calculate the loss to fluid shearing; in the present work the same assumption is not applied, as the flow is of a higher velocity and is not considered laminar. The equations used to calculate pressure loss across the filter medium also omit the inertial term in the Darcy equation, and use a temporal resistance term for the filter medium based on the clogging evolution of a planar medium. While Rebaï's model is shown to demonstrate good agreement with experiment, it is deemed inadequate to deal with the anticipated flow conditions of IBF pleated filters, hence the use of CFD in the present study.

4.2.1 Computational Domain

The first task is to decide how the pleat is represented computationally and which dimensions are to be varied. Figure 4.2 shows a computer aided design (CAD) drawing of an IBF pleat. There can be some confusion as to the meaning of a "pleat": in some studies a pleat refers to just one side of the fold; in the present work a "filter pleat" corresponds to the whole fold, shaded green in Figure 4.2. The pleat is represented by a two-dimensional (2D) porous domain, which resembles the cross-sectional profile of half a pleat. Using only half is permitted thanks to symmetry, and reduces computational time. The rest of the domain is designated "fluid", and extends one times the filter thickness upstream and four times the pleat depth downstream as shown in Figure 4.3. The formation of the cake is represented by a number of thin layers drawn adjacent to and upstream from the main filter medium. An assumption here is that the cake is distributed uniformly across the leading surface of the filter. For consistency, the cake layer thickness is proportional to the filter thickness ($\simeq 4.5\%$ of the thickness). There are 9 cake layers in total, as shown in Figure 4.3b.

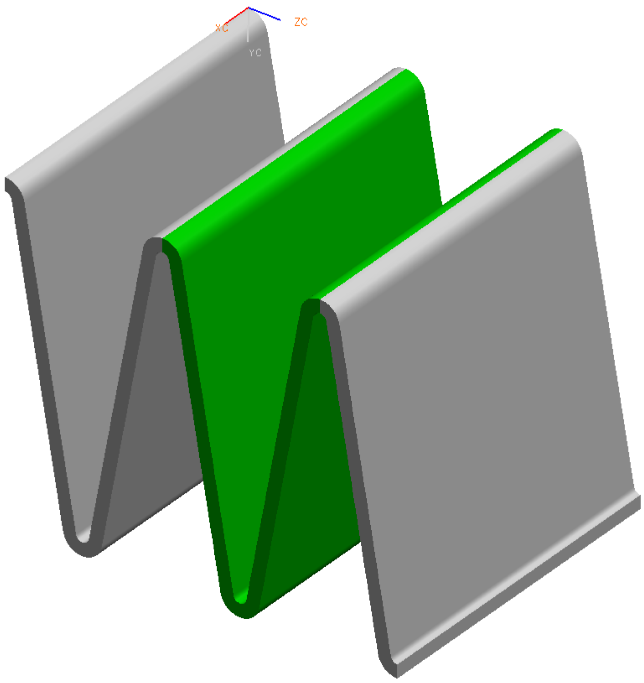

Figure 4.2: *CAD drawing of a section of IBF pleats, with a single pleat shaded in green.*

The CFD exercise is conducted using AnsysFluent. While known for being highly numerically dissipative and therefore potentially inaccurate, the solution speed offered by Fluent was preferred due to the volume of tests to be run. Future work could verify the code's accuracy, but until there are experimental results against which to validate the methodology, the more important outcome is to obtain sufficient data to make conclusions about pleat design. The software has the capability to solve the Navier-Stokes equations for free fluid flow, which are derived from the basic principles of mass momentum and energy. In the present work the fluid is treated as incompressible therefore considered conservation of only mass and momentum. The conservation of mass for an incompressible fluid is given as:

$$\nabla(\rho\vec{u}) = 0 \tag{4.1}$$

where $\vec{u}$ is the local velocity vector. The conservation of momentum is essentially an application of Newton's second law for a continuous fluid. For incompressible flow it is given as:

$$\frac{\partial}{\partial t}(\rho\vec{u}) + \nabla(\rho\vec{u}\vec{u}) = -\nabla p + \mu\nabla^2\vec{u} + \rho\vec{g} + \vec{F} \tag{4.2}$$

where p is the static pressure, $\mu\nabla^2\vec{u}$ is the viscous diffusion term, and $\vec{F}$ is a term that accounts for any external force applied to the fluid, such as a porous medium. Hence in the cell zones lying within the designated porous zone and cake layers (differentiated in Figure 4.3c), Fluent adds a momentum source term to Equation 4.2 to account for the presence of a filter:

$$\vec{F} = S_i = -\left(\sum_{j=1}^{2} C_{ij}\mu u_j + \sum_{j=1}^{2} \frac{1}{2}\rho_g u_j v_{mag}\right) \tag{4.3}$$

where S_i is the source term for the ith (x or y) momentum equation, and C and D are the viscous and inertial resistance coefficients described in Section 3.3.1. This momentum sink term corresponds to the pressure gradient given by Equation 3.56. In addition to the porous zones, the domain is bounded by four surfaces: a velocity inlet, (far left in Figure 4.3a) at which the flow conditions of initial velocity and pressure are prescribed; an outflow (far right in Figure 4.3a); and two symmetry boundaries (top and bottom in Figure 4.3a).

4.2.2 Pleat Properties

Figure 4.3 illustrates the key dimensions to be varied in this parametric study. The pleat assumes a shape seen in the real IBF: a triangular-shaped pleat channel with rounded folds. Incidentally, existing CFD studies have elected to represent different pleat depth/width combinations using a purely rectangular planform, for ease of meshing; in the current study a more realistically-shaped planform is employed, both to facilitate the objectives easier and to broaden the literature. Recalling the objective of finding an optimum design, the pleat density (or width, number) is varied by altering the angle θ in Figure 4.3b, while the depth and thickness are varied by varying the dimensions labelled Z_{pl} and Z_F respectively in Figure 4.3a. The fold radius, characterised by the inside edge of the fold, has a length of half the filter thickness. The narrowest pleat angle tested is 0 degrees, a configuration in which the pleat channel walls are parallel to each other; in Figure 4.3 the pleat has an angle of 10 degrees.

The exact properties of the filter medium and pleat geometry cannot be sought without obtaining a real IBF panel. It is not possible to purchase such a panel from the manufacturers. Fortunately, from the few contributions in the literature that pertain to IBF and filters for automotive applications, an educated estimate of the key properties can be inferred. The patent by Scimone [40] suggests the pleat depth lies in the range of 2.5 to 7.5 cm, with a pleat pitch (spacing) of 0.42 to 0.85 cm. From direct measurement of the IBF for the MD500 (Figure 4.1b) the pleat width is 1 cm. Estimates of the filter properties are taken from the study of Rebaï *et al.* [52] automotive applications, which employ a fibrous filter of porosity 0.95, fibre diameter of 15 microns, and thickness of 1.5 mm. The filter medium in planar form has a holding capacity of 0.4 kgm^{-2}. These give some suitable dimensions to carry out the parametric study. Each pleat

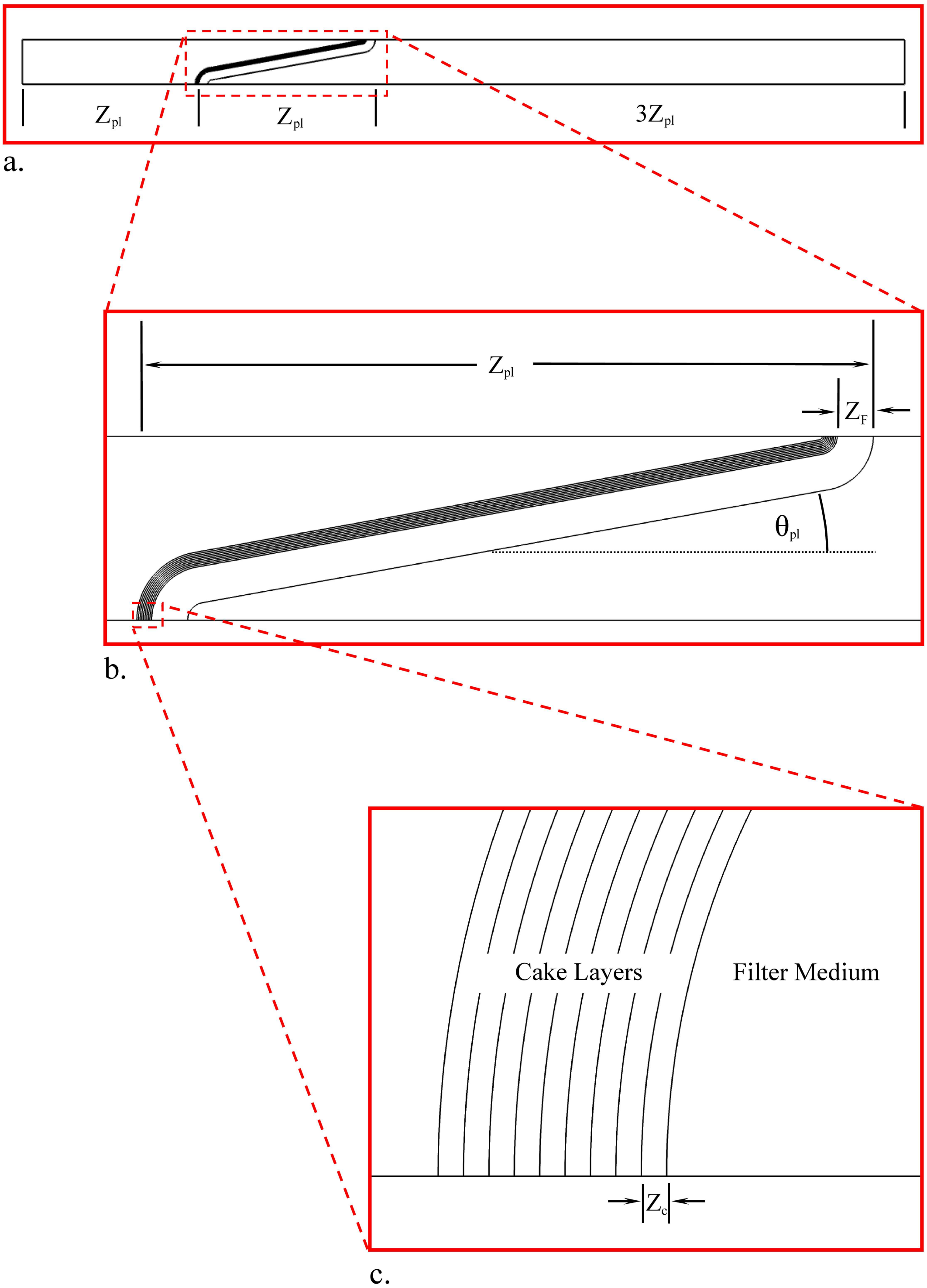

Figure 4.3: *IBF pleat as a computational domain, with filter medium and cake layers represented by porous zones. 3-view diagram, showing a. extent of the computational domain; b. key dimensions of the pleat geometry; c. close-up of cake layers and filter medium.*

section is subjected to a flow of varying velocity between 2 and 12 ms^{-1} to reflect a range of engine mass flow rates, at Standard Day conditions. A breakdown of all filter parameters and the value ranges of those tested is given in Appendix A.

4.2.3 Solution Setup

The important parts of the solution setup here are the viscous and inertial resistance coefficients featured in Equation 4.3, which are prescribed to the porous zones that represent the filter pleat and the cake layers. For the filter medium, the coefficients are given by Equations 3.57 and 3.58. To simulate clogging, each pleat shape is tested under the same flow conditions over a range of resistances. The increase in filter medium resistance is imitated by decreasing the porosity according to Equation 3.60, in which the volume of particles captured by the medium is subtracted from the filter volume. To facilitate this procedure with a degree of automation, a user-defined function (UDF) for the porous zone is employed, which exploits the unsteady solver by changing the properties of the porous zone each time step. During each time step the solution is run until convergence; the only change from one time step to the next is the resistance of the porous zone, hence a series of time steps run like an unsteady solution is akin to running a number of consecutive individual simulations. At each time step, the filter porosity decreases by a quantity equivalent to collecting a fixed mass of particles.

When the total mass collected is equal to the filter capacity, the filter resistance coefficients are held constant and the first cake layer is “activated” i.e. is no longer invisible to the flow and exhibits non-zero resistance terms. The clogging has now reached the “cake formation” stage. After each subsequent time step the next cake layer is activated and so on until each of the 9 layers has been tested in the flow. Since the filter capacity is expressed as a mass per unit projected area, it follows that each different pleat shape has a unique holding capacity: a filter containing pleats of a smaller angle (narrower pleat channel) packs more material into a given projected area hence has a greater capacity. Since all is desired from these simulations is an evolution of the pressure loss as a function of captured mass, a constant number of times steps between the clean filter condition and the clogged filter condition is chosen for each pleat. At the cake layer stage the mass interval is determined by the pleat surface area, the cake thickness and the cake density.

The viscous and inertial resistances for the cake layers are slightly more difficult to render, since the pressure drop equation for the cake is of a different form to Equation 4.3 (contrast with Equation 3.70). To obtain the linear and quadratic term coefficients (C and D) required for Fluent’s porous model, the cake pressure drop equation, Equation 3.69, is plotted over a range of velocities of value expected in this application. All other variables in the equation are known. The cake properties of the test dusts are borrowed from Endo *et al.* [77]. A second order polynomial is fitted to the resulting curve, yielding the two required coefficients. While compression of the cake layers may occur under the drag pressure, initial calculations showed this to be insignificant [45] hence it is assumed that the cake porosity is constant for each layer.

In summary, to achieve the objective of plotting the pressure drop versus the mass collected for each case, the unsteady solver is utilised to vary the resistance properties of a porous zone in a fluid domain. A steady state solution is calculated first, with the clean filter properties prescribed to the filter section. The unsteady stage is then commenced, during which the filter resistance increases by an amount reflective of the capture of an incremental mass of particles, until the total captured mass equals the filter capacity. At this point the previously "invisible" cake layers are activated in turn after each subsequent time step, until 9 time steps have passed. For each time step the solution is converged. The relevant parameters varied at each time step are listed below. If n is the number of time steps, N_{FC} is the number of time steps to filter capacity, and N_c is the number of time steps for all cake layers to form and M_{FC} is the mass captured per unit volume of filter, the mass interval (Δm), filter porosity (ϵ_F) and cake porosity (ϵ_c) are expressed accordingly:

$$\Delta m = \begin{cases} (1-\epsilon_{F,0})Z_F A_{pl}(M_{FC}-\rho_f) & \text{if } n \leq N_{FC} \\ (1-\epsilon_{c,0})Z_c A_{pl}\bar{\rho_p} & \text{if } n > N_{FC} \end{cases} \tag{4.4}$$

$$\epsilon_F = \begin{cases} \epsilon_{F,0} - \frac{n\bar{\rho_p}\Delta m}{Z_F A_{pl}} & \text{if } n \leq N_{FC} \\ \epsilon_{F,FC} & \text{if } n > N_{FC} \end{cases} \tag{4.5}$$

$$\epsilon_c = \begin{cases} 0 & \text{if } n \leq N_{FC} \\ \epsilon_{c,0} & \text{if } n > N_{FC} \end{cases} \tag{4.6}$$

4.2.4 Grid Independence

To solve the Navier-Stokes equations for the free fluid flow, the domain is discretised into a mesh of cells each of which updates the flow each iteration in response to input changes from the cells surrounding it. Generally speaking, the greater the number of cells in an area of complex geometry, for example the cake-fluid interface, the more accurate the result. However, when increasing the cell resolution there comes a point at which the solution shows very little change. Depending on the tolerance set by the user, at this point the solution is said to be *grid independent*, i.e. no longer depends on the grid resolution; increasing the grid size would only cost more computation time. Grid independence checks are essential for any CFD exercise, if any faith is to be placed in the results and computational resources are to be maximised.

In the present study, the grid independence check is made more cumbersome by the multitude of pleat designs tested. To be consistent across all designs, the cake thickness is used as a reference for the minimum cell size in the domain, since it is the shortest length in each domain tested. The mesh resolution is not homogeneous throughout the domain: in some areas such as porous interfaces the flow is under more strain than in other areas and will contain steeper gradients of velocity; areas of steep flow property gradients require higher resolution grids for greater accuracy and speed of convergence. The global solution is more sensitive to the accuracy of these areas, hence in designing an appropriate mesh it is necessary to concentrate efforts on grid independence here. Similarly in areas of little disturbance to the flow such as far upstream/downstream, it is a waste of computational time to discretise with high resolution.

In the present case, the area of greatest flow contraction is in the cusp of the upstream pleat channel. The radius of the cusp is two times the cake thickness, and remains this for all pleat shapes studied. This justifies the use of the cake thickness as a reference length. Other areas of steepest velocity gradient are at the fluid-porous medium interfaces, i.e. the filter surfaces and each cake surface; in these areas the cell size is similarly small. A triangular mesh is used here to conform smoothly to the curves of the pleat folds; see Figure 4.5b. As the domain extends upstream and downstream, the cell size is increased (grid resolution decreased) and a paved quadrilateral cell distribution is adopted. The range of cell sizes adopted for the pleat domains can be seen in Figures 4.4 and 4.5.

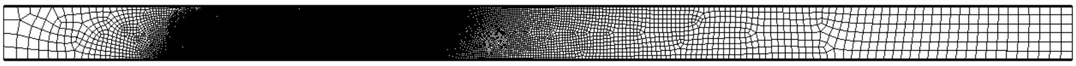

Figure 4.4: *Discretisation of a typical pleat domain, illustrating a coarse mesh at the upstream and downstream extents, and a finer mesh around the pleat.*

To reach grid independence, the minimum cell in the domain is varied in size as a fraction of the cake thickness, i.e. by altering the number of cells across the cake thickness. The pleat of smallest angle (narrowest channel, 0 degrees) is used as a test case in the highest velocity flow (12 ms^{-1}), since it is these channels under these conditions in which the flow contracts the greatest. A number of sizes were tested; the results of three are presented in Figure 4.6 for illustrative purposes. Figure 4.6a shows the spanwise-averaged non-dimensional static pressure across the pleat in the streamwise direction. There are notable differences between each result, but the static pressure at $1.5Z_{pl}$ appears to be the same for the two most refined grids. This suggests that increasing the number of cells across the cake thickness beyond four cells does not have a profound affect on the result. This is backed up by Figure 4.6b, in which the total pressure at the domain exit is monitored for the range of mass intervals. This is the key value in the exercise. The results illustrate little discrepancy when increasing the grid from the medium to the largest resolution, hence a minimum cell size of one quarter of the cake thickness is chosen for the parametric study.

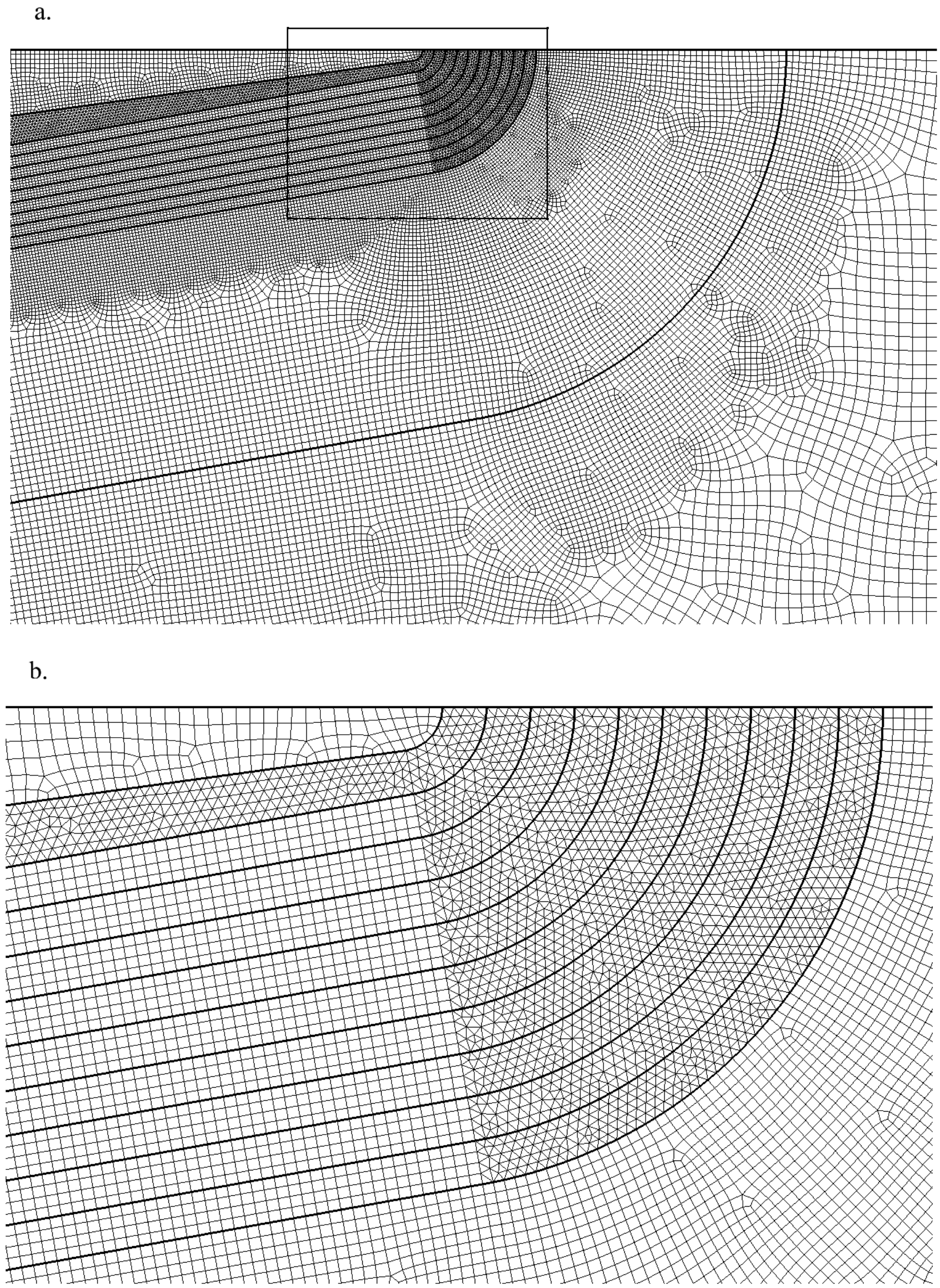

Figure 4.5: *Discretisation of a typical pleat domain, illustrating area of highest cell density, in which the flow is anticipated to be under the most strain, producing the steepest velocity gradients: a. representation of cake layers; b. close-up of highly refined mesh.*

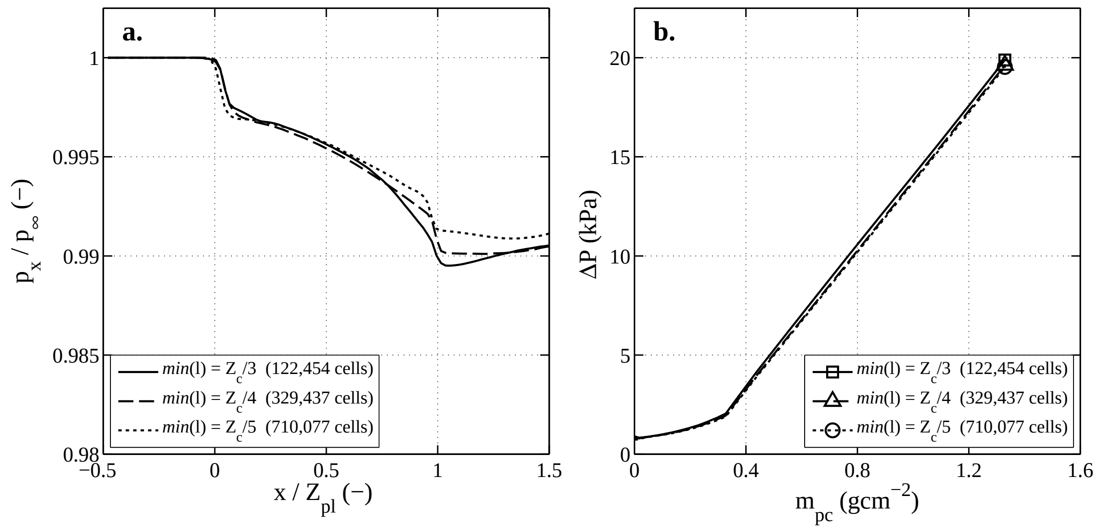

Figure 4.6: *Grid independence checks for pleat simulations, displaying: a. spanwise-averaged normalised static pressure; b. pressure drop as a function of accumulated mass per unit area.*

4.2.5 Turbulence Model

There are several options available for modifying the way Fluent solves the governing equations in each cell, such as the way the scalar quantities at the cell centres are evaluated. The suitability of any one method is usually a compromise between accuracy and computation time, which are themselves functions of the geometry complexity. In the absence of real data to compare results with, an in depth study into the differences between each numerical scheme and solution method would merely be academic and not advance the present work at this stage. The theory of these methods is well represented in the literature (see Ferziger & Perić [84]) and is therefore not exhaustively covered here.

To reflect reality of flow through IBF filters, the fluid is prescribed with a level of turbulence, which is a measure of the kinetic energy of the eddies in the flow produced by fluid shear, friction, buoyancy or external forcing. Turbulent flows are characterised by fluctuating velocity fields, which aid the mixing of and cause fluctuations of momentum, energy, species concentration and other transported properties. To simulate these fluctuations fully by directly solving the governing equations would require a great computational resource. To surmount this problem, the turbulence can be simplified by removing the small scale velocity fluctuations through time-averaging, ensemble-averaging or other manipulation to form modified versions of the governing equations. However, this process creates additional unknowns, which require turbulence models for determination.

One such method of removing the small scale fluctuations is by Reynolds-averaging, whereby the solution variables in the instantaneous Navier-Stokes equations are decomposed into the mean (ensemble-averaged or time-averaged) and fluctuating components. For the velocity components:

$$u_i = \bar{u}_i + u_i' \tag{4.7}$$

where $\bar{u}_i$ and u_i' are the mean and fluctuating velocity components. Substituting these into Equations 4.1 and 4.2, and expanding the difference operator (∇) (and removing the overbar from the mean velocity), yields the well-known Reynolds-averaged Navier-Stokes equations for mass and momentum continuity:

$$\frac{\partial \rho}{\partial t} + \frac{\partial}{\partial x_i}(\rho u_i) = 0 \tag{4.8}$$

$$\frac{\partial}{\partial t}(\rho u_i) + \frac{\partial}{\partial x_i}(\rho u_i u_j) = -\frac{\partial p}{\partial x_i} + \frac{\partial}{\partial x_i}\left[\mu\left(\frac{\partial u_i}{\partial x_j} + \frac{\partial u_i}{\partial x_j} - \frac{2}{3}\delta_{ij}\frac{\partial u_l}{\partial x_l}\right)\right] + \frac{\partial}{\partial x_j}(-\rho\overline{u_i' u_j'}) \tag{4.9}$$

The additional terms that appear represent the effects of turbulence. In particular, $-\rho\overline{u_i' u_j'}$ are known as the Reynolds stresses, which must be modelled in order to close the momentum equation. There are several approaches to modelling the Reynolds stresses, each of which are determined by the choice of turbulence model. The choice of turbulence model will depend on a number of factors such as the physics of the problem, the level of accuracy required and the computational resources available. In the present work, a suitable model must chosen to account for high fluid strain rates anticipated in the pleat channels. Again, a lack of real data makes verification quite difficult to ascertain the accuracy of a particular model, therefore some computational cost may be required to guarantee greater assumed accuracy. The 5-equation Reynolds Stress Model (RSM) is one such model, which is the most elaborate model that Fluent provides. It costs approximately 50-60% more computation time over the simpler RANS models, but it has greater potential to give accurate predictions for complex flows. To simulate turbulence, the user inputs a turbulence intensity and a turbulence lengthscale, which are used by the RSM to determine the turbulent viscosity.

There are current studies in the literature that use CFD to calculate the pressure drop across a pleated filter, but they invariably solve for laminar flow only. To compare the RSM with the $k-\epsilon$ model (a two-equation RANS model), a number of pleat domains are drawn to replicate the laminar solution obtained by Chen *et al.* [47]. A low level of turbulence (0.5%) is prescribed to the flow to justify the requirement of a RANS model, but to permit comparison with the laminar solutions. The flow conditions are exactly as is prescribed in the literature. The results are shown in Figure 4.7. At narrow pleat channel widths the accuracy of the k-ϵ appears to diminish, while the RSM produces just slightly higher pressure drop results than the literature. While this does not necessarily confirm the suitability of the RSM, it at least suggests that its use will yield results of a reliable order of magnitude. For completeness the present work uses: a segregated solver to solve the governing equations for the conservation of momentum and mass; a 1st Order Upwind scheme to discretise the momentum and turbulence terms since no change in the results was found when using a higher order scheme; the PRESTO! scheme, which is recommended for pressure discretisation when using the porous media model; and the PISO algorithm, which is selected for pressure-velocity coupling based on its recommendation for transient calculations.

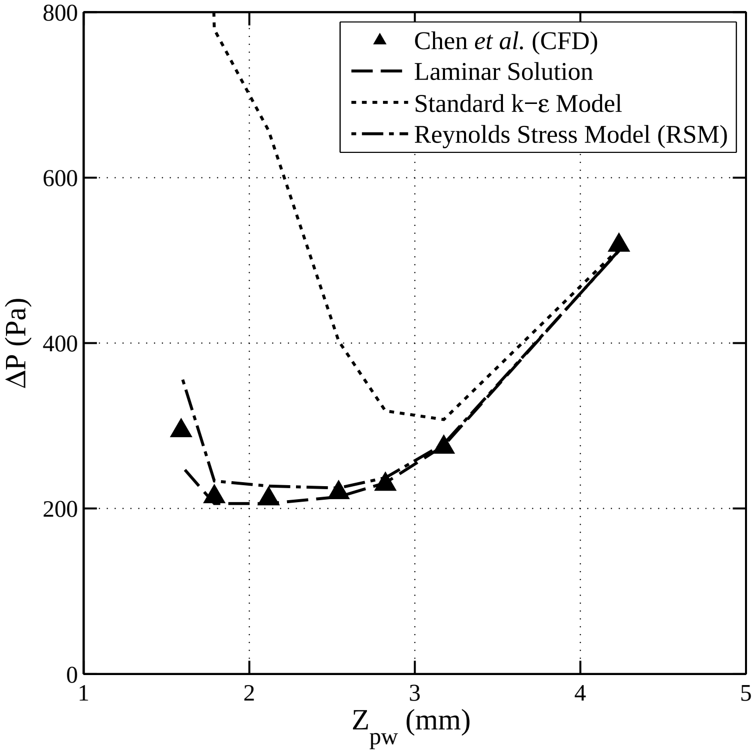

Figure 4.7: *Suitability checks for pleat simulations of two different turbulence models, along with the laminar solution, on the domain featured in the CFD study of Chen et al. [47], where Z_{pw} is the pleat width.*

4.3 Installed Filter Performance

As mentioned in Section 2.5 there is very little in the technical literature that pertains to installed IBF performance. From the few contributions available, data are sanitised. What is known is that the IBF for the EC145 lasts about 12 minutes in a heavy dust cloud before the pressure drop reaches the maximum permissible, which equates to around 30 brownout landings & takeoffs [46]. Whether this varies between rotorcraft is not known. A plot of the temporally rising pressure loss provided in the contribution by Ockier *et al.* [46] suggests a linear relationship, but the pattern is inconclusive and no technical detail is provided for the prevailing conditions. These gaps in the knowledge provide the motivation for the parametric study conducted using CFD at this scale. The pleat scale results yield a relationship between mass collected and pressure loss across a single pleat; for the pleat scale results to be useful to the bigger picture, the "mass collected" on the pleat needs to be converted to a "'time spent" in the dust cloud. This is achieved by way of a particle mass flow rate. The particle mass flow rate is expected to vary spanwise across the filter, therefore each pleat will have its own pressure drop evolution. To examine how this is effected, a CFD study is performed to simulate the intake of particulate-laden flow into a helicopter engine. The three main objectives of the intake scale parametric study are to:

1. Investigate the influence of IBF integration on the spanwise distribution of particles on a filter panel.

2. Investigate the difference in performance of forward-facing and side-facing intakes.

3. Investigate the effect of dust properties on IBF performance.

4.3.1 Computational Domain & Boundary Conditions

A simplified computational domain is constructed to reflect typical intake-IBF configurations found across the range of rotorcraft. Figure 4.1a shows an upward facing IBF module for the MD500; in other embodiments such as the MD902 the filter panel faces to the side or may be angled into the flow to offer a level of pressure recovery in forward flight. Two representative domains are shown in Figures 4.8a and 4.8b. Each intake type is subjected to a range of forward flight speeds, including hover, in two distributions of dust (explained below). Three levels of intake resistance are tested: no filter; clean filter; and clogged filter. In all cases the filter orientation to the flow is varied through an angle of θ.

The domain is defined by five types of boundary, as labelled in Figure 4.8. The green boundary represents the engine, and is prescribed with an "outlet-vent" boundary which will adjust the static pressure to meet a user-specified target mass flow rate. If any restriction is placed ahead of the outlet vent, the static pressure at the boundary will decrease accordingly in order to achieve the required mass flow. The remaining boundary types are dependent on the freestream conditions: during hover, the three blue boundaries are prescribed as "pressure inlet" boundaries, which allows the atmospheric pressure and turbulence quantities to be prescribed at a far distance from the inlet; during forward flight the far left boundary is a pressure inlet prescribed with a dynamic pressure that corresponds to a user-specified forward speed (which is added

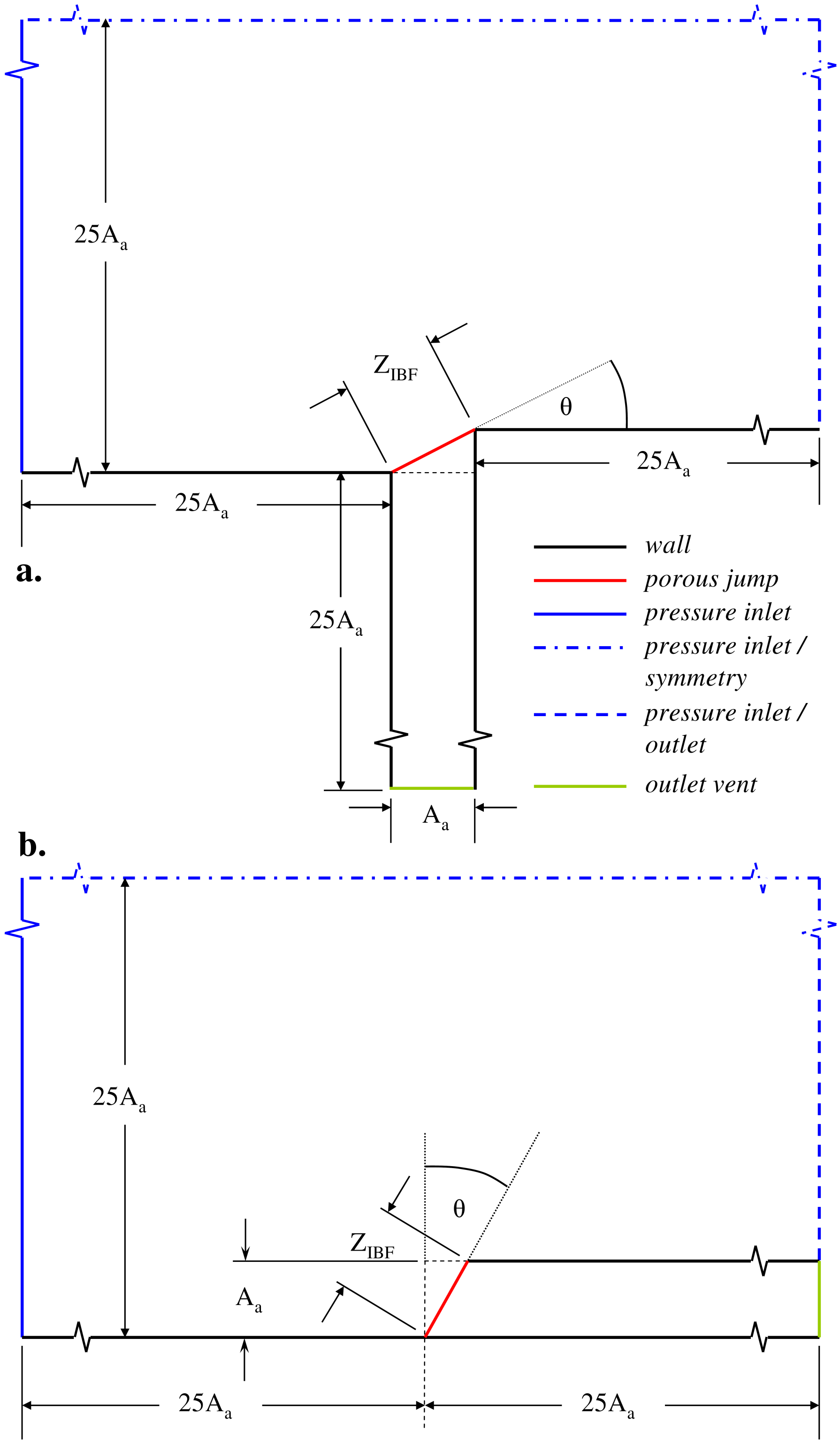

Figure 4.8: *Computational domains representing two types of rotorcraft intake and IBF installation, and illustrating boundary type prescribed to domain edges for: a. side-facing (or upward-facing) intakes; b. forward-facing intakes.*

to the atmospheric operating pressure), the top boundary is symmetrical to simulate far field conditions, and the far left is a velocity outlet. The prescription to the far right boundary is a compromise of sorts. The removal of mass flow from the domain at the engine boundary must be balanced by the mass flow entering at the inlet, and the mass flow leaving the domain in order to observe conservation laws. Hence the velocity at the domain outlet must correspond to a mass flow that when summed with the engine mass flow is equal to the mass inflow rate. The extent of the domain in the x- and y-directions (see Figure 4.8) is large enough to ensure that the fraction of the mass flow leaving the domain at the outlet is almost unity, thus preserving the simulated freestream velocity. All walls in the domain are prescribed with a no-slip condition. The energy equation is suppressed, as the flow is treated as incompressible; while gravity is neglected.

The filter is represented by a "porous jump" boundary, which is essentially a one-dimensional simplification of the porous media model described in Section 4.2 that calculates the pressure drop according to the following equation:

$$\Delta p = -\left(Cu + \frac{1}{2}D\rho u^2\right)\Delta Z_F \tag{4.10}$$

where ΔZ is the porous medium (virtual) thickness and u is the filtration velocity orthogonal to the filter surface. A viscous resistance term (C) and an inertial resistance term (D) are again required; while instead of being inferred from the number of cells across a porous zone, the medium thickness is inputted by the user: the porous medium is merely a membrane between cells. Since mass conservation is observed in the intake and density is constant, the filtration velocity is a function of the filter area and the engine mass flow rate only. The filter area increases as the angle θ increases, which decreases the filtration velocity as:

$$u = \frac{\dot{m}_a}{\rho_g Z_{IBF}} = \frac{\dot{m}_a \cos\theta}{\rho_g A_a} \tag{4.11}$$

where Z_{IBF} is the filter projected area and A_a is the engine face area. One objective of the study is to investigate the effect of filter angle on the flow at various stages of clogging. The stages of clogging are simulated by prescribing values of resistance and thickness to the porous jump that result in fixed pressure drops. For example, prescribing a thickness of zero renders the porous jump invisible to the flow, hence there is no loss in pressure, which simulates the case of there being no filter fitted. For the cases of clean and clogged filters, pressure drops of 600 Pa and 3000 Pa respectively are desired across the filter. Since the filtration velocity can be determined from Equation 4.11 which is held constant for all test cases, the remaining variables in Equation 4.10 can be tuned to ensure the pressure drop across each filter, irrespective of angle, is as desired and consistent for each test case. In fact, by rearranging Equation 4.10 for Z_F it can be seen that only the filter thickness needs to be adjusted to achieve the three different pressure drops. The solution is set up in this way in order to facilitate a fair comparison of the effect of filter angle on the influent flow; since the pressure drop (at a given clogging state) is equal for each angle, any difference in pressure loss at the engine face can be attributed to the geometrical setup of the intake.

4.3.2 Solution Setup

The influence of IBF installation on intake performance is determined by simulating two intake types to a range of freestream velocities, for a number of filter angles and filter clogging states. A level of turbulence intensity consistent with the pleat scale simulations is prescribed, and the flow properties reflect Standard Day conditions. A breakdown of the parameter ranges is given in Appendix A. Another set of parameters is introduced to fulfill the objectives of the study. By injecting particles into the domain at a fixed distance from the filter, the distribution of particles on the filter can be found. By injecting particles of different size, the effect of different environments can be investigated.

There are a number of ways to model particle transport in Fluent. One such method is the Discrete Phase Model (DPM) which simulates the trajectories of particles in a Lagrangian framework as they interact with the continuous fluid phase. If the particulate concentration is large enough, the impact of the two-way coupling between the two phases on the continuous phase can also be included. In the present study the dispersion of particles is sparse: particle on particle interactions can be neglected and the particle volume fraction, which is typically less than $\simeq 0.5\%$, is small enough to have negligible effect on the gas phase. The effect of turbulence on particle trajectories can also be modelled with stochastic tracking or otherwise if desired, but since there are no real data to compare with it was considered an unnecessary use of computational resources.

Once the steady-state continuous phase is solved, the particles are injected into the domain and their motion computed according to the equations given in Section 3.2.5 of Chapter 3. The filter edge in the domain is invisible to the particles, but in tracking a particle it is possible to record the position at which it crosses a boundary i.e. intercepts the filter. The general procedure for setting up and solving a steady state discrete-phase problem and obtaining the particle distribution at the filter is outlined below:

1. Solve the continuous-phase flow.

2. Create the discrete-phase injections.

3. Track the discrete-phase injections.
4. Record the positions of all particles that cross the filter.

4.3.3 Dust Representation

The discrete phase injections are used to replicate a dust distribution in a brownout cloud. Since the exact distributions at the inlet are unknown, established test dusts are adopted as surrogates. As illustrated by Figure 3.3, dust samples can be represented by a particle size distribution (PSD) that gives the percentage by mass of each particle diameter in the range. In particle sample analysis it is often the case that a PSD is given by a of particle size groups. The following data in Tables 4.1 and 4.2 were obtained from a test dust manufacturer for Arizona Air Cleaner (AC) Fine dust and Arizona AC Coarse Test Dust. All particles are treated as spherical.

Table 4.1: *Particle size groups by mass fractions for AC Fine test dust, as provided by Particle Technology.*

d_p (μm)	1	3.5	7.5	15	30	57.5
% by mass $(m/M)_i$	17.5	17.5	14	18	17	14

Table 4.2: *Particle size groups by mass fractions for AC Coarse test dust, as provided by Particle Technology.*

d_p (μm)	2.75	8.25	16.5	33	66	132
% by mass $(m/M)_i$	13	11	13	19	28	16

These data are translated into injection parameters in the intake scale computational domain. Each group is distributed along an injection surface, which lies a distance of $5A_A$ from the filter and spans an injection area of $5A_a$. The injection properties for each particle size group include: the number of particles; a representative diameter for the particle group; the velocity of the particles; and the mass flow rate of a single particle stream. To calculate these values requires a degree of algebraic manipulation.

The number of particles of a given size group is found by determining the mass concentration of that group. If the dust mass concentration of the whole sample is known (which is interpreted from sources such as the Sandblaster II study [16]), then the group concentration is simply:

$$c_{m,i} = c_m \left(\frac{m}{M}\right)_i \tag{4.12}$$

where c_m is the brownout mass concentration given by Equation 3.2 and $(m/M)_i$ is the mass fraction of the particle size group. The interparticle spacing is given by:

$$s_{p,i} = d_{p,i}\left(k_v \frac{1 + c_{m,i}}{c_{m,i}}\right)^{1/3} \tag{4.13}$$

where k_v is the volume shape coefficient as discussed in Section 3.2.2. This can be proven by simple geometry; a proof is given by Crowe *et al.* [85]. The number of particles in a size group injection is derived from the interparticle spacing and injection area as follows:

$$n_i = \frac{A_{inj}}{s_{p,i}} \tag{4.14}$$

where A_{inj} is the particle injection area. The representative diameter of the particle group is known; the injection velocity of the particles is assumed to be equal to the freestream velocity. The remaining requirement is to assign a particle stream mass flow rate, which is the particle size group mass flow divided by the number of particles:

$$\dot{m}_{ij} = \frac{\dot{m}_i}{n_i} = \frac{1}{n_i}\left(\frac{m}{M}\right)_i c_{m,i}\rho_g U_\infty A_{inj} \tag{4.15}$$

where U_∞ is the freestream velocity and j is the particle index within the ith size group.

4.3.4 Particle Data Processing

As a particle stream propagates through the computational domain, its trajectory is recorded by Fluent. If the stream passes through a permeable boundary (set as "interior"; a porous jump is one such boundary) its position on that boundary, along with several other properties of the stream, can be reported by Fluent. Note: in difference to reality, particles are not arrested in the simulation. If the two phases were coupled this may affect the flow aft of the filter; in fact a higher order simulation could employ a user-defined function to increase the resistance of the porous jump as a function of the particles captured, however a far greater computational resource would be required. Of the information recorded at the boundary, the particle position, velocity and diameter are extracted for processing in the present work. With this information it is possible to ascertain the spanwise variation in mass flow rate.

Firstly the particle velocity is used to infer the stream's mass flow rate. The particle stream has an initial mass flow rate and an initial velocity; dividing the mass flow by the velocity gives a measure of the mass contained per unit length of particle stream line which by conservation cannot change. If the local velocity at any point along the stream is known, this can be used to determine the instantaneous mass flow rate, for example at the filter:

$$\dot{m}_{s,ij} = \frac{\dot{m}_{ij}}{U_\infty} U_{IBF,ij} \tag{4.16}$$

where the subscript s implies a value along the filter. Consider a small portion of the filter, for example the length of a pleat width. The mass flow rate of particles reaching that portion is a summation of all individual streams contained within it. Since the positions of all the particle streams are known, it is possible to ascertain the accumulation rate of a pleat at a given spanwise position, for each size group:

$$\dot{m}_{s,i} = \sum_{j=1}^{n_{s,i}} \dot{m}_{s,ij} \tag{4.17}$$

here n_j is the number of particle streams of a given size group passing through the filter boundary at a position s along the filter. Likewise, summing all particle size group mass flow rates at the local position gives the total pleat accumulation rate:

$$\dot{m}_s = \sum_{i=1}^{n_i} \dot{m}_{s,i} \tag{4.18}$$

The number of pleats across the filter, n_{pl}, is found by dividing the filter width by the pleat width:

$$n_{pl} = \frac{Z_{IBF}}{Z_{pw}} \tag{4.19}$$

where Z_{pw} is the pleat width. Hence the total particle accumulation rate, or mass flow rate for the whole filter is:

$$\dot{m}_{p,IBF} = \sum_{s=1}^{n_{pl}} \dot{m}_s \tag{4.20}$$

This can be used as a reference to normalise the local mass flow rate given by Equation 4.18, to illustrate the spanwise distribution of dust mass collecting on the filter.

The particle mass flow rates can also be expressed as a concentration, to permit comparison with the brownout concentration in the freestream. The mass concentration is the particle mass flow rate divided by the engine air flow rate:

$$c_{m,IBF} = \frac{\dot{m}_{p,IBF}}{\dot{m}_a} \tag{4.21}$$

This can be used to asses the inherent separation ability of the IBF installation. A value lower than the brownout dust concentration implies that due to the way it is integrated into the airframe, a degree of dust separation from the air can be achieved through particle inertia alone, prior to passing through the filter.

4.3.5 Grid Independence

The particulars of the numerical solution are similar to the pleat scale. The iterations are stopped when the convergence residuals reach 0.00005. A second order upwind scheme is used to compute quantities at the cell centres, and the pressure-velocity coupling is solved with the well-known PISO scheme. The PRESTO! scheme was used for pressure discretisation. The domain is discretised into quadrilateral cells to solve the Navier-Stokes equations iteratively. The cell size distribution is set to cater for areas of high velocity gradient, namely at the boundary walls and around the filter entrance, visible in Figure 4.9. The grids for the two intake types are very similar; a structured mesh can be used for the majority of the domain, but the area surrounding the filter is made up of a quadrilateral pave, as shown in Figure 4.10.

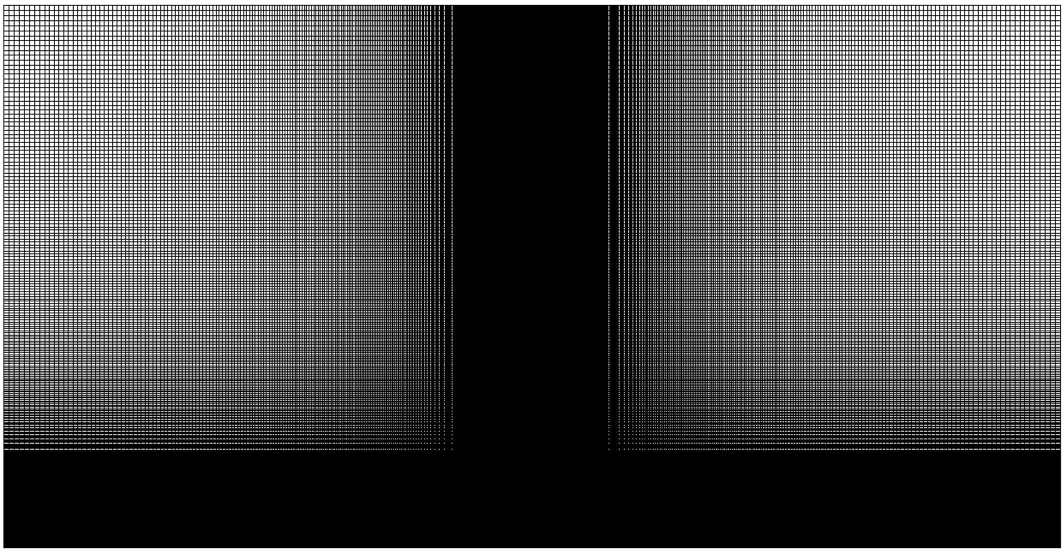

Figure 4.9: *Discretisation of forward-facing intake computational domain. The cell distribution is the same for the side-facing intake domain.*

An independence test with cells of different minimum size is performed for the maximum filter angle (50 degrees) for the largest engine mass flow rate (12 kg/s) across a range of freestream velocities. It is found that a minimum cell size around the filter of $0.005A_a$ for both intake types is sufficient to satisfy grid independence. This is consistently applied to the grids of all domains in the parametric study. Results of the grid independence test are given in Figures 4.11 and 4.12. Figure 4.11 shows the local spanwise total pressure distribution taken at two streamwise cut locations, for the forward-facing intake. The distance of each cut from the intake entrance is measured from the most rearward point on the filter. The flow conditions illustrated here represent hover, since in this condition the largest degree of flow separation within the intake is expected, due to the air being drawn from a multitude of angles. By comparing the ability of each grid size to capture this separation region, a grid independence can be finalised. The procedure is repeated at other flow conditions, for the side-facing intake. Coarser meshes than those discussed are also tested, but the results are not presented here.

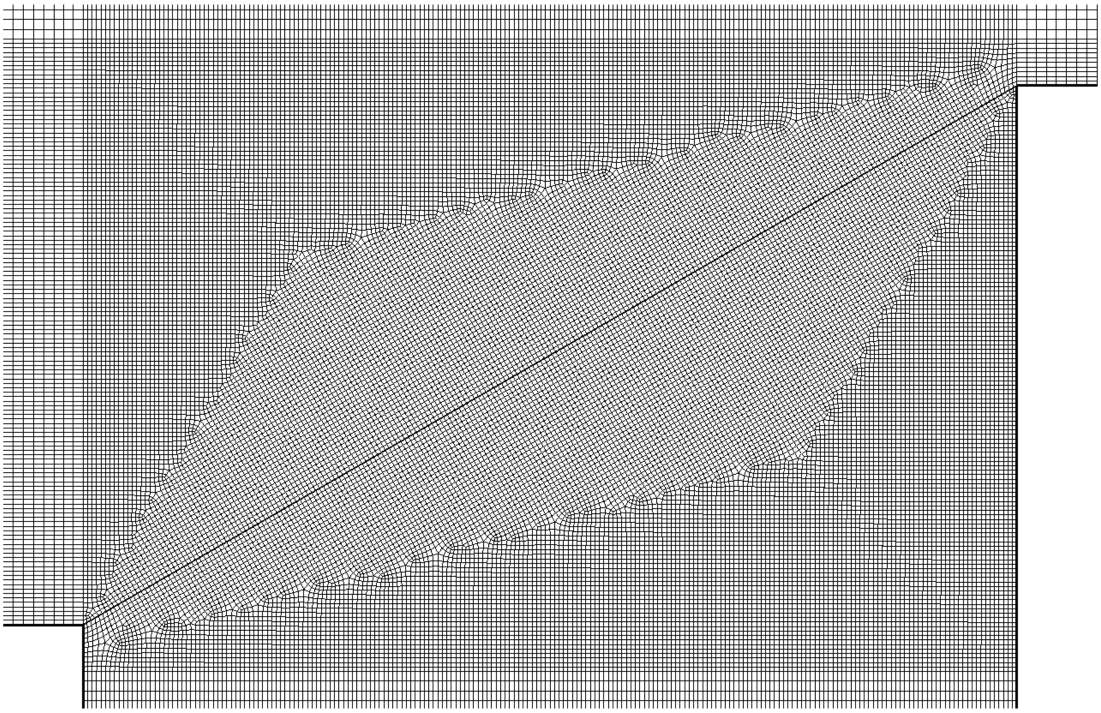

Figure 4.10: *Close-up of discretised domain for side-facing intake in the region of the filter and intake entry.*

The pressure cuts provide the data for comparison. The two streamwise locations are chosen because they intersect the separated flow region. This is recognisable in Figure 4.11 by the large depression in total pressure at a spanwise section of $s/A_a =$ 0.6 to 1.0. A drop in total pressure is also noticeable at a spanwise position of $s/A_a =$ 0 due to the presence of the boundary layer. The absence of this on the opposite wall indicates stagnant flow, symptomatic of a separated region. The three curves on each plot represent three grid sizes. Looking at Figure 4.11a, across the majority of the span the curves are aligned, but at the edge of the boundary layer there is a divergence of the coarser grid from the two finer grids. This trend continues in Figure 4.11b, and indeed was observed for other similar cuts along the intake duct. An even greater disparity was noticed for coarser grids not shown in these results. The difference between the two finer grids, however, is marginal, indicating the reaching of grid independence. Hence the choice of the intermediate cell size here, of $0.005A_a$, for use in the parametric study.

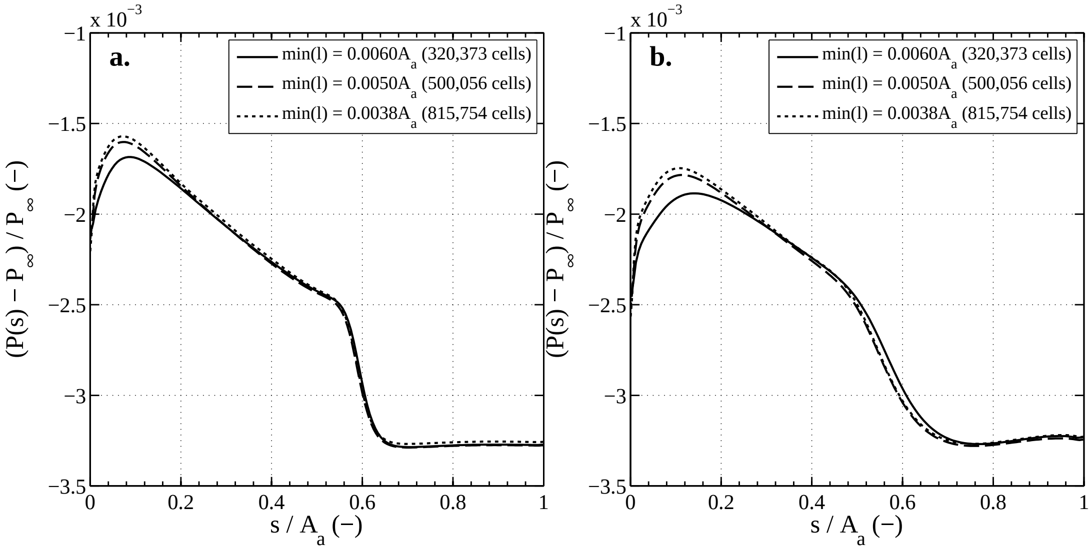

Figure 4.11: *Assessment of intake scale grid independence by spanwise cuts of static pressure across the forward-facing inlet width at two streamwise locations: a. $s/A_a = 0$; b. $s/A_a = 1$; where s is the distance from the inlet entrance (outer edge).*

To further confirm the adequacy of the chosen grid size, one of the main flow properties of interest — the total pressure at the engine inlet face — is plotted for all forward speeds to be tested in the parametric study. The results are shown in Figure 4.12, illustrating the loss in total pressure as a function of freestream velocity, expressed in dimensionless terms. A discussion of the reasons for the trend in pressure loss is left for later chapters, however the results show very little difference between the three grid sizes.

4.3.6 Turbulence Model

Assurances are sought to confirm the appropriateness of the turbulence model used. For the same reasons given for the pleat scale, the RSM model is used for turbulence closure, with the standard wall function used to approximate the solution of the boundary layer. In the absence of real data, the results are compared with a theoretical model proposed by Seddon [21] for the prediction of intake performance, in which losses are attributed to friction with the airframe and intake duct walls. the model is derived from momentum theory and neglects flow separation. The total pressure lost to friction is split into two sources: approach loss and duct loss. Approach loss refers to loss of energy to friction with the airframe — the larger the wetted surface area, the larger the approach loss. For this reason, pitot intakes (that take in very little airframe boundary layer) perform better in cruise than the intakes tested in this study. The duct loss is attributable to

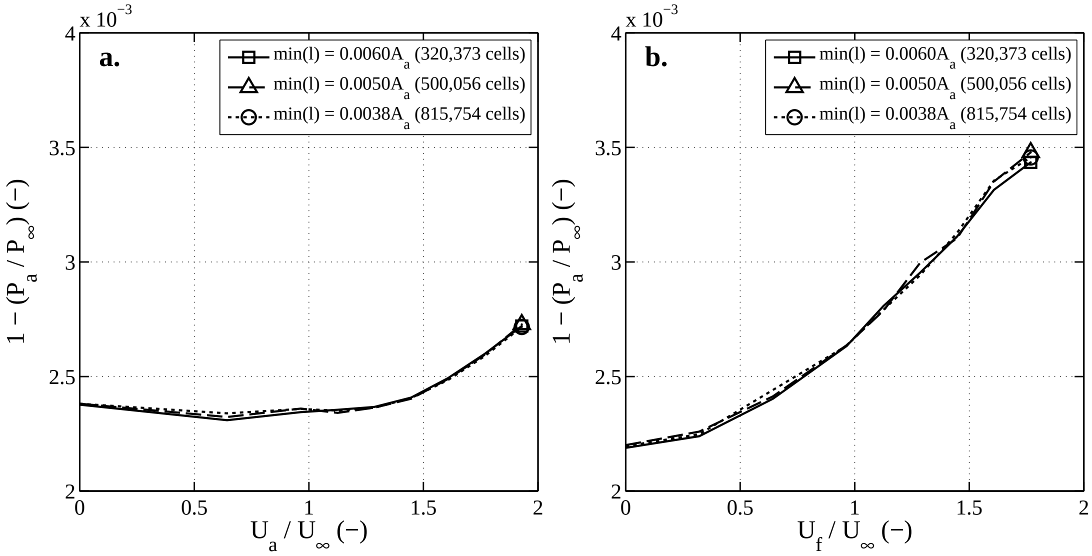

Figure 4.12: *Assessment of intake scale grid independence by total pressure loss between the freestream and engine inlet face, for: a. forward-facing intake; b. side-facing intake.*

friction from contact with the internal walls of the intake. The approach loss is given by:

$$\frac{\Delta P_A}{q_a} = C_{f,A}\left(\frac{A_a}{A_\infty}\right)^3 k\frac{S_A}{A_a} \tag{4.22}$$

where $C_{f,A}$ is the overall friction coefficient for the approach, A_a is the intake entry cross-sectional area, A_∞ is the capture streamtube cross-sectional area in the far freestream, and S_A is the wetted area of the approach. k is an empirical factor with a value close to 1.0, which accounts for boundary layer effects at the ends of the intake. It is assumed to be unity in this study. The ratio A_a/A_∞ is the inverse of the freestream to engine face velocity ratio, U_a/U_∞, if the flow is treated as incompressible. The duct loss is given as:

$$\frac{\Delta P_D}{q_a} = C_{f,D}\int_{l_1}^{l_2}\left(\frac{A_a}{A_\infty}\right)^2 \frac{g}{A}dl \tag{4.23}$$

where $C_{f,D}$ is the overall friction coefficient for the duct, A is the local duct cross-sectional area, g is the local duct perimeter, and the limits l_1 and l_2 refer to the streamwise position of the section under analysis. Of these variables, the only unknown is the skin friction coefficient. To compare the numerical solution to the analytical solution requires two approaches to approximate the skin friction coefficient. From the two-dimensional CFD results, the skin friction coefficient is calculated by its definition of the overall wall shear stress divided by the dynamic pressure. For the approach it is:

$$C_{f,A} = \frac{\tau_{w,A}}{\frac{1}{2}\rho_g U_\infty^2} \tag{4.24}$$

where $\tau_{w,A}$ is the overall wall shear stress over the approach, which is given as an output by the CFD software. For the duct it is:

$$C_{f,D} = \frac{\tau_{w,D}}{\frac{1}{2}\rho_g U_a^2} \tag{4.25}$$

where $\tau_{w,D}$ is the overall wall shear stress over one side of the duct, and S_D is the length of the duct side. Theoretically, there are several approximations for the skin friction coefficient of a flat plate with a turbulent boundary layer, that can be applied in the present study. One such approximation is the widely used 1/7th power law, which defines the skin friction coefficient as:

$$C_f = 0.0576\mathrm{Re}_x^{-1/5} \tag{4.26}$$

which is applicable for $0.5{\cdot}10^6 < \mathrm{Re}_x < 10{\cdot}10^6$. Substituting Equation 4.25 and 4.26 into Equation 4.23 affords the comparison of calculated duct loss given in Figure 4.13. The forward-facing intake shows a good agreement with the theoretical at velocities above full-flow. Below full-flow there is a noticeable increase in pressure loss, which occurs due to lip spillage (discussed in the foregoing sections). Since lip spillage disappears at higher forward speeds, the numerical prediction with the chosen turbulence model more closely matches the analytical solution. For the side intake, the difference between the analytical and numerical solutions is greater, and increases with forward speed. This again is indicative of lip spillage, which for side intakes worsens with forward speed. These results demonstrate both the appropriateness of the turbulence model used, and the benefit of the numerical solution over the analytical for such flow predictions that involve separation.

4.4 Summary

The methodology described hitherto was employed to generate results for a parametric study of IBF performance, and the development of a design protocol. Due to the wide range of parameters involved, the study is split into two scales, which are taken forward for analysis by CFD. The results of the CFD are used in the foregoing chapters to gain an insight into the fluid dynamics of IBF for helicopters.

The first scale is the pleat scale. The pleat scale idealises an IBF filter pleat as a two dimensional section representing half a pleat. The CFD solver simulates the loss of energy of the air to the filter by extracting momentum from the flow in accordance with the resistive properties of the porous medium. The resistance coefficients of the porous zone are varied over time to reflect the accumulation of particles within the pleat. When the pleat reaches a pre-determined capacity, the cake layers in the domain

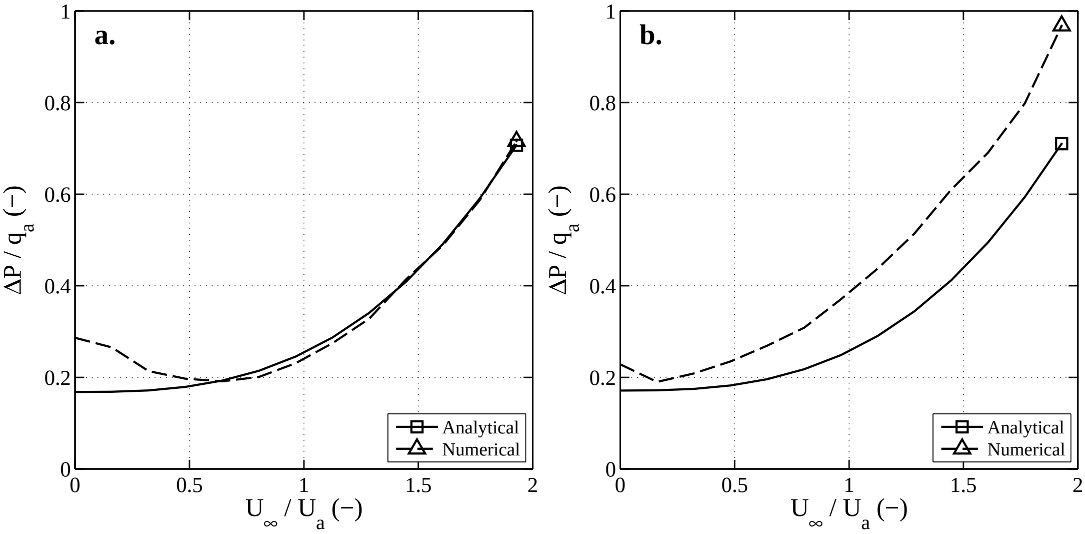

Figure 4.13: *Suitability check for turbulence model used, showing comparison of numerical and analytical duct loss, for: a. forward-facing intake; and b. side-facing intake.*

are activated, to simulate the reduction in flow area caused by the building up of surface material. As well as allowing the flow through a pleat to be analysed, this approach yields a relationship between pressure loss and mass accumulated, which can be used to compare pleats of different design.

The second scale is the intake scale. This scale is used to simulate the flow into and around two types of helicopter intake. The intake geometries are simplified, being composed of flat plates rather than aerodynamically profiled inlets, and are represented in two dimensions. One objective of the intake scale results is to examine whether there is any advantage or disadvantage induced by the installed filter on intake performance. Another objective is to investigate the distribution of particles across the filter at different flow conditions. This is achieved by first solving the continuous flow field, then injecting particles into the domain, whose motion is subsequently determined by solving the equations of motion as a response to the continuum flow field.

In isolation, the results generated from the two scales afford useful conclusions about pleat performance and intake performance. However the results can also be combined to give a picture of the overall IBF performance. The pressure loss as a function of mass from the pleat scale results can be married with local dust mass flow rate found from the intake scale results, to build a temporal characteristic for a given IBF design. This is investigated in Section 6.4.

Chapter 5

Results & Discussion

This chapter presents the results from the investigation into IBF performance. The investigation was split into three scales to facilitate this investigation. Where computational fluid dynamics is employed, the flow features and parametric study results are discussed; where analytical models are applied, the myriad of performance permutations are explored for the key design parameters.

5.1 Introduction

The absence of research into inlet barrier filters in the literature prompted a full investigation into the effect of design and operational parameters on IBF performance. In contrast to the other EAPS technology, there was very little technical data upon which to perform a comparative study of the EAPS devices, which is the ultimate goal of the present work. On further investigation into IBF function, it was decided that the parametric study should take place on three levels, in order to facilitate easier analysis of the wide range of lengthscales. This chapter presents the main findings from the three scales, and discusses their importance with respect to IBF-installed intake performance.

5.2 Fabric Filter Scale

The theory of separation efficiency and pressure drop for IBF filters presented in Section 3.3, introduced several parameters that can be tailored to produce a high performance filtration medium. While very little is known about the medium used for IBF, it is possible to apply this theory to variable ranges to ascertain the sensitivity of certain design parameters. The following presents the results of a brief parametric study performed to investigate the effects of varying properties of the filter medium. The filter is idealised as a planar fibrous medium (i.e. without pleats), with a uniform fibre diameter and packing fraction. The numerous filter performance prediction equations given in Section 3.3 are used to carry out this parametric study.

5.2.1 Internal Fabric Parameters

In the present work, the internal parameters of the fabric refer to the packing fraction and the fibre diameter, however a more in-depth study may investigate the layer sequencing, the arrangement of the fibres, the size distribution of the fibres, and the homogeneity of the porosity. Figure 5.1 shows the effect of altering the fibre diameter on the grade efficiency (separation efficiency over a range of diameters, expressed here as Stokes number) and the pressure drop. The Stokes number of a given particle is inversely proportional to the fibre diameter (see Equation 3.82); from Figure 5.1a it is clear that the grade efficiency is sensitive to changes in fibre diameter, improving with a decrease in diameter. This is due to the formulation for inertial impaction efficiency given by Equation 3.87. The improvement offered by decreasing the fibre diameter is compromised by an increase in the viscous resistance hence pressure drop, which scales with fibre diameter squared according to Equation 3.57.

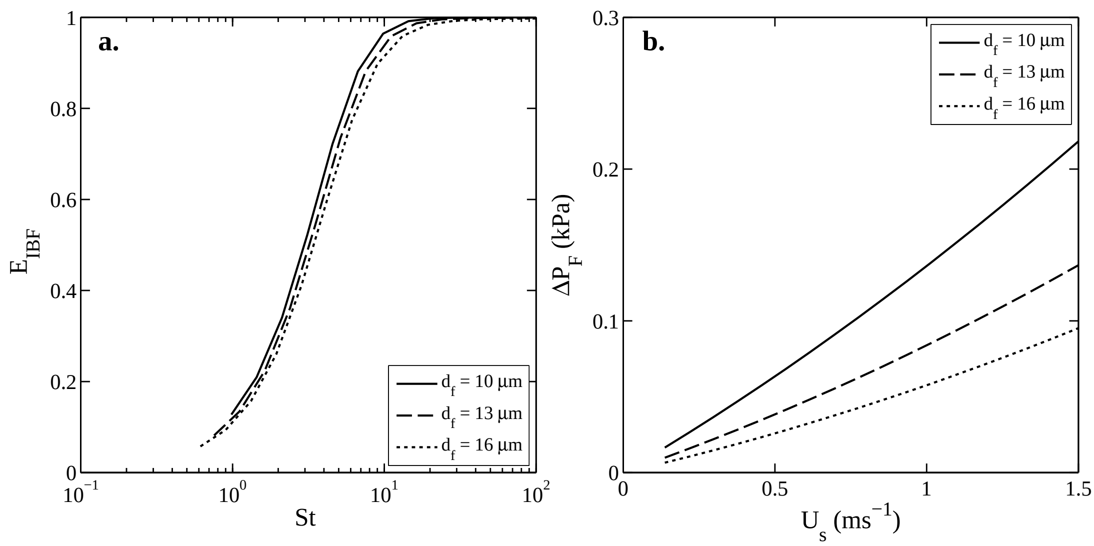

Figure 5.1: *The effect of Stokes number and filtration velocity for three filter fibre diameters on: a. grade efficiency; b. pressure drop. (α = 0.05).*

Fibrous filters usually have a packing fraction of no greater than 10%. Figure 5.2b illustrates that increasing the packing fraction by just 4% can triple the pressure drop across the fibrous mat. As always it is a battle of compromises: the same increase in packing fraction can remove 18% more of the smallest particles, which can sometimes be the most harmful to engines if they breach the filter and manage to reach the turbine blade cooling passages, hence it may be worthwhile sacrificing pressure loss for the benefit of prolonging engine life.

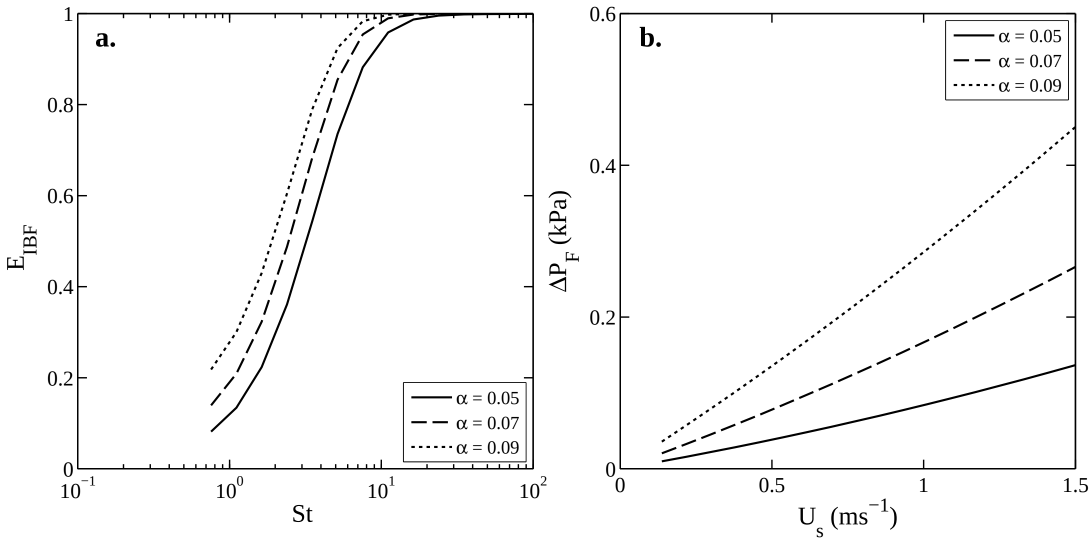

Figure 5.2: *The effect of Stokes number and filtration velocity for three filter packing fractions on: a. grade efficiency; b. pressure drop. (d_f = 13 μm).*

5.2.2 External Fabric Parameters

The external fabric parameters concern the outer filter dimensions, namely the fibrous mat thickness and if the filter is pleated, the depth and fold angle of the filter pleats. Additional parameters not investigated in the present study are the properties of the wire mesh that sandwiches the filter medium and retains the pleat shape. The concept of the pleat is virtual at this scale; it is known that pleating introduces a secondary source of pressure loss, and this is investigated at the pleat scale. At the fabric scale the only effect of pleating considered is its effect on the filtration velocity, which is seen to decrease with decreasing pleat angle. The superficial velocity may also be decreased by increasing the pleat depth.

The effect of modifying these parameters is shown in Figures 5.3 and 5.4. In the former, the effect of increasing pleat depth is to slightly diminish the grade efficiency due to a drop in superficial velocity. The same reduction in velocity however leads to a non-negligible drop in pressure loss, although the reduction rate appears to lessen with increasing depth. A similar phenomenon is observed when the pleat angle is changed — a very marginal decrease in grade efficiency, approximately 3%, but a saving of around 50 Pa pressure loss for a decrease of 2 degrees pleat angle. However, this is an idealised situation. In practice, in addition to the secondary loss of pressure loss in the resulting channels, the fluid streamlines are likely to be affected by the process of pleating the filter, which will influence the particle trajectories. This is investigated in the foregoing chapters.

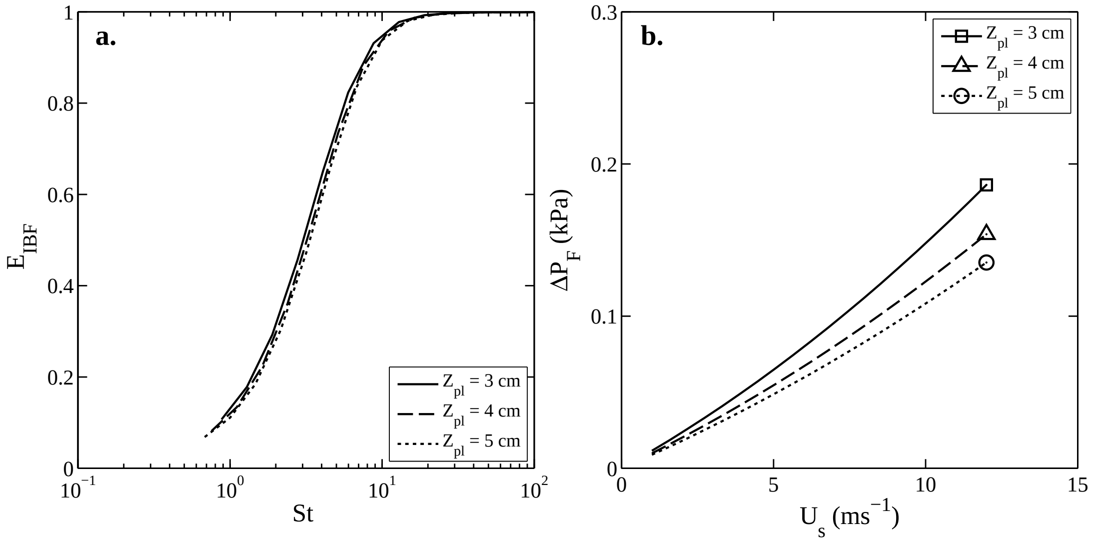

Figure 5.3: *The effect of Stokes number and filtration velocity for three planar medium thicknesses on: a. grade efficiency; b. pressure drop. (θ_{pl} = 4 degrees, d_f = 13 μm, α = 0.05).*

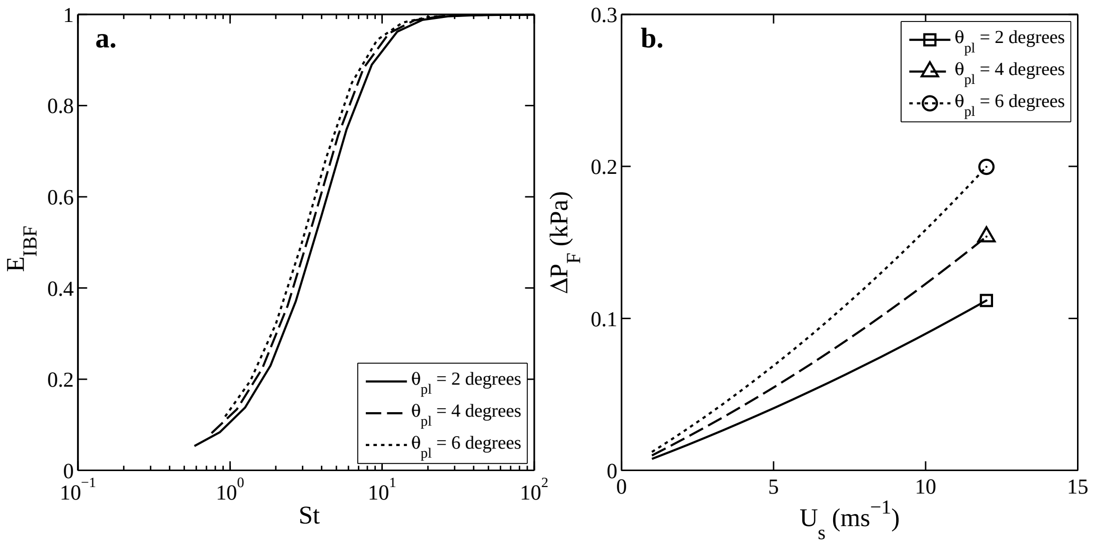

Figure 5.4: *The effect of Stokes number and filtration velocity for three virtual pleat angles on: a. grade efficiency; b. pressure drop. (θ_{pl} = 4 degrees, d_f = 13 μm, α = 0.05).*

The multitude of variable parameters, only a few of which have been discussed in this section, gives rise to an opportunity for filter medium optimisation. A filter of smaller fibre diameters may be capable of capturing smaller particles, but at the cost of an elevated pressure loss. Ultimately a filter medium must be chosen that will perform best in its intended environment of operation, or for a target particle size. Of course, this task is made more difficult in extension to helicopter particle filtration, since the particulate of interest contains a range of particle sizes. However, scope for optimum performance is present, and represents a possible area of future work.

5.3 Pleat Scale

The flow through the folds of a pleated filter has been studied by several authors in the past. In Section 2.5.3 the compromise of pleating was discussed, in which the the benefit of the reduction of filtration velocity that decreases filter medium pressure loss is increasingly nullified by fluid shear stresses caused by contraction within the pleat channels. The phenomenon leads to an optimum design point for a given flow condition, which will be discussed in the foregoing sections. Much of the previous research performed in the past on pleated filters is case-specific, often using simplified domains. There are currently no computational studies on inlet barrier filter design in the open literature, and much of the information relating to IBF has been derived from international patents and a couple of conference papers. The current work aims to generate data from CFD solutions of flow through pleats of varying dimension, in varying flow conditions. During the investigation into IBF pleat design, it was found that there is a wide spectrum of parameters that govern IBF performance, with each parameter possessing the potential for tuning for optimum design. However, due to various constraints, it is not possible to test all parameters and ultimately some assumptions have had to be made. Of all the parameters, properties of the filter medium are the most difficult to obtain, as these data are often proprietary. Instead, values are assumed from real filter fabrics tested in the literature, from one study in particular (Ref. [52]) which analysed filters for automotive applications. For the pleat scale study, the values relating to the filter medium are mostly fixed, although a brief insight into their effect is provided here. The following presents the results of a parametric study of the effects of pleat sizing, the optimum design point, and the influence of flow conditions and sand properties on pleat performance.

5.3.1 Flow Analysis

The effect of increasing the number of pleat folds per unit length of span is shown in Figure 5.5. It is clear that decreasing the pleat angle increases the degree of flow contraction, which is indicated by the bunching of streamlines and the red areas of faster flow in Figures 5.5d and 5.5e. The blue areas indicate slow flow, especially through the filter medium, in which the prescribed porous zone condition performs the

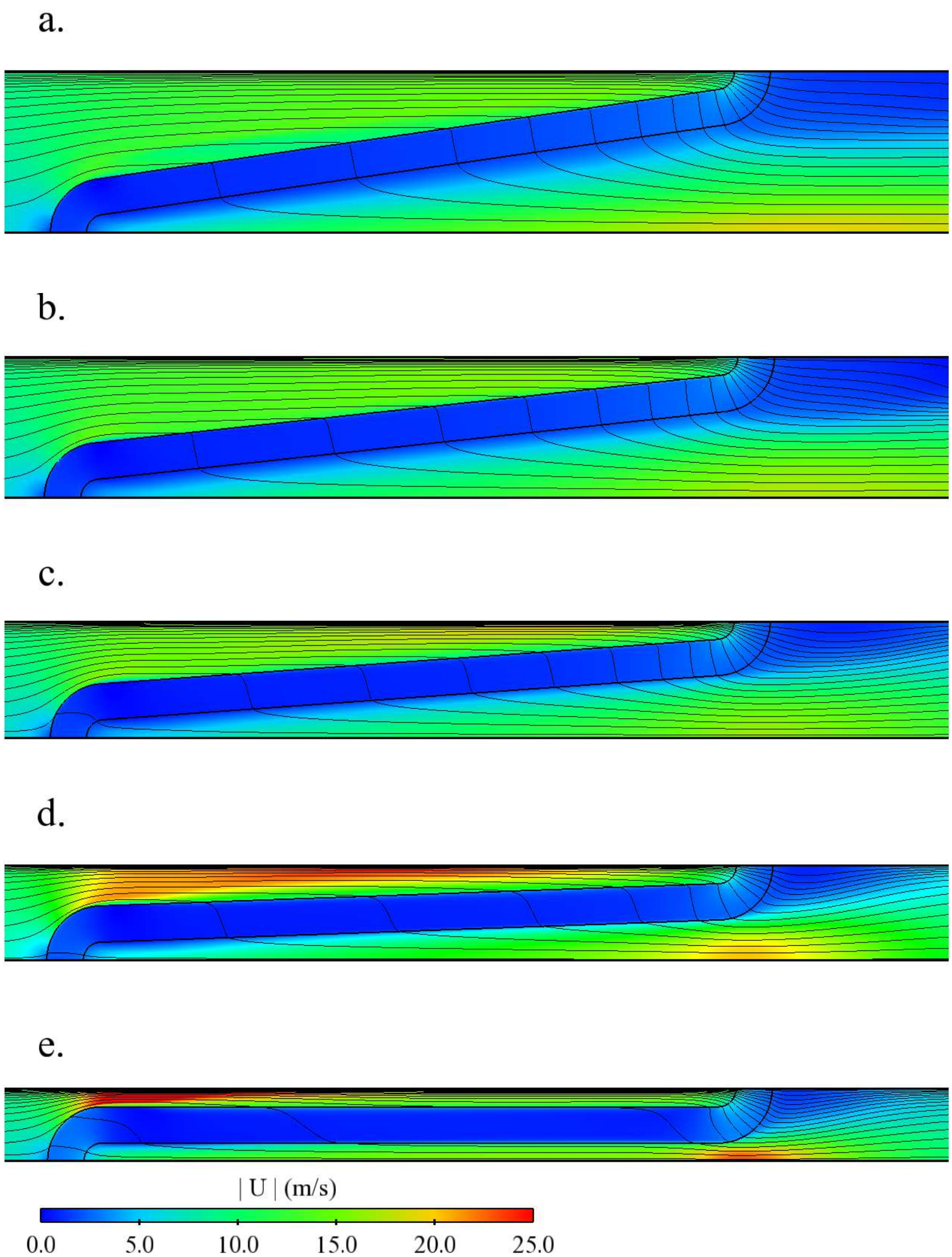

Figure 5.5: *Contours of velocity magnitude and flow streamlines through half-pleat sections of the following angles, with initial flow velocity of 8 m/s through a pleat of depth 3 cm: a. 8 degrees; b. 6 degrees; c. 4 degrees; d. 2 degrees; e. 0 degrees.*

task of removing momentum from the flow, to simulate resistance. In reality, locally, the fluid is fast flowing through the pores of the medium, losing energy to friction and separation, but it appears here as a superficial velocity. The superficial velocity is much lower than the approach velocity because the volume flow is spread over the entire frontal surface area of the pleat.

At large pleat angles, the flow through the medium is generally perpendicular to the surface of the pleat as shown for the case of 8 degrees in Figure 5.5a. However as the pleat angle decreases, the degree of orthogonality weakens. This is indicative of a more uniformly-streamwise pressure gradient: it can be inferred from the case of 0 degrees at Figure 5.5e that the velocity through the front fold of the pleat is larger than its counterparts, since the flow is being squeezed through an ever-tightening gap. This distorts the fluid streamlines and actually increases the flow path length at the mid-section of the pleat. From a filtration point of view this is advantageous, as the probability of particle capture is increased.

Also evident is the expansion of flow back to the inlet condition. This is not initially uniform across the pleat span, and the non-uniformity extends further downstream for pleats of larger angle — under these initial flow conditions the flow velocity equalises at around $2Z_{pl}$ downstream for an angle of 8 degrees, which is in contrast to the case of 2 degrees in which the flow stabilises at around $0.5Z_{pl}$. From this it can be ascertained that the disturbance to the flow path imposed by the pleat on the fluid is not significant enough to cause downstream problems, since the engine inlet face will be positioned much further downstream of the filter (see Figure 2.14).

The flow acceleration in the pleat channels creates shear layers within the flow, akin to a boundary layer. If the velocity gradients are large, the loss to viscous shearing becomes a source of total pressure loss. This is depicted in Figure 5.6, which shows total pressure contours (expressed as a gauge pressure by the atmospheric pressure) and fluid strain rate. For Newtonian fluids such as air, the strain rate is directly proportional to shear stress, hence acts as a good marker for areas of total pressure loss. It can be seen from Figure 5.6b that the strain rate closely matches areas of high velocity gradient in Figure 5.5d, and results in the sharp drop in total pressure in the same area in Figure 5.6a.

Since the velocity distribution ultimately determines the pleat channel pressure loss, it is usually the focus of any studies in the literature that attempts to derive analytical or semi-analytical predictions of pleated filter pressure loss. This is discussed further in Section 2.5.3. Such derivations often require approximations as to the shape of the velocity profiles of low Reynolds number laminar flow through pleat channels that are often rectangular in shape, for simplicity. The slightly more complex, semi-analytical model proposed by Rebaï *et al.* [51] for higher Reynolds number (but still

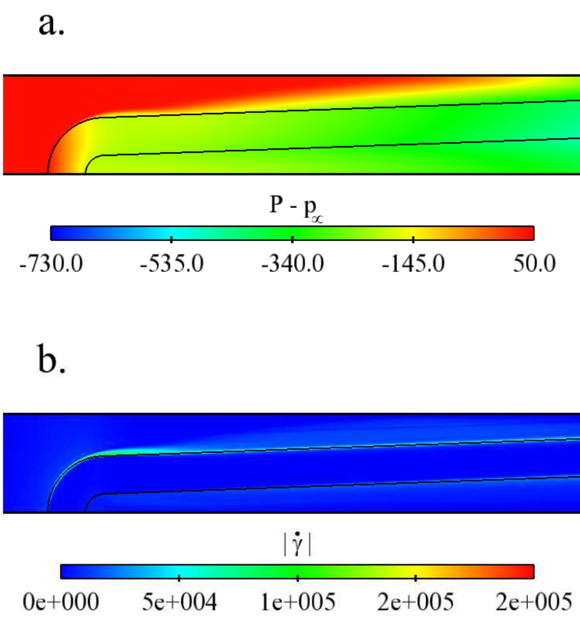

Figure 5.6: *Illustration of the causes of pressure loss in the pleat channels, as indicated by contour plots of: a. total pressure contours; b. strain rate magnitude.*

laminar) flows relies on the assumption that the velocity profiles resemble the shape of turbulent boundary layer, allowing their solution through similarity. The present study is conducted at higher Reynolds number flow prescribed with a level of turbulence to more closely match the real situation. An analysis of the applicability of Rebaï's model can be made by examining the pleat channel velocity profiles from the current work.

To carry out the examination, spanwise cuts are taken at 9 streamwise locations along the length of the pleat. These are shown in Figure 5.7. The letters under each cut are references for the plots given in Figure 5.8, which superimposes the streamwise velocity component at each location for two pleats of differing pleat angle. Dimensions are normalised to facilitate comparison. There are clear differences between the two pleat angles, although some can be attributed to a misalignment of the boundary layers — the filter medium's upstream and downstream surfaces appear at different spanwise locations for the same streamwise location; the filter medium region in each plot is indicated by the almost zero value of streamwise velocity. In Figure 5.8a both pleats exhibit a flow deceleration ($u/U < 1$) at the bottom, and an acceleration towards the top, but the wider pleat profile is flatter for a greater proportion of the channel width. This trend is evident at almost all locations along the pleat length. A flatter profile more closely resembles the assumption made by Rebaï *et al.*, but is not present at all streamwise locations, and cannot be applied for the smaller angle pleats.

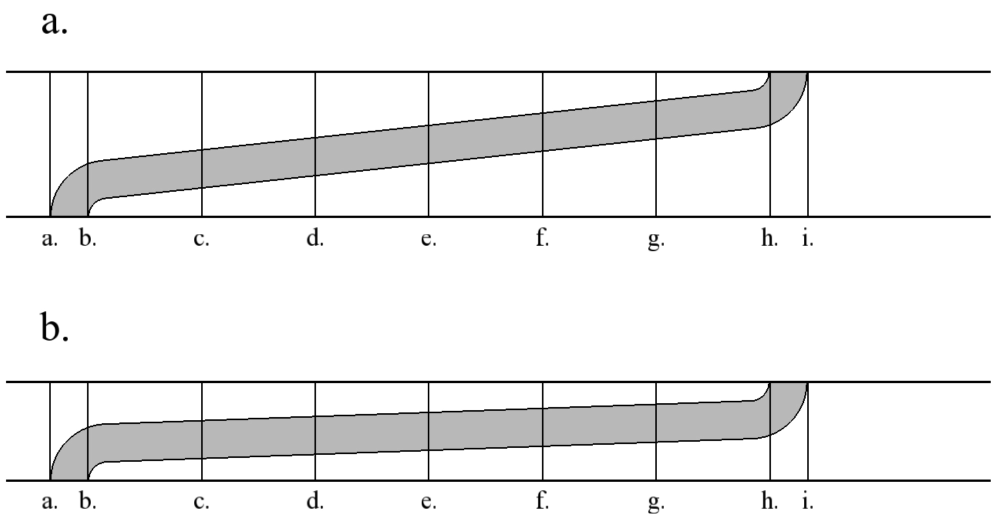

Figure 5.7: *Streamwise cuts for velocity profile sampling of half-pleats with pleat angles of: a. 6 degrees; b. 2 degrees.*

In the downstream channel the velocity profiles do not resemble flat, turbulent boundary layer profiles. These are most clear in Figures 5.8g to 5.8i. For the 2 degree case the profiles seem perfectly parabolic; at higher pleat angles the streamwise velocity tends to a linear relationship with span. This is in contrast to the approximation, but may provide scope for future development of a semi-analytical model for pleats of this nature. However, the non-conformity of the upstream channel profiles to a common shape may hinder development. Indeed at the streamwise location "b", the profile reflects the large local acceleration of flow due to contraction; at this region the velocity profiles might be more difficult to predict with an analytical model, which is particularly pertinent when one considers that this is the principle source of channel pressure loss.

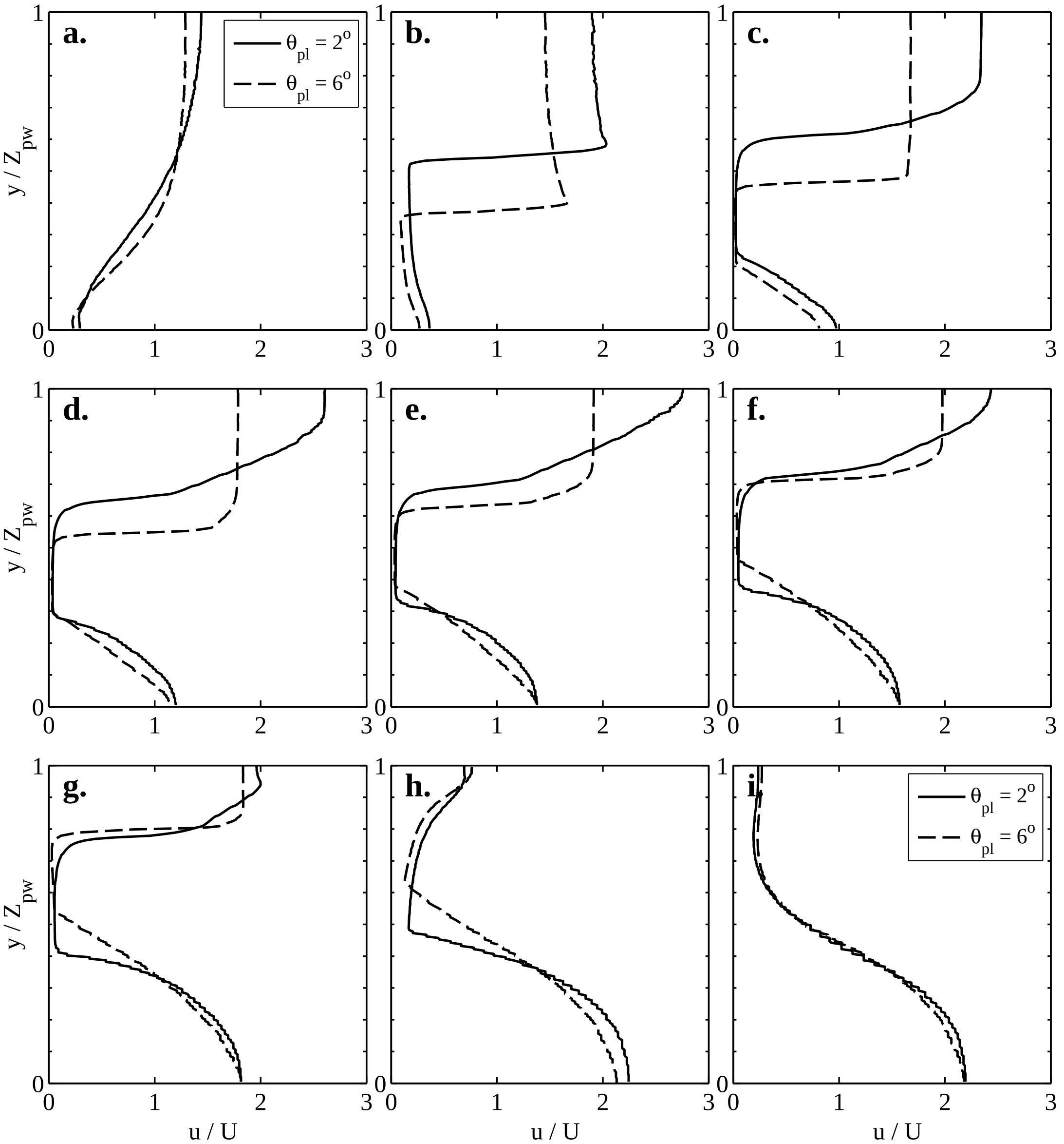

Figure 5.8: *Comparison of x-velocity profiles of two pleat angles at streamwise locations of* $x/Z_{pl} =$ *: a. 0.0; b. 0.05; c. 0.2; d. 0.35; e. 0.5; f. 0.65; g. 0.8; h. 0.95 i. 1.0.*

5.3.2 Geometry Effects

As a point of context, an insight into the quantitative effect of varying geometrical parameters of the pleat is provided. It has been discussed throughout that increasing the filter surface area by pleating benefits the filtration process. Figure 5.9a shows the increase in filter surface area per unit of projected area across the range of pleat dimensions tested in the present work. A four or fivefold increase in surface area can be achieved with a pleat angle of just 10 degrees, which will result in a filtration velocity reduced by the same amount. This translates to a much lower filter medium pressure loss. As filter angle decreases, the area is increased further still, and the gap between pleats of different depth widens. The patent that provides the most information on pleat design (Ref. [40]) states that pleating is performed to achieve a roughly sixfold increase in surface area. Figure 5.9a suggest, therefore, that the chosen pleat angle would be around 4 - 6 degrees. This provides a reference point for the present study.

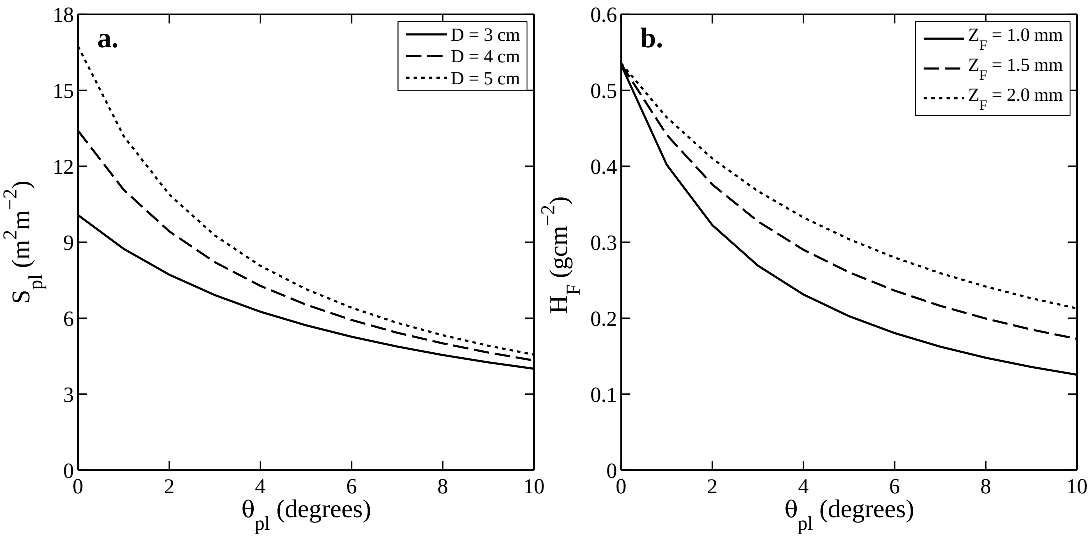

Figure 5.9: *Effect of pleat geometrical parameters on key performance parameters of: a. filter surface area per unit projected area (constant thickness of 1.5 mm); b. filter medium particulate mass capacity per unit projected area (constant depth of 4 cm).*

Figure 5.9b shows the effect of pleat angle on the holding capacity of the filter medium for three filter thicknesses. Since holding capacity is related to the total volume of the filter per unit projected area, it follows that the relationship resembles that of specific surface area. A large holding capacity is desired to delay the onset of the cake accumulation stage, in which the pressure drop generally grows faster per unit mass collected than during the filter medium clogging stage. The improvement offered by increasing the filter thickness appears to diminish with decreasing filter angle, but for a pleat angle of 4 degrees, the time sustained in a brownout cloud before cake buildup occurs can be lengthened by 44% by simply doubling the filter thickness from 1.0 mm to 2.0 mm.

5.3.3 Pleat Performance

The two pressure loss sources have been described quantitatively and analytically, but to understand how the optimum design point is established, it is useful to illustrate graphically a breakdown of the pressure loss contributions. Figure 5.10 shows the filter medium pressure loss and pleat channel pressure loss as functions of the pleat angle at two filter states. In both plots the contrasting consequences of decreasing the pleat angle is shown. The slope of the channel pressure loss curve steepens at a greater rate than the filter medium, a fact that becomes important when considering the two clogging stages. Figure 5.10b shows the loss contributions at filter capacity. At this stage the filter medium has a much higher resistance to the flow, as evidenced by the elevated curve. The plot also implies that pleats of larger angle behave worse if the initial permeability of the medium were lower. One reason for increasing the permeability would be to improve the capture efficiency of the filter; a conclusion to draw is that the optimum pleat angle for minimum pressure drop decreases with decreasing filter permeability.

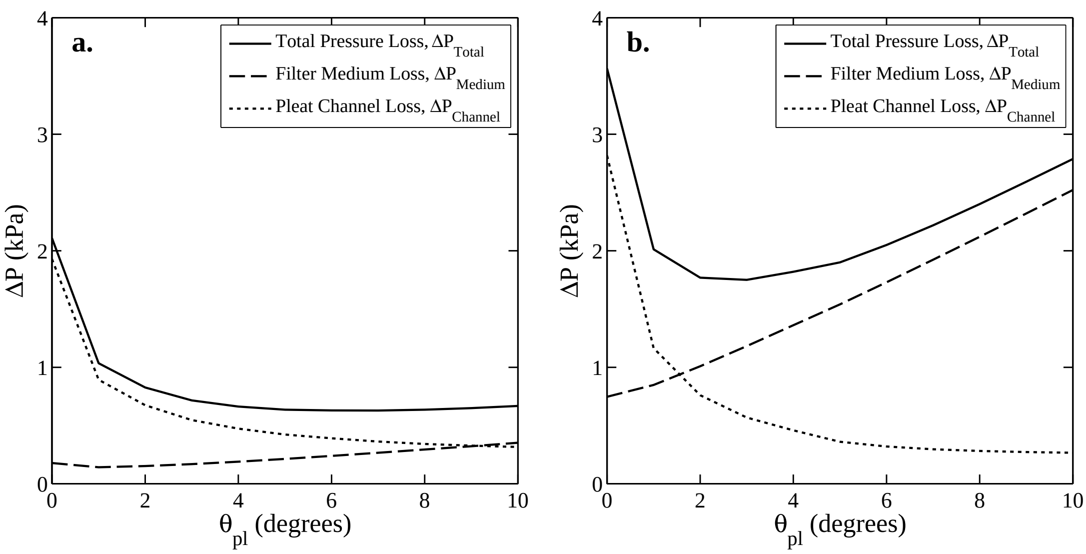

Figure 5.10: *Sources of pressure loss across a filter pleat (Z_{pl} = 5 cm, AC Fine test dust, U_∞ = 12 m/s), showing characteristic U-shape curve and contributions from filter medium and pleat channels, for: a. clean filter (Δm_{pc} = 0); b. clogged filter ($\Delta m_{pc} = M_{FC}$).*

The effect of rising medium permeability also appears to affect the flow in the pleat channel, which is elevated in Figure 5.10b, especially at small pleat angles. This is because a larger proportion of flow is forced further into the pleat channels as it meets greater resistance at the filter medium. The contribution of the channel loss increases further when the cake begins to form, but this is accompanied by the additional resistance offered by the accumulating particles. From the discussion, and the two total pressure loss curves presented here, it is clear to see that the optimum design point is highly dependent on the flow conditions and filter properties.

Another filter parameter that affects the performance is the pleat depth. Figure 5.11 shows the effect of increasing the depth of three pleats of varying angles, for two filter states (analogous to two initial filter permeabilities). In all cases, the effect is to decrease the pressure drop, although a lack of data for depths of beyond 5 cm hinders conclusions. In fact, the 2 degrees curve in Figure 5.11b appears to level out at $Z_{pl} = 5$ cm, suggesting it may have reached a minimum. At large pleat angles, the effect of increasing the pleat depth is small as suggested by the almost flat gradient. This is because the pleat width scales with pleat depth: as depth is increased, the pleat density decreases, which would ordinarily lead to increased superficial filtration velocity but for the additional surface area across which the volume flow is spread. One consideration which is not considered here is the system weight. Figure 5.11 suggests that there is only a benefit to increasing pleat depth. However, when the weight of the filter panel is considered, and indeed the space constraints, it may well be sufficient to cap the filter depth at a value beyond which improvement to the pressure loss is negligible for all pleat angles. For the pleats in this example, this is approximately 4 cm for both the clean and clogged cases.

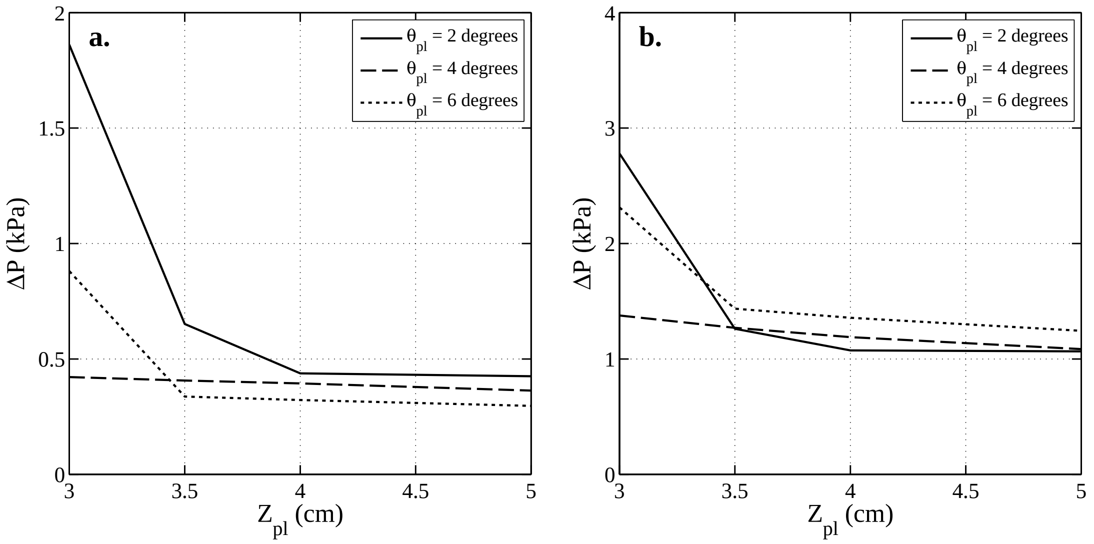

Figure 5.11: *The effect of pleat depth on the pressure drop across 3 pleats of different pleat angle in a flow of 8 m/s, for: a. clean filter ($\Delta m_{pc} = 0$); b. clogged filter ($\Delta m_{pc} = M_{FC}$).*

The transiency of the pressure drop across an IBF has been discussed throughout the current work. The numerous parameters that define this temporal characteristic have also been identified. The results obtained in the pleat scale parametric study permit an investigation into the effect of altering certain pleat properties on the pressure drop evolution, which can also be studied. In Figure 5.12, the pressure drop as a function of mass collected is given for three pleat depths at a fixed pleat angle, and three pleat angles at a fixed pleat depth. The "elbow" in each curve represents the transition from the filter medium clogging stage to the cake accumulation stage. This shape is consistent with the literature on clogging of planar media; both stages exhibit a linear relationship between collected mass and pressure drop. The cake accumulation stage is identified by a much steeper curve, highlighting the undesirable consequence of cake filtration.

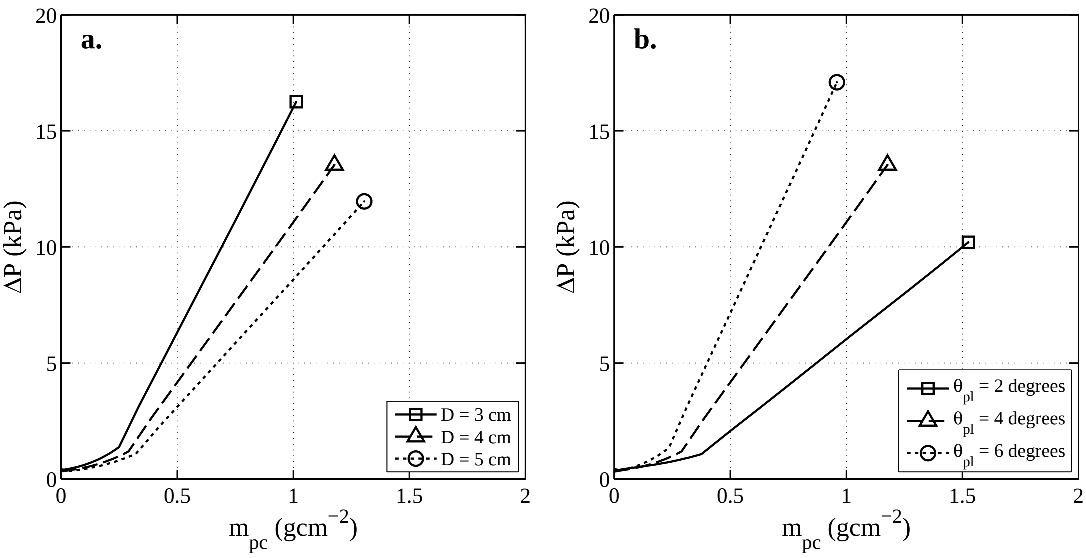

Figure 5.12: *Evolution of pressure loss as a function of mass of AC Fine test dust collected per square centimetre of projected filter area, across 3 filter pleats of varying: a. pleat depth (θ_{pl} = 4 degrees); b. pleat angle (Z_{pl} = 4 cm); while U_∞ = 8 m/s.*

There are noticeable differences between the curves. Firstly looking at Figure 5.12a, the effect of increasing pleat depth on holding capacity, as discussed above in Section 5.3.2, is to prolong the transition to cake accumulation by approximately 0.5 gcm^{-2} per centimetre of added depth. A similar benefit is realised in Figure 5.12b for a decrease in filter angle: narrowing the pleat angle by 4 degrees can double the filter medium clogging stage. To compare the overall temporal performance of each parameter, consider a limiting pressure drop of 3 kPa, which may be a maximum pressure loss permissible across an IBF imposed by the operator. When the pressure drop reaches this level, the filter would be removed and cleaned, or replaced. Figure 5.12a indicates that at this point a pleat of depth of 5 cm would have captured around 0.65 gcm^{-2}, which is in contrast to the pleat of depth of 4 cm, which would have captured 0.55 gcm^{-2}. Comparing pleat angles, the difference is greater still. The extra surface area offered by a pleat of angle of 2 degrees permits the capture of 0.85 gcm^{-2}, which is 0.3 gcm^{-2} more than a pleat angle of 4 degrees. A larger mass of particulate captured for the same pressure drop penalty decreases the number of wash cycles required, which translates to a saving in maintenance time.

Once in operation, the filter can be expected to experience a number of flow conditions and receive a range of particle sizes. Provision for anticipated conditions can be made at the design stage, but it is likely that the filter will have to work off-design during its lifetime. To illustrate the effect of these parameters, the pressure drop is plotted as a function of flow velocity for three clean pleated filter designs; and plotted as a function of collected mass for two flow velocities and two sand types. The result is shown in Figure 5.13. Figure 5.13a shows that a non-linear relationship exists between flow velocity and pressure loss, the slope of which can be alleviated by increasing the pleat angle. This suggests that the pleat channel pressure loss is more sensitive to changes in flow velocity than the medium pressure loss. This is supported by examination of the curves of same angle but contrasting depths, for which there is very little difference — since the angle remains constant, there is no change in the channel's shape.

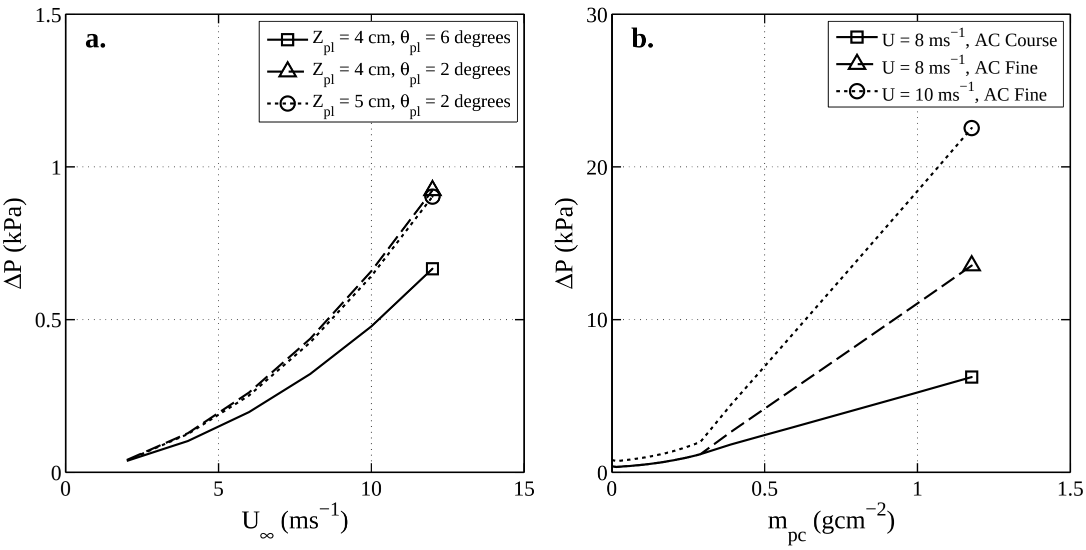

Figure 5.13: *Effect of two parameters that lead to off-design performance, showing a. influence of flow velocity on clean pressure drop for two pleat depths and two pleat angles; and b. pressure loss as a function of mass collected when filtering AC Fine and AC Course dust, at two flow velocities.*

In Figure 5.13b, the temporal pressure drop is shown to be affected by sand type in only the cake accumulation stage. This is not a phenomenological effect but a consequence of the modelling procedure. In the simulations the filter medium porosity is decreased as a function of mass collected (which translates to a rise in resistance), but no provision is made for the size of the particles. In reality is it likely that the medium clogging stage will exhibit differing trends between sand types, as particles of different size collect at different locations within the medium yielding a non-uniform solidosity. The effect of uniformity of solidosity on pressure drop is not investigated here, however if a homogeneous porous matrix is assumed, the temporal rate at which the solidosity increases can be found for each sand type, based on the temporally-variant separation efficiency. This is investigated in later sections.

During the cake accumulation stage, the rate of increase of pressure loss is approximately halved, when composed of the larger-grained AC Course test dust ($\bar{d}_{p,3} = 28.4\mu$m, $\sigma = 3.7$) rather than the AC Fine test dust ($\bar{d}_{p,3} = 8.8\mu$m, $\sigma = 3.9$). Since the properties of the brownout dust will vary from one area of operation to the next, it may be difficult to accurately predict the temporal pressure drop rise. Figure 5.13b also highlights the importance of the volume flow rate through the filter's projected area. Suppose the accepted pressure drop limit is 10 kPa, the results show that increasing the IBF projected area by 20% (hence reducing the flow velocity) increases the length of a filter cycle by as much as 46%. This again highlights the importance of optimised IBF design.

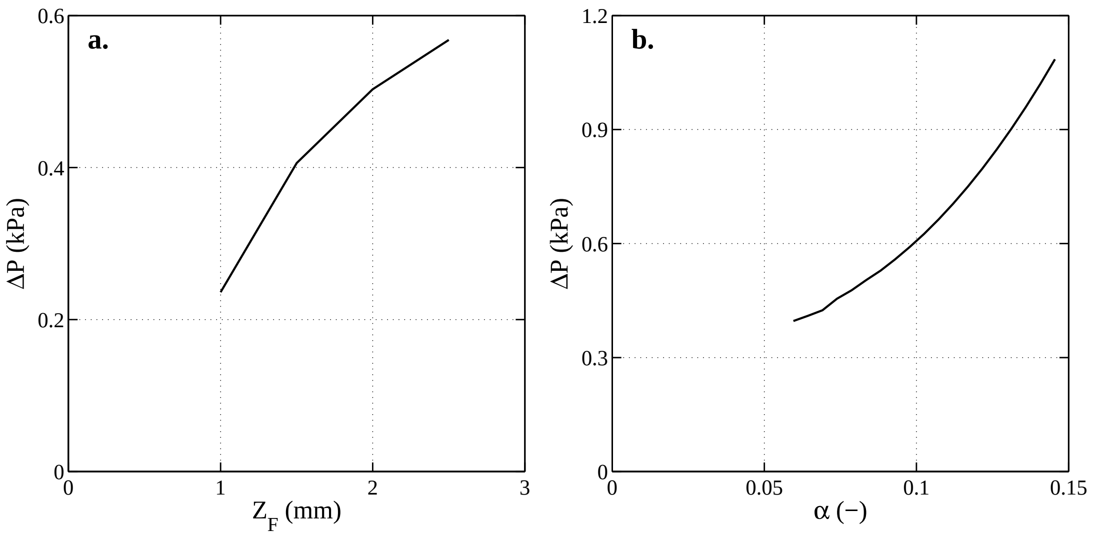

Figure 5.14: *Effect of filter medium properties on clean filter pressure drop for single pleat ($\theta = 3$ degrees, $Z_{pl} = 4$ cm, $U = 8$ m/s) showing: a. influence of medium thickness; b. influence of medium packing fraction (hence permeability).*

For completeness, the parametric study is finished with a brief insight into the effects of two filter medium parameters. Figure 5.14 shows the response of the pressure drop to a change in filter thickness, and a change in filter packing fraction. The former may be enacted at the design stage to increase the holding capacity (as discussed in Section 5.3.2), while the latter can improve the separation efficiency, as shown in Figure 5.2. In this section it was discussed that the time delay in the onset of cake accumulation can be increased by 44% by doubling the thickness from 1 mm to 2 mm; in Figure 5.14a the compromise is a more than doubling of clean filter pressure loss. A similar compromise is inferred from Figure 5.14b when increasing the filter medium packing fraction, α.

5.3.4 Optimum Design Point

The multifarious parameters that decide the performance of a pleated filter for IBF can be used to optimise design. Gathering together all parameters discussed thus far, the data are used to establish the optimum pleat angle for minimum initial pressure drop and maximum filter cycle time. The maximum filter cycle time is expressed in terms of mass collected. Since the flow rate of particles reaching the filter is likely to vary throughout the life cycle, it is more appropriate to express the endurance in this way. The pleat scale results yielded trends for each parametric case of pressure drop as a function of mass collected. A filter cycle is "complete" upon reaching a maximum pressure drop level (although in practice the filters are more often withdrawn prematurely) that is considered significantly detrimental to engine performance. A typical value is 3 kPa, which translates to a total pressure loss of around 3% in hover. By matching this level on each trendline with the mass collected, it is possible to compare each case based on their mass capture capability. While minimum initial pressure drop on installation is important, it may be more advantageous from a mission perspective to prolong the clogging. For such pleat designs of good holding capacity the maintenance time is reduced, and the power available diminishes at a slower rate. The pilot may have to cope initially with a larger shortfall in power, but will not experience such a steep drop off.

Figure 5.15a shows the optimum pleat angle for minimum pressure loss across the clean filter. The trend lines are 5th order polynomial fits to the data generated from the parametric study. Owing to the relatively low filter medium permeability assumed, the effect of increasing pleat angle appears to be minimal beyond a pleat angle of 5 degrees. Interestingly, this corresponds to a pleat shape that offers a sixfold increase in surface area (according to Figure 5.9, which matches the design proposed in Scimone's patent (Ref. [41]). A more pronounced "U-shape" would be in evidence if the filter medium were thicker, or the permeability were lower (as in Figure 5.10b). From these data, there is no visible difference to the optimum design point for pleats of different depth, in flows of contrasting velocity. This is useful to know from a design point of view: throughout its lifetime the filter can be expected to experience flows of varying velocity magnitude; since the optimum point does not vary considerably with velocity, the filter will be performing at peak performance across a range of engine mass flow rates.

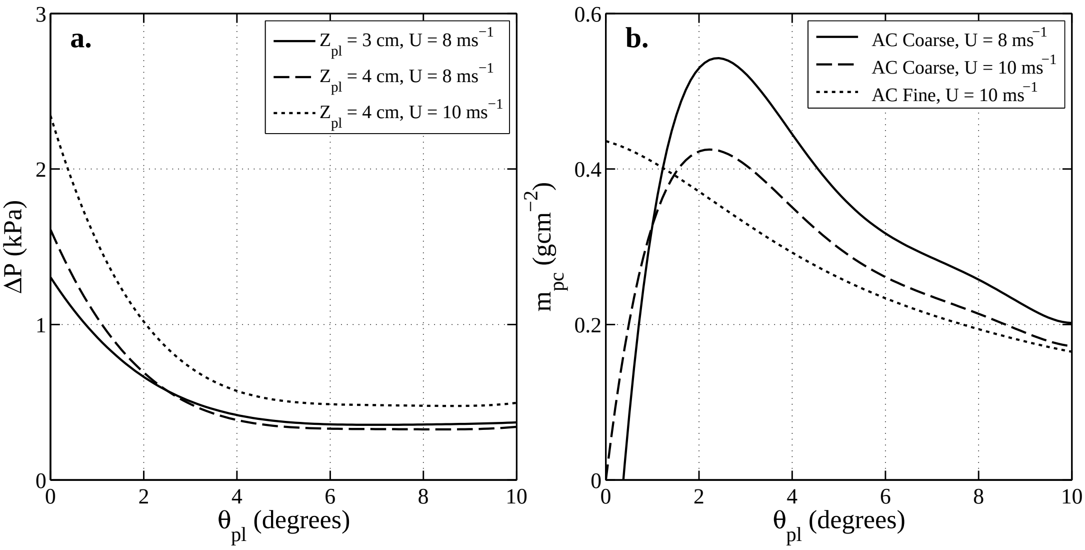

Figure 5.15: *Optimum pleat angle for three pleat depths and a flow velocity of $U = 12$ m/s, for two design criteria: a. minimum clean filter pressure drop; b. maximum mass of AC Course test dust collected at $\Delta P_{IBF} = 3$ kPa.*

In contrast, Figure 5.15b indicates that for maximum filter cycle lifetime, the pleat angle ought to be much narrower than the optimum angle for pressure drop. In similarity with the pressure drop results, there is not a great disparity between the optimum angle (approximately 2.5 degrees) for a flow of 8 m/s and a flow of 10 m/s, when AC Course test dust is being filtered. Notably however, the results confirm that a lower flow velocity allows a larger mass of particles to be captured at the optimum design point. For a flow of finer dust-laden air, it is advantageous to pack more pleats into the available projected area. In these conditions, with this filter, the optimum point is not instantly recognisable from the plot. In such a case the best design would be a pleat of 0 degrees angle.

By comparing the two plots in Figure 5.15, it becomes clear that there is a conflict in pleat design — does one design for minimum pressure drop of maximum endurance? The multitude of tailorable parameters creates a flexible and sometimes confusing array of options for design optimisation. However, the pleat scale parametric study provides abundant data to afford reliable qualitative analysis and the formation of an IBF design protocol, presented in Chapter 6.

5.4 Intake Scale

A simple parametric study is conducted to provide an insight into the effects of IBF installation on intake performance. The exercise is conducted in two dimensions for two types of intake domain: forward-facing and sideways-facing intakes. The latter shape also includes intakes that face upward, but for conciseness will be referred to as a "side-facing intake" hereon in. The intakes are constructed from straight thin plates: no attention has been paid to aerodynamic profiling to alleviate flow spillage (unintententional flow separation caused by an adverse pressure gradient). This approach is adopted to permit a simple, systematic parametric study, in which the principle geometrical parameter of filter angle is investigated. Hence it is anticipated that from an aerodynamics standpoint, the intake may perform unfavourably. Additionally, in order to satisfy computational solution conditions, the domain is extended far forward, backward, an outward to produce unrealistically long analogues for the airframe-intake approach (the surface leading up to an intake) and intake duct (the section extending from the airframe to the engine inlet). Following initial solution of the continuous phase, particles are injected into the domain and their trajectories tracked. Particle injections are also idealised: all particles of a certain size group are assumed to be evenly distributed along an injection plane, a highly improbable situation in reality. These simplifications nevertheless afford a less computationally-expensive insight into IBF performance at the "intake scale"; more robust analysis could be made in three dimensions, but the added complexity adds to the already long list of unknowns. By performing initial studies such as these, extension to three-dimensions can be made with a greater degree of engineering foresight, which may save computational cost.

5.4.1 Flow Feature Analysis

The analysis begins with a diagnosis of the intake capture streamtube. The capture streamtube is common to all intakes, and is bounded by the outermost streamline of flow entering the intake duct. It is visible in all parts of Figure 5.16, and is well described by Seddon in Chapter 1 of his book on Intake Aerodynamics [21]. The capture streamtube splits the flow ahead of the engine into two components: internal and external flow. It is important because it relates to the amount of air mass that is ingested by an engine, which is a critical parameter for calculating the engine thrust, or power delivered. The internal flow represents the portion of freestream air that enters the engine inlet duct, while the external passes around the intake and is associated with airframe drag. Assuming the engine mass flow rate remains constant (which is actually not true of helicopter engines throughout their flight regimes, due to a variation in shaft power demand), the capture streamtube will change shape. Since helicopters are sometimes

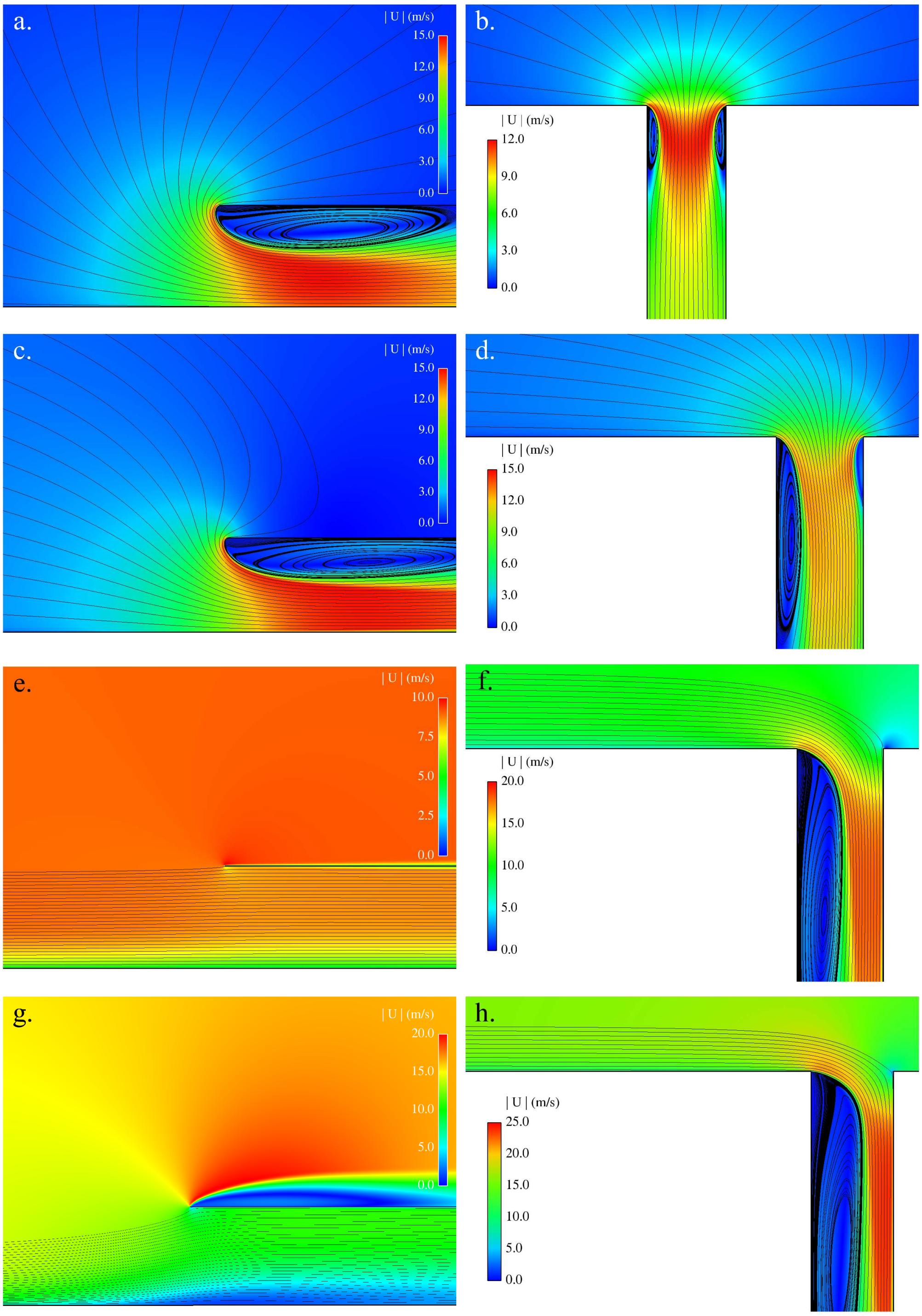

Figure 5.16: *Inlet capture streamtube shown by fluid streamlines and velocity plots for two intake types at four freestream velocities: a. forward-facing, hover; b. side-facing, hover; c. forward-facing,* $U_a/U_\infty \simeq 0.15$*; d. side-facing,* $U_a/U_\infty \simeq 0.15$*; e. forward-facing,* $U_a/U_\infty \simeq 1$*; f. side-facing,* $U_a/U_\infty \simeq 1$*; g. forward-facing,* $U_a/U_\infty \simeq 2$*; h. side-facing,* $U_a/U_\infty \simeq 2$*.*

in hover, there will be times during its operation in which the engine gathers air from all directions - this is illustrated for both intake types in Figures 5.16a and 5.16b.

The capture streamtube is important during a brownout cloud because it represents the flow catchment area of the intake. The concept of the "aerodynamic duct" is an analogue of the capture streamtube, and requires the assumption of incompressible flow, whereby the density of the fluid is considered constant which is true in low-speed, subsonic flows below Mach 0.3. It can be understood by analysing the transition from hover to forward flight of a forward-facing helicopter intake. During hover, the catchment area of an intake is large, which means that particles are drawn from a large area surrounding the intake. As the helicopter begins to transition to forward flight, the streamtube takes more of a duct-like shape and reduces in radius. At low forward speeds, when the freestream velocity is a smaller fraction than the engine volume flow rate per unit of face area (or engine face velocity), the streamtube has a larger radius than the intake duct. This is depicted in Figure 5.16c. As the freestream velocity reaches the same level as the engine face velocity, the intake is said to be operating at *full flow*: the streamtube radius is equal to the inlet radius. This is depicted in Figure 5.16e.

At speeds below the full-flow condition, an intake duct may experience a flow phenomenon known as "spillage", whereby air drawn into the duct cannot negotiate the sharp turn and consequently "separates" from the contours of the duct. This is illustrated by the large blue area, known as a *separation bubble*, shown in Figures 5.16a and 5.16c. Intakes that are expected to operate in low speed flight, such as helicopter intakes, are often profiled to ease the flow into the intake, in order to alleviate this source of pressure loss. A similar approach is required in the design of side or upward-facing intakes, as the same flow effect occurs to a worse degree, and at all flight speeds. This is evident in Figures 5.16b, 5.16d, 5.16f, and 5.16h. This is the principle reason why side-facing helicopter intakes perform worse than forward-facing intakes, as will be shown later. As the freestream velocity increases, the forward motion of the aircraft provides an excess of mass flow to the engine. The streamtube responds by narrowing in diameter: the concept of the aerodynamic duct observes conservation of mass; the mass flow at upstream infinity must be equal to the engine mass flow, hence if the freestream velocity is larger than the engine face velocity, the streamtube area must reduce. This is illustrated in Figure 5.16g. Incidentally, the principle is also applicable to side-facing intakes as shown in Figure 5.16h. The remainder of this chapter discusses why this is important for intake performance in brownout clouds, and ultimately how this may affect IBF design.

5.4.2 Unprotected Intake Performance

Before introducing the IBF into the intake, the performance of the unprotected intake is assessed. There are several metrics for measuring the performance of an intake, eloquently described once again by Seddon. To quantify the losses described qualitatively in Figure 5.16, the pressure loss due to friction is analysed across a range of flight speeds, from 0 to 30 knots, which represents the transition from hover to forward flight at twice the engine face velocity.

The breakdown of frictional losses is given in Figure 5.17. The calculation of each loss component (approach and duct loss) is made using Equations 4.22 and 4.23. The loss is normalised with the engine flow dynamic pressure, which is constant at all freestream velocities due to mass conservation. Since both intake types ingest boundary layer flow from the same surface, the approach loss curves are identical, and increase as a function of forward speed. The duct loss curves, however, are different. This can be attributed to the flow separation within the two intakes, which affects the local flow velocity — a theoretical intake would not contain separated flow. In particular, owing to the presence of the separation bubble the flow accelerates, causing greater amounts of shear stress with walls of the duct. It appears that the effect of lip spillage is greater for forward-facing intakes at hover and low speed than for side-facing intakes. This is consistent with Figures 5.16a and 5.16b. The lip spillage for side-facing intakes is smaller due to the flow being drawn from a less adverse angle. Since helicopters are often required to operate during hover, these results justify profiling the intake with a generally decreasing area in order to conform to the wide streamtube shape. The additional frictional losses during cruise (when power required is at less of a premium) from such a shape would be outweighed by the elimination of the spillage loss.

The comparison of spillage loss between the two intake types is best made by looking at the total pressure difference between the freestream and engine face, normalised with the constant duct dynamic pressure. The data are displayed in Figure 5.18a. For the forward-facing intake, the lip spillage loss falls with increasing forward speed, to a minimum at around $U_a/U_\infty = 1$. However, for the side-facing intake the trend is different. The lip spillage continues to increase with forward-speed due to the separation shown in Figures 5.16. For this simplified intake it exceeds the theoretical frictional losses almost sixfold at $U_a/U_\infty = 2$, and confirms why the side intake is the inferior performer at cruise conditions. Helicopter intake aerodynamicists may account for spillage in their designs, but it is more likely that attention will be paid to the hover and low flight conditions, as these are more power-critical situations. Therefore it is likely that a degree of lip separation will always be experienced by side intakes.

A final metric for assessing intake performance is to examine pressure recovery. This is an intake's ability to convert the available dynamic pressure to static pressure at the

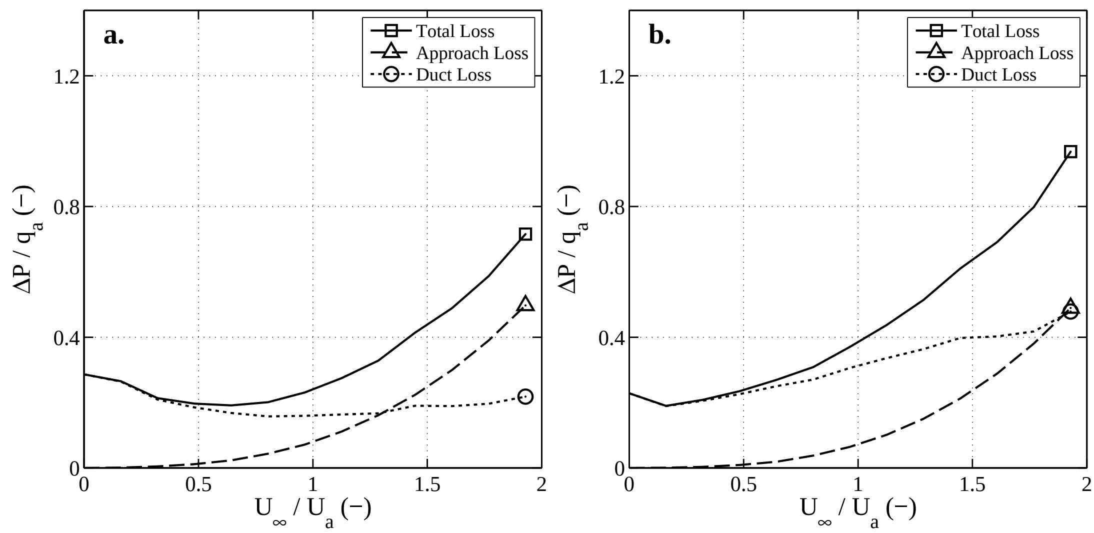

Figure 5.17: *Breakdown of the loss of pressure to friction between the capture stream-tube and walls of the intake for: a. forward-facing intake; b. side-facing intake.*

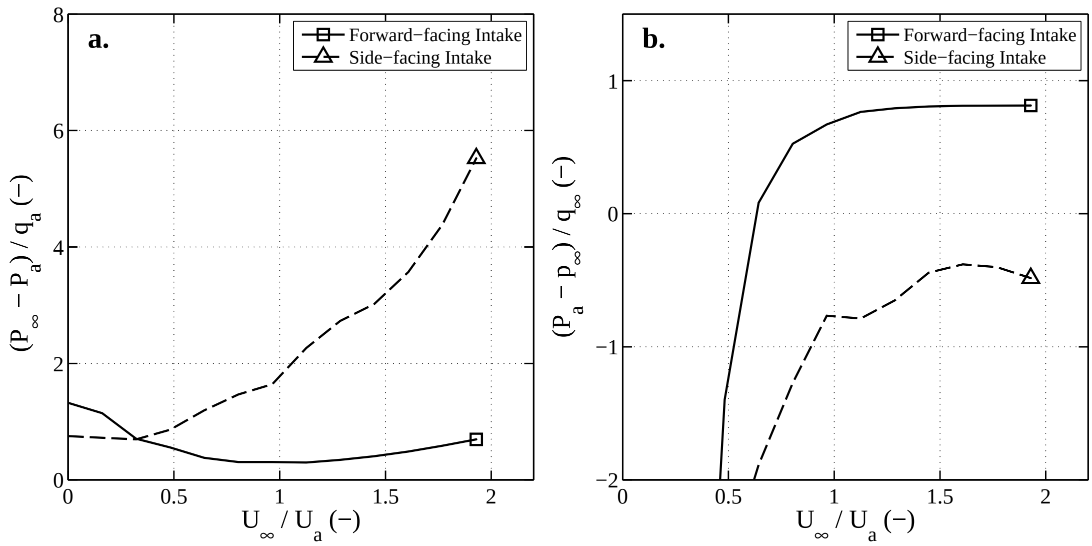

Figure 5.18: *Two metrics for assessing and comparing intake performance over a range of flight speeds: a. normalised total pressure loss; b. pressure recovery.*

engine face, which is beneficial to the engine. An ideal intake would have a pressure recovery of 1; in practice this is impossible to achieve when the intake is ingesting boundary layer air, as in the present study. Well-engineered pitot intakes, however, can get close. Seddon predicts a maximum pressure recovery of around 0.9 for forward-facing intakes at $U_a/U_\infty = 1.5$, a maximum of around 0.3 at the same forward speed for side-facing intakes. Figure 5.18b shows the pressure recovery characteristic of the intakes tested in the present study. In both cases the shape is as predicted by Seddon, although a lack of data does not confirm this beyond $U_a/U_\infty = 2$. The forward-facing intake reaches a maximum of around 0.8 at high forward speeds, however due to the large penalty sustained through lip spillage, the side-facing intake fails to achieve the levels quoted by Seddon. In fact, the pressure recovery never breaches zero, implying that energy is always required by the engine to achieve its required mass flow.

5.4.3 IBF-fitted Intake Performance

The performance of a helicopter intake fitted with an IBF is investigated for the case of forward-facing and side-facing inlets. The objective of the study is to ascertain the impact of the filter presence on the intake flowfield. The pressure loss across a filter is fixed for all designs in order to attribute any additional losses to skin friction or separation. One of the IBF design criteria is to minimise the superficial velocity through the filter, which is achieved by increasing the filter projected surface area. The setup described in Section 4.3.1 allows the surface area to be changed by orientating the filter at different angles to the flow.

The effect of filter angle in hover is examined. In this situation out of ground effect, the helicopter engine is running close to maximum power. In Figure 5.19 the filter angle for both intake types is shown for two filter states: clean (ΔP = 0.6 kPa) and clogged (ΔP = 3 kPa). The non-filter pressure losses are isolated by subtracting the prescribed filter pressure drops from the total pressure loss at the engine face. In both cases there is negligible variation in total pressure loss across the range of filter angles — a maximum of 0.01% increase from 0 degrees to 50 degrees is observed for the side intakes, which is very little when compared with the fraction of total pressure expended by the air through the filter ($\simeq$ 0.6% and $\simeq$ 3.0% for the clean and clogged states respectively). The non-filter losses are caused by friction with the walls and the creation of separation bubbles at the walls of the ducts, as illustrated in Figure 5.16a and 5.16b. In this respect, the side-facing intakes perform better than forward-facing intakes, and the clogged filter appears to alleviate the pressure loss, but the difference in real terms is negligible.

The non-uniformity of total pressure during low speed flight and hover can be inferred from Figure 5.16, in which there are regions of recirculating flow. To maintain

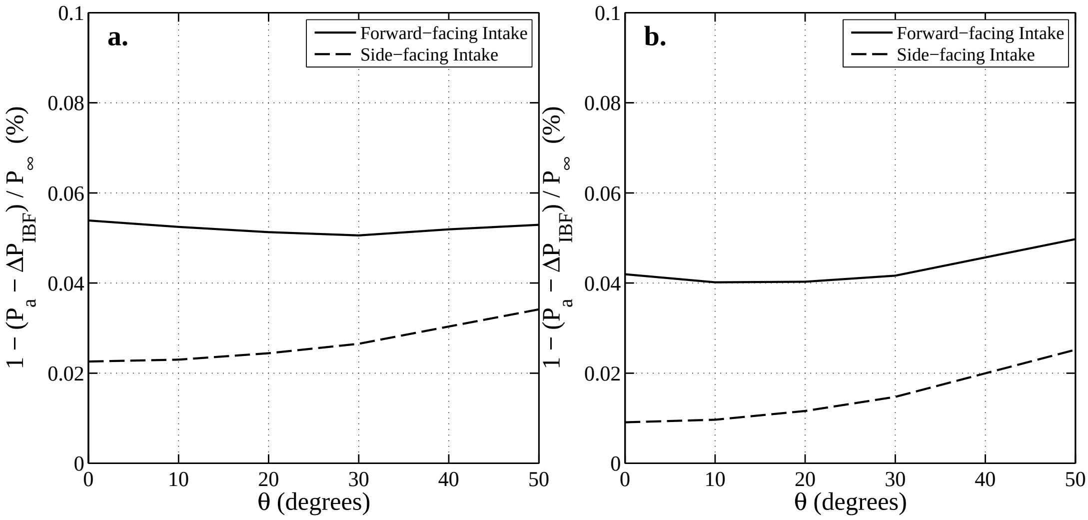

Figure 5.19: *Effect of filter orientation angle on total pressure loss during hover for two intake types when the pressure drop across the filter is prescribed as: a. 600 Pa; b. 3000 Pa.*

mass flow, the air must navigate these separation bubbles. The reduction in effective flow area causes an increase in local flow velocity, which can cause shearing of the fluid layers and additional pressure loss, while disturbing the flow uniformity. Taking spanwise cuts at various locations reveals the resultant inhomogeneity of the total pressure. Despite their power-related encumbrance, IBF have been known to benefit engine performance by equalising the distribution of pressure at the engine face. Non-uniform pressure distribution, or *distortion*, leads to an imbalance of aerodynamic loading of the compressor which has the effect of bringing the surge line closer to the engine operating line (or reducing the working surge margin). This is not a favourable off-design condition. Exploration of the full effect of IBF on the total pressure on the operating line represents scope for further work, but as a starting point the data of the current work can be interpreted to illustrate this benefit of the IBF.

Figure 5.20 shows the spanwise distribution of total pressure at two streamwise locations in the intake dust, downstream of the filter. The example used is the forward-facing intake in hover. Each curve represents a different state of resistance at the intake entrance: no resistance, when no filter is present; a resistance of 0.6 kPa, when the filter is “clean”; and 3 kPa, when the filter is “clogged”. The results have been normalised to permit fair comparison — where a pressure drop is artificially prescribed at the intake such as the case of a clean filter, the pressure lost is re-added to the total pressure loss at the engine face in order to isolate the losses due wholly to separation and boundary layer.

Due to the stagnant or low-speed reversed flow symptomatic of a separated flow

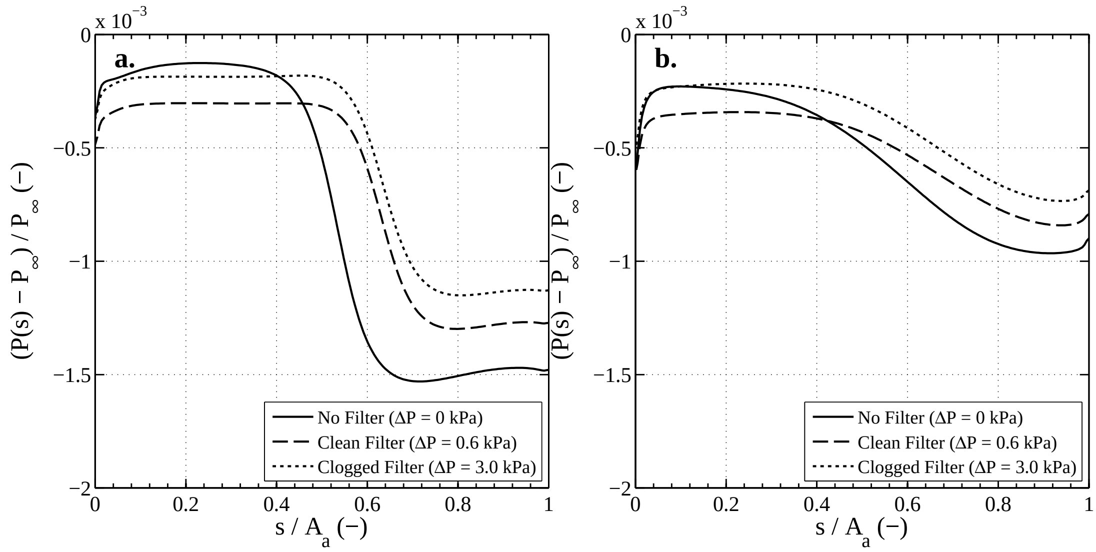

Figure 5.20: *Effect of filter presence on spanwise total pressure distribution at two downstream locations in the intake duct: a. at $s = A_a$; b. at $s = 3A_a$; where s is the distance from the inlet entrance.*

region, the total pressure is locally lower than the freestream, or in this case the duct flow. The depression shown in the right hand side of each plot Figure 5.20 is therefore indicative of a separation bubble. The spanwise extent of this depression can also be viewed as a low total pressure "footprint", that gives an impression of the size of the separated region. While several more cuts would be needed to illustrate comprehensively, Figure 5.20 suggests that the effect of increasing filter resistance is to reduce the loss of total pressure to lip spillage during hover or low-speed flight. This effect can be attributed to the deceleration of the airflow as it approaches the filter, and is a phenomenon that could be exploited in filter design to reduce total pressure distortion.

5.4.4 External Intake Drag

In forward flight, the effect of increasing the filter angle on intake performance concerns an interesting area of intake aerodynamics: drag. It is perhaps intuitive that orientating the filter at an angle to the flow will result in a less airframe drag at high forward speeds; the anticipated result is explained by analysis of the total pressure distribution in the external flow, as depicted in Figure 5.21. The consequence of a reduced-diameter streamtube at high forward speeds is the development of spillage drag, as the external flow fails to negotiate the intake lip and separates from the nacelle surface. This creates a region of low pressure and stagnant air, identified by the yellow areas in Figure 5.21 (and blue areas of low velocity in Figure 5.16, which is a type of airframe drag known as *form drag.*

The distinction between internal and external drag needs to be made in intake design, as it can lead to some confusion. It is well discussed in Chapter 9 of Seddon's book. Internal drag accounts for all losses within the capture streamtube, which must be overcome by the engine in order to maintain core mass flow. The power required by the engine to perform this task is a summation of the momentum traded with the air, and the frictional and inertial losses expended in the process. Since a filter is placed within the confines of the streamtube, it contributes only to these losses, hence does not directly contribute to airframe drag, despite exerting a form of drag on the core engine air flow. However, Figure 5.21 shows that strategic integration design can alleviate the drag resulting from spillage over the intake cowl.

5.4.5 Particle Distribution

The particles are injected into the domain as described in Section 4.3.3 and their trajectories are tracked. The distribution of particles on the filter is recorded to gain a first order qualitative idea of whether the integration of the filter into the intake may be designed in such a way that is beneficial to engine performance. Ultimately, IBF integration may be constrained by intake-airframe architecture, however the following provides a useful insight into what may be expected. A fine test dust is selected that contains a range of particles of Reynolds number that is in the inertial and viscous flow regimes ($\mathrm{Re}_p = 1$ to 30).

The particle distribution data is expressed as a particulate concentration, normalised with the freestream condition. A ratio of greater than unity indicates a greater quantity of particles per unit mass of carrier phase than the freestream condition is accumulating on the filter. The capture streamtube, discussed above in Section 5.4.1, is the main influence on particle trajectory. As it changes shape with forward speed or intake type, the catchment area is altered. The other main property affecting the fate of a given particle is its Reynolds number. The particle size distribution of AC Fine test dust contains a great range diameters; over the spectrum of forward speeds there is an even greater range of Reynolds numbers. Furthermore, the flow either accelerates or decelerates up to the intake face. Using the intake superficial velocity (volume flow rate per unit area — 8 m/s) as a reference, the particle Reynolds number for AC Fine dust varies from 1 to 32. The spanwise position is given as a distance along the filter, normalised by the intake area. The pressure drop across the filter in each of the following cases is 0.6 kPa, corresponding to the "clean" condition.

Figure 5.22 displays the distribution of three differently-sized particles corresponding to characteristic group diameters of AC Fine test dust, and a filter angle θ of 0 degrees. The distribution of particulate is important because non-uniformity will result in an inhomogeneous total pressure distribution. For the result of the forward-facing

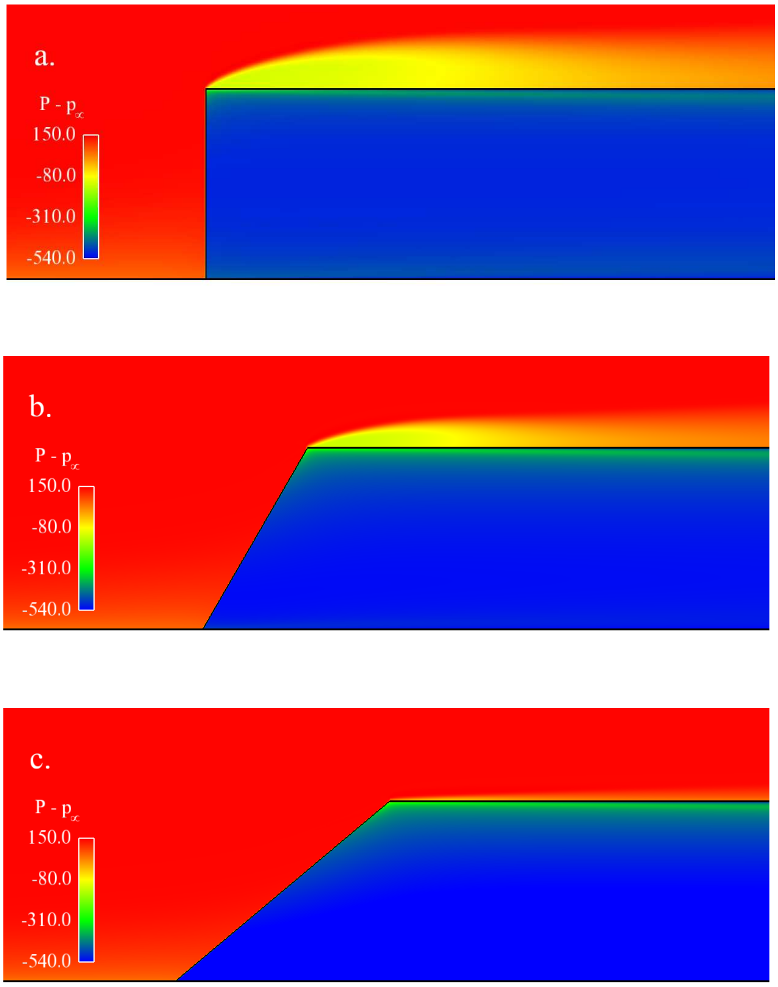

Figure 5.21: *Separation of external flow leading to airframe drag due to a forward-facing intake, at three filter orientation angles: a. 0 degrees; b. 30 degrees; c. 50 degrees.*

filter in low speed flight, below the full flow condition, the peak in the particles of smaller size (1μm and to a lesser degree 15 μm) at the innermost spanwise location arises from a local acceleration of the flow as the intake tries to maintain plug flow whilst contending a separation bubble. The non-uniform distribution becomes important when considering the accumulation of particles — certain parts of the filter will clog at different rates to others, distorting the total pressure distribution, the effect of which was discussed earlier.

The side-facing intake generally displays an even distribution of particles for the low-speed condition. There is a lull in particulate concentration of 57.5 μm at the foremost end of the filter due to particle inertia; by contrast there is a slight peak in concentration of smaller particles due to a local acceleration of flow caused by a separation bubble within the intake (see Figure 5.16d). This effect is evident at the location of the other separation bubble in the intake, just aft of the filter at the rearmost spanwise location. The flow acceleration in the presence of such a separation bubble is further evidenced at higher forward speed, during which the flow separation occurs to a greater extent (see Figure 5.16h). The smaller particles act like *tracer particles* in this situation, hence their peak at the foremost spanwise location. For the forward-facing case, the smaller particles are distributed evenly, which is symptomatic of their following the fluid streamlines, whereas the larger particles are deposited to a greater degree at the outermost section due to being influenced slightly by the external flow.

The effect of filter orientation angle, θ, on particle distribution is also investigated. The geometrical effect of the change of angle is illustrated in Figure 4.8. For this, the particle groups are combined to represent AC Fine test dust as described in Section 4.3.3. It can be seen in both Figures 5.23a and 4.8b that orientating the filter at an angle to the flow has the effect of reducing the local particulate concentration. In practice, this would result in a slower increase of pressure loss over time, hence is beneficial to engine performance. The reduction can be attributed to the increase in filter area, which reduces the filtration velocity for the same engine mass flow rate. Also evident in Figure 5.23a is the effect of filter angle on the characteristic concentration peak at the outermost end of the forward-facing filter. The peak appears to reduce in relative amplitude, which helps to alleviate a possible source of total pressure distortion.

In summary, the particle distribution is a function of airspeed, particle diameter, filter angle, and intake type. The distribution is important for the evolution of the pressure drop and total pressure distortion, although the transient distortion or two-dimensional distortion has not been investigated here. A particle's Reynolds number is the principle property that determines its distribution across a filter. Particles of Reynolds number below around 0.2 tend to follow fluid streamlines, hence almost act like tracer particles and reflect local variations in flow velocity. At forward speeds

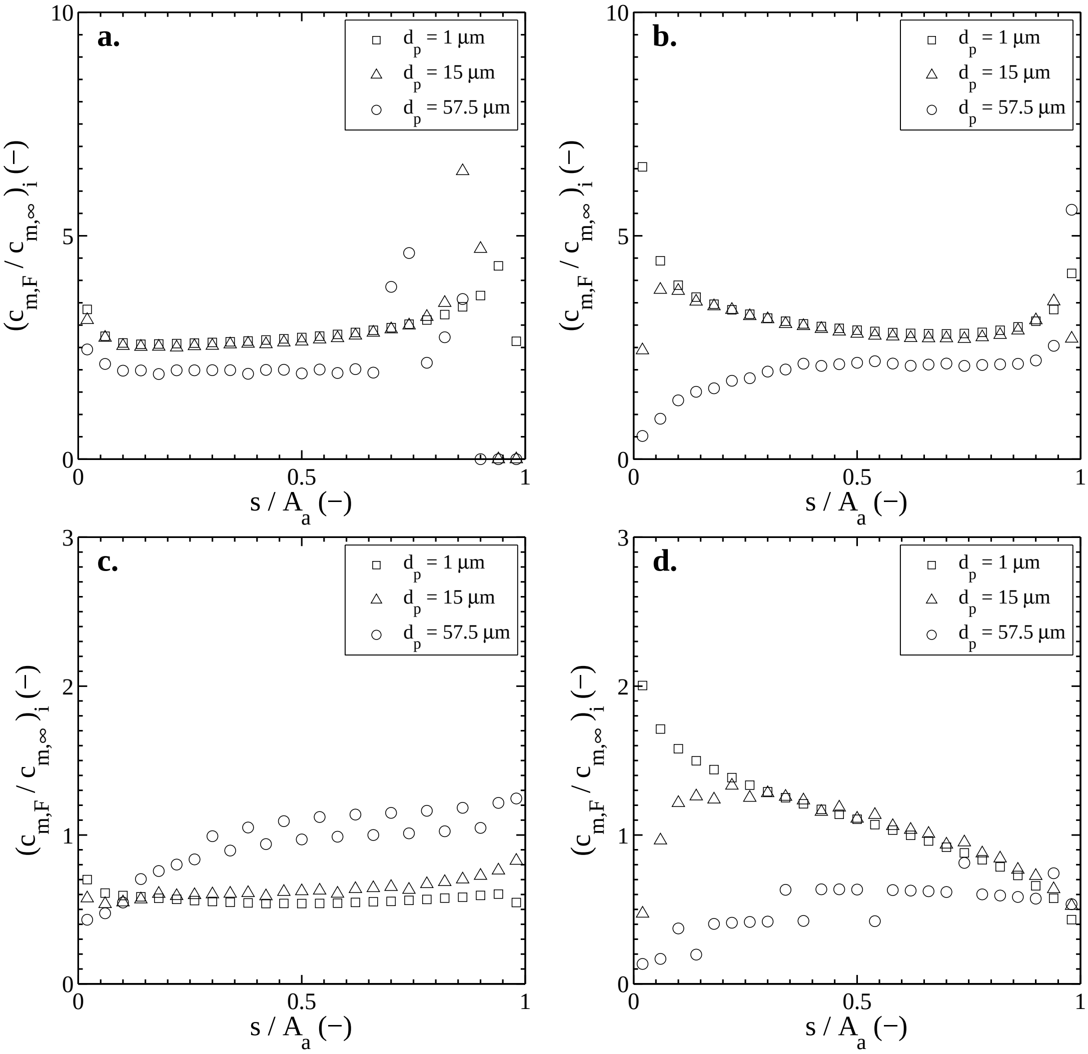

Figure 5.22: *Spanwise distribution of three particle sizes quantified by normalised concentration, on a IBF filter (θ = 0 degrees) in two intake configurations, under two flow conditions: a. forward-facing intake, 2.5-knot flow normal to filter; b. side-facing intake, 2.5-knot flow parallel to filter; c. forward-facing intake, 15-knot flow normal to filter; d. side-facing intake, 15-knot flow parallel to filter.*

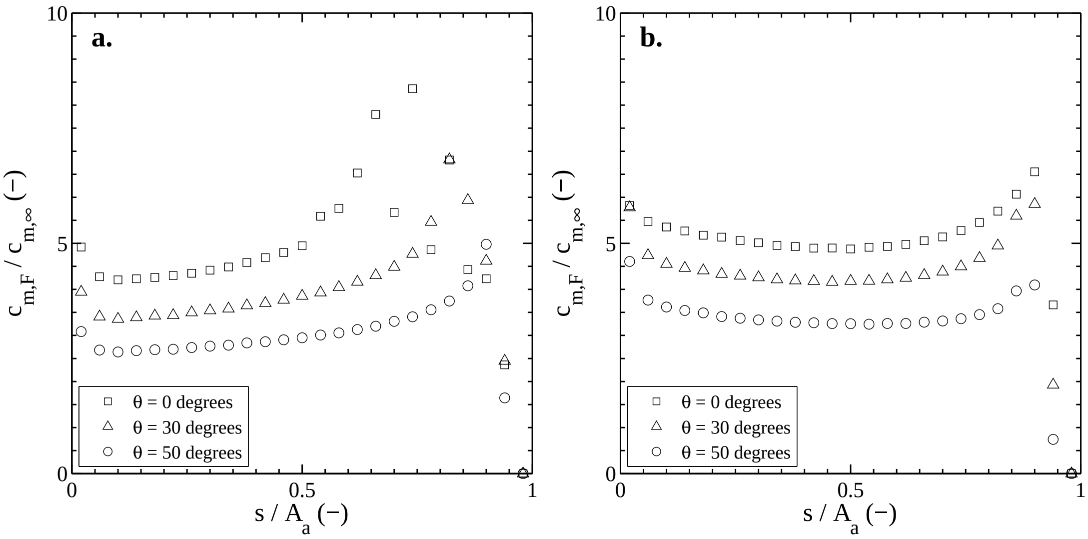

Figure 5.23: *Spanwise distribution of three orientation angles quantified by normalised concentration, on a IBF filter in two intake configurations for: a. forward-facing intake in a 2.5-knot flow; b. side-facing intake in a 2.5-knot flow.*

greater than the full flow conditions, such particles are evenly distributed across the filter. This is in contrast to particle of larger Reynolds number, whose trajectories are influenced by the capture streamtube but to a lesser extent, resulting in an uneven distribution of particles, weighted towards one end of the filter. The effect of angling the filter to the flow is to alleviate the non-uniformity created by unequal flow distribution, and to reduce the concentration of particulate reaching the filter.

5.4.6 Particle Concentration

The expressing of particulate concentration at the filter as a fraction of the freestream dust concentration (or local brownout severity) permits an assessment of the intake's inherent potential to reduce the quantity of particulate reaching the engine. For example, intuitively it is easy to understand that a degree of particle inertial separation is achieved by sideward-facing intakes in forward flight. The following examines the effect of varying flow conditions and intake geometry changes that influence this.

The first investigation demonstrates the inherent separation capability of a helicopter intake. Tests were performed with no resistance prescribed at the intake face to ascertain how much particulate could be removed from influent air without the use of an IBF, or any EAPS system. Figure 5.24 shows the effect of increasing the forward speed of the helicopter on particulate concentration at the intake. Comparing the two intake types, the results are perhaps counter-intuitive: in Figure 5.24a the anticipated increase of separation ability at higher forward speeds for side-facing intakes is in evidence; but is also exhibited by the forward-facing intake. In fact, the forward facing intake performs better than the side-facing intake at all flight speeds, approximately 30% better at speeds greater than full flow.

To explain this, it must be remembered that the particles in this sample are of a relatively low Reynolds number. The equations of motion of a particle are given in Section 3.2.5. In particular, the drag coefficient of a particle (Equation 3.40) is shown to be inversely proportional to the particle Reynolds number (Equation 3.39). The extent to which a particle responds to a change in carrier fluid direction is expressed by its acceleration in that direction (see Equations 3.34 and 3.38), which is proportional to the relative velocity and particle drag coefficient. Hence a steeper flow relative velocity gradient combined with a low particle Reynolds number will result in a particle's motion more closely reflecting the fluid streamline that has thus far carried it.

As the freestream velocity increases, the capture streamtube becomes "trumpet bell-shaped". The curvature of the "bell" steepens with increasing velocity, which elevates the relative velocity and means that particles more closely follow fluid streamlines. This has the effect of decreasing the "catchment area" of particles upstream of the intake. Hence by increasing the forward speed of the rotorcraft one is able to create an inherent separation capability for a forward facing intake, the consequence of which is seen in Figure 5.24a. Of course, as airframe speed increases, so too does the inertia of the approaching particles. Particles of larger diameter, and therefore mass, are increasingly unable to negotiate the sharp change in fluid curvature. Thus the inherent separation ability of a forward-facing intake is diminished as particle diameter increases. This is evident in Figure 5.24b, which is a plot of the maximum particle size in the test dust range. It is clear that in this case the curves are more similar, and of a higher level of concentration than that of the whole distribution. It is expected that a coarser dust distribution would exhibit the more intuitive result described by Seddon [21], whereby the side intake is the better performer of the two intake types.

Another, perhaps more important observation from Figure 5.24, is that the performance of both intake types tends to deteriorate with decreasing flight speed. Crucially, at speeds below full flow the concentration ratio is above unity: for this particular particle size distribution, the dust concentration during hover intensifies by almost 15 times, which is not an ideal situation for IBF longevity. (Note: while the results shown in Figure 5.24 are for the situation of no porous jump at the inlet face, when a resistance was prescribed, only negligible differences in the trend were observed). This occurs because the catchment area described above increases at low speed, as the capture streamtube dilates. However, Figure 5.24b shows that particles of larger size are less sensitive to the effects of this dilation.

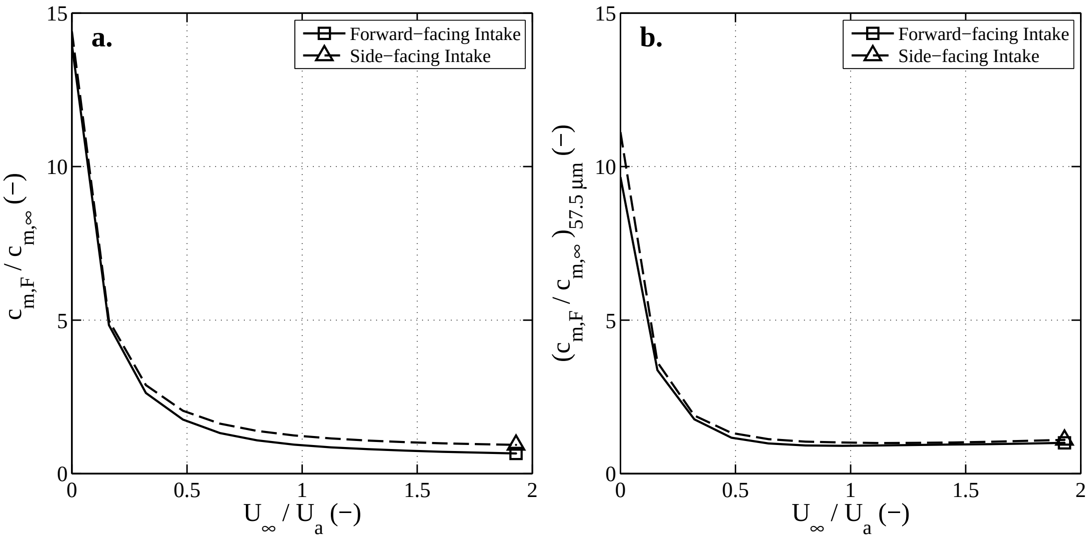

Figure 5.24: *The variation of particulate concentration with freestream velocity of forward-facing and side-facing intakes (with no IBF attached), for: a. AC Fine test dust; b. monodisperse dust of 50μm diameter.*

In practice the streamtube is unlikely to look like the idealised situation shown in Figure 5.16a due to the influence of the rotor downwash. Indeed, conclusions on the effect of forward speed on particle concentration need to made with consideration of the unsteady nature of dust cloud generation and downwash-intake flow interaction. For a better idea of particle ingestion during hover would require a huge research effort to examine three-dimensional effects, and may provide scope for future work. Additionally, the engine mass flow rate is reduced with increasing forward speed (across this relatively low-speed range), due to the associated decrease in required rotor power when moving forward. Therefore the condition of constant engine mass flow is ideal; in reality the concentration ratio at the intake will be further reduced.

A second investigation is conducted to ascertain whether there is any benefit to orientating the filter at an angle to the oncoming flow. It has already been shown in Section 5.4.3 that a slight reduction in pressure loss can be achieved by increasing the angle at forward speeds below full flow, however no difference was found for the situation of hover. Figure 5.25 shows the effect of filter angle on particulate concentration in three forward speeds. For both intake types, there is a reduction of as much as 30% for a filter angled at 50 degrees to the duct axis of symmetry. Not shown in the current figure is the case of hover, in which an even greater reduction of around 40% is exhibited. Since in all cases the engine mass flow rate is held constant hence the capture streamtube shape is almost identical for each angle, the difference can be explained by the fact that the particulate is distributed over a larger area, and that the filtration superficial velocity is reduced. It was discussed in Section 2.5.2 that from an IBF design standpoint, it is

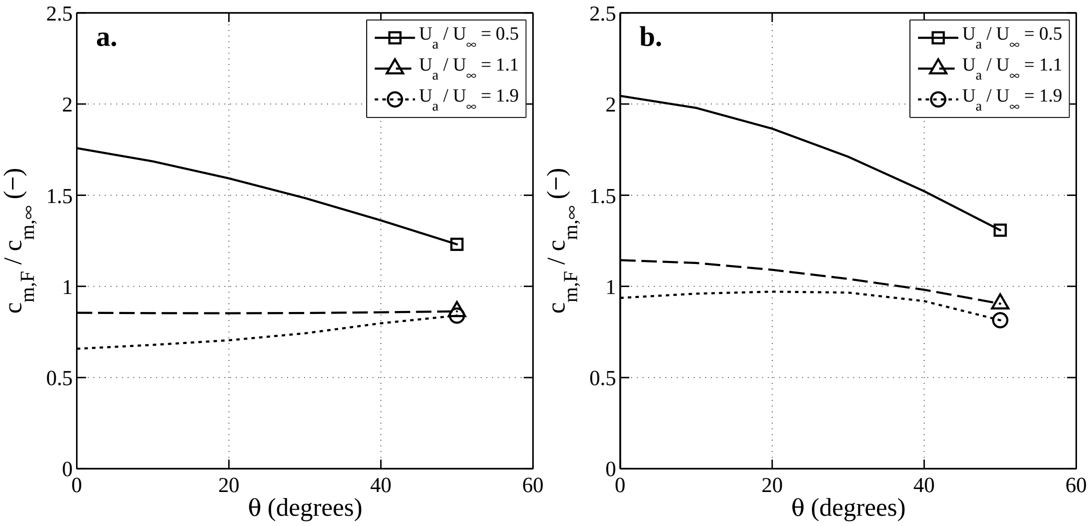

Figure 5.25: *The variation of particulate concentration with filter angle θ in three different freestream velocities, for: a. forward-facing intake; b. side-facing intake.*

beneficial to maximise projected area; the case can also be made in consideration of the transient situation in hover and low speed, the most common regime for a helicopter in brownout.

As forward speed increases, the similar trend shared by both intake types ceases. For the case of the forward-facing intake at around full flow there is no variation in particulate concentration with filter angle; at higher forward speeds the effect of an angled filter is to collect more particles. This is shown in Figure 5.25a. As intimated above, the streamtube shape has an influence on the degree of particle capture. In forward flight the pre-inlet streamtube is shaped like a trumpet bell, as shown in Figure 5.16g; the curvature of the bell is gentler if the filter is angled, hence the outward radial drag force exerted by the air on the particles is reduced. This means fewer particles bypass the filter, thus the concentration is greater.

For the case of the side-facing intake at a freestream velocity approximately equal to the engine face velocity, the trend exhibited in low speed and hover is also evident, but to a much lesser degree. The overall particle capture has also decreased at all angles. Increasing freestream velocity beyond full flow sees a further reduction in concentration across the range of angles, but the reduction rate is greater at small angles. This is indicative of the inertial separation capability that is expected of a side-facing intake; at larger angles, the intake "juts-out", capturing high-inertia particles at higher forward speeds. However, a larger filter angle still benefits from spreading the particulate over a larger area, hence the characteristic peak visible in the (U_a/U_∞ =1.9) of Figure 5.25b.

5.5 Summary

The results from a parametric study into IBF design on two scales are presented. The first scale concerns the pleats of the filter. The pleats can be tailored to exploit a phenomenological consequence of pleating, which is the emergence of a secondary source of pressure loss as the pleat channel is narrowed, yielding an optimum pleat design for a given set of flow conditions. As the pleat takes on particles the pressure drop rises, until the filter medium can no longer support further internal accumulation. At this point the particles collect on the filter surface in the form of a cake. During the surface clogging stage, the rate of increase of pressure drop is much greater than internal clogging stage. By increasing the pleat depth or decreasing the pleat angle, the onset of this second phase can be delayed.

For the properties used in this study, there appears to be no further benefit or cost to pressure loss as the pleat angle for a filter of fixed pleat depth is increased, and very little change to this trend as the flow velocity is increased. This means a filter with these properties will perform at its maximum "clean" performance for all engine mass flow rates. A lower flow velocity allows more particles to be retained for the same maximum pressure loss, which extends the cycle life of the filter. This can be achieved by increasing the filter projected surface area. The optimum design point changes depending on the initial conditions. A filter of higher initial permeability favours a wider pleat channel in terms of pressure loss, while a narrower pleat is favoured when finer particles are to be captured to ensure the pleat is achieving maximum holding capacity at a prescribed maximum pressure drop.

The second scale investigates the effect of the installed IBF on intake performance, however results pertaining to the unprotected intake are provided first. The use of CFD was justified by the modelling of the separation bubble, which is not predicted by the analytical theory. The effect of lip spillage was seen to be greater for the forward-facing intake during hover, due to the more extreme change in direction of the flow. When a filter is installed into the intake, the loss in pressure due to separation and duct loss was almost negligible in comparison with the pressure drop across the filter. However, the filter's presence was shown to benefit total pressure distortion by homogenising the distribution. The effect was increased as the pressure drop increased, indicating that despite causing a temporally increasing pressure loss, the clogged filter can still benefit engine performance. The filter's presence does not directly contribute to airframe drag, but it was shown that strategic integration could result in less external spillage drag at high forward speeds.

When particles were introduced, it was shown that the particle distribution across a filter is very much dependent on the particle size, and the forward speed relative to the intake face velocity. At low forward speeds, the forward-facing intake has an even distribution of most particle sizes, but particles of 1 μm tend to follow the fluid streamlines, responding to local flow velocities hence accumulating to a greater degree at more radially outboard positions. For side-facing intakes the trend is reversed — it is the larger particles that are less-evenly distributed along the filter due to their inertia throwing them rearward. The effect of a greater filter angle is to spread the particles over a larger area, which reduces the overall concentration and would lead to a slower rise in pressure loss.

The particulate concentration was analysed across the range of forward speeds for both intake types. Contrary to expectation, if the particle size is small enough the forward-facing intake ingested a smaller quantity of particulate than the side-facing intake. As dust size increases, it was shown that the inherent inertial separation ability of the side-facing intake becomes more prominent. It would also offer a greater degree of protection against FOD. For both intake types it was shown that an increase in forward speed results in a decrease in the amount of particulate ingested, due to the narrowing of the capture streamtube. However at low flight speeds, when the particle catchment area is greater, the intakes were shown to ingest particulate at a much greater concentration than the atmospheric conditions. The results also showed that the filter particulate concentration in hover can be reduced by angling the filter, which increases the surface area. For side-facing intakes this trend continues but to a lesser degree at higher forward speeds; for the forward-facing intake the trend reverses at higher forward speeds due to the curvature of the trumpet-bell shaped capture streamtube decreasing in severity, thus reducing the inherent separating ability of the intake.

Chapter 6

Inlet Barrier Filter Design & Performance

This chapter puts into practice the results of the parametric study. It begins with a discussion of optimum design, followed by the proposal of a design protocol based on the findings. It then adopts the design protocol to propose a solution for the Eurocopter EC145 helicopter and presents a temporal performance analysis.

6.1 Introduction

The purpose of this chapter is to put into practice some of the quantitative results of the preceding section, in order to demonstrate a framework for IBF design. The concept of optimum design for minimum pressure loss and maximum endurance is discussed and applied to create a solution for the Eurocopter EC145. Once a design is fixed, the transient performance is predicted using the results of the two scales.

In contrast to the other EAPS technology the IBF performance is transient. The choice of filter media and pleat design have been shown to dictate this performance in Chapter 5; a discussion of the filter medium and pleat design considerations is given in Sections 2.5.2 and 2.5.3. Installation design considerations for a retrofitable filtration system are multitudinous, relating to much more than the just the tuning of the filter parameters. Since it is a retrofit technology, many of the design considerations concern changes to the intake architecture, which introduce new constraints relating to operability. A breakdown of the key design constraints is provided by Scimone & Frey [41]:

1. Filter media design and pleat configuration must maximise filtering capability.

2. The configuration should limit pressure drop variation with airspeed to minimise the engine's susceptibility to surge.

3. Surface area must be maximised without sacrificing aircraft handling qualities, operability, maintainability and structural capabilities.

4. Structural design must consider weight, replaceable panels must be durable, air loads and crash loads must be addressed.

5. Maintainability design must consider installation and panel removal with flight safety-assured fastener configurations.

6. Integral seals must be incorporated to maintain filtering integrity.

7. A secondary air source system in the form of a bypass door must be included as a contingency for severe clogging.

Of these design constraints only the first is comprehensively considered in the present work. The rest are rather case-specific. For larger mass flow requirements, the complexity of the design is increased, as it becomes more difficult to achieve the desired flow rate per unit area with a single filter panel. The solution in this case is a multi-faceted appendage like that shown in Figure 2.10c. When the filter system is external to the confines of the normal inlet area, the performance may be enhanced through the use of multiple filter panels, some of which are tailored to take advantage of the flow conditions in hover, others of which are orientated to recover pressure during forward flight. The case of the multi-faceted IBF is not investigated in the present work, however the benefits to particle distribution and the pressure recovery of panels in forward flight is discussed in Section 5.4.

For a full qualitative discussion on all aspects of IBF design, see Scimone & Frey [41]. What follows in the current chapter is an quantitative elaboration of the first design constraint: maximising filtering capability. The use of CFD to perform a parametric study affords the investigation of the optimum filter pleat shape for superior IBF performance. In terms of results it is by no means conclusive, due to a shortage of data for all contributory parameters, but some of the methods presented to determine the optimum designs are unique to IBF, hence the following can be considered a proof of concept.

6.2 Optimum Pleat Design

In Section 5.3.4 the concept of the optimum pleat shape was discussed and illustrated with Figure 5.15. The minima and maxima in the pressure drop and mass collected plots correspond to the best pleat shape for that particular configuration and set of flow conditions. Crucially these optimum points are not aligned. For this reason a new design metric — the Pleat Quality Factor (PQF) — is introduced which bases the optimum pleat design on both performance indicators. It is given as:

$$\mathrm{PQF} = \frac{100 m_{pc,\max(\Delta P)}}{\Delta P} \tag{6.1}$$

where $m_{pc,\max}$ is the total mass collected at the maximum permissible pressure loss. The Pleat Quality Factor can be used to examine the effects of altering certain flow properties and filter properties on an optimum design point that caters for both pressure drop and holding capacity. It is expressed as "grams collected per square centimetre of projected filter area, per kilopascal of pressure loss (across the clean filter)"; a larger quantity indicates a better performance. The following sections demonstrate how this can be used to design a pleated filter for IBF applications.

6.2.1 Pleat Design Quality Factor

The PQF is plotted for a number of filter properties and flow properties to determine their effect on the optimum IBF design. Figure 6.1 shows the PQF as a function of pleat angle for three different depths, for two different test dusts. The first obvious trend is that the PQF is improved with increasing pleat depth, suggesting that it would be advantageous to extend the pleat as deep as possible. Since the optimum pleat angle varies very little with pleat depth (a marginal decrease of optimum angle with increasing depth), this trend implies that it is in fact an optimum pleat *aspect ratio* for a filter medium of this thickness and permeability. In effect this means the IBF would achieve the best PQF if it contained just a single, large pleat spread across its whole span, as long as the pleat angle were the optimum. Of course such a solution does not exist — it would be impractical to design such a configuration into an intake and provide the necessary support. Furthermore increasing the pleat depth has the effect of decreasing the filtration velocity which reduces the separation efficiency of the filter. Figure 6.1 also shows that a better filter performance is achieved when a coarser sand is being filtered.

Next, the influence of volume flow rate per unit projected area (throughput velocity) is investigated. The results are presented in Figure 6.2. Again, a superior performance is achieved by the same filter when a coarser dust accumulates, a trend that will be seen throughout. The importance of reducing the throughput velocity is noticeable here: reducing the velocity by just 2 m/s can double the PQF, which translates to longer endurance and lower initial pressure loss. However the optimum pleat angle appears almost unaffected by velocity, possibly exhibiting a preference to a smaller angle at higher velocities. The proportion of pressure loss attributable to the medium or the pleat channel is not directly shown here, but the result suggests that they both increase at the same rate. This becomes significant when it is considered that throughout its life the IBF will be required to perform at a number of engine power settings, or mass flow rates; the result implies that even when operating "off-design" the filter is achieving maximum performance possible.

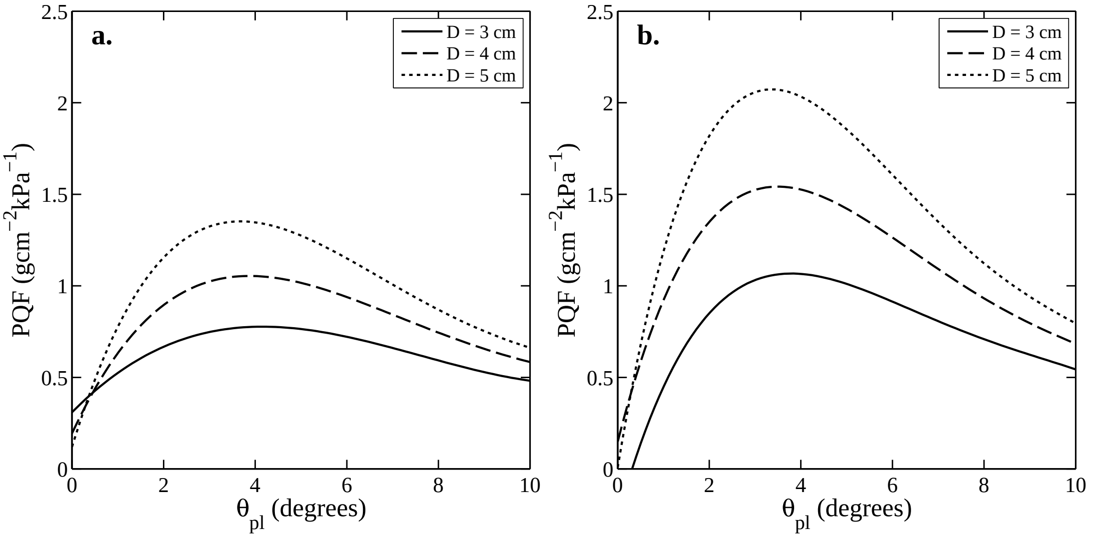

Figure 6.1: *Pleat Quality Factor as a function of pleat angle, for three different pleat depths when filtering: a. AC Fine test dust; b. AC Coarse test dust. (Z_F = 1.5 mm, α = 0.05, U_a = 8 m/s, max(ΔP) = 3 kPa).*

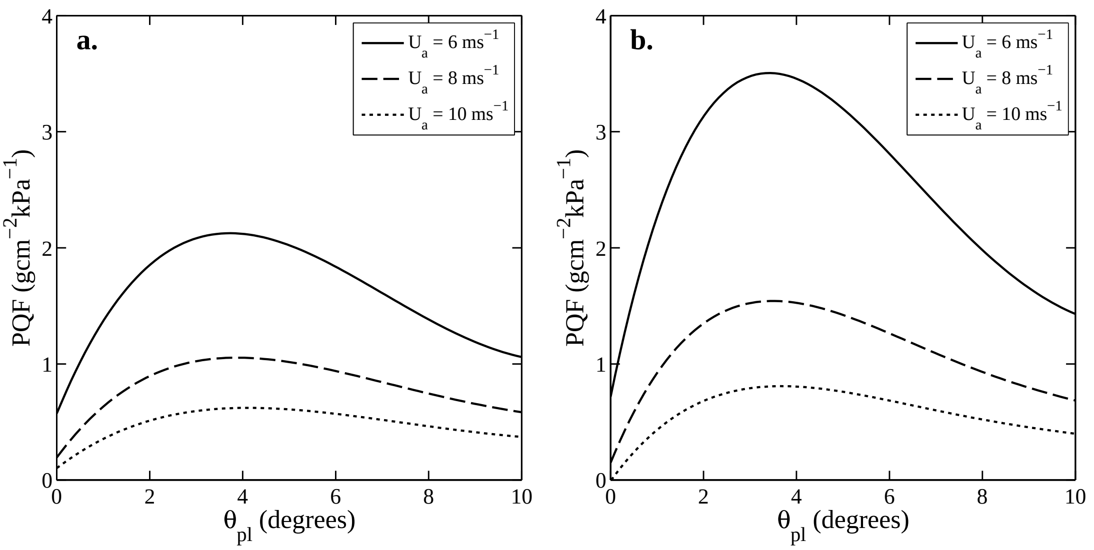

Figure 6.2: *Pleat Quality Factor as a function of pleat angle, for three different throughput velocities when filtering: a. AC Fine test dust; b. AC Coarse test dust. (Z_F = 1.5 mm, α = 0.05, Z_{pl} = 4 cm, max(ΔP) = 3 kPa).*

In all examples presented thus far, the initial filter permeability has been fixed. The permeability is a function of the filter packing fraction; in the next example the effect of using a filter with a different packing fraction is investigated. The packing fraction may be increased to improve the separation efficiency of the filter, as demonstrated by Figure 5.2. In Figure 6.3 an increase in packing fraction is seen to decrease the PQF, albeit by a modest amount in comparison with the other parameters investigated, and shift the optimum point to a smaller pleat angle.

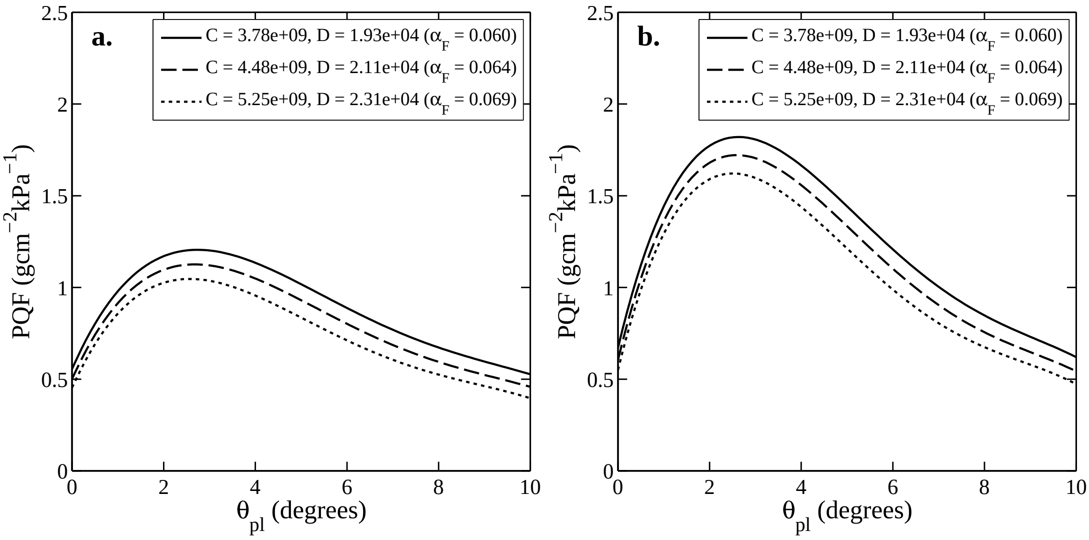

Figure 6.3: *Pleat Quality Factor as a function of pleat angle, for three different packing fractions when filtering: a. AC Fine test dust; b. AC Coarse test dust. (Z_F = 1.5 mm, α = 0.05, Z_{pl} = 4 cm, U_a = 8 m/s, max(ΔP) = 3 kPa).*

All examples presented so far have also had a maximum allowable pressure drop of 3 kPa prescribed. In the following example the limit is varied. Figure 6.4 shows three curves for the two test dusts representing maximum allowable pressure drops of 2.5, 3.0 and 3.5 kPa. The effect of increasing the pressure drop limit is to improve the filter's performance, which is understandable when considering the definition of PQF. Two further trends are observed: firstly, the coarser the sand, the more sensitive is the PQF to the maximum allowable pressure drop; secondly, for finer dusts the optimum pleat angle appears to decrease with increasing maximum pressure drop. From a design standpoint this is significant: the maximum permissible pressure drop may be set by considering the predicted cost to the engine as a percentage of power loss. For example, power loss may be more critical to military rotorcraft, which employ a greater numeracy of additional engine systems such as bleed air or infra-red suppression units than the typical civil rotorcraft. Hence the maximum allowable limit of pressure drop may be lower for military applications, thus may require a different filter design.

By calculating the Pleat Quality Factor, it has been possible to examine the effect of flow conditions and filter properties on the optimum pleat angle. Notably, there was no significant affect on optimum angle observed when different pleat depths were chosen. This is important from an IBF design perspective because it eliminates one of the many variables to be considered when tuning a filter for optimum performance.

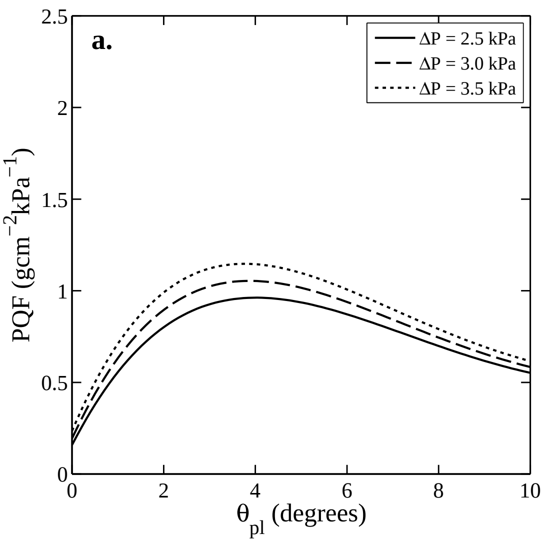

Figure 6.4: *Pleat Quality Factor as a function of pleat angle, for three different maximum pressure drops when filtering: a. AC Fine test dust; b. AC Coarse test dust. (Z_F = 1.5 mm, α = 0.05, Z_{pl} = 4 cm, U_a = 8 m/s).*

6.3 IBF Design

To demonstrate the utility of the optimum pleated filter design point, the findings of the previous section are put to use in surmising an IBF solution to the Eurocopter EC145. The EC145 is a light twin-engine utility helicopter with a maximum takeoff weight of 3585 kg, powered by two Turbomeca 1E2 engines that deliver a maximum power of 575 kW. More than two hundred EC145 helicopters have been delivered so far to customers worldwide (2009) [46]. The largest operator of the EC145 is the US Army, which operates the aircraft, designated as the UH-72A, in the Light Utility Helicopter role. As part of its remit, the EC145 is required to operate in dusty environments, and therefore can expect to experience a number of brownout landings during its mission profile. The helicopter is chosen to validate a design protocol, and to allow later comparison with the solution described by Ockier *et al.* [46]. It is pictured in Figure 6.5.

6.3.1 Pleat Design Map

From a design standpoint the filter must be made to achieve maximum filtering capability, which is judged by particle removal rate (separation efficiency), pressure drop, and endurance (maximum holding capacity). Unfortunately, altering the filter parameters to achieve a high performance by one criterion is usually to the detriment of another. For example in Section 5.3.4 it was shown that a low pleat density is favoured for a low clean filter pressure drop, whereas a high pleat count is favoured for holding more mass; in Section 5.2.1 it was shown that increasing the packing fraction gives the filter more capture ability at the expense of heightened medium pressure loss.

Figure 6.5: *Photograph of Eurocopter EC145*. (*Image reproduced under Creative Commons licence (CC BY-NC-SA 3.0), © Angie Norcup).*

The results presented in Section 6.2.1 generated a number of optimum design points that are seen to alter to varying degree with the flow conditions, filter properties, and dust properties. The results have been generated for a fixed particle size distribution and using fixed filter medium properties, which limits their applicability somewhat. The pleat depth is also constant, however it was discussed in Section 6.2.1 that the optimum pleat angle varies only marginally with pleat depth. If it assumed that these represent likely values in practice, the results can be taken forward to demonstrate a design protocol for IBF. Further work would focus on broadening the envelope of application. Clear trends already discussed are visible in this map, namely that: a better Pleat Quality Factor is achievable by driving down the throughput velocity; and a higher maximum pressure drop favours a narrower pleat design to achieve maximum performance.

The optimum points are used to create a parameter map for IBF design, shown in Figure 6.6. Each point on the grid represents an optimum design for a given throughput velocity and a given prescribed maximum permissible pressure drop. The throughput velocity is decided by the design point engine mass flow rate, at which the gas turbine generator is running at 100% speed and producing maximum continuous power, which is required during takeoff and landing. The off-design conditions may prevail for the majority of the filter life, therefore a more encompassing design may consider the cruise condition. However in the present case the IBF is designed for the condition at which the engine is at most risk from particle ingestion, i.e. hover.

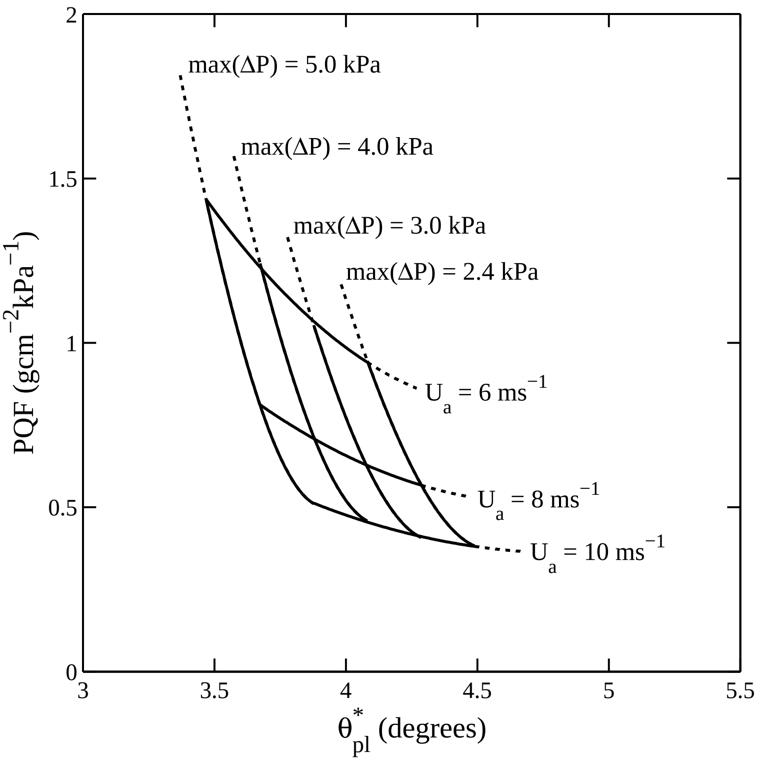

Figure 6.6: *Parameter map for optimum pleat design showing iso-lines of throughput velocity and maximum permissible pressure drop.*

The Turbomeca 1E2 has a mass flow rate in the region of 2.1 kg/s. Without knowing the airframe geometry around the engine intake, it is difficult to assess the available space for integration of an IBF. However, the solution proposed by Ockier *et al.* modifies the roof of the engine compartment nacelle (see Ref. [46]) to accommodate the IBF panel. The result is a design that does not look too dissimilar to the solution shown in Figure 2.14. There are two upward-facing filter panels with separate ducting to two forward facing axial gas turbines. A bypass door allows a portion of the air entering at the front of the nacelle through the plenum chamber intakes (visible in Figure 6.5) in case of component malfunction or extreme blockage. To achieve a reasonable throughput velocity of 8 m/s, the projected filter area required at Standard Day conditions would be 0.205 m^2 which, to put it into context, could be achieved with a panel of dimensions of approximately 0.3 m $\times$ 0.7 m.

With the throughput velocity fixed, the next step is to decide the maximum permissible pressure drop. As a first estimate, the maximum engine power is used as a reference. Suppose the maximum loss of power that the engine could afford is 1.3%. For the Turbomeca 1E2 this translates to a power loss of 7.5 kW. Simplifying the power required as the energy expended servicing a pressure loss at a given mass flow (as given by Equation 3.140), at the design mass flow the maximum pressure loss permitted would be 3.5 kPa. These values are quite malleable to the designer, but are chosen here in this way to demonstrate a proof of concept; in practice it is possible to use the map to select the design point based on the power loss requested, and how much space is available to implement the IBF. Additionally, these are only "design-point" values. In reality the IBF may spend a lot of its life working "off-design". Nevertheless there is a justification for a design based on scientific reasoning. In this example, the chosen throughput velocity and maximum pressure drop would achieve maximum performance with a pleat of 4 degrees angle.

6.3.2 Tuning the Filter

The design map yields the optimum pleat angle. While initially created from a filter with a depth of 4 cm, the fact that depth does not significantly affect the optimum point allows the map to be assumed for all pleat depths (within the same order of magnitude). What remains in setting the pleat geometry, therefore, is to decide the ideal pleat depth. So far the performance criteria of pressure loss and endurance have been satisfied. The third criterion is the required separation efficiency. In Section 5.2 it was shown that the separation efficiency is a function of the Stokes number, which itself is a function of the particle diameter, the fibre diameter, and the filtration velocity. Since the first two parameters are "fixed" in the present case, this leaves the filtration velocity as the main parameter to tune the filter.

The filtration velocity is directly related to the total filtration surface area. Without a more thorough investigation of particle velocity in the vicinity of the pleats, it is assumed that the filtration velocity is equal to the velocity of the fluid at the porous medium interface, or the superficial velocity. Theory dictates that the superficial velocity is the volume flow rate divided by the filtration area. Therefore for a fixed pleat angle the superficial velocity decreases as the pleat depth increases. This is demonstrated in Figure 5.3.2, which illustrates graphically the effect of pleat depth on specific surface area. Increasing the pleat depth was shown in Figure 5.11 to reduce the clean filter pressure drop, however it is also known that separation efficiency increases with filtration velocity. This gives rise to another compromise. Since the pleat depth governs the superficial velocity, it can be tuned to find a balance between pressure loss and separation efficiency.

The dependence of separation efficiency on superficial velocity is shown in Figure 6.7a, for the two test dusts used throughout the present work. The overall efficiency is calculated from the equations given in Chapter 3, using the given properties of the filter and inflow conditions. For AC Fine test dust, the maximum efficiency is approximately 96%, which is achievable at high superficial velocities. For AC Coarse test dust the efficiency is much greater, reaching a maximum of close to unity for all velocities above 3 m/s. This illustrates the difference in performance when the properties of the target dust are changed. (It should be remembered that since the same governing equations are applied, the AC Fine dust particles that escape capture are the same size as those of the AC Coarse dust that escape capture, but comprise a greater proportion of the overall particulate mass).

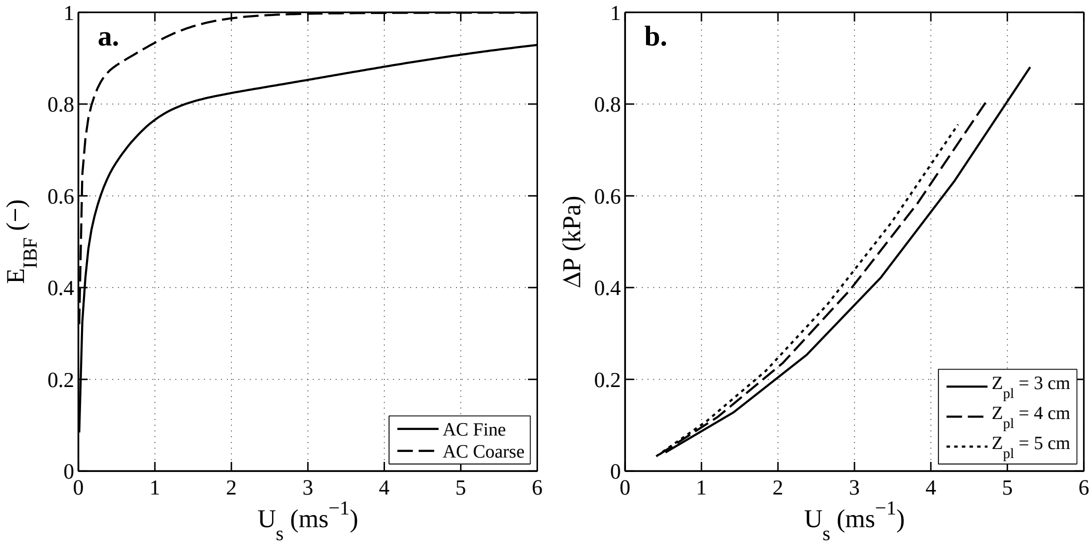

Figure 6.7: *Effect of superficial velocity on: a. separation efficiency for the two test dusts; b. pressure drop for three pleat depths (when $\theta_{pl} = 4$ degrees).*

Keeping with the case in hand, it is desirable to aim for a large superficial velocity. In fact, based on the theory of superficial velocity, Figure 6.7a suggests that for a throughput velocity of 8 m/s it is preferable to have as little pleating as possible, if any at all. Since this is not seen in practice, there is either a problem with the filtration theory, or a problem in the simple derivation of superficial velocity. In fact, when analysing the results from the CFD simulations, it is found that the area-weighted average velocity magnitude of the flow at the filter front surface is more than three times the predicted superficial velocity (although this is not necessarily reflective of the flow through the body of the filter medium). To see the secondary effect of superficial velocity, the pressure loss across a number of pleat depths, all with a fixed pleat angle of 4 degrees, is plotted in Figure 6.7b. The data are taken from the pleat scale parametric study, and the superficial velocity is the average of the readings of the front and rear surface area-weighted average velocity magnitudes. It can be seen that a shallower pleat permits a faster superficial velocity for the same overall pressure drop. With the assumption that the filtration velocity is equal to the superficial velocity, this suggests that a shallower pleat will achieve a higher separation efficiency.

While the assumption of equality perhaps limits the accuracy of the model, it is probable that the speed at which the particles penetrate the filter is at least proportional to the superficial velocity. More work is needed here to establish the relationship between pleat depth and filtration velocity. Using the assumption however allows the superficial velocity (ergo filtration velocity) to be plotted as a function of pleat depth, in order to complete the pleat geometry. In Figure 6.8 the relationship is illustrated for three throughput velocities. The data are extrapolated to span the range of depths suggested in U.S Patent 6,595,742 with a linear proportionality agreement, although this underpredicts the superficial velocity at lower pleat depths, which should tend to the throughput velocity. The pleat depth is chosen by assessing Figures 6.7a and 6.8. For the case in hand, a depth of 4 cm is chosen, which corresponds to superficial velocity of 3.02 m/s and yields a separation efficiency of AC Fine test dust of 85.3%.

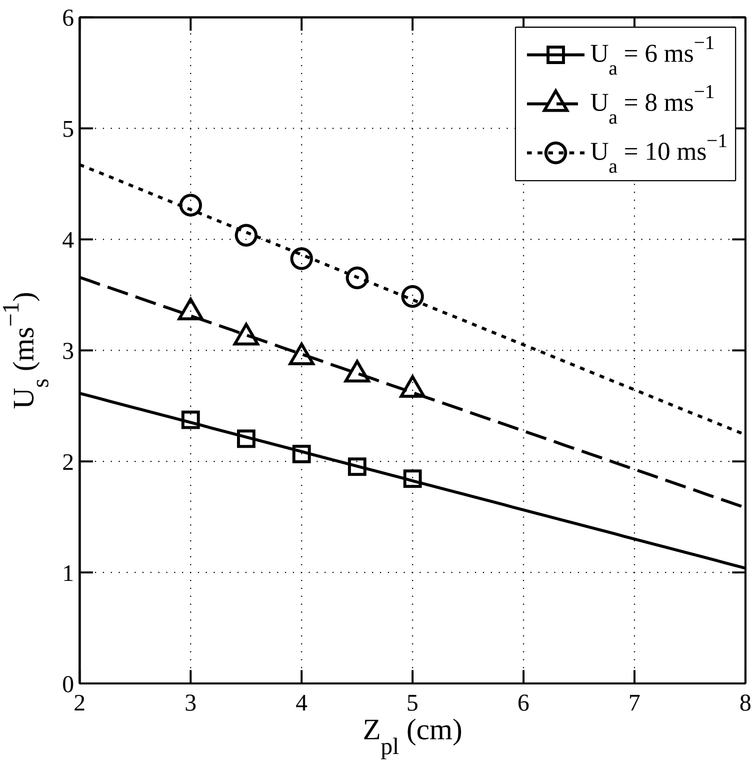

Figure 6.8: *Relationship between superficial velocity and pleat depth for three flow velocities.*

6.3.3 IBF Design Protocol

The steps taken to settle on the pleat design can be summarised as a design protocol for IBF pleat shape optimisation. Despite lacking validation by experiment, the results afford at least a qualitative analysis that permits the establishment of a framework for IBF design. The protocol is as follows:

1. Settle on a target Particle Size Distribution against which to protect the engine.
2. Settle on the maximum permissible pressure loss for helicopter engine.
3. Generate a pleat design map using established models or empirical data.
4. Establish a target throughput velocity based on engine mass flow rate and available intake area.
5. Select a pleat angle based on the pleat design map.
6. Select a pleat depth to achieve desirable separation efficiency

Of these steps, points 3. and 6. represent areas that could be investigated more deeply to expand the range of results generated in the present study. In particular, if an analytical or semi-analytical model were used to calculate the quantities required to build the pleat design map, then the steps could be applied iteratively to arrive at the ideal solution, since many of the parameters are interdependent. For example the pleat depth sets the filtration velocity, which in turn determines the separation efficiency, which dictates how much particulate is captured and potentially alters the pleat design map, and so on. However some parameters such as the particle size distribution must be fixed in order to initiate the process, and it is these that ultimately represent the target capability of the filter.

6.4 IBF Performance

Continuing with the development of a practical IBF solution, the filter design fixed in the previous section is used to generate transient performance plots for comparison with the results of the abovementioned study by Ockier *et al.* [46]. Full comparison is hindered by a lack of quantitative description pertaining to the filter and intake geometry used in Ockier's work, and an absence of data relating to the transient pressure loss and properties of the dust cloud. As has been discussed, these are essential parameters in determining the performance of an IBF. However, certain details are provided about the filter cycle life in dust clouds of varying severity, which can be used at least as benchmarks for comparison.

The proposed design has a pleat angle (or rather "half-angle") of 4 degrees, and a depth of 4 cm. This equates to a single fold-to-fold pleat width of just under 1 cm. The filter panel is suggested to have a length of 0.7 m and a width of 0.3 m. Assuming the pleats run widthways, i.e. their ridges are parallel with the shorter panel length, the specified dimensions equate to a total pleat number of 72.5, or 145 half-pleat sections. The filter panel in which the pleats are contained faces upwards, flush with the airframe. Each of these facts presents an opportunity to use the results of both the pleat scale parametric study and the intake scale study.

The pleat scale results yielded the relationship of pressure drop as a function of mass collected for a number of different pleat designs, including one with dimensions equal to the proposed solution here. The intake scale results yielded the spanwise distribution of particulate across a number of IBF-intake configurations, including the case of a filter orientated tangentially to the flow, such as the case of an upwards-facing IBF panel. The spanwise distribution was expressed in dimensionless form, normalised by the atmospheric dust concentration, allowing the distribution to be determined for any brownout density. Discretising the span into sections of length equal to the proposed pleat width yields a unique local dust concentration for each pleat. If each pleat takes an equal share of the total engine mass flow rate, it is possible to ascertain the mass flow rate for each pleat along the filter (see Equation 3.1), for a given atmospheric dust concentration. Combining this with the results of the pleat scale allows the pressure drop of each pleat on the filter to be expressed as a function of time. In both sets of results the particle size distribution resembles AC Fine test dust, in keeping with the rest of the chapter.

The benefit of marrying the two scales in this way is that the transient performance obtained by averaging the individual pleat temporal pressure drops accounts not only for the particulate properties, but also the two dimensional flow field of the intake streamtube. For side and upwards-facing intakes this is especially pertinent, as the particle distribution is rarely even across the filter, due to particle inertia. Such an approach allows the effect of this feature on transient IBF performance to be predicted. The following sections apply the theory to the proposed solution for the EC145 to generate a temporal evolution of the pressure drop across an IBF.

6.4.1 Transient Performance by Mass Collected

The pressure drop obtained from the merged scales is first expressed for three flight speeds, as a function of total mass collected on the filter. In this way the transient pressure drop is independent of the brownout dust concentration, therefore any difference between the flight speeds can be attributed wholly to the particulate distribution across the filter. The results are shown in Figure 6.9. The warning level refers to the maximum permissible pressure drop prescribed earlier in the chapter. There is only a very marginal difference between the two forward flight speeds, however in hover the pressure drop appears slightly larger for the same quantity of mass collected. During hover, local variations in the velocity distribution at the filter cause peaks in mass concentration. These portions of the filter clog at a much quicker rate than the rest of the filter, taking a disproportionate fraction of the total accumulated mass on the filter and reaching the unfavourable "cake" stage much sooner. Incidentally, this is the reason why the curve ends prematurely — while the average pressure drop across the whole filter remains at a reasonable level, the local pressure drop in those areas of high concentration reaches the limit of the data obtained.

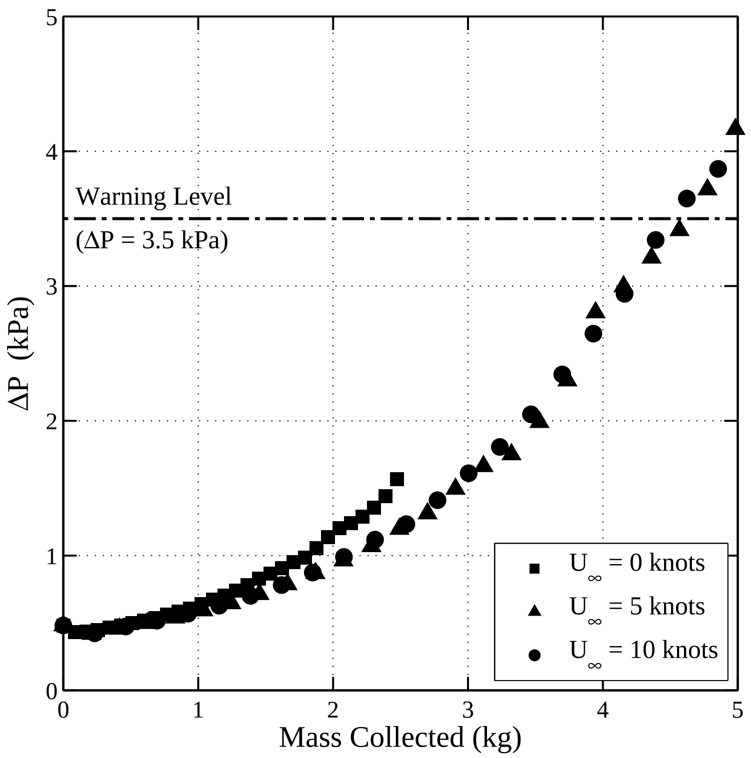

Figure 6.9: *Pressure drop evolution as a function of total mass collected across a suggested IBF solution for the Eurocopter EC145.*

In comparison with the pressure drop evolution curves shown in Section 5.3.3 for the single pleat, there is a notable difference. When considering all pleats along the filter, the transition from internal clogging to cake growth occurs much more smoothly. This is important from a handling qualities standpoint because it removes any abrupt loss of engine power. The smooth transition can be attributed to the non-uniform distribution of particulate across the filter, which leads to some pleats reaching the cake stage quicker than others. Since the pressure drop is an area-weighted average of all the individual pleats, the abrupt change in pressure drop evolution in one pleat is merely absorbed into the total pressure drop. While this is beneficial to filter performance, there is probably also an adverse effect of non-uniformity such as total pressure distortion. However this observation demonstrates the advantage of merging the two scales over using the pleat scale results alone to determine pressure loss.

The results confirm further the dangerous situation of hover in a brownout cloud. Not only does the filter draw in particulate from a much larger area (see discussion in Section 5.4.6), the resulting distribution also exacerbates the pressure loss. The results of the tests by Ockier *et al.* make no allusion to the performance difference between hover and forward flight in a dust cloud, however they do state that between 0.5 and 1.0 kg of dust and sand were captured by the filter before the critical level was reached. Figure 6.9 suggests that up to 4.5 kg can be captured before the prescribed limit is reached, although comparison of the two is fairly meaningless without knowing the warning level adopted in Ockier's work, or indeed the dust properties, intake flow properties and so on.

6.4.2 Transient Performance by Duration

Despite the lack of comparable data, some useful figures are provided by Ockier *et al.* that pertain to the filter longevity. In a "heavy" dust cloud, which is described as a condition which "creates an enveloping cloud with full *brownout*. [The] horizon and references more than 6 ft away disappear completely", the authors state that the time spent in the dust cloud was 12 minutes before the warning level was reached, which equated to 30 brownout landings. While it is known that the severity of the brownout cloud is a function of local environment, such observations could be crucial in ascertaining the IBF's worthiness as a viable EAPS device. In certain roles, such as medical evacuations (MEDEVAC), it may not be possible to change the filter on landing, therefore it would be very useful from a mission planning perspective to know how many landings the filter will last before the bypass door is activated. When assessing the through-life costs of EAPS systems, knowledge of the transient condition would enable an estimation of maintenance or cleaning frequency. It would also embellish the performance charts that exist in rotorcraft flight manuals that by default provide performance data on operating with a pre-inlet pressure-losing device.

The results from the present work can be used in this respect too. Figure 6.10 displays the pressure drop evolution of the IBF for the EC145 in three dust cloud concentrations. The filter is seen to last from as long as 8.5 minutes in a light dust cloud, to a time of 1.8 minutes in a heavy dust cloud of 2.5 gm^{-3}. (The Sandblaster II [16] test results give an indication of the approximate concentration levels that can be designated as "heavy"; see Sections 2.2.3 and 7.2.3). For a heavy dust cloud, this estimate is substantially less than that recorded in the work of Ockier, although that the figures for lower concentrations are of the same order of magnitude is encouraging. To more reliably assess the numerical validity of the model would require real data sampling for the concentration at the intake of the EC145, and the respective engine mass flow rate. Qualitatively there is a similar trend too, in that the evolution becomes increasingly less affected by particle concentration. Incidentally, the reference velocity used here corresponds to 5 knots; other results not displayed here show that the endurance of a filter increases from 3.7 minutes to 6.4 minutes if the reference velocity is increased from 5 to 10 knots.

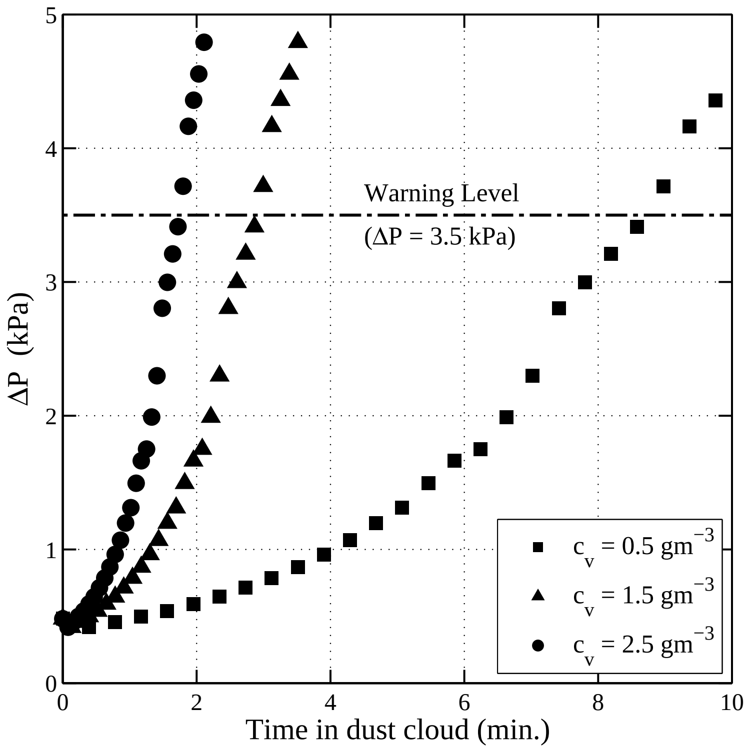

Figure 6.10: *Pressure drop evolution as a function of time spent in a dust cloud across a suggested IBF solution for the Eurocopter EC145, for three dust concentrations (U_∞ = 5 knots).*

Based on the figures provided by Ockier, a typical brownout landing takes approximately 24 seconds. For the data shown in Figure 6.10, the IBF solution proposed in this chapter allows the EC145 to make 22, 7.5 and 4.5 landings in dust concentrations of 0.5 gm^{-3}, 1.5 gm^{-3}, 2.5 gm^{-3} respectively, per filter cycle. However, the great multitude of parameters makes prediction difficult without validation from the field. With data such as sand samples from the region of operation and recordings of the quantity of dust captured per filter cycle, correlated with knowledge of the number of landings per cycle, it may be possible to comprehensively assess the operational and ultimately economic benefit of an IBF.

6.5 Summary

The concept of the optimum pleat design is ambiguous in the case of IBF. The pleat angle for minimum pressure drop and maximum holding capacity are not aligned. For this reason a new metric is introduced. The Pleat Quality Factor gives an indication of the performance of a given filter, and also exhibits an optimum design point. Both the magnitude of the PQF and the optimum design point are shown to vary as parameters of the filter or the flow change. For example, a lower throughput velocity results in a better PQF, and marginally favours a narrower pleat. These relationships are combined to create a optimised IBF design map, which can be used to set the pleat angle of a filter for a given test dust and filter medium. The map provides a number of optimum design points which are arranged by lines of constant velocity and maximum pressure drop, allowing the user to find the ideal pleat angle for a given set of constraints.

The map is demonstrated by development of a solution for the Eurocopter EC145. Using results from the two parametric studies performed, the temporal performance of the IBF installed into the EC145 is given. The rate of increase of pressure drop is proportional to the dust concentration and is exacerbated when the helicopter is in hover. A typical filter cycle time is around 11 minutes in a brownout cloud, before the pressure drop exceeds the prescribed limit. This equates to 28 "heavy" brownout landings. The results are facilitated by merging the two parametric study scales, which allows a feature of non-uniform spanwise particle accumulation to be noticed. Since each pleat along the filter has a unique mass flow rate, the abrupt transition to the cake stage of clogging is effectively "smoothed out", as each pleat reaches the critical mass at different times. This is beneficial to handling qualities of the aircraft.

The results of the performance prediction showed good agreement with the work of Ockier *et al.*, but confidence is limited by the absence of technical data. It is hoped that future work would enable real data from the field to be obtained in order to validate the models proposed and provide a greater capability to predict IBF maintenance scheduling and ultimately transient performance.

Chapter 7

Comparative Study of EAPS Technology

This chapter puts into context all the modelling performed in the preceding chapters. It uses the example of an Aérospatiale Puma helicopter operating in a dusty environment to provide data with which to compare the three main protective devices, based on a number of performance criteria.

7.1 Introduction

The physical phenomena utilised to separate particulate from engine bound air have been shown to give rise to a number of types of EAPS technology. The mechanism of capture or scavenge, the typical flow rates, and the size of each device is different. Therefore it is unsurprising that device performance varies. The aim of this chapter is to corral the results of the research on each device, into a comprehensive method for quantitative comparison. As a starting point, Table 7.1 gives a qualitative overview of each device's advantages and disadvantages.

From an engineering perspective, qualitative analysis will not suffice. Indeed it is the lack of detail in Table 7.1 that has prompted much of the research in the present work. Therefore the study is completed with a quantitative comparison of the three EAPS technologies. The aim of the comparative study is to utilise new EAPS performance indices that can be used to ascertain the most suitable form of engine protection in dusty environments. To facilitate this, a model rotorcraft is chosen to which the theory of EAPS performance is applied. Using known technical data from the literature, the key rotorcraft and engine design parameters can be sought to provide the intake flow conditions.

Table 7.1: *The main advantages and disadvantages of each EAPS system.*

EAPS Device	Advantages	Disadvantages
Vortex Tube Separators (VTS)	• Low pressure drop. • High separation efficiency. • Bypass door available if needed.	• Large frontal area to achieve required mass flow. • Icing issues. • Susceptible to FOD. • Scavenge pump required. • Inlet mass flow extracted to scavenge particles ($\simeq$ 5-10%). • Integration difficulties.
Inlet Particle Separators (IPS)	• High airflow per unit area, hence low drag. • Easily integrated to engine inlet face. • Low total pressure distortion. • Ease of optimisation.	• Relatively low separation efficiency. • Inlet mass flow extracted to scavenge particles ($\simeq$ 15-20%). • No bypass capability. • Scavenge pump required.
Inlet Barrier Filters (IBF)	• Very high, temporally increasing separation efficiency. • Reduction of total pressure distortion. • No scavenge mass flow. • No bleed flow required thus lower MGT over engine lifetime.	• Temporally increasing pressure drop due to particle accumulation. • Maintenance heavy, thus more time-on -ground (for cleaning). • Large surface area required to minimise pressure drop. • Integration difficulties.

The Aérospatiale SA 330 Puma is chosen as a test case for EAPS comparison. Of the limited technical data in the literature, this platform is the only rotorcraft alluded to in analyses of EAPS systems (in addition to the EC145 discussed in Section 6.3). Elsewhere, authors may be obliged to conceal certain technical data of the engine studied in order to preserve confidential information of the collaborating manufacturer. Nevertheless it is still possible to construct a case study from any data available in order to demonstrate the theory presented in the Chapter 3. If data were to become available in the future, the models could be applied with ease.

The SA 330 is a four-bladed, twin-engine, medium sized utility helicopter operated both within the civil and military markets. It was widely-sold and is still in service today, but is no longer produced. Its successor, based on the same airframe but enlarged with a new engine, is the highly successful Eurocopter AS 332 Super Puma, which is pictured in Figure 2.10a with a VTS system attached. Its intakes are the *forward-facing* type described in Section 2.2.4. The AS 330 Puma is powered by two Turbomeca Turmo IVB engines, and is selected as the case due to its use in the work of van der Walt & Nurick [24]. In this work, an engine power deterioration model is proposed for the erosion of engines fitted with dust filters. The model is verified with experimental test results on a Turmo fitted with a VTS particle separating device. The study reveals certain data pertaining to this engine that would otherwise be unavailable. One such key property of the engine is the erosion rate factor kU^{β}. The erosion factor kU^{β} is calculated and validated with experimental data from test with a feed of SAE Coarse test dust (identical to Arizona AC Coarse). The mass flow rate is given indirectly as $\simeq$ 5.3 kgs^{-1}, a figure which is also given in Flight International's repository of engine data [86] for this model. To enable a fair comparison of EAPS technologies, the same engine and operating conditions must be used; hence these known engine data provide a useful reference upon which to base the performance prediction of each form of protection.

The suitability of this engine for retrofitting with a VTS system is illustrated in Figure 2.10a. Currently there is no IBF solution for this aircraft but a system *is* available for the Sikorsky UH-60 Blackhawk (see Figure 2.10c), another medium twin engine rotorcraft, which suggests that a solution is not beyond possibility for an engine size of this order of magnitude. Owing to the depth of the study into IBF design presented in Chapter 6, a reasonable assertion for how such a solution may manifest can be made.

The suitability of the engine for installation of an IPS, however, is slightly more challenging since these devices are normally not retro-fitted, and come as part of the finished engine product. Additionally, the theoretical performance of this device is not covered in the present work. No analytical solutions exist in the literature, but there are several studies that solve the governing flow equations numerically and subsequently provide some IPS performance data. One such study is by Taslim & Spring [61], in which CFD is used to obtain the separation efficiency and pressure loss across an IPS for an unnamed engine. The geometry was tested in flows of different mass flow rate. Notably, the range of mass flow rates covered 0 to 6.5 kgs^{-1}. Assuming the upper limit is around the design point (N_{GG} = 100% rpm) mass flow of the engine, it is supposed that IPS being tested is designed for an engine of similar size to the Turmo. For this reason, and owing to a lack of data elsewhere, the results are extrapolated to the present work for use in comparing EAPS devices.

The foregoing presents findings of a comparison study of the three EAPS devices, in which four performance indicators are assessed: separation efficiency; power required; engine life extension; and engine deterioration rate.

7.2 Model Verification

To facilitate the study, real EAPS solutions for the Turmo engine are imagined. The design point engine mass flow rate of the engine is 5.3 kgs^{-1}, and the rotorcraft is operating in a dust cloud composition resembling Arizona AC Coarse test dust.

Despite there currently being no IBF solution for the Puma, an educated assumption can be made as to how one may be built. A simple initial solution would resemble a box-like structure attached to the contiguous intakes. Assuming an engine mass flow of 5.3 kgs^{-1}, the twin engines would require 8.6 m^{3}s^{-1} of air to operate at the design point at static sea level. To achieve a desirable IBF performance, the total projected area would need to be at least 0.87 m^2, which would give a volume flow per unit area through the IBF of 10 ms^{-1}. This can be used with the method given in Chapter 6 to determine the dimensions of the pleat, which for optimum performance has a depth of 5 cm, angle of 4 degrees, and a medium thickness of 1.5 mm. As with the pleat scale tests, the filter internal properties (fibre diameter, packing fraction, initial permeability) are adopted from the material used in the automotive study by Rebaï *et al.* [51].

For the VTS, the tubes take the dimensions of those used by van der Walt & Nurick, assumed to have a mass flow rate of 4.5 gs^{-1} and a scavenge proportion of 10%. There are 1176 tubes in the array, each of which has a diameter of 18 mm and a length of 60 mm. Unfortunately no details are given about their internal structure. Van der Walt & Nurick suggest that the frontal area of the VTS panel is of the order of 0.5 m^2; calculated using the data given, the total tube frontal area would be less than this, around 0.3 m^2 which suggests that 40% additional frontal area is required to support the tubes in an array. This can be implemented into the relevant equation. For simplicity, it is assumed that vortex tubes are all arranged on one panel and orientated to the same direction; in reality the array may be arranged around a cone as in Figure 2.10a.

The simplification ensures that all tubes achieve the same ram pressure recovery in forward flight.

The results of the flow solution for the IPS are borrowed from the study by Taslim & Spring [61], in which a CFD analysis of four inlet geometries was carried out. Three dimensional Navier-Stokes equations for air and the conservation equations for the sand particles were solved simultaneously in the Lagrangian framework. An elastic rebound condition was applied at the walls, and the $k-\epsilon$ model was used with the generalised wall functions for turbulence closure. Of the four tilt angles investigated, the "0 degrees" setting gave the best separation efficiency for AC Coarse test dust, and will be the assumed design in the comparison study. Of the three technologies featured, the IPS is the least explored despite its relative simplicity, and therefore represents a possible subject of future research. However, due to its integration with the engine, analysis of an IPS system would be difficult without collaboration with an engine manufacturer. The results presented by Taslim & Spring are verified with experimental data and are in accordance with what is known in the literature about these devices.

The main purpose of an EAPS device is to remove particulate from the air, therefore the first assessment metric for cross comparison is the separation efficiency. The calculation of separation efficiency for each device is not simple, and is invariably a function of the particle size and the flow field resulting from the construction of the device. To quote a single figure for separation efficiency would be misleading; an EAPS device is expected to function across a range of mass flow rates, to filter particles of a large size spectrum, therefore it is more relevant to compare devices in their transient performance.

The research presented in the previous chapters can be used to compare device performance over such ranges. To create a meaningful set of data for comparison requires application of the theory to consistent dust and flow properties. As stated above, the sand used as a sample case is the AC Coarse test dust, and the mass flow is over the range of mass flow rates operated by the Turmo engine. However, before applying the models, the dimensions of the devices and the dust cloud concentration need to be fixed.

7.2.1 Verification of Vortex Tubes Theory

While the vortex tube theory proposed by Ramachandran [32] was shown to correlate well with experimental data, it is accepted that there are many potential sources of error in predicting the particle trajectory through such a complex geometry. The study by van der Walt & Nurick [22] (from which the engine erosion model is borrowed) provides test results of three different vortex tubes attached to the intake of a Turbomeca Turmo, tasked with filtering AC Coarse test dust over a range of tube mass flow rates. While some key separator tube dimensions are given by van der Walt & Nurick, the data are not complete. Of the tube design parameters stated, the helix pitch is omitted. This is a key parameter in VTS theory, as it determines the radial velocity of the particle and is a key contributor to pressure loss across the tube. The tube diameter, length, and scavenge proportion are known, which leaves the collector length (which dictates the length of the separating region) as the only other unknown.

To determine the unknowns requires a degree of concession. Without proper analysis of the tube it would be difficult to validate the model for this application. However, if the unknowns were fixed at values that achieved similar results to the experimental results, then a level of applicability can be assumed. Figure 7.1 shows the separation efficiency of AC Coarse test dust as a function of tube mass flow, calculated by theory for three collector length / helix pitch combinations, correlated with the test data available. The grade efficiency at each tube mass flow is calculated by the equations set out in Section 3.4.2, then extended to the efficiency for the whole distribution by Equation 3.129. For realistic values of helix length (40% and 55% of the tube length) the theory appears to predict the separation efficiency quite well for tube mass flow rates around the design point of 4.5 gs^{-1}, but overpredicts the efficiency below 2.5 gs^{-1}. This could be for a number of reasons. Firstly, particle bounce has been neglected in the theoretical model, although one would suppose that this assumption affects to a greater extent the higher inertia particles. Secondly, the particle forces are assumed to be balanced, which means there is no acceleration of the particle relative to the air. Clearly, for a particle to transition from purely axial motion to one composed additionally of a radial and tangential component, requires acceleration. Thirdly, no accounting for any air-particle mixing in the separating region is made. The separating region will contain a vortex, with a low pressure core. As the vortex decays the air pressure will tend to equalise, which may drag some lower inertia particles into the core flow. The complexity of the physics of flow inside a vortex tube can be appreciated, and indeed may provide scope for future investigation into this type of EAPS device.

Despite the discrepancies, the agreement around the design mass flow rate permits use of the theory for further performance calculations. The separation efficiency appears to be less sensitive to changes to the collector length than the helix pitch. A widely quoted figure for the separation efficiency of a VTS for AC Coarse test dust is 95%. Tuning the variable parameters around the values presented in Figure 7.1 to achieve this (albeit arbitrary) figure yields a set of tube dimensions with which to progress.

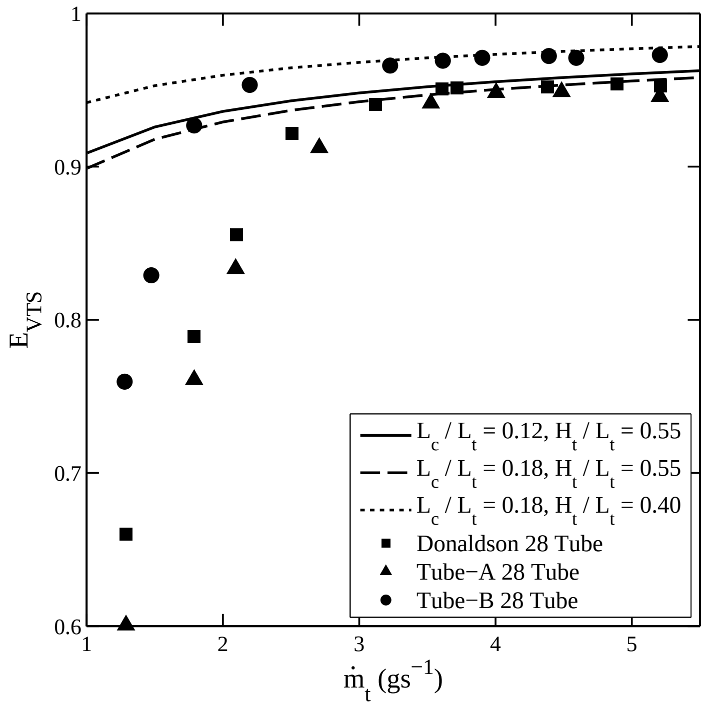

Figure 7.1: *Theoretically-derived separation efficiency for a range of tube mass flow rates, of three tube designs of varying collector length / helix pitch combinations, plotted with test data from van der Walt & Nurick [22] for three real vortex tubes.*

7.2.2 Verification of Inlet Barrier Filter Model

The lack of experimental data relating to IBF makes verification of the model more troublesome. Instead the degree of applicability is dependent on the reliability of the theoretical models used to derive the governing equations. These models are all supported by experimental data, although it is accepted that model inaccuracies may aggregate, and increase the overall error. Hence the models and results stated hitherto must be applied with a degree of latitude for their accuracy in predicting IBF performance. Nevertheless the CFD model used is well-established and has been applied elsewhere to success within industry. Its applicability for the current case was discussed in Section 4.2.5 and the results match the literature, albeit qualitatively, enough to yield a proof-of-method design protocol for IBF (see Section 6.3).

To use the results to compare the performance of the EAPS systems available requires a unifying of the fabric scale and pleat scale results. The fabric scale results give the transient separation efficiency of the medium, while the pleat scale results yield the temporal pressure loss across the chosen pleat size. The main stumbling block lies in determining the filtration velocity for use in the separation efficiency equation. As has been demonstrated in Figure 5.5, the presence of the pleat significantly modifies the flow field in the approach to the filter surface. This is likely to influence the entry Reynolds number of a particle hence its penetration. For planar media, the filtration velocity is simply the flow rate divided by the surface area; pleated filter theory can similarly be applied to determine the superficial velocity, using the increased area as a reference for the total filter surface area. However, when studying the flowfield, it was found that the area-weighted average velocity magnitude at the filter surface was greater than the theoretical velocity based on surface area. One explanation for this is that the air decelerates before *and whilst* entering the filter medium. During passage through the filter medium, the velocity is considerably lower than the approach flow. This is exemplified by the local minima shown in Figure 5.8.

Deciding the filtration velocity is one conundrum; determining the velocity at which the particle permeates the medium is perhaps even more troublesome. A more in-depth study may have applied the methods of the intake scale to introduce particles to the solved flow field of the pleat scale results to record the velocity of the particle passing across the filter boundary. But such a study is exhaustive alone: ultimately the velocity depends not only on the properties of the individual particle (size, shape, density) but also the spanwise position at which it enters the domain. Ultimately a more general approach is required. To demonstrate the sensitivity of the separation efficiency model to filtration velocity, Figure 7.2 displays the predicted efficiency of separating AC Coarse test dust from the influent air for three methods. The first two have been discussed already; the third is based on the inflow velocity, and assumes that the pleat has no effect on the particle's velocity. This may not be too far from reality for the heavier particles in the spectrum.

The curves essentially represent an envelope of separation efficiency for a filter of these properties, over a range of typical IBF inflow velocities. The curves appear to converge with increasing velocity, reaching a minimum discrepancy at 12 ms^{-1} of around 4.5%. Theory dictates that the probability of particle capture is improved as the velocity increases, as the particles possess too much inertia to navigate the fibres. For this reason a high filtration velocity is desired. For the range of particle sizes found in the AC Coarse test distribution, the Reynolds number at an initial flow speed of 10 ms^{-1} varies from 1.4 to 140; the mean particle size by mass for the sample of test dust used here is 28.4 μm, which equates to a particle Reynolds number of around 20 in this flow. To provide a first order solution to the dilemma of which filtration velocity to use, a simple calculation based on Newton's Second Law is performed to calculate the response time of a particle of the mass mean diameter. If the flow decelerates from 10 ms^{-1} to 1.24 ms^{-1} (the theoretical superficial velocity), a particle of size 28.4 μm and of drag coefficient 1 would require around 30 cm to reach the same velocity, which is an order of magnitude higher than the pleat depth. If the same particle were decelerating to a velocity of 5.089 ms^{-1} (the area-weighted surface filtration velocity recorded in the CFD simulation), it would require 4 cm to reach the filtration velocity. This is of the same order of magnitude as the pleat depth. It is likely that the true average filtration velocity lies within the lower bracket of velocities featured in Figure 7.2. In the short distance it has to decelerate to this velocity, a mean size particle of AC Coarse test dust will probably decelerate to a velocity that lies within the upper bracket. Hence, a reasonable engineered guess for the particle penetration velocity is that of the middle curve in Figure 7.2, taken from the CFD simulations. Based on this assertion, the separation efficiency of a clean filter based on the properties stated above in an inlet flow of 10 ms^{-1}, is 98.4%. This is 1% less than the (single) value quoted by IBF manufacturers, but will increase as the filter takes on particles.

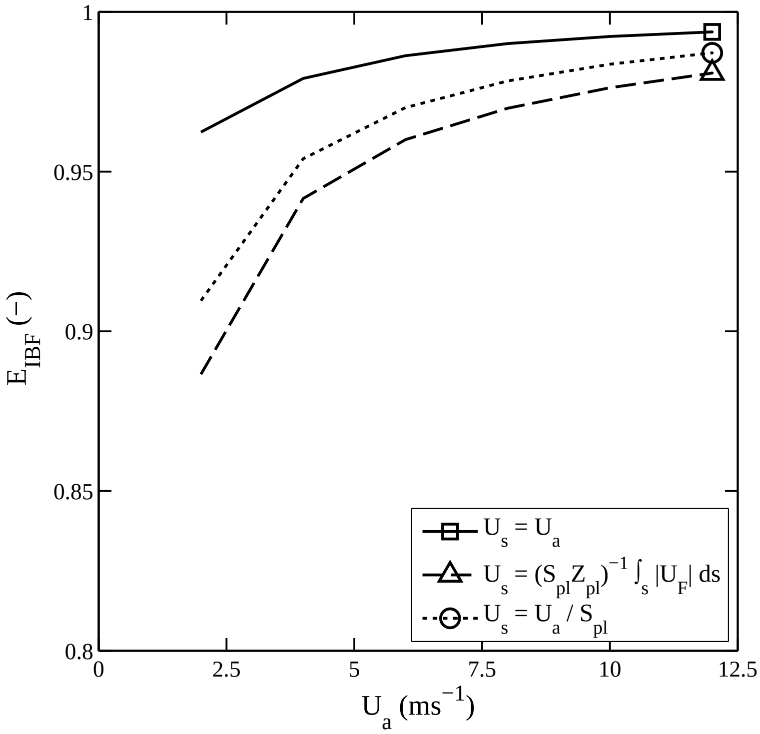

Figure 7.2: *Pleated IBF separation efficiency prediction as a function of volume flow per unit area (throughput velocity), for three filtration velocity methods (where U_s is the superficial velocity, S_F is the filter surface area, and S_{pl} is the specific surface area).*

7.2.3 Establishing a Usable Brownout Concentration

To investigate the transiency of EAPS performance requires knowledge of the local dust concentration. In Section 2.2.3 the results from the Sandblaster II [16] tests were presented; while in Section 3.2.7, a theory of predicting brownout severity based on rotorcraft parameters by authors Milluzzo & Leishman [3] was outlined. These are combined to make an educated guess of the dust concentration around a Puma in a Brownout landing.

The main rotorcraft design parameters are first compared with a similar aircraft — the Sikorsky HH-60. The parameters of the two aircraft are listed in Table 7.2. One of the more important parameters in the generation of brownout is the disk loading, which is shown to be very similar here. It is combined with the remaining parameters to derive the severity metrics given by Milluzzo & Leishman. These can be compared with the brackets provided in Table 3.2 to predict the severity of the brownout cloud. The normalised wake strength Γ_w^* is a measure of the cloud intensity; the reduced frequency k_s is a measure of the speed at which the cloud forms; while the normalised average downwash is a measure of rate at which the cloud convects radially away from the rotorcraft. The values given in Table 3.2 suggest that both aircraft suffer a rapid development of the dust cloud (Level 3), but that the overall intensity of the cloud is low (Level 1). The HH-60 has a stronger downwash than the Puma (Level 3 versus Level 2), which may be beneficial from a engine damage standpoint since the risk of dust reingestion through the rotor disk is reduced.

Table 7.2: *Particle size and shape distribution parameters of the four powders tested by Endo et al. [77] to verify Equation 3.69.*

Rotorcraft/ Parameter	HH-60		Puma	
N_r	1		1	
N_b	4		4	
c_b	0.53	m	0.50	m
R_R	8.17	m	7.00	m
Ω_R	258	rpm	270	rpm
DL	383	Nm^{-2}	390	Nm^{-2}
W	8187	kg	7000	kg
Γ_w^*	0.040		0.045	
w^*	0.119		0.113	
k_s	0.130		0.134	
c_v (“A1” from Ref. [16])	1.16	kgm^{-3}	—	

The theoretical severity levels can be compared with the real data obtained from the Sandblaster II tests, to gain a greater understanding of the dust concentration at the intakes of a Puma, assuming the similarity of the parameters given in Table 3.2 permit use of the HH-60 as a surrogate. While no dust concentrations are correlated with the theoretical severity model, certain patterns are observed between the two approaches. The peak dust concentration for the HH-60 brownout cloud is recorded at station “B1”, which is at a distance of 30 m away from the rotorcraft, at a height of 0.5 m above the ground. The dust concentration at this location is 2.50 gm^{-3}; with increasing height the concentration falls, to a level of 1.59 gm^{-3} at 7 m. Closer inboard, the dust concentration at a radial distance equal to the rotor radius is 2.09 gm^{-3} at 0.5 m, and 1.16 gm^{-3} at 1.4 m. While these data do not depict fully the density distribution completely, they at least give the impression of a cloud evolution that begins with a dense layer close to the ground, and radiates outward with increasing intensity. Such a shape is symptomatic of a rotorcraft with high downwash, from which a groundwash is produced jet that pushes material away from the aircraft.

With low reingestion rates through the rotor disk, one could make the assumption that the brownout concentration at the engine intakes may not be quite as high as the peak concentrations found elsewhere in the dust cloud. The preceding discussion may ultimately be academic, because the reality of the situation is that the dust cloud topology is unsteady and very difficult to predict. A rough estimate for the dust concentration at the intake of a Puma is based on the closest station — “A2” — to the rotor disk, which is 1.16 gm^{-3}. A more reliable estimation is desired, but perhaps not possible without data recordings from the field. This figure can be inputted into Equation 3.2 to find the mass concentration c_m, which can be substituted into Equation 3.1 to find the mass of dust fed into the EAPS device or engine, per second. The composition of the dust is another potential error source. The use of AC Coarse test dust is a best estimate at the current state of the art. As discussed, it is used as a reference PSD both in the literature and as a standard in the industry; the practice is extended here too.

7.3 Separation Efficiency

With the dimensions of the devices set, it is possible to begin comparing the devices. PSD data for SAE Coarse test dust is extracted from van der Walt & Nurick’s study. The sample mass proportions for each particle size are more expansive than the sample used thus far in the study, and are adopted as the reference sand for the VTS and IBF models due to their use in deriving the engine erosion model. The particles are treated as spherical. For the IPS prediction, results are limited to what is published by Taslim & Spring [61]. One of the size distributions tested in this study is indeed AC Coarse test, but has been sampled differently and consequently exhibits a different mass fraction curve. However, the concurrence of the cumulative mass fraction curves used in the two studies confirms that the sand data relate to a similar composition (the discrepancy can be attributed to the van der Walt PSD data being more refined). This is shown in Figure 7.3.

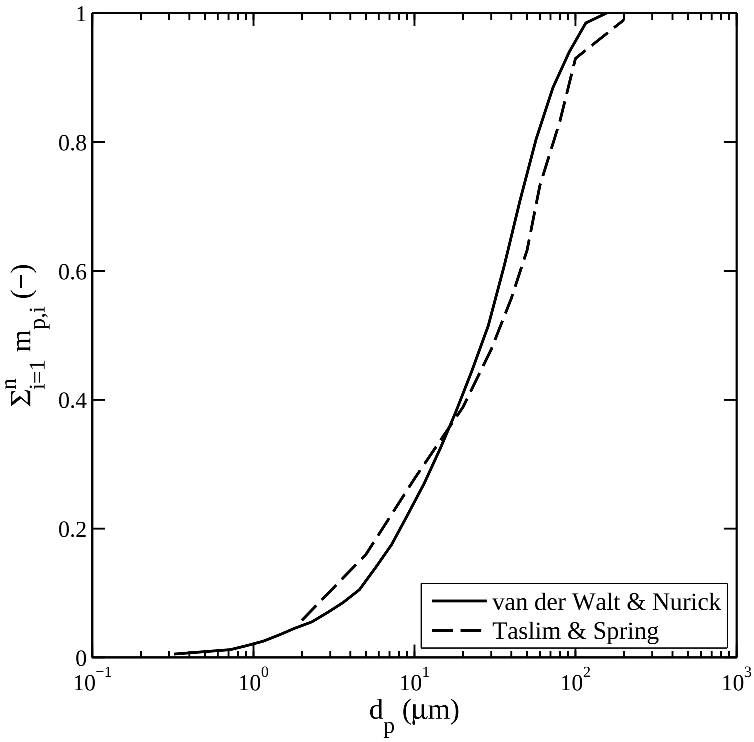

Figure 7.3: *Cumulative mass fraction curves of AC Coarse PSD data used in the studies of van der Walt & Nurick [24], and Taslim & Spring [61].*

7.3.1 Grade Efficiency

The grade efficiency is first compared, to assess the separation capability of each device over the range of sizes found in AC Coarse test dust. The results are shown in Figure 7.4. Both the VTS and IBF separate fully the majority of the range, although the IBF performs better at removing the smallest particles in the range. This is significant given that damage can be caused by particles as small as 1μm in diameter. The data for the IPS are displayed separately due the misalignment of sample size groups, but illustrate a similar trend, in that beyond a certain particle diameter all particles are removed from the flow. Notably, the value at which this occurs is a much larger diameter, around 20 μm, than the maximum size that evades capture by the VTS (9.0 μm) and IBF (4.6 μm) devices.

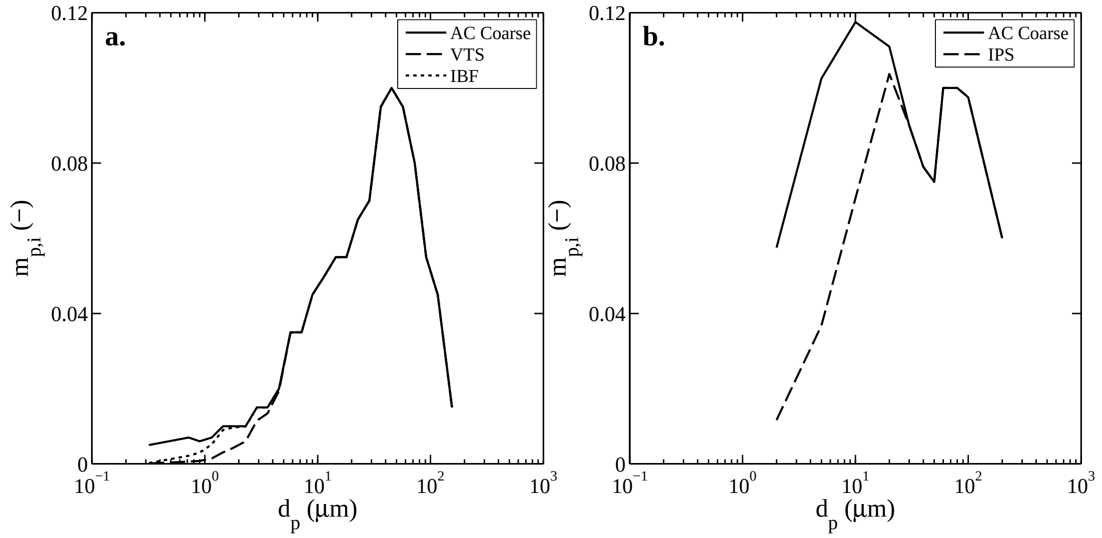

Figure 7.4: *Proportion of mass scavenged or captured for the range of particle sizes that comprise AC Coarse test dust, when filtered by a. VTS and IBF; b. IPS.*

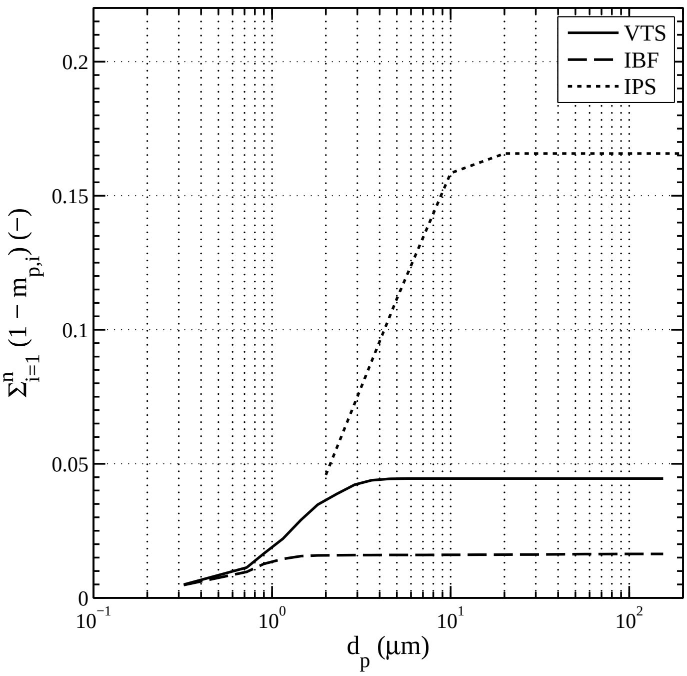

Figure 7.5: *Cumulative mass fraction of ingested particulate for the range of particle sizes that comprise AC Coarse test dust, when filtered by a. VTS and IBF; b. IPS.*

The difference in separation efficiency between the three devices becomes meaningful when it is considered how much of the ingested mass evades capture to reach the engine. Figure 7.5 displays the cumulative mass fraction of particles that evade capture to be ingested by the engine. A steeper gradient indicates the portion of size range that will most dominate the PSD of the ingested particulate, while a flat section indicates that no particles of that size are ingested (since the cumulative total does not rise). The last ordinate value on the curve represents the fraction of total mass fed that escapes capture. Clearly from this plot the IBF performs best, closely followed by the VTS and then the IPS. A diagnosis of the ingested particulate will be dealt with in the foregoing sections.

7.3.2 Overall Efficiency

The total mass ingested indirectly leads to assessing the overall efficiency of the device. As detailed in Section 3.5.1, the overall efficiency of an EAPS device is the mean separation efficiency over the range of grade efficiencies. For devices that scavenge a proportion of the influent mass flow, the efficiency is corrected according to Equation 3.132. Figure 7.6 shows the variation in overall separation efficiency as a function of engine mass flow rate for the VTS and IBF devices. The comparison with IPS cannot be made due to a lack of data. Both devices illustrate a dependency on engine mass flow rate, with the IBF outperforming the VTS by approximately 3.5%, which is consistent across the range. The plot shows that even at low mass flow rates both devices perform well although the most crucial times for EAPS use are when the helicopter engine is performing at close to full power, during landing and takeoff.

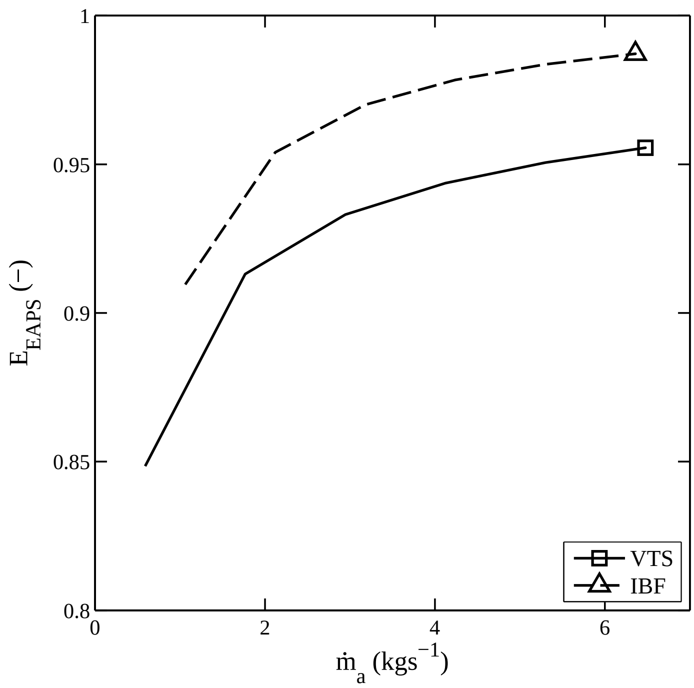

Figure 7.6: *Overall separation efficiency of VTS and IBF devices as a function of engine mass flow.*

The transient performance of the EAPS systems is also compared. In comparison with the other technologies, the IBF possesses the advantage of a temporally increasing separation efficiency, due to the captured particles decreasing the medium porosity. Figure 7.7 shows the temporal characteristic of the overall separation efficiency of each EAPS device. The abscissa relates to the time spent in a brownout cloud of constant concentration of 1.16 $\mathrm{kgm^{-3}}$, comprising a composition resembling AC Coarse test dust. Of course this is an idealised situation: in practice the concentration itself is likely to be unsteady, as indeed will be the size distribution. Expressing the temporal characteristic as a function of collected mass may be more appropriate for comparison with other filters, but from a helicopter operations perspective, expressing it in this way provides context.

Clearly the only time-variant device is the IBF; the apparent "jump" to an efficiency of 100% is a modelling assumption. This point represents the transition to cake filtration, when the filter medium has reached capacity. At this clogging stage the efficiency is assumed to be unity due to the creation of much lower porosity cake (compare a typical cake porosity of 0.65 with the filter medium porosity of 0.95). The transition occurs here once the filter has spent approximately 3 minutes in the brownout cloud.

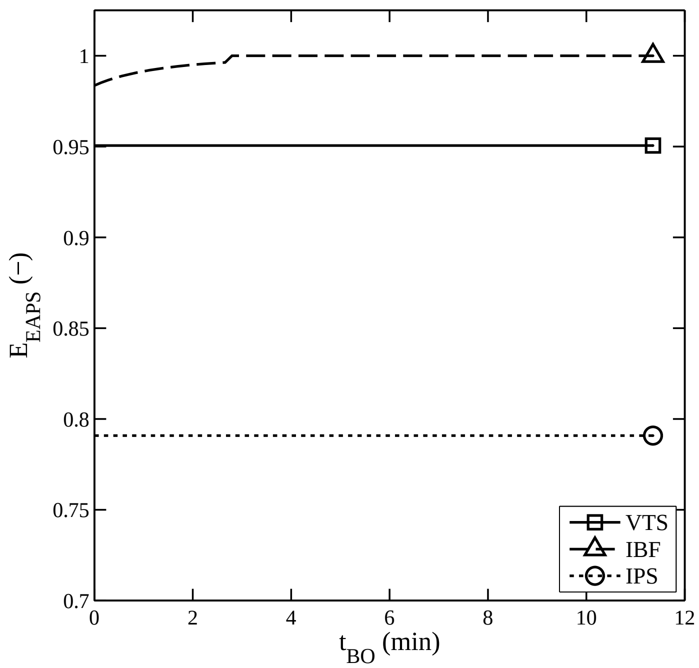

Figure 7.7: *Transient overall separation of EAPS devices, in particular showing the temporal increase in IBF efficiency.*

7.4 Power Requirements

While separation efficiency defines the proficiency of each device at performing the main task, the power required to enact the forces of separation is a measure of the cost. The main source of power is the pressure lost by the flow through the device, however in some devices power is also required to service a pump to scavenge a portion of the flow and extracted particles away from the core flow. Additionally, the size and location of the device on the airframe has an impact on the extra work required by the engine in the form of accompanying drag. Therefore the method of comparing devices by power consumed affords a practical assessment of the main drawback of employing EAPS technology.

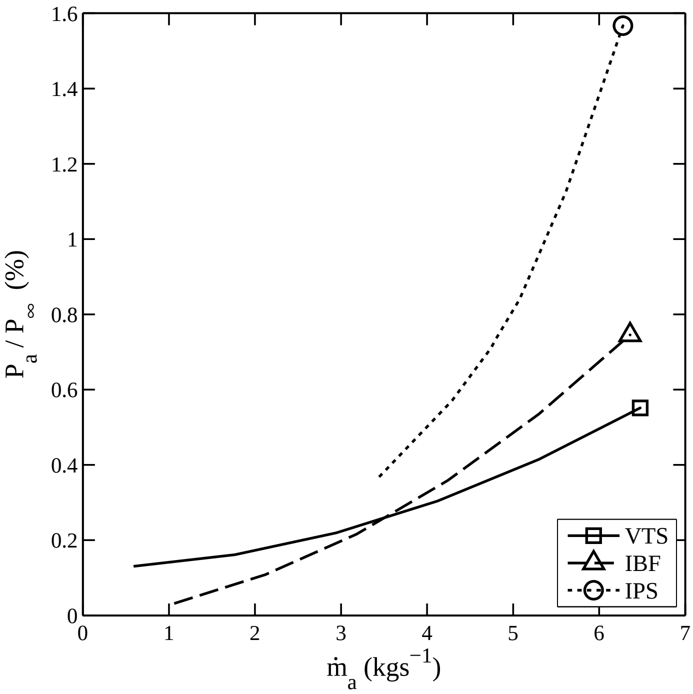

Figure 7.8: *Effect of engine mass flow rate on EAPS device total pressure loss normalised with available pressure in hover at Standard Sea Level conditions.*

7.4.1 Pressure Drop

An initial comparison of the pressure loss across each EAPS device is presented first. Figure 7.8 shows the variation of pressure drop across a range of Turmo engine mass flow rates for each device. The results suggest that the VTS suffers the least loss of pressure at the design point mass flow rate of 5.3 kgs^{-1}, and is least sensitive to changes in mass flow. The IBF performs best at low mass flow rates, although there are data missing for the IPS at the same operating point. The IPS pressure loss rises sharply with mass flow rate and is more than double the IBF pressure loss at a mass flow rate of 6 kgs^{-1}. Expressed as a percentage of the total pressure available, the total pressure loss at the design mass flow rate of 5.3 kgs^{-1} for the VTS, IBF and IPS devices is 0.42%, 0.54% and 0.96% respectively. This of course is only true of one engine speed, during hover, and excludes the capture of particles.

7.4.2 Power Consumption

A more complete picture of the effect of the EAPS system on engine performance is found by collecting all sources of loss together, calculated from the equations given in Section 3.5, and plotting the power expended on servicing the EAPS as a fraction of the maximum power that the engine can deliver, in two scenarios. The first scenario is the transient condition, in which the helicopter is hovering in a brownout cloud and the is engine working at the design point mass flow. The second scenario investigates the power required to service the EAPS in forward flight in order to consider the effect of device drag, although an assumption is made in that the engine mass flow rate remains constant, when in practice the engine power requirement (ergo mass flow) reduces with helicopter forward speed (up to a point — see Chapter 13.2 of Filippone [87] for a comprehensive discussion of helicopter power requirements in hover and forward flight).

The results are shown in Figure 7.9. In Figure 7.9a the abscissa refers to the total time spent in the brownout cloud. The fluctuating power required by the IBF is a manifestation of the cleaning cycles discussed throughout the present work: the pressure drop across the filter is monitored by a sensor, which notifies the pilot when the difference reaches an unacceptable level. This may differ between aircraft, depending on the size of the engine. In the current example a pressure drop limit of 3 kPa was assigned. It can be seen that the power required at this limit reaches a peak of 1.27% before the IBF panel is cleaned or replaced after 10 minutes. This equates to 6 filter cycles per hour in a brownout cloud. Incidentally, the manufacturers of IBF recommend replacing the filter after 15 wash cycles, which at the current rate is every 2.5 hours total time spent in a brownout cloud. Of course, the constant conditions are unlikely to prevail for longer than the 10 or 20 seconds it takes to land or takeoff, but this figure gives some indication of IBF endurance.

The evolution of the IBF curve is interesting: initially it is the least power-hungry device, but after approximately 5 minutes its state pushes the IBF beyond the requirements of even the IPS. The IPS and VTS are invariant in time, with the VTS requiring approximately half the power of the IPS. In transition to forward flight, all devices are assumed to recover pressure from the forward motion of the helicopter with 100% efficiency, while the drag is seen to act on the area containing the streamtube when the freestream velocity exceeds the core flow velocity. Pressure recovery is possible if the axial flow velocity through the device is less than the freestream velocity. When the engine face velocity exceeds the freestream velocity, a small amount of thrust (or negative drag) is produced in effect; this thrust is neglected here. (A short discussion of intake drag is given in Section 5.4.4).

The IPS is positioned just in front of the engine inlet, and therefore does not contain any components that could cause additional drag. The decrease in power required is attributable to pressure recovery, which relieves some of the work of the scavenge pump. For the same reason, a initial decrease in required power is seen to service the VTS up to a forward speed of around 18 knots, beyond which the power increases due to the emergence of form drag. The form drag appears at a freestream velocity greater than the average capture streamtube velocity, hence for much of the range the power required to service the IBF is constant. The assessment of performance in forward flight is important in determining the performance of the helicopter in cruise when EAPS are fitted, which may help to justify the use of engine protection.

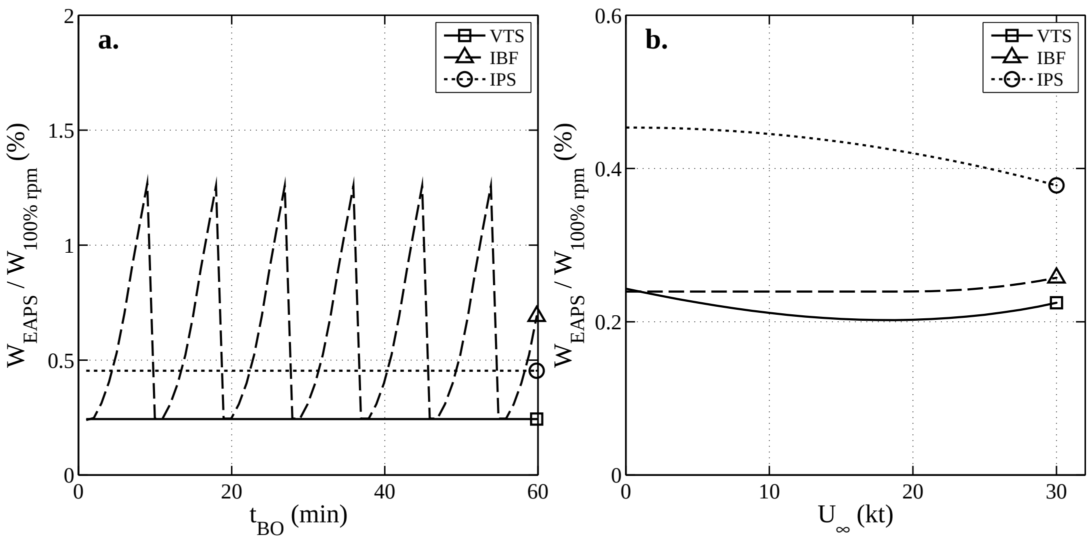

Figure 7.9: *Comparison of the power required by each system in two operational scenarios: a. hover in a brownout cloud of concentration 1.16 kgm^{-3}; b. transition from hover to forward flight up to 30 knots, with clean IBF and constant engine mass flow.*

From this relatively simple analysis, it is established that the IPS requires the most power for the range studied. However, if the data were extrapolated to higher cruise speeds, there may be a switching of this trend. Furthermore, the simple modelling excludes the additional airframe drag created as a consequence of the EAPS device's presence, such as described in Section 5.4.4, which would surely become significant at high freestream velocities. Investigation of this requires further work beyond the remit of the current study. A final point to make is that it could be argued that since the IPS is integrated into the engine from the outset by the manufacturers, its effect on engine performance has already been accounted for. It is the engine manufacturer's obligation to deliver the power requested by the client. If optional extras are included in the specification, they must already be catered for by the power output of the engine. From a performance loss standpoint, this may make the IPS more favourable over the other devices, but as will be seen in the forthcoming section, the costs of an inferior separation efficiency may still dominate the comparison.

7.5 Engine Life

In the preceding section, the three EAPS devices were shown to achieve differing separation efficiencies. The separation efficiency of a device can be expressed as a single number for a given dust, but such detail is not sufficient to assess the efficacy of a device. By looking instead at the grade efficiency that can be achieved by a particle separator, it is possible to ascertain the size distribution of the particles that evade capture. No device is 100% efficient, therefore it can be expected that some damage will be incurred by the engine as a result of erosion or otherwise. Therefore it is important to know the properties of the particles that are not removed by the EAPS. The size distribution of the unfiltered particulate can be determined using the same methods used to ascertain the PSD of the initial dust, as outlined in Section 3.2.2, and can be calculated theoretically as the opposite of the captured mass of a given particle size.

7.5.1 Engine Lifetime Extension

The financial worth of employing an EAPS system can be quickly established by estimating the extension to engine life over the unprotected case. The Engine Improvement Index is a metric proposed by van der Walt & Nurick [22] which gives a single number to express the factor by which an engine life can be extended due to the removal of particles. The simple metric may also be used to compare EAPS devices with other protection methods such as blade coatings. The authors use an experimentally-derived size distribution of unfiltered dust to validate a proposed engine erosion model, which is described in Section 3.5.3. Using the same expressions for grade efficiency that were used to create Figure 7.4, the PSD of the particles that evade captured can be found. From this, an effective mean diameter of the unfiltered particles can be determined and implemented into Equation 3.158 along with the overall separation efficiency of the device to yield the Lifetime Improvement Factor (LIF). The results are summarised in Table 7.3. The condition of hover in a brownout cloud of AC Coarse test dust at the engine design mass flow rate is used as the test case.

Looking firstly at the Lifetime Improvement Factor, there is a stark contrast between the three devices. The VTS and IBF eclipse the IPS in terms of extending engine life,

Table 7.3: *Summary of Lifetime Improvement Factors of the three EAPS devices, with mass mean diameters (ϕ_{eff}) of escaped particulate.*

EAPS Type	$\overline{E}_{EAPS}$	d$_{eff}$ (AC Coarse)	ϕ_{eff}	LIF
VTS	95.06 %	38.74 μm	1.79 μm	530
IBF	98.36 %	38.74 μm	1.48 μm	1325
IPS	79.08 %	49.38 μm	6.24 μm	38

by over ten and twenty times respectively. Thanks to its superior overall separation efficiency, the IBF also outperforms the VTS by more than double, although the mean particle size of the escaped particulate is slightly larger than the VTS. This can be explained by examining more closely the grade efficiency of the IBF at these conditions: across the range of particle sizes, even the largest sizes in the distribution of 100 μm, the efficiency does not reach unity, unlike its counterpart. Theoretically therefore, a very small fraction of larger-diameter particulate evades capture and contributes to the mean diameter seen in Table 7.3. Over time the efficiency does reach 100%, which will gradually decrease the mean particle size, however the transient case is not considered here. As a point of clarity, the mean particle size of the initial AC Coarse dust is larger for the case of the IPS due to use the of different data for the PSD.

Clearly, employment of any device is favourable from a financial perspective, although it would be interesting to carry out a full fiscal comparison study that also included life extension due to blade coating. It is true that these are unverified theoretical estimates, and reflective of just one operational condition, but if it is considered that an unprotected engine can last just 25 hours in such conditions, an LIF of just 150 can push the engine lifetime due to erosion to a level that is on parity with the regular MTBO.

7.5.2 Engine Power Deterioration

The main objective of the experiment conducted by van der Walt & Nurick was to predict the rate of power loss as a function of ingested mass. After an initial unsteady phase, during which the power was actually observed to increase due to surface polishing, their results showed a linear decrease of engine power with total mass ingested, but the rate of decrease was observed to lessen with decreasing particle size. This linearity is observed for up to 10% power loss. The reduction in power was fully attributed to erosion of the compressor; in practice the smaller particles can impact and coalesce with the turbine blades at the hot end, causing further deterioration of power, but this aspect of damage is not modelled here. The proposed formula for engine deterioration rate is given in Equation 3.151. It requires knowledge of the size distribution of the particulate that evades capture, and knowledge of the erosion factor kU^{β}, which is dependent on the impact velocity of the erodent, the properties of the erodent, and the properties of the compressor blade. The erosion factor is essentially the ratio of the power deterioration rate and the effective ingested particle size. It was calculated after two experiments: firstly after recording the power loss due to the ingestion of unfiltered SAE Coarse test, and secondly after ingesting particulate unscavenged by a Donaldson vortex tube separator array; and found to be very similar (-1.40 and -1.45 respectively), suggesting that while some dust properties may influence k, the effect is minimal.

The findings from the study are applied in the present work. The grade efficiency of each device gives the mass fraction of each particle size group removed from the initial test dust; what is not removed contributes to the "ingested" dust particle size distribution. These data are inputted into Equation 3.151 to give the power deterioration rate as a function of particulate mass fed into the system. Combining this with the power required to operate the EAPS systems, as discussed in Section 7.4, allows a holistic assessment of the impact of EAPS on prolonging engine life in harsh environments. The results are given in Figure 7.10.

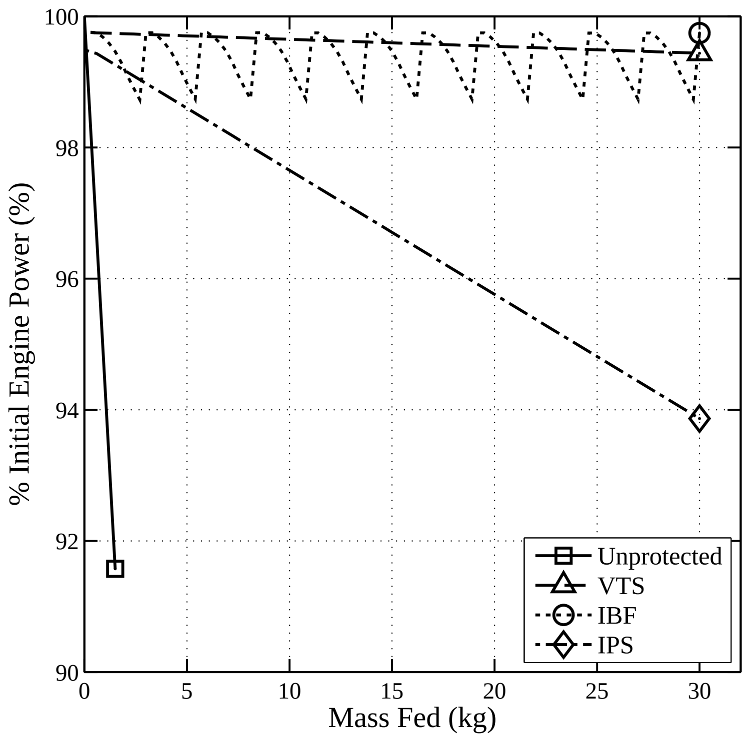

Figure 7.10: *Engine power deterioration as a function of mass fed, as predicted by van der Walt & Nurick comparing case of no protection with longevity achieved by the three EAPS devices.*

The ordinate of Figure 7.10 expresses the power loss as a percentage of the initial power, while the abscissa provides a reference for the total mass fed. The mass fed refers to the mass of particulate reaching the intake *before* passing through the EAPS. Expressing the power loss as a function of mass fed eliminates the need to know the local dust concentration. However, it must still be assumed that the engine is working at the design mass flow rate, as this affects the separation efficiency. A striking trend visible in Figure 7.10 is the rate at which the unprotected engine loses power. After ingesting just 2 kg of AC Coarse test dust the power is reduced by 8.4%. In contrast, all EAPS systems exhibit a saving of engine power, even after filtering as much as 30 kg of dust. At this point, the dust that was not scavenged by the IPS and VTS systems has contributed to a power loss of 6.1% and 0.6%, which includes the initial power required to service the device.

The power loss signature of the IBF displays the characteristic fluctuations symptomatic of the cleaning cycles. Interestingly the gradient of the power loss during a cycle is steeper than the IPS slope. If the maximum permissible pressure loss were greater, the troughs would extend lower. The power loss of the IBF generally varies between a minimum of 0.25% to a maximum of 1.25%, with only a slight decrease in the average quantity. The power loss of the VTS appears to encroach increasingly into the trend of the IBF, but over the range shown remains less than the average power lost due to use of an IBF. Extrapolation of the data suggests that the IBF will outperform the VTS after around 50 kg of dust fed. For a dust concentration of 1.16 gm^{-3}, this equates to 166 minutes of brownout landing time.

7.6 Summary

The motivation of this Chapter was to contextualise all the work carried out in the present study. It pits the three main EAPS devices against each other using theoretical models of varying levels of fidelity. The EAPS are assessed on a number of performance indicators: grade efficiency, separation efficiency, pressure drop, power required, engine lifetime extension and engine erosion rate. To facilitate the cross examination, a test case was set up using the rotorcraft and engine design parameters of an Aérospatiale SA 330 Puma and the properties of AC Coarse Test dust.

The results show that the VTS is the superior device when assessed on pressure loss alone at the design point conditions, but show that it is outperformed by the separation efficiency offered by the IBF. The IPS performance falls short of both the retro fit technologies in terms of particulate removal, but if the pressure loss is already catered for in the engine design, the presence of the IPS does not directly affect engine performance. However, both the IPS and VTS require power to service a scavenge pump to extract the particulate, which depreciates their worthiness somewhat over their passive counterpart. The IBF differs from the other technologies by exhibiting a time-variant power loss, but its superior separation efficiency translates to a much longer lifetime extension than the VTS and IPS.

All devices permit a fraction of the ingested mass through their systems, which means the engine does not completely escape damage by erosion. However the extension to life in harsh environments offered by the VTS and IBF devices would return the MTBO to more recognisable levels, inasmuch as their removal is scheduled for reasons other than erosion by particle ingestion. The effect of the power penalty on rotorcraft performance is not modelled here, but if investigated could provide enough information to more-holistically assess the financial benefits of employing an engine air particle separation device.

Chapter 8

Conclusions

The work is concluded with a summary of the main findings of the research, in which a qualitative and quantitative analysis of particle separation for helicopter engines was presented.

1 Inlet Barrier Filter performance can be enhanced significantly by altering the parameters of the internal fabric structure.

In Section 5.2 it was shown that increasing the packing fraction by 4% can increase the capture efficiency of a fibrous filter by up to 18%, however the same change causes the pressure drop to triple. In Section 5.3.2 it was shown that the time sustained in a brownout cloud before excessive pressure loss occurs can be lengthened by 44% by doubling the filter thickness.

2 The transition from internal clogging to cake accumulation causes a marked increase in pressure loss rise, but an additional 0.5 gcm^{-2} can be collected for the same pressure drop by increasing the pleat depth by 1 cm.

The characteristic "elbow" on the pressure loss curve is a feature of the relationship between pressure loss and mass collected, which signifies the transition from internal filter clogging to cake accumulation. This situation is potentially dangerous for the helicopter, as the available engine power may suddenly drop off. In Section 5.3.3 it was shown that the transition can be delayed by employing deeper or narrower pleats. This also translates to an extension of the MTBO. However as demonstrated in Section 6.3.2, this must be balanced with retaining a good separation efficiency, which decreases in accordance with such techniques.

3 The optimum pleat angle for minimum pressure drop decreases with decreasing filter medium permeability, while the optimum angle for maximum holding capacity decreases as the dust becomes finer.

The discussion of the optimum pleat shape for IBF design has prevailed throughout. In Section 5.3.3 it was revealed that the larger the filter medium resistance, the smaller the optimum pleat angle for minimum pressure loss. In the same section it was identified that the pleat channel pressure loss is more sensitive to changes in flow velocity than the medium pressure loss. In Section 5.3.4 the optimum pleat angle for maximum holding capacity of AC Coarse test dust was found to be 2.5 degrees, and was found to decrease when finer dusts are being filtered.

4 Increasing the IBF projected area by 20% increases the duration of a filter cycle by 46%, due to the reduction in the flow velocity.

In Section 5.3.4, it was shown that an increase in the projected filter area distributes the volume flow rate over a larger area, reducing the throughput velocity. This reduces the pressure loss per kilogram of particulate captured, hence extends the length of the filter cycle. The optimum design point for minimum clean filter pressure drop was shown to be invariant with flow velocity.

5 The total pressure lost due to the use of an IBF far outweighs any loss through flow separation, but the presence of the filter reduces the non-uniformity of total pressure distortion, and to an increasing degree as the filter becomes more clogged.

The presence of separated flow, otherwise known as lip spillage, arises in the intake of forward and side-facing intakes. Its presence causes the flow to accelerate at certain portions of the filter causing a local increase in particulate density, but the effect on pressure loss is around 0.05% which is small in comparison with the pressure loss of 0.6% in hover, when a clean filter is installed. However the presence of the filter helps to homogenise the distorted total pressure that occurs due to the presence of the filter. This is discussed in Section 5.4.3.

6 In hover, an intake can ingest as much as ten times the quantity of particles in an area equal to the intake entrance, but this can be reduced by 44% by angling the filter at 50 degrees to the flow.

The effect of angling the filter was shown to have little impact on the non-filter pressure drop, however for IBF performance its benefit is twofold. Firstly, the projected area is increased which reduces the throughput velocity and therefore pressure loss. Secondly, it spreads the ingested particulate over a larger area, as demonstrated in Section 5.4.5. In hover for forward-facing intakes, a filter angle of 50 degrees results in a 44% reduction in the particulate concentration at the filter. The mass of particulate reaching the filter during hover is much higher than the mass contained in the same area in the atmospheric conditions, due to a dilation of the capture streamtube.

7 In forward flight beyond the condition of full flow, both forward-facing and side-facing intakes ingest less particulate per unit area than is concentrated in the freestream condition, with the former outperforming the latter by 30% when the sand is AC Fine test dust.

In forward flight, the capture streamtube of each intake type tested changes shape due to conservation of mass. The narrowing of the capture streamtube to a smaller area than the intake area at forward speeds greater than the intake face velocity reduces the particulate catchment area. It was shown in Section 5.4.6 that if the particulate is small enough to be influenced by the fluid streamlines, which for AC Fine test dust it is, then this results in an inherent separation capability. The influence of the fluid streamtube on the particulate decreases with an increase in particle inertia, but for the sand tested this allows the forward-facing intake to outperform the side-facing intake, in terms of passive inertial separation, by up to 30%. The observation adds deviation from the side-facing superiority trend suggested by Seddon, although the advantage in avoiding FOD still stands for all forward flight speeds.

8 The optimum pleat design for minimum pressure drop and the optimum point for maximum holding capacity are not aligned; combining them creates a new metric which is sensitive to flow properties, dust properties and filter parameters.

Since the optimum design point for minimum pressure drop and the optimum point for maximum holding capacity are not aligned, a new metric called the Pleat Quality Factor was proposed in Section 6.2. A larger value of PQF means a better IBF performance. Key conclusions about IBF design are inherited from this metric. Increasing the pleat depth improves the PQF at the expense of separation efficiency, but the optimum point is invariant. A lower throughput velocity results in a better PQF, but also reduces the filtration efficiency. The optimum design point changes marginally, slightly favouring a narrower pleat angle. Increasing the filter medium packing fraction decreases the PQF and nudges the optimum point to a narrower pleat angle, however the separation efficiency is increased. The same filter performs better when filtering a coarser dust with a higher prescribed maximum pressure drop.

9 A proposed inlet barrier filter solution for the Eurocopter EC145 lasts less than 2 minutes in a dust cloud of concentration 2.5 grams per cubic metre, which equates to approximately 4.5 brownout landings.

Application of a design protocol in Section6.3 for IBF generated a solution for the Eurocopter EC145, which was combined with the results of the parametric study to yield a prediction of IBF performance. The pressure drop across the IBF reaches the critical pressure drop level after 2 minutes in a cloud of 2.5 gm^{-3}, and after 8.5 minutes in a cloud of 0.5 gm^{-3}. This equates to 4.5 and 22 brownout landings respectively. The influence of particulate concentration on the gradient of the pressure drop curve is seen to weaken with increasing concentration. The hover condition is shown to exhibit an inferior pressure drop rise over forward flight due to a non-uniformity of particulate distribution.

10 The two stages of filter clogging — internal and surface — are identified by a discontinuity in the pressure loss curve, however the transition is "smoothed out" when each pleat is prescribed its own mass flow rate based on the non-uniform spanwise particle distribution along the filter.

By marrying the two scales of parametric study in Section 6.4, it was shown that the abrupt transition to surface clogging disappears. The merger works by taking the spanwise particle distribution from the intake results and using it to generate a unique pleat mass flow rate that depends on the spanwise distance along the filter. Since each pleat has its own mass flow rate, some pleats reach capacity quicker than others, but their heightened pressure loss is dissipated into the average for the whole filter.

11 The Vortex Tube Separator is the superior device when assessed on pressure loss alone, but is outperformed by the Inlet Barrier Filter when judged on separation efficiency; the Inlet Particle Separator has the lowest drag.

A comparison study in Chapter 7 revealed the key differences between each technology, and used the performance criteria of separation efficiency, total pressure loss and power required to assess their utility as EAPS devices. A case study was set up using the Turbomeca Turmo engine to apply the theories gathered throughout the work. AC Coarse test dust was used as the test sand. The comparison study revealed that the VTS exhibited the lowest pressure drop, although the scavenge chamber losses were only loosely accounted for. The IBF exhibited the highest separation efficiency, which increased temporally at the expense of increased pressure loss due to the accumulation of particles, while the IPS contributed the least to drag due to it having no external parts.

12 When protecting a Turbomeca Turmo engine from the ingestion of AC Coarse test dust, the Inlet Barrier Filter outperforms the Vortex Tubes Separator after fifty kilograms of dust have been fed.

The comparison study also investigated the effect of EAPS, both beneficial and costly, on engine power. The superior separation efficiency offered by the IBF results in a slower rate of engine erosion than the VTS, but at the expense of a shorter term shortfall in power due to pressure loss. The VTS exhibits no temporal variation in pressure loss, but cannot achieve the high efficiency of the IBF. However it achieves the best performance of all the devices for the first 50 kg of particulate fed to the engine.

Chapter 9

Future Work

This chapter presents some recommendations for further work. In some ways the project has been like charting a new territory. A corner of the map is now settled, but there are still unknown pastures to explore beyond the hinterland.

1 Extension of EAPS modelling into three dimensions.

All simulations performed in the current work are in two dimensions, and only focus on the Inlet Barrier Filter. Indeed it would be difficult to develop a two dimensional model of a vortex tube. However, with the knowledge garnered from the numerical and analytical solutions described within the present work, it is a natural step to progress to three dimensions. This would allow more case-specific, complex geometries to be tested, given that the fundamental behaviour of these devices has been established. This would also permit an investigation into the effects on total pressure distortion.

2 Development of an analytical or semi-analytical model for performance prediction.

The potential saving in time and money by developing an analytical or semi-analytical model for IBF pleat design would be of huge benefit to the industry. This would require careful analysis of the flow in the pleat channels and in particular the development of a relationship between pleat geometry and filtration velocity. Current theories rely on assumption that Stokes number is low enough for particles to follow streamlines. This is inadequate for IBF, for which there is a large range of particle Reynolds number, and high range of flow velocities.

Bibliography

[1] F. Colucci, “Safety spotlight: Enduring power,” *Vertifilte*, vol. 53, no. 2, pp. 25—27, 2007.

[2] R. Prouty, *Helicopter Performance, Stability, and Control.* PWS Engineering, 1986.

[3] J. Milluzzo and G. Leishman, “Assessment of rotorcraft brownout severity in terms of rotor design parameters,” *Journal of the American Helicopter Society*, vol. 55, no. 3, pp. 032009–1–9, 2010.

[4] R.T.O, “Rotary-wing brownout mitigation: Technologies and training (Remedes contre le phenomene de brownout sur les appareils a voilure tournante: Technologies et entrainement),” tech. rep., NATO Research & Technology Organisation, 2012.

[5] C. Phillips, H. Kim, and R. Brown, “Helicopter brownout - can it be modelled?,” *Aeronautical Journal*, vol. 115, no. 1164, pp. 123–133, 2011.

[6] B. Johnson, J. G. Leishman, and A. Sydney, “Investigation of sediment entrainment using dual-phase, high-speed particle image velocimetry,” *Journal of the American Helicopter Society*, vol. 55, no. 4, pp. 42003–1–16, 2010.

[7] R. Bagnold, *The physics of blown sand and desert dunes.* Methuen, 1941.

[8] J. Leishman, “Investigation of sediment entrainment in brownout using high-speed particle image velocimetry,” in *Proceedings of the 65th Annual American Helicopter Society Forum*, (Grapevine, Texas), May 2009.

[9] M. Syal, J. Rauleder, J. K. Tritschler, and J. G. Leishman, “Possibilities of brownout mitigation using a slotted-tip blade,” in *Proceedings of the 29th AIAA Applied Aerodynamics Conference*, (Honolulu, Hawaii), AIAA, June 2011.

[10] J. D. Keller, G. R. Whitehouse, D. A. Wachspress, M. E. Teske, and T. R. Quackenbush, "A physics-based model of rotorcraft brownout for flight simulation applications," in *Proceedings of the 62nd American Helicopter Society Annual Forum*, vol. 62, (Phoenix, Arizona), p. 1098, May 2006.

[11] G. R. Whitehouse, D. A. Wachspress, and T. R. Quackenbush, "Aerodynamic design of helicopter rotors for reduced brownout," in *Proceedings of the International Powered Lift Conference*, (Philadelphia, PA), American Helicopter Society International, Inc., Oct. 2010.

[12] D. A. Wachspress, G. R. Whitehouse, J. D. Keller, K. McClure, P. Gilmore, and M. Dorsett, "Physics based modeling of helicopter brownout for piloted simulation applications," in *The Interservice/Industry Training, Simulation & Education Conference (I/ITSEC)*, vol. 2008, 2008.

[13] D. A. W. G. R. Whitehouse, J. D. K. K. Yu, P. Gilmore, M. Dorsett, K. McClure, and R. A. SAIC, "A high fidelity brownout model for real-time flight simulations and trainers," in *Proceedings of the 65th Annual American Helicopter Society Forum*, (Grapevine, Texas), American Helicopter Society International, Inc., 2009.

[14] C. Phillips and R. E. Brown, "The effect of helicopter configuration on the fluid dynamics of brownout," in *34th European Rotorcraft Forum*, (Liverpool, UK), 2008.

[15] C. Phillips, *Computational study of rotorcraft aerodynamics in ground effect and brownout*. PhD thesis, University of Glasgow, 2010.

[16] C. Cowherd Jr, "Sandblaster 2 support of see-through technologies for particulate brownout," tech. rep., DTIC Document, 2007.

[17] T. Lueken, N. Peinecke, H. U. Doehler, and R. Lantzsch, "ALLFlight: tackling the brownout problem," *CEAS Aeronautical Journal*, vol. 3, no. 1, pp. 1–15, 2011.

[18] H. U. Doehler and N. Peinecke, "Image-based drift and height estimation for helicopter landings in brownout," *Image Analysis and Recognition*, pp. 366–377, 2010.

[19] M. Hagelen, G. Briese, H. Essen, T. Bertuch, P. Knott, and A. Tessmann, "A millimetrewave landing aid approach for helicopters under brown-out conditions," in *Radar Conference, 2008. RADAR'08. IEEE*, pp. 1–4, 2008.

[20] A. J. Wadcock, L. A. Ewing, E. Solis, M. Potsdam, and G. Rajagopalan, "Rotorcraft downwash flow field study to understand the aerodynamics of helicopter brownout," in *American Helicopter Society Southwest Region Technical Specialists' Meeting*, (Dallas-Fort Worth, TX), Ames Research Center, Oct. 2008.

[21] J. Seddon and E. L. Goldsmith, *Intake aerodynamics.* Amer Inst of Aeronautics & Aero, 1999.

[22] J. P. V. D. Van Der Walt and A. Nurick, "Erosion of dust-filtered helicopter turbine engines part i: Basic theoretical considerations," *Journal of Aircraft*, vol. 32, pp. 106–111, Jan. 1995.

[23] A. Hamed, W. Tabakoff, and R. Wenglarz, "Erosion and deposition in turbomachinery," *Journal of Propulsion and Power*, vol. 22, no. 2, pp. 350–360, 2006.

[24] J. P. Van Der Walt and A. Nurick, "Erosion of dust-filtered helicopter turbine engines part II: erosion reduction," *Journal of Aircraft*, vol. 32, pp. 112–117, Jan. 1995.

[25] P. Stallard, "Helicopter engine protection," *Perfusion*, vol. 1997, pp. 263–267, July 1997.

[26] J. R. Ballard, "Impact of IPS and IRS configurations on engine installation design," Tech. Rep. LS-148, AGARD, 1986.

[27] W. J. C. Prinsloo, P. D. Villiers, and M. C. V. Dijken, "Vortex tube separating device," Jan. 1991. U.S. Patent 4,985,058.

[28] R. G. Holdich, *Fundamentals of particle technology.* Midland Information Technology and Publishing, 2002.

[29] U. A. M. Department, *Engineering Design Handbook. Helicopter Engineering. Part One. Preliminary Design.* Pamphlet A-700200, Alexandria, VA: AMCA, 1974.

[30] L. A. C. Klujszo, P. K. Songfack, M. Rafaelof, and R. K. Rajamani, "Design of a stationary guide vane swirl air cleaner," *Minerals engineering*, vol. 12, no. 11, pp. 1375–1392, 1999.

[31] A. M. Hobbs, *Design and optimization of a vortex particle separator for a hot mix asphalt plant using computational fluid dynamics.* PhD thesis, Georgia Institute of Technology, 2002.

[32] O. Ramachandran, P. C. Raynor, and D. Leith, "Collection efficiency and pressure drop for a rotary-flow cyclone," *Filtration & separation*, vol. 31, no. 6, pp. 631–636, 1994.

[33] J. Campolong, "Vortex separator," July 1975. U.S. Patent 3,895,930.

[34] D. R. Monson and T. E. Rosendahl, "Centrifugal separator," Feb. 1977. U.S. Patent 4,008,059.

[35] D. R. Monson, D. E. Keller, and J. C. Rothman, “Deflecting element for centrifugal separators,” June 1970. U.S. Patent 3,517,821.

[36] H. Brockmann, “Multi-stage cyclone separator,” Sept. 1981. U.S. Patent 4,289,611.

[37] T. W. Simpson, “Separator,” Mar. 1981. U.S. Patent 4,255,174.

[38] C. J. Roach, “Vortex air cleaner assembly with acoustic attenuator,” Sept. 1977. U.S. Patent 4,050,913.

[39] H. N. Shohet, A. F. Amelio, and J. F. Kowalonek, “Engine inlet air particle separator,” June 1969. U.S. Patent 3,449,891.

[40] M. J. Scimone, “Aircraft engine air filter and method,” July 2003. U.S. Patent 6,595,742.

[41] M. J. Scimone, D. Flesher, and S. Frey, “High performance barrier filtration systems,” in *Proceedings of the 56th American Helicopter Society Annual Forum*, (Virginia Beach, VA), American Helicopter Society International, Inc., May 2000.

[42] A. Filippone and N. Bojdo, “Turboshaft engine air particle separation,” *Progress in Aerospace Sciences*, vol. 46, pp. 224–245, July 2010.

[43] N. Bojdo and A. Filippone, “Performance prediction of inlet barrier filter systems for rotorcraft engines,” *Journal of Aircraft*, vol. 48, pp. 1903–1912, June 2011.

[44] N. Bojdo and A. Filippone, “Operational performance parameters of engine inlet barrier filtration systems for rotorcraft,” *The Aeronautical Journal*, vol. 116, Sept. 2012.

[45] N. Bojdo and A. Filippone, “Fabric filter performance of helicopter inlet barrier filters,” *Journal of the American Helicopter Society*, vol. 57, no. 3, pp. 1–13, 2012.

[46] C. Ockier, H. Muller, L. Wolfgang, C. Kolb, and S. Benedikt, “Flight testing an engine inlet barrier filter for the EC145,” in *Proceedings of the 65th Annual American Helicopter Society Forum*, (Grapevine, Texas), American Helicopter Society International, Inc., May 2009.

[47] D. Y. H. Pui Da-Ren Chen and B. Y. H. Liu, “Optimization of pleated filter design using a finite-element numerical method,” *Journal of Aerosol Science*, vol. 24, no. Supplement 1, pp. S39–S40, 1993.

[48] T. Lücke and H. Fissan, “The prediction of filtration performance of high efficiency gas filter elements,” *Chemical Engineering Science*, vol. 51, pp. 1199–1208, Apr. 1996.

[49] A. Subrenat, J. N. Balo, and P. Le Cloirec, "Analysis of pressure drops in pleated activated carbon cloth filters," *Journal of Environmental Engineering*, vol. 126, no. 6, pp. 562–568, 2000.

[50] R. J. Wakeman, N. S. Hanspal, A. N. Waghode, and V. Nassehi, "Analysis of pleat crowding and medium compression in pleated cartridge filters," *Chemical Engineering Research and Design*, vol. 83, no. 10, pp. 1246–1255, 2005.

[51] M. Rebaï, M. Prat, M. Meireles, P. Schmitz, and R. Baclet, "A semi-analytical model for gas flow in pleated filters," *Chemical Engineering Science*, vol. 65, pp. 2835–2846, May 2010.

[52] M. Rebaï, M. Prat, M. Meireles, P. Schmitz, and R. Baclet, "Clogging modeling in pleated filters for gas filtration," *Chemical Engineering Research and Design*, vol. 88, pp. 476–486, Apr. 2010.

[53] J. F. Stelzer and T. L. Newman, "Engine air filter and sealing system," Mar. 2007. U.S. Patent 7,192,462.

[54] J. R. Hobbs, "Gas turbine engine air intake," June 1983. U.S. Patent 4,389,227.

[55] M. D. Stoten, "Integral inertial particle separator for radial inlet gas turbine engine," Oct. 2000. U.S. Patent 6,134,874.

[56] S. R. Barr, "Particle separator for turbine engines of aircraft," Nov. 1976. U.S. Patent 3,993,463.

[57] A. Hamed, Y. D. Jun, and J. J. Yeuan, "Particle dynamics simulations in inlet separator with an experimentally based bounce model," *Journal of Propulsion and Power*, vol. 11, no. 2, pp. 230–235, 1995.

[58] B. V. R. Vittal, W. A. Bennett, and D. L. Tipton, "Development of an advanced vaneless inlet particle separator for helicopter engines," *Journal of Propulsion and Power*, vol. 2, pp. 438–444, Sept. 1986.

[59] G. O. Musgrove, M. D. Barringer, K. A. Thole, E. Grover, and J. Barker, "Computational design of a louver particle separator for gas turbine engines," *ASME Paper No. GT2009-60199, Proceedings of ASME Turbo Exp, Orlando, FL*, 2009.

[60] F. Saeed and A. Al-Garni, "Analysis method for inertial particle separator," *Journal of Aircraft*, vol. 44, no. 4, pp. 1150–1158, 2007.

[61] M. Taslim, A. Khanicheh, and S. Spring, "A numerical study of sand separation applicable to engine inlet particle separator systems," *Journal of the American Helicopter Society*, vol. 54, no. 4, pp. 042001–1–10, 2009.

[62] V. Glinas and D. Vidal, "Determination of particle shape distribution of clay using an automated AFM image analysis method," *Powder Technology*, vol. 203, no. 2, pp. 254–264, 2010.

[63] L. Uthus, I. Hoff, and I. Horvli, "Evaluation of grain shape characterization methods for unbound aggregates," in *Proceedings of the Seventh International Conference on the Bearing Capacity of Road, Railways and Airfields (BCRA)*, 2005.

[64] J. P. Van Der Walt and A. Nurick, "Life prediction of helicopter engines fitted with dust filters," *Journal of Aircraft*, vol. 32, pp. 118–123, Jan. 1995.

[65] A. Haider and O. Levenspiel, "Drag coefficient and terminal velocity of spherical and nonspherical particles," *Powder technology*, vol. 58, no. 1, pp. 63–70, 1989.

[66] R. C. Brown, *Air Filtration: An Integrated Approach to the Theory and Applications of Fibrous Filters.* Pergamon Press, 1993.

[67] C. N. Davies, *Air Filtration.* Academic Press, 1973.

[68] J. Bear, *Dynamics of Fluids in Porous Media.* Elsevier, 1st ed., 1972.

[69] F. M. Tiller and H. Cooper, "The role of porosity in filtration: V. porosity variation in filter cakes," *AIChE Journal*, vol. 8, no. 4, pp. 445–449, 1962.

[70] F. M. Tiller and M. Shirato, "The role of porosity in filtration: VI. new definition of filtration resistance," *AIChE Journal*, vol. 10, no. 1, pp. 61–67, 1964.

[71] F. M. Tiller, N. B. Hsyung, and D. Z. Cong, "Role of porosity in filtration: XII. filtration with sedimentation," *AIChE Journal*, vol. 41, no. 5, pp. 1153–1153, 1995.

[72] F. M. Tiller and J. H. Kwon, "Role of porosity in filtration: XIII. behavior of highly compactible cakes," *AIChE Journal*, vol. 44, no. 10, pp. 2159–2167, 1998.

[73] M. Aguiar and J. Coury, "Cake formation in fabric filtration of gases," *Industrial and Engineering Chemistry Research*, vol. 35, no. 10, pp. 3673–3679, 1996.

[74] L. X. Ito and M. L. Aguiar, "A study of the porosity of gas filtration cakes," *Brazilian Journal of Chemical Engineering*, vol. 26, pp. 307–315, 2009.

[75] E. H. Tanabe, P. M. Barros, K. B. Rodrigues, and M. L. Aguiar, "Experimental investigation of deposition and removal of particles during gas filtration with various fabric filters," *Separation and Purification Technology*, pp. 187–195, 2011.

[76] R. Wakeman, "The influence of particle properties on filtration," *Separation and Purification Technology*, vol. 58, pp. 234–241, Dec. 2007.

[77] Y. Endo, D.-R. Chen, and D. Y. H. Pui, “Effects of particle polydispersity and shape factor during dust cake loading on air filters,” *Powder Technology*, vol. 98, pp. 241–249, Aug. 1998.

[78] Y. Kousaka, K. Okuyama, A. Shimizu, and T. Yoshida, “Dispersion mechanism of aggregate particles in air,” *J. Chemical Engineering JPN*, vol. 12, no. 2, pp. 152–157, 1979.

[79] J. H. Choi, S. J. Ha, and H. J. Jang, “Compression properties of dust cake of fine fly ashes from a fluidized bed coal combustor on a ceramic filter,” *Powder technology*, vol. 140, no. 1, pp. 106–115, 2004.

[80] D. P. Purchas and K. Sutherland, *Handbook of Filter Media.* Elsevier, 2nd ed., 2002.

[81] M. Bénesse, L. Le Coq, and C. Solliec, “Study of particle capture mechanisms in woven activated carbon filters: Image analysis,” in *World Filtration Congress*, (New Orleans, LA), 2004.

[82] M. Bénesse, L. L. Coq, and C. Solliec, “Collection efficiency of a woven filter made of multifiber yarn: Experimental characterization during loading and clean filter modeling based on a two-tier single fiber approach,” *Journal of Aerosol Science*, vol. 37, pp. 974–989, Aug. 2006.

[83] F. M. White, *Fluid Mechanics.* McGraw-Hill, New York, 2nd ed., 1986.

[84] J. H. Ferziger and M. Perić, *Computational methods for fluid dynamics*, vol. 3. Springer Berlin etc, 1999.

[85] C. T. Crowe, M. Sommerfeld, and Y. Tsuji, *Multiphase flows with particles and droplets.* CRC Press, New York, 1998.

[86] F. International, “Flight archive | 1978 | 0057,” *FLIGHT International*, vol. 1978, p. 69, Jan. 1978.

[87] A. Filippone, A. I. o. Aeronautics, and Astronautics, *Flight performance of fixed and rotary wing aircraft.* Butterworth-Heinemann, 2006.

Appendix A

Filter Parameters and Parameter Ranges

The following is a summary of the flow properties, geometric properties, and parameters that were varied in the pleat scale and intake scale CFD simulations.

A.1 Pleat Scale Parameters

Parameter	Symbol	Value	Unit
Flow Properties			
Operating Pressure	p_∞	101325	Pa
Air Density	ρ_g	1.225	kgs^{-1}
Air Viscosity	μ_g	$1.7894{\cdot}10^{-5}$	$kgs^{-1}m^{-1}$
Intake Geometry			
Pleat Depth	Z_{pl}	30 — 50	mm
Pleat Half-Angle	θ_{pl}	0 — 10	degrees
Pleat Width	Z_{pw}	2.0 — 12.8	mm
Filter Thickness	Z_F	1.0 — 2.5	mm
Engine Properties			
Engine Velocity	U_a	2 — 12	ms^{-1}
Filter Properties			
Filter Medium Capacity	M_{FC}	0.399	kgm^{-2}
Filter Fibre Diameter	d_f	13	μm
Filter Medium Porosity	ϵ_F	0.95	(—)
Viscous Resistance Coefficient	C	$2.588{\cdot}10^9$	m^2
Inertial Resistance Coefficient	$1.570{\cdot}10^4$	m^{-1}	

Particulate Properties			
Test Dust	PSD	AC Fine, AC Coarse	(–)
Mean Diameter by Mass	$\overline{d}_{p,3}$	8.83, 28.41	μm
Standard Deviation by Mass	σ	3.72, 3.85	μm
Particle Properties			
Particle Density	ρ_p	2650	kgm^{-3}
Particle Shape	(–)	Spherical	(–)
Particle Shape Coefficient	Φ	0.524	(–)
Cake Properties			
Resistance Model	(–)	Endo *et al.*	(–)
Cake Porosity	ϵ_c	0.65	(–)
Viscous Resistance Coefficient	C	$3.149{\cdot}10^{11}$	m^2
Inertial Resistance Coefficient	D	$2.229{\cdot}10^{6}$	m^{-1}
Solution Details			
Min. Cell Size	min(l)	$0.005A_a$	m
Pressure Discretisation Scheme	(–)	PRESTO!	(–)
Momentum Discretisation Scheme	(–)	1st Order Upwind	(–)
Pressure-Velocity Coupling Scheme	(–)	PISO	(–)
Turbulence Modelling			
Turbulence Model	(–)	Reynolds Stress	(–)
Turbulence Lengthscale	l_t	0.01	m
Turbulence Intensity	I_t	3	%

A.2 Intake Scale Parameters

Parameter	Symbol	Value	Unit
Flow Properties			
Operating Pressure	p_∞	101325	Pa
Air Density	ρ_g	1.225	kgs^{-1}
Air Viscosity	μ_g	$1.7894 \cdot 10^{-5}$	$\mathrm{kgs}^{-1}\mathrm{m}^{-1}$
Intake Geometry			
Inlet Width	A_a	0.3	m
Filter Angle	θ	0 — 50	degrees
Filter Width	Z_{IBF}	0.3 — 0.42	m
Engine Properties			
Engine Mass Flow Rate	$\dot{m}_e$	2.94	kgs^{-1}
Engine Inlet Velocity	U_a	8	ms^{-1}
Porous Jump Properties			
Viscous Resistance Coefficient	C	$2.588 \cdot 10^{9}$	m^2
Inertial Resistance Coefficient	D	$1.570 \cdot 10^{4}$	m^{-1}
Pressure Drop	ΔP	0 — 3.0	kPa
Medium Thickness	Z_F	0 — 3.043	mm
Particulate Properties			
Particulate Concentration	c_v	1.0 — 3.0	kgm^{-3}
Test Dust	PSD	AC Fine, AC Coarse	(–)
Mean Diameter by Mass	$\overline{d}_{p,3}$	8.83, 28.41	μm
Standard Deviation by Mass	σ	3.72, 3.85	μm
Particle Properties			
Particle Density	ρ_p	2650	kgm^{-3}
Particle Shape	(–)	Spherical	(–)
Particle Shape Coefficient	Φ	0.524	(–)
Solution Details			
Min. Cell Size	$\min(l)$	$0.005A_a$	m
Pressure Discretisation Scheme	(–)	PRESTO!	(–)
Momentum Discretisation Scheme	(–)	2nd Order Upwind	(–)
Pressure-Velocity Coupling Scheme	(–)	PISO	(–)
Turbulence Modelling			
Turbulence Model	(–)	Reynolds Stress	(–)
Turbulence Lengthscale	l_t	0.01	m
Turbulence Intensity	I_t	3	%